

OIL-MICROBE INTERACTIONS: HYDRODYNAMIC AND CHEMOTACTIC
INFLUENCES

A Dissertation

Submitted to the Faculty

of

Purdue University

by

Nikhil Desai

In Partial Fulfillment of the

Requirements for the Degree

of

Doctor of Philosophy

December 2019

Purdue University

West Lafayette, Indiana

**THE PURDUE UNIVERSITY GRADUATE SCHOOL
STATEMENT OF DISSERTATION APPROVAL**

Dr. Arezoo M. Ardekani, Chair

School of Mechanical Engineering

Dr. Jun Chen

School of Mechanical Engineering

Dr. Suchuan Dong

Department of Mathematics

Dr. Steven T. Wereley

School of Mechanical Engineering

Approved by:

Dr. Nicole L. Key

School of Mechanical Engineering

To *Aai* and *Baba*.

ACKNOWLEDGMENTS

I begin by thanking my advisor Dr. Arezoo Ardekani for providing me this wonderful opportunity to pursue a PhD, guiding me in my research work and motivating me to work harder towards my short- and long-term goals. I am very grateful for the flexibility she has offered me while deciding the problem statements for my thesis. I also appreciate her trust in my abilities and her patience with my progress. Her work ethic and dedication toward research is truly inspiring.

I am thankful to Dr. Jun Chen, Dr. Suchuan Dong and Dr. Steven T. Wereley for agreeing to be in my Doctoral Advisory Committee, and for taking time out of their schedules for my PhD Defense.

I gratefully thank Dr. Sadegh Dabiri for helping me with the code for my first research problem at Purdue and for his collaboration in the ensuing paper. I thank all Professors who taught me at Purdue University. I owe a special thanks to Dr. Osman Basaran for teaching me the basics of the Finite Element Method, which was used directly in my research work. Dr. Basaran's course on Stability, Instability in Transport Phenomena enabled me to understand a significant section of the stability-related literature in my field. I want to thank the staff at the Rosen Center for Advanced Computing (RCAC) at Purdue University for assisting me with my questions about their computing facilities. I thank the School of Mechanical Engineering at Purdue for providing me with an idyllic atmosphere to perform my research, for awarding me the Lambert Teaching Fellowship and for giving me the prized opportunity to teach undergraduate Fluid Mechanics. I am extremely indebted to Dr. Hector Gomez for his mentorship on 'how to teach' undergraduate Fluid Mechanics at Purdue, and to Dr. Sadegh Dabiri for allowing me to teach few lectures to his section for valuable teaching exposure. I am also indebted to Dr. Carl Wassgren for his useful instruction-

related insights and to Dr. Ivan Christov for helping me immensely in preparing my lectures.

I thank the Ardekani Lab members: Vaseem, Amir, Soroush, Ziyang, Adib, Rishabh, Manish and Rajat. I specially thank Vaseem for the many intellectually rewarding discussions I've had with him and for his contributions in papers that we have collaborated on. I acknowledge Amir's help during the initial stages of my research. To my ME309 section, I am very thankful for their patience and attention during classes and their contribution toward laying the foundation for my teaching and its continual improvement over the course of this semester.

I thank my instructors, advisors and mentors from IIT Kharagpur; especially Dr. Suman Chakraborty, Dr. Jeevanjyoti Chakraborty, Dr. Aditya Bandopadhyay and Dr. Uddipta Ghosh. They were my first inspirations toward the pursuance of a PhD. An extra special thanks to my wonderful friends: Ruchir, Himanshu, Akshay, Rajat, Deepak, Sajal; for their unwavering camaraderie over the past decade!

Lastly, I express the *greatest* sense of gratitude to my family for loving me unconditionally, supporting me in all my pursuits and always inspiring me to improve in life.

TABLE OF CONTENTS

	Page
LIST OF TABLES	ix
LIST OF FIGURES	x
ABSTRACT	xxv
1. INTRODUCTION	1
1.1 Overview	1
1.2 Motion of a single microorganism in a Newtonian fluid	2
1.2.1 Hydrodynamics	2
1.2.2 Chemotaxis	7
1.3 Motion of a suspension of microorganisms in a Newtonian fluid	9
1.4 Outline of the thesis	11
2. NUTRIENT UPTAKE BY CHEMOTACTIC MICROORGANISMS IN PRESENCE OF RISING OIL DROPS	14
2.1 Introduction	14
2.2 Mathematical model	16
2.3 Results and Discussion	24
2.3.1 Influence of biological parameters, α_C , β_C and V_s	27
2.3.2 Influence of physical parameters: drop diameter and volume fraction	35
2.4 Chemotactic amplification vis-à-vis nutrient availability	40
2.5 Conclusion	42
2.6 Appendix	43
3. HYDRODYNAMICS-MEDIATED TRAPPING OF MICRO-SWIMMERS NEAR DROPS	50
3.1 Introduction	50
3.2 Mathematical model	52
3.3 Deterministic scattering and trapping	59
3.3.1 Critical trapping radius, A_c	60
3.3.2 Basin of attraction, h^*	63
3.3.3 Swimming dynamics: $h(t) - \theta(t)$ phase space analysis	66
3.3.4 Scaling laws for A_c and h^* , as $\lambda \rightarrow 0$	70
3.4 Effects of diffusive motion	74
3.5 Conclusion	79
3.6 Appendix A: Velocity of a swimmer outside a clean/surfactant laden drop	82

	Page
3.7 Appendix B: Velocity of a swimmer outside a clean bubble	84
4. COMBINED INFLUENCE OF HYDRODYNAMICS AND CHEMOTAXIS IN THE DISTRIBUTION OF MICROORGANISMS AROUND SPHERI- CAL NUTRIENT SOURCES	86
4.1 Introduction	86
4.2 Mathematical modeling and methodology	90
4.2.1 Hydrodynamic Interaction	90
4.2.2 Chemotactic Re-orientation	93
4.2.3 Near wall Effects	97
4.3 Results and Discussion	99
4.3.1 Interplay between hydrodynamic interaction and chemotaxis	99
4.3.2 Types of behaviors	104
4.3.3 Influence of the dipole strength α_D and the rotary diffusivity D	105
4.3.4 Variability in chemotactic factors: C_0/K_D and τ^*	109
4.4 Conclusion	111
4.5 Appendix	116
5. HYDRODYNAMIC INTERACTION ENHANCES COLONIZATION OF SINKING NUTRIENT SOURCES BY MOTILE MICROORGANISMS	120
5.1 Introduction	120
5.2 Influence of Hydrodynamics and Chemotaxis	122
5.2.1 Bacterium as a force dipole	124
5.2.2 Bulk nutrient distribution and chemotaxis	126
5.3 Results	128
5.3.1 Hydrodynamic trapping: with and without orientational diffusion	128
5.3.2 Average nutrient exposure and the hydrodynamic amplification	136
5.3.3 Motile, non-chemotactic bacteria versus non-motile bacteria	144
5.4 Conclusion	145
5.5 Appendix	149
6. BIOFILMS AT INTERFACES: MICROBIAL DISTRIBUTION IN FLOAT- ING FILMS	159
6.1 Introduction	159
6.2 Mathematical model	161
6.2.1 Stokeslet in a floating film	163
6.2.2 Hydrodynamic interactions: Higher order multipoles	165
6.3 Results	169
6.3.1 Dimensionless parameters and simulation methodology	169
6.3.2 Microorganisms in a stagnant, floating film	170
6.3.3 Microorganisms in a flowing film	183
6.4 Discussion and conclusion	188
6.5 Appendix	192
6.5.1 Hydrodynamically induced linear and angular velocities	192

	Page
6.5.2 Accumulation characteristics: additional information	193
7. CONCLUDING REMARKS	195
7.1 Conclusion	195
7.2 Future Work	199
REFERENCES	201
VITA	219

LIST OF TABLES

Table	Page
2.1 List of simulation parameters.	25
4.1 Summary of various mechanisms dictating swimming behavior near a rigid, spherical surface exuding a chemoattractant with a specified concentration at the surface of the source.	99
5.1 List of parameters and their values used in the numerical simulations. . .	158

LIST OF FIGURES

Figure	Page
1.1	Signs of the multipole strengths for different microorganisms, based on the flow-fields generated by them and their morphologies/geometries. ‘N.A.’ denotes that the sign is not decipherable based on the geometry alone. More details about the significance of these signs can be found in Chapter 6. 6
2.1	(a) The initial distribution of the chemoattractant/nutrient. (b) The distribution of the nutrient after some time has elapsed in the simulations. (c) The distribution of the motile bacteria at the same instant of time as in (b). Notice higher concentrations of motile bacteria B_M in the nutrient-rich regions, due to chemotaxis. (d) The distribution of the non-motile bacteria at the same instant of time as in (b). Note that the distribution of the non-motile bacteria remains more or less uniform, as there is no bias in their motion. 17
2.2	(Color online) Time evolution of the fluctuation Reynolds numbers $Re_{u'+v'+w'}$ of the drops in the simulations; see the Appendix and the ref. [70, 71] for the definition of the drop fluctuation Reynolds number. The statistical steady states can be easily identified in all 5 cases (at $\bar{t} \approx 50$), the background flow-fields (and drop positions) at these instants are used as the initial condition for the fluid velocity $\mathbf{u}(t = 0)$ in the simulations that are performed to ascertain the chemotactic advantage. 23
2.3	(Color online) (a) Time evolution of the dimensionless motility benefit for different uptake rate constants (α_C). $\beta_C = 40.0 \mu\text{Mcm}^{-1}\text{s}$. (b) Time evolution of the dimensionless motility benefit for different inverse chemotactic sensitivities (β_C); the units of β_C are $\mu\text{Mcm}^{-1}\text{s}$. $\alpha_C = 1 \times 10^{-8} \text{cm}^3\text{s}^{-1}\text{cell}^{-1}$. The other parameters are: $d = 1.32 \text{mm}$; $\phi \approx 11\%$; $V_s = 100 \mu\text{ms}^{-1}$; $D_m = D_b = 5 \times 10^{-4} \text{cm}^2/\text{s}$; $C_0 = 25 \mu\text{M}$; $B_0 = 1.5 \times 10^5 \text{cells}/\text{cm}^3$; $Eu = 0.40$; $Ga = 2 \times 10^4$ 29

Figure	Page
2.4 (Color online) (a) Time evolution of the chemotactic amplification factor for different uptake rate constants (α_C). $\beta_C = 40.0 \mu\text{Mcm}^{-1}\text{s}$. Clearly, a change in α_C does not affect the relative consumption rates significantly, because it proportionately enhances the values of \dot{C}_M and \dot{C}_{NM} . (b) Time evolution of the chemotactic amplification factor for different inverse chemotactic sensitivities (β_C); the units of β_C are $\mu\text{Mcm}^{-1}\text{s}$. $\alpha_C = 1 \times 10^{-8} \text{cm}^3\text{s}^{-1}\text{cell}^{-1}$. The other parameters are: $d = 1.32 \text{mm}$; $\phi \approx 11\%$; $V_s = 100 \mu\text{ms}^{-1}$; $D_m = D_b = 5 \times 10^{-4} \text{cm}^2/\text{s}$; $C_0 = 25 \mu\text{M}$; $B_0 = 1.5 \times 10^5 \text{cells}/\text{cm}^3$; $Eo = 0.40$; $Ga = 2 \times 10^4$	30
2.5 (Color online) Variation of the maximum value of the dimensionless instantaneous motility benefit, $\max\{\Delta\bar{U}\}$, with β_C scaled by $(\nabla C _{ref} l_{ref}/u_{ref})$. The motility benefit increases with the chemotactic sensitivity (inverse of β_C), but not indefinitely; a saturation occurs for $\beta_C < 0.4 \mu\text{Mcm}^{-1}\text{s}$	32
2.6 (Color online) (a) Time evolution of the dimensionless motility benefit for different swimming speeds. (b) Time evolution of the chemotactic amplification for different swimming speeds; the units of V_s are $\mu\text{m}/\text{s}$. (c) The maximum motility benefit scales linearly with the swimming speed ($V_{s,0} = 100 \mu\text{m}/\text{s}$). The other parameters are: $d = 1.32 \text{mm}$; $\phi \approx 11\%$; $\alpha_C = 1 \times 10^{-8} \text{cm}^3\text{s}^{-1}\text{cell}^{-1}$; $\beta_C = 40.0 \mu\text{Mcm}^{-1}\text{s}$; $D_m = D_b = 5 \times 10^{-4} \text{cm}^2/\text{s}$; $C_0 = 25 \mu\text{M}$; $B_0 = 1.5 \times 10^5 \text{cells}/\text{cm}^3$; $Eo = 0.40$; $Ga = 2 \times 10^4$	33
2.7 (Color online) (a) Time evolution of the chemotactic amplification factor, for different drop diameters, but same volume fraction in all cases: $\phi \approx 11\%$. The units of V_s are $\mu\text{m}/\text{s}$, and of β_C are $\mu\text{Mcm}^{-1}\text{s}$. (b) Time evolution of the chemotactic amplification factor, for different volume fractions, but same drop diameters in all cases. $Eo = 0.40$; $Ga = 2 \times 10^4$. $d \approx 1 \text{mm}$. The other parameters are: $\alpha_C = 1 \times 10^{-8} \text{cm}^3\text{s}^{-1}\text{cell}^{-1}$; $D_m = D_b = 5 \times 10^{-4} \text{cm}^2/\text{s}$; $C_0 = 25 \mu\text{M}$; $B_0 = 1.5 \times 10^5 \text{cells}/\text{cm}^3$. We would like to emphasize that the motility benefit, $\Delta\bar{U}$, follows an identical trend as the amplification factor, R_U , and therefore is not shown here ($\max\{\Delta\bar{U}\} = 0.006$).	36

Figure	Page
2.8 (Color online) (a) Time evolution of the dimensionless motility benefit, for different nutrient availabilities (volume of the nutrient patch V_p , normalized by the volume of the computational domain L^3). (b) Time evolution of the chemotactic amplification factor, for the same nutrient availabilities as in part (a). The inset shows the case of maximum $R_U \approx 24\%$ obtained in our study (for $d \approx 1$ mm, $\phi \approx 6\%$, $V_s = 300$ $\mu\text{m/s}$, $\beta_C = 0.4$ $\mu\text{Mcm}^{-1}\text{s}$, and $V_p/L^3 = 2\%$). Note the significant increase in the time taken to reach a maximum in R_U , and as a consequence, an almost 4-fold prolongation of the motility benefit as compared to the baseline simulations. While the maximum is reached somewhere around $\bar{t} \approx 50$ in the baseline simulations, it takes $\bar{t} \approx 200$ to observe a maximum for the inset. The other parameters for the main figures (a) and (b) are: $EO = 0.40$; $Ga = 2 \times 10^4$; $d \approx 1$ mm; $\phi = 6\%$; $\alpha_C = 1 \times 10^{-8}$ $\text{cm}^3\text{s}^{-1}\text{cell}^{-1}$; $D_m = D_b = 5 \times 10^{-4}$ cm^2/s ; $C_0 = 25$ μM ; $B_0 = 1.5 \times 10^5$ cells/cm^3 .	41
2.9 The effect of rotary diffusivity (in the equation governing the orientation of the bacteria, i.e., equation 2.4) on the instantaneous motility benefit $\Delta\bar{U}$ and the chemotactic amplification R_U . We conclude that as long as there exists a background flow that is strong enough, the rotary diffusivity can be safely neglected. The value of D_R is borrowed from a reference calculating the same for the marine bacterium <i>V. alginolyticus</i> [98].	45
2.10 The effect of nutrient diffusivity on the chemotactic amplification R_U . The variation is shown as a function of the swimming speed V_s (200 (red) and 300 $\mu\text{m/s}$ (blue)). As evident from Fig. 2.6, the higher R_U values correspond to the higher swimming speeds. Inset: A significant chemotactic amplification of 45% is observed for $D_m = 1.5 \times 10^{-5}$ cm^2/s ($Sc = 666$), if the nutrient availability is lowered to $V_p/L^3 = 1\%$. The values of the hydrodynamic parameters for the inset are the same as those for $\phi \approx 6\%$ in Fig. 2.7, and the values of the biological parameters are given in the main text.	47
2.11 Time evolution of the (a) instantaneous motility benefit $\Delta\bar{U}$, and, (b) amplification factor R_U , as a function of the initial shape of the chemoattractant patch. The spherical patch has the same volume as the cylindrical; ‘axis’ refers to the direction along which the axis of the cylindrical patch is oriented. The other parameters are: $\alpha_C = 1 \times 10^{-8}$ $\text{cm}^3\text{s}^{-1}\text{cell}^{-1}$; $\beta_C = 40.0$ $\mu\text{Mcm}^{-1}\text{s}$; $V_s = 100$ $\mu\text{m/s}$; $D_m = D_b = 5 \times 10^{-4}$ cm^2/s ; $C_0 = 25$ μM ; $B_0 = 1.5 \times 10^5$ cells/cm^3 .	48

Figure	Page
2.12 (Color online) (a) Time evolution of the nutrient heterogeneity length-scale l_C normalized by the drop diameter $d_0 = 0.13$ cm, for the background flows corresponding to different drop diameters, d . (b) Time evolution of the volume-averaged nutrient gradient $ \nabla C $ normalized by a reference gradient C_0/l_{ref} , for the background flows corresponding to different drop diameters, d . The other parameters are: $\alpha_C = 1 \times 10^{-8}$ cm ³ s ⁻¹ cell ⁻¹ ; $\beta_C = 40.0$ μ Mcm ⁻¹ s; $V_s = 100$ μ m/s; $D_m = D_b = 5 \times 10^{-4}$ cm ² /s; $C_0 = 25$ μ M; $B_0 = 1.5 \times 10^5$ cells/cm ³	49
3.1 A schematic of the problem being solved, showing a spherical drop covered with surfactant. The origin of a ‘fixed’ coordinate system XYZ lies at the center of the spherical drop. In a quiescent, unbounded, fluid, the swimmer will swim along the direction \mathbf{p} . In cases where the swimmer’s diffusive motion is negligible, the swimming trajectory is restricted to the plane defined by the vectors $\hat{\mathbf{r}}^\perp$ and \mathbf{p} , with the motion governed by eqns. 3.14, and the unit vector $\hat{\mathbf{r}}^\perp \times \hat{\mathbf{r}}$ always directed along \mathbf{e}_Z . Note that h is the <i>dimensionless</i> separation of the swimmer from the surface of the drop.	53
3.2 Schematics showing the idea of the critical trapping radius [127]. Notice how the trajectories around smaller drops escape (a-c), while those around drops with radius larger than the critical trapping radius ($A > A_c \sim 10.7$) get trapped, and orbit the surface (d,e).	61
3.3 Variation of the critical trapping radius, $A_{c, clean}$, with the swimmers’ dipole strengths, α , for different viscosity ratios, λ . The origin is located at the center of the drop, and the swimmer is initially placed at $(X_0, Y_0, Z_0) = (0.1, -(A + 20.0), 0)$. Eqn. 3.10 are integrated using the explicit-Euler method, with time-interval $\Delta t = 10^{-3}$	62
3.4 Variation of the critical trapping radius for surfactant-laden drops, $A_{c, surf.}$, with the swimmers’ dipole strengths, α , for different viscosity ratios, λ . (a) $\beta = 0$; and (b) $\beta = 1$	63
3.5 A comparison between the critical trapping radii for three cases: the rigid sphere, a surfactant-laden drop ($\beta = 0$; $\lambda = 1$), and a clean drop ($\lambda = 1$). It is seen that surfactant-laden drops with negligible surface viscosities have the smallest critical trapping radius.	64
3.6 An example of the basin of attraction: the magenta trajectory falls just inside the basin of attraction h^* and so begins to orbit the interface; the green trajectory on the other hand, falls outside h^* , and hence escapes the interface. Note that the radius of the drop is large enough to trap any directly impacting swimmers, and the escape in this case is only because of an increased initial separation, i.e., $h > h^*$	65

Figure	Page
3.7 Variation of the basin of attraction for a clean drop, as a function of the swimmer's dipole strength (α), the drop radius (A), and the viscosity ratio (λ).	66
3.8 Variation of the basin of attraction for a surfactant-laden drop, as a function of the swimmer's dipole strength (α), the drop radius (A), and the viscosity ratio (λ). The dimensionless surface viscosity $\beta = 0$.	67
3.9 Phase space plots for, (a) a surfactant-laden drop with radius less than the corresponding A_c , and, (b) one with radius larger than A_c . There are no trajectories that eventually get trapped at $h = 1$ in (a), while in (b) there are a host of such trajectories, most notably the ones marked with symbols. The $h = 1$ region can easily be discerned by the bottom-most row of vectors. The dashed lines bound the regions in the $h - \theta$ space that we term as 'escaping' regions, while the solid lines bound all initial (h, θ) pairs that will eventually get trapped onto the surface of the drop, or the 'trapping' region. For the lines in the legend, $\theta(0) = 0$; these correspond to the tangential release used to define the basin of attraction (see Fig. 3.6). Notice the change in the swimmer dynamics (from trapping to escape) as $h(0)$ increases beyond h^* (~ 3 in the case shown).	68
3.10 (a) Variation of the saddle point location (h_s, θ_s) as a function of the drop radius, for a surfactant covered drop. Similar behavior is also seen for all other cases, i.e., for clean drops, and for a rigid sphere (not shown here). (b) Variation of the saddle point location (h_s, θ_s) as a function of the viscosity ratio, for a clean drop (filled symbols), and a surfactant covered drop (hollow symbols, $\beta = 0.01$). The meaning of the symbols is: triangles $\rightarrow \lambda = 0.1$, circles $\rightarrow \lambda = 1.0$, squares $\rightarrow \lambda = 10.0$, diamond \rightarrow rigid sphere, i.e., eqn. 3.13.	69
3.11 A comparison between the scaling for the critical trapping radius of a clean bubble, as derived in eqn. 3.19 (solid line), and by the numerical solution to eqns. 3.10 (asterisks). Also shown is the comparison between numerics (circles) and scaling analysis (dashed lines) for a rigid sphere, as derived by Spagnolie <i>et al.</i> [127].	73
3.12 Variation of the basin of attraction (h^*) with (a) the product of the square of swimmer's dipole strength and drop radius ($\alpha^2 A$) and (b) the drop radius (A) for the motion of swimmer near a clean bubble ($\lambda = 0$). Symbols denote the numerical results while the lines indicate the scaling laws. For $h^* = 0.8(\alpha^2 A)^{1/5}$, the numerical results match with the scaling laws.	75

Figure	Page
3.13 Trajectories of 20 instances of direct impact on to a (a) surfactant-laden drop with $\beta = 0.1$ and $\lambda = 1.0$, and, (b) clean drop with $\lambda = 1.0$. The radius $A = 20$ and the dimensionless translational diffusivity $D = 5 \times 10^{-4}$. Notice that in the former case, there is only one swimmer that escapes the hydrodynamic attraction, which might be due to the low value of D [127]. In the latter case, a greater number of swimmers are able to escape the confinements of the drop, even for low diffusivities.	77
3.14 Probability distributions $f(t)$ for the case of tangential release of microswimmer from an initial separation, $h(0) = 1.001$, from the drop's surface, for (a) a clean drop at different viscosity ratios (simulations run until $t_{end} = 120$); and surfactant-laden drop with: (b) $\lambda = 10.0$ ($t_{end} = 200$), (c) $\lambda = 1.0$ ($t_{end} = 200$), (d) $\lambda = 0.1$ ($t_{end} = 200$; except for the case when $\beta = 0.1$, where $t_{end} = 400$), and different surface viscosities. The other parameters are: $A = 20$, $\alpha = 0.8$, $D = 2 \times 10^{-3}$	78
3.15 Mean trapping times (\bar{T}_h) as a function of diffusivity D and radius of drop A , for (a) a clean drop ($\lambda = 12$), (b) surfactant-laden drop with λ same as (a), and $\beta = 0.1$. Results have been obtained from 100 trials, with simulations running until $t = 100$. The other parameters are: $\alpha = 0.8$	80
4.1 (Color online) A schematic of the problem being solved, showing a spherical nutrient source of radius R , a spherical swimming microorganism of radius b oriented along the unit vector \mathbf{p} , and the spherically symmetric chemoattractant distribution around it $C(r)$. The origin of a 'fixed' coordinate system XYZ lies at the center of the source. The coordinate system defined by the unit vectors $\hat{\mathbf{r}}$, $\hat{\mathbf{r}}^\perp$ and $\hat{\mathbf{r}}^\perp \times \hat{\mathbf{r}}$ can rotate and translate with respect to the fixed coordinate system, as the microorganism moves through the fluid. In a quiescent, unbounded, fluid ($h \rightarrow \infty$), the microorganism will swim along the direction \mathbf{p} . The hydrodynamic interaction induced translational velocity, \mathbf{u}_{HI} , and rotational velocity, $\boldsymbol{\Omega}_{HI}$, of the microorganism is expressed as functions of the microorganism separation from the surface h , and its in-plane orientation θ (see equations 4.4 and 4.5). Note that h is the dimensionless separation of the microorganism from the source.	91

- 4.2 (a) The concept of the critical trapping radius [127]: the swimmer trajectory around the smaller sphere escapes, while that around the larger sphere (whose radius is greater than a critical trapping radius) gets trapped. The swimmers' initial orientation, $\mathbf{p}(0) = \mathbf{e}_Y$. (b) Alternatively, for a fixed radius, only the swimmer with α_D larger than a 'critical dipole strength' will get trapped around the sphere. (c) The concept of the basin of attraction [127]: the swimmer whose initial location is marked by a circle (resp. square) and whose trajectory is shown by a solid line (resp. by a dashed line), starts inside (resp. outside) the basin of hydrodynamic attraction, and thus it gets trapped onto (resp. escapes) the surface. The swimmers' initial orientation, $\mathbf{p}(0) = \mathbf{e}_X$. It is important to note that the basin of attraction is defined only in cases when hydrodynamic trapping is ensured. 101
- 4.3 (Color online) An illustration of the effect of hydrodynamics on the motion of the microorganism as it gets trapped onto the surface of the nutrient source. The thin blue arrows are the microorganism's intrinsic motility $V_s \mathbf{p}$, the thick orange arrows are the hydrodynamic component of microorganism's motion toward the center of the nutrient ($\mathbf{u}_{HI} \cdot \hat{\mathbf{r}}$), and the black arrows are the instantaneous velocity $d\mathbf{x}_2/dt$ (eqn. 4.17). (i-ii) Hydrodynamics—if strong enough—rotates the microorganism such that it always maintains a constant separation $h_t (\approx 1)$ and in-plane angle θ_t , and such that $(\mathbf{u}_{HI} + V_s \mathbf{p}) \cdot \hat{\mathbf{r}} \leq 0$. As a result, the microorganism swims tangentially along the surface and stays trapped. (iii) Rotary diffusion—if significant—can cause the microorganism to rotate to an in-plane angle greater than θ_t which reduces the hydrodynamic attraction, causes $(\mathbf{u}_{HI} + V_s \mathbf{p}) \cdot \hat{\mathbf{r}} > 0$, and thus leads to escape. 103
- 4.4 (Color online) A schematic of the effect of chemotaxis strength on the accumulation around the nutrient source. The left, central and right columns show the x - y , y - z and x - z projections, respectively, of the microorganisms' trajectories. The microorganisms are located initially at $(x(0), y(0), z(0)) = (0, -40, 0)$, and oriented arbitrarily. It is important to note that in the absence of chemotaxis, most of the microorganisms would just 'swim away' from the source without appreciably changing their orientations. The upper (resp. lower) row represents strong (resp. weak) chemotaxis, which could either be due to $C_0/K_D = 1.0$ (resp. $C_0/K_D \ll 1.0$), or a small (resp. large) value of τ^* . Clearly, strong (resp. weak) chemotaxis leads to the microorganisms being, in general, closer to (resp. further from) the nutrient. 104

Figure	Page
4.5 (Color online) (a) Visualization of the different behaviors elicited by the mechanisms discussed in Table 4.1. The starting positions are shown by black dots. Red: this microorganism is unable to locate the source in the time for which the simulations were run. Blue: this microorganism ‘chemotaxes’ close enough to the source, but does not enter the basin of hydrodynamic attraction. Magenta: in this case, the microorganism does make contact with the source, but the hydrodynamic attraction is not strong enough for trapping to occur. Green: an example of a successful trapping wherein chemotaxis and hydrodynamics work in conjunction to bring and trap a microorganism onto the source. See main text for details about the regimes in which such behaviors occur. (b) The time evolution of the distance from the source, $h(t)$, of trajectories in panel (a).	106
4.6 (Color online) (a) Variation of the surface concentration, C_s , with the dipole strength α_D for $D \approx 0$ (negligible rotary diffusion), and $D = 7.5 \times 10^{-4}$ (moderate rotary diffusion). (b) Main figure: The distribution $f(r)$ for $D \approx 0$, and $\alpha_D = 0.1$ (green dashed line), $\alpha_D = 0.6$ (orange dash-dotted line), $\alpha_D = 0.7$ (blue solid line), $\alpha_D = 1.0$ (red dotted line). Inset: The distribution $f(r)$ for $\alpha_D = 0.7$ for $D \approx 0$ and 7.5×10^{-4} (corresponding surface concentrations are shown in panel (a) by filled symbols). Notice the drastic difference in the values of C_s and $f(r)$ for the two different values of rotary diffusivities.	108
4.7 (Color online) Variation of the surface concentration C_s with (a) C_0/K_D , and, (b) τ^* . In each case, C_s is highest when $\alpha_D > 0.65$ and D is negligible, as expected based on the discussion in Section 4.3.3. Also, the results are independent of D for $\alpha_D \approx 0$. For small τ^* , C_s varies almost linearly with τ^*	110
4.8 (Color online) The bulk distribution $f(r)$ as a function of (a-b) C_0/K_D , and, (c-d) τ^* . Note the almost similar distributions for $C_0/K_D = 0.1, 1.0, 10.0$, just like the corresponding C_s values in Fig. 4.7. In conjunction with Fig. 4.7, it is evident how rotary diffusion causes more microorganisms to stay in the bulk. For weak chemotaxis, there is no appreciable accumulation anywhere in the bulk. $f(r)$ increases to a maximum and then decays to zero for weak chemotaxis in the panels (b) and (d). See main text for details.	112
4.9 (Color online) The four qualitatively different behaviors, or spatial distributions $f(r)$, that can be realized due to the combined influence of hydrodynamics (abbreviated in the legend as H.I.) and chemotaxis (abbreviated in the legend as Ch.) on the locomotion of microorganisms around a spherical nutrient source. \uparrow (resp. \downarrow) denotes a strong (resp. weak) influence. The inset shows the surface colonization C_s for each of the four behaviors, with correspondence based on marker type.	114

Figure	Page
4.10 (Color online) The bulk distribution $f(r)$ as a function of (a) C_0/K_D , and, (b) τ^* , for negligibly small hydrodynamic attraction ($\alpha_D \approx 0$) and $D \approx 0$, $D = 7.5 \times 10^{-4}$	116
4.11 (Color online) The bulk distribution $f(r)$ for two different cases: (i) when the value of D_r in eqn. 4.8 is taken to be half of the rotary diffusivity in an unbounded fluid, D_{r0} , in the <i>entire</i> domain (solid line), and, (ii) when eqn. 4.19 is used to assign bacterial rotary diffusivities based on separation of the microorganism from the source (dashed line marked with circles). The surface colonization values are within 1.25% of each other. The value of the dimensionless rotary diffusivity in unbounded fluid is 7.5×10^{-4} , i.e., $D_{r0}b/V_s = 7.5 \times 10^{-4}$	118
4.12 Comparison of the bulk distribution $f(r)$ for combined chemotactic and hydrodynamic attraction to (i) a rigid sphere (asterisks), and, (ii) a clean drop with viscosity ratio $\lambda = 10$ corresponding to crude oil (circles), for the baseline simulation parameters given in Section 4.3.1. The difference between the two cases is not very significant. The surface colonization for the rigid sphere ($C_{s,\text{rigid}}=0.3589$) is 4 % larger than that for the drop ($C_{s,\text{drop}}=0.3446$). For motion around the drop, the hydrodynamics induced linear and angular velocities are taken from ref. [134].	119
5.1 A schematic of the problem being solved. A marine snow aggregate of radius a sinks under the influence of an external force (gravity) \mathbf{F}_{ext} . A chemoattractant emanates from the surface of marine snow, and forms a plume ‘behind’ the marine snow. We consider a system of N_b bacteria (of size b) that are not interacting with each other but can perform chemotaxis toward nutrient hot-spots (the concentration boundary layer and the plume around the aggregate), and interact hydrodynamically with the aggregate upon encountering it. We consider the motion of each bacterium by simulating its trajectory, i.e., the time evolution of its position with respect to the aggregate \mathbf{x}_2 , and its orientation \mathbf{p} , as dictated by hydrodynamic and chemotactic effects.	123
5.2 The drag, $f_d\mathbf{p}$, and thrust, $-\mathbf{f}$, exerted by a (a) pusher, and, (b) puller, on the surrounding fluid. \mathbf{p} is the direction in which the microorganism swims in an unbounded, quiescent fluid.	124

Figure	Page
<p>5.3 (a) The critical trapping radius for a stationary sphere: a bacterium gets trapped (resp. escapes) if the radius of the sphere being encountered is larger (resp. smaller) than a critical value. (b) Bacterium with dipole strength larger (resp. smaller) than the critical dipole strength, $\alpha_{D,c0}$ is trapped (resp. escapes) around a sphere of given radius R. (c) Trapping around a settling sphere: the trajectories are plotted in the frame of reference moving with the sphere and gravity acts along the $-z$ direction; $\alpha_{D,c}$ is the critical dipole strength above which hydrodynamic trapping occurs (for a settling sphere). (d) Variation of the critical trapping radius of a sphere settling under gravity, R_{ct}, with the bacterium's dipole strength, for different values of dimensionless excess density $K_{\Delta\rho}$. R_{c0} is the value of the critical trapping radius for a stationary sphere. (e) An illustration of the fact that hydrodynamic capture fails to occur if the dimensionless excess density $K_{\Delta\rho}$ exceeds 4×10^{-2}.</p>	129
<p>5.4 (a) Ten trajectories of bacteria/micro-swimmers (dipole strength $\alpha_D = 0.6$, dimensionless rotary diffusivity $D = 10^{-3}$) encountering a sinking sphere of radius $R = 40$, $K_{\Delta\rho} = 4.36 \times 10^{-4}$. (b) Ten trajectories of micro-swimmers with a higher dipole strength ($\alpha_D = 1.2$) than case (a), but same dimensionless rotary diffusivity ($D = 10^{-3}$) encountering the same sinking sphere as in (a). (c) The trapping fraction \mathcal{F}_{trap} as a function of the dipole strength for parameter values given in the title, with $T_{end} = 500$. Clearly, $\mathcal{F}_{trap} \rightarrow 1$ if the swimmer's dipole strength is large enough. (d) The trapping fraction as a function of the aggregate's settling speed (U_p) normalized by the bacterium's swimming speed (V_s). The legend contains values of the dipole strength, along with the parameter that was varied (to vary U_p) in each case. In the plots marked by circles and squares, $T_{end} = 500$; U_p is changed by changing the excess density ($\Delta\rho$) of the aggregate from 10^{-4} g/cm³ to 2×10^{-3} g/cm³, and aggregate radius is fixed at $a = 45$ μm. In the plots marked by triangles, $T_{end} = 3000$; U_p is changed by changing the aggregate radius from 20 μm to 450 μm, and excess density is fixed at 5×10^{-4} g/cm³.</p>	134
<p>5.5 Variation in average nutrient exposure, \bar{C}, as a function of the dimensionless bacterial dipole strength α_D, for chemotactic (Ch.) and non-chemotactic (N.Ch.) bacteria. Inset: The trajectories of three chemotactic bacteria with different α_D values (these are given in the legend). It can be seen that all three trajectories begin just outside the aggregate's swept volume but are able to 'chemotax' onto the surface. The amount of time each bacterium spends on the surface of the source depends on their dipole strengths. The other parameters are: $R = 45$, $K_{\Delta\rho} = 0.0109$, $Sc = 1000$, $\tau^* = 1$.</p>	138

Figure	Page
<p>5.6 (a) Spatial variation of the nutrient's (normalized) concentration around the sinking sphere. The thickness of the concentration boundary layer, δ_C, reduces as the nutrient diffusivity reduces. The corresponding values of the Péclet number are 100, 2000, 5000. (b) The variation in the average nutrient exposure, \bar{C}, for chemotactic and non-chemotactic bacteria, with strong and weak hydrodynamic interactions, as a function of the Schmidt number. The legends in the main figure are as follows: Diamonds - chemotactic, $\alpha_D = 2$; Boxes - chemotactic, $\alpha_D = 0.1$; Triangles - non-chemotactic, $\alpha_D = 2$; Circles - non-chemotactic, $\alpha_D = 0.1$. The filled symbols (for $Sc = 2500$) correspond to simulation results with $N_b = 5000$ bacteria. Inset: The hydrodynamic amplification, A_C, as a function of Sc, comparing separately the percentage increase in nutrient exposures for chemotactic and non-chemotactic bacteria (recall the definition of A_C from eqn. 5.7). The other parameters are: $R = 45$, $K_{\Delta\rho} = 0.0109$, $\tau^* = 1$.</p>	140
<p>5.7 The variation in the average nutrient exposure, \bar{C}, for chemotactic and non-chemotactic bacteria, with strong and weak hydrodynamic interactions, as a function of the (dimensionless) mean run-time τ^*. The legends in the main figure are as follows: Diamonds - chemotactic, $\alpha_D = 2$; Boxes - chemotactic, $\alpha_D = 0.1$; Triangles - non-chemotactic, $\alpha_D = 2$; Circles - non-chemotactic, $\alpha_D = 0.1$. Inset: The hydrodynamic amplification, A_C, as a function of τ^*. The other parameters are: $R = 45$, $K_{\Delta\rho} = 0.0109$, $Sc = 1000$.</p>	142
<p>5.8 The variation in the average nutrient exposure, \bar{C}, for chemotactic and non-chemotactic bacteria, with strong and weak hydrodynamic interactions, as a function of the (dimensionless) radius of the marine snow particle R. The legends in the main figure are as follows: Diamonds - chemotactic, $\alpha_D = 2$; Boxes - chemotactic, $\alpha_D = 0.1$; Triangles - non-chemotactic, $\alpha_D = 2$; Circles - non-chemotactic, $\alpha_D = 0.1$. Inset: The hydrodynamic amplification, A_C, as a function of R. The other parameters are: $K_{\Delta\rho} = 0.0109$, $\tau^* = 1$, $Sc = 2000$.</p>	144

Figure	Page	
5.9	A comparison of the average nutrient exposure, \bar{C} , between motile but non-chemotactic bacteria and non-motile bacteria, as a function of (a) the nutrient diffusivity, and (b) the (dimensionless) radius of the marine snow particle, R . (c) Sample trajectories for the three cases whose nutrient exposures are plotted in panels (a-b), with correspondence based on line colors. The blue and brown trajectories are indistinguishable until they near the aggregate, and the latter gets trapped. Notice the ‘smoothness’ of the non-motile trajectory (black) versus that of the non-chemotactic trajectory of bacterium with weak hydrodynamic interaction (blue). The nutrient exposure for motile, non-chemotactic bacteria has been evaluated for both strong ($\alpha_D = 2$) and weak ($\alpha_D = 10^{-3}$) hydrodynamic interactions. The other parameters are: $K_{\Delta\rho} = 0.0109$, $\tau^* = 1$	146
5.10	Schematic depicting the coordinate systems, the vectors and the symbols used to describe the linear and angular velocities of the aggregate and the bacterium. The simulations are performed in the coordinate system xyz , which is fixed to the center of the marine snow particle, with the y axis pointing into the plane of the figure. The coordinate system defined by the orthogonal vectors $\hat{\mathbf{r}}$, $\hat{\mathbf{r}}^\perp$ and $\hat{\mathbf{r}}^\perp \times \hat{\mathbf{r}}$ can translate and rotate with respect to xyz . Note that h is the dimensionless separation of the bacterium (assumed to be spherical in our analysis) from the aggregate and θ is the in-plane angle, i.e., the angle between the bacterium’s orientation \mathbf{p} and the unit vector $\hat{\mathbf{r}}^\perp$	150
5.11	The Sherwood number—a dimensionless measure of the mass transfer rate at the sphere surface—as a function of the Péclet number evaluated using numerical simulations and compared against analytical predictions for $Pe \gg 1$ [dashed line, by [205]] and numerical predictions valid for all Péclet numbers [solid line, by [206]].	154
5.12	The variation in the average nutrient exposure, \bar{C} , for chemotactic and non-chemotactic bacteria, with $r_{lim} = 25$ (thick lines) and $r_{lim} = 50$ (thin lines). The legends in the main figure are as follows: Diamonds - chemotactic, $\alpha_D = 2$; Boxes - chemotactic, $\alpha_D = 0.1$; Triangles - non-chemotactic, $\alpha_D = 2$; Circles - non-chemotactic, $\alpha_D = 0.1$. Note how r_{lim} affects \bar{C} the most for chemotactic bacteria with $\alpha_D = 2$: this is because the bacteria that get hydrodynamically trapped contribute the same amount to the overall mean nutrient exposure irrespective of the value of r_{lim}	157

Figure	Page
6.1 A schematic of the problem being solved. Shown here is the microorganism located at $\mathbf{x} = \mathbf{y}$, along with its ‘images’ at \mathbf{y}^* (w.r.t. the fluid-fluid interface) and at \mathbf{y}^{**} (w.r.t. the air-fluid interface). $A - F$ (resp. $F - F$) refers to the air-fluid (fluid-fluid) interface. Note that the \mathbf{e}_2 component of the swimmer’s orientation has been set to zero without loss of generality. The vertical distribution of a suspension of non-interacting microorganisms depends on the morphology of the microorganisms and the viscosity ratio, $\lambda \equiv \mu_2/\mu_1$, of the fluids involved.	162
6.2 Swimmer distribution in the film, $\mathcal{F}(\bar{z})$, as a function of λ and γ , for $\kappa' \neq 0, \sigma' = \nu' = 0$. Notice no appreciable difference between $\mathcal{F}(\bar{z} = 0)$ and $\mathcal{F}(\bar{z} = 1)$ for a wide range of swimmer elongation, γ , and the normalized film viscosity λ . The value of the dimensionless rotational diffusivity of the swimmers is $D_r/(V_s/H) = 0.2$	172
6.3 (a-b) Swimmer distribution in the film, $\mathcal{F}(\bar{z})$, as a function of λ for $\gamma = 8$, for $\sigma' \neq 0, \kappa' = \nu' = 0$. (c) Trajectories for a source dipole swimmer with $\sigma' = 0.002$ and $\gamma = 8$. The value of the dimensionless rotational diffusivity of the swimmers is $D_r/(V_s/H) = 0.2$. The trajectories are shown for two different viscosity ratio values, $\lambda = 0.1, 10$. The initial position of the swimmer, $(x'(0), z'(0)) = (0, 0.5)$, is marked by the black circle and the initial orientation is horizontal, $\theta(0) = 0$	174
6.4 (a-b) Swimmer distribution in the film, $\mathcal{F}(\bar{z})$, as a function of λ for $\gamma = 1$, for $\sigma' \neq 0, \kappa' = \nu' = 0$. Panel (a) marks a slight peak near $\bar{z} \approx 0.1$ by the text ‘brief retention near F-F’. This corresponds to the brief time spent by swimmers near the F-F as they reorient from $\theta > \pi$ to $\theta < \pi$ and then begin their swimming toward the A-F. This peak is even smaller (barely visible) for $\lambda = 10$. (c-d) $z' - \theta$ phase planes for spherical swimmers with non-zero source dipoles, demonstrating how/why hydrodynamics in conjunction with rotary diffusion causes, (c) ‘top accumulation’ for $\sigma' > 0$, and, (d) ‘bottom accumulation’ for $\sigma' < 0$. The contour represents the angular velocity, Ω_{HI} , of the swimmer; note that $\Omega_{HI} \approx 0$ near the A-F, i.e., near $z' = 1$. The thick dotted lines in panels (a-b) represent the distributions for swimmers with negative source dipolar coefficients when the rotary diffusion is neglected. In all other cases, the swimmers’ rotational diffusivity is taken to be $D_r = 0.2V_s/H$	175
6.5 Swimmer distribution in the film, $\mathcal{F}(\bar{z})$, as a function of λ and γ , for $\nu' \neq 0, \kappa' = \sigma' = 0$. Diamonds (resp. circles) denote maximum values of \mathcal{F} for $\nu' < 0$ (resp. $\nu' > 0$). The value of the dimensionless rotational diffusivity of the swimmers is $D_r/(V_s/H) = 0.2$	178

Figure	Page
6.6 $z'(t) - \theta(t)$ phase plane for force quadrupole swimmers with (a) $\nu' < 0$ corresponding to microorganisms with relatively shorter flagella, and, (b) $\nu' > 0$ corresponding to microorganisms with longer flagella. In panel (b), the hexagrams at $z' \approx 0.08, \theta \approx 3\pi/2$ show the fixed points near the fluid-fluid interface. These correspond to the stable swimming regime where the microorganism swims parallel to the interface. All other multipole coefficients are set to zero and the viscosity ratio is $\lambda = 10$. The phase plane diagrams for $\lambda \rightarrow \infty$ are quite similar, thus highlighting the similarities in swimming behavior between our reduced-order model and the numerical simulations involving bacteria with cell body and flagella.	180
6.7 Summary of boundary accumulation and bulk fraction, as a function of swimmer elongation (γ) and viscosity ratio (λ), for force quadrupole swimmers, i.e., for $\nu' \neq 0, \kappa' = \sigma' = 0$. The horizontal axis is logarithmically spaced (with base 2) until $\lambda = 1$, beyond which it is linear.	182
6.8 Swimmer trajectories in a flowing film under external flow given by eqn. 6.23. (a) Trajectories without inclusion of hydrodynamic interactions (H.I.s), and, (b) trajectories with inclusion of H.I.s. The starting position (marked by the filled black circle) and orientation are $(x'(0), z'(0), \theta(0)) = (0, 0.1, \pi/4)$. It is important to note the enhanced time spent at the free surface (resp. near bottom wall) for weaker (resp. stronger) flows. The inset in panel (b) denotes how the swimmers under moderate external flow, $v_{max} = 8V_s$, can escape the rigid wall at $z' = 0$ and be trapped at the free surface at $z' = 1$; while under strong flows, $v_{max} = 20V_s$, the swimmers traverse the film centerline in ‘swinging’ trajectories.	186
6.9 The minimum/critical external flow required to detach swimmers off a wall, $v_{max}^{cr.}/V_s$, as a function of the swimmer dipole strength, κ , and swimmer elongation γ . Note that $v_{max}^{cr.}$ is higher for spherical pullers ($\gamma = 1, \kappa < 0$) than for spherical pushers ($\gamma = 1, \kappa > 0$). $v_{max}^{cr.}$ is lower for elongated pullers ($\gamma > 1, \kappa < 0$) than for elongated pushers ($\gamma > 1, \kappa > 0$). The thick lines represent the analytical estimates for the spherical swimmer case, borrowed from ref. [18] and the blue circles are the results of numerical calculations from ref. [18]. $\kappa > 0$ (resp. $\kappa < 0$) denotes pushers (resp. pullers). The swimmers are initially located near the wall at $z'(0) = a/H$ and oriented such that $\theta(0) = 3\pi/2$	187

Figure	Page
6.10 Schematic depiction of why elongated pullers can escape from a wall at lower values of the critical external flow, v_{max}^{cr} . The angular velocity due to the external flow, Ω_{ext} , is largest when the swimmer is oriented toward the wall, and the angular velocity due to the hydrodynamic interactions, Ω_{HI} , is same for any perturbations to the stable swimmer orientation, i.e., $\theta = 3\pi/2 - \Delta\theta$ (resp. $\theta = \pi - \Delta\theta$) for a puller (resp. pusher). In this way, pullers face a greater ‘overtuning’ effect due to the external flow.	189
6.11 The difference in interface accumulation $\Delta\mathcal{F}$ (see eqn. 6.20) for dipolar swimmers: (a) pushers, and, (b) pullers. As discussed in Section 6.3.2, and shown more qualitatively in Fig. 6.2, the accumulation when considering only the dipole effects is more or less symmetric with $\Delta\mathcal{F} > 0$, $\sim O(10^{-3})$.	194

ABSTRACT

Desai, Nikhil Ph.D., Purdue University, December 2019. Oil-microbe Interactions: Hydrodynamic and Chemotactic Influences. Major Professor: Dr. Arezoo M. Ardekani, School of Mechanical Engineering.

Advances in modern research have unveiled numerous fundamental and practical benefits of studying the hydrodynamics of microorganisms. Many microorganisms, especially bacteria, actively search for nutrients via a process called chemotaxis. The physical constraints posed by hydrodynamics in the locomotion of microorganisms can combine with their chemotactic ability to significantly affect functions like colonization of nutrient sources. In this thesis, we investigate the interplay between hydrodynamics and chemotaxis toward dictating bacterial distribution around fluid-fluid interfaces, which often act as a source of nutrition. We approach our problem statements using mathematical models and numerical and/or semi-analytical tools. Our studies are particularly relevant in the context of hydrocarbon degradation after oil-spills.

We begin by showing that the flow generated by rising oil drops delocalizes dissolved nutrient patches in the ocean, and aids chemotactic bacteria in improving their nutrition (over non-chemotactic bacteria) by 45%. We then move from studying colonization of soluble nutrient *patches* to colonization around nutrient *sources*, e.g., oil drops, marine snow. Towards this, we first demonstrate the phenomenon of hydrodynamics-mediated ‘trapping’ of bacteria around oil drops and show that a surfactant-laden drop can retain an approaching bacterium on its surface for $\approx 35\%$ longer times than a clean drop. We also analyze hydrodynamic trapping of bacteria around settling marine snow particles and show how bacteria can collide with and colonize the marine snow, even when the latter moves 10 times faster than the former. In all the cases above, we show how the hydrodynamic interactions are com-

plemented by chemotaxis to enable extremely effective bacterial foraging. We next explore how propulsion mechanisms of microorganisms affect their ability to form biofilms on fluid-fluid interfaces and unveil the hydrodynamic origins behind the tendency of flagellated bacteria to swim parallel to plane surfactant-laden interfaces. Finally, we summarize our results, identify further avenues of research and propose problem statements related to them.

1. INTRODUCTION

1.1 Overview

Micro-organisms exist, naturally and otherwise, across a plethora of habitats around us, ranging from inside our own bodies to some of the most uninhabitable places on Earth. They are the essential entities for sustaining life as we know it today; and advances in science and technology continue to unravel their fundamental and practical importance [1]. Scientists strive to understand the behavior of microorganisms in isolation, and under external stimuli—e.g., light, heat, pH, electromagnetic fields, oxygen and/or other nutrients—to answer questions in fields like evolutionary biology, applied microbiology, condensed matter physics, chemistry, biochemistry, limnology, oceanography and ecology, to name a few. A significant number of these questions pertain to the motion of microorganisms, particularly bacteria, in their immediate surroundings, i.e., in a fluid; and so the concepts of fluid mechanics enter the fray to explain much of what is observed in this most interdisciplinary of modern sciences.

In this thesis, we investigate how fluid flow and nutrient availability around bacteria dictates their motion, and subsequent distribution, near fluid-fluid interfaces. In particular, we wish to identify how hydrodynamics affects critical oil-microbe interactions like bacterial bioremediation, i.e., the disintegration of (hydrocarbon rich) oil drops by bacteria, leading to substantial reduction in any adverse effects on the environment, and/or on organisms that are higher in the food chain.

⁰Some parts of this chapter have been reprinted with minor changes, with permission, from the material as it appears in the article “*Modeling of active swimmer suspensions and their interactions with the environment*”, by N. Desai and A. M. Ardekani, *Soft Matter*, vol. **13**, pp. 6033, 2017 (DOI: 10.1039/c7sm00766c). Copyright (2017) of The Royal Society of Chemistry.

The role of marine bacteria in the biodegradation of hydrocarbons emanating from sub-oceanic sources—natural oil seeps and anthropogenic oil spills—is well studied [2–4]. However, little is known about the fundamental mechanisms that initiate and promote biodegradation by bacteria. In general, the motion of motile bacteria is influenced by local physicochemical properties, like nutrient distribution, fluid flow, and proximity to interfaces. For example, marine bacteria perform chemotaxis, i.e., sense gradients in ambient nutrient concentrations and alter their motility based on the feedback, to colonize nutrient ‘hotspots’ in the ocean [5,6]. In addition, fluid flow interacts with the morphology of the bacteria to produce rotation and linear drift in their motion. Moreover, the mere presence of a rigid or a compliant boundary near a motile bacterium affects its trajectory non-trivially. The above influences are extensively coupled, and result in microbial patchiness on different length-scales and concomitant changes in the marine biogeochemistry [7]. They are also expected to affect the rate of attraction and adhesion of microbes to oil drops, and thus are likely to alter the rates of biodegradation.

An understanding of the ideas presented in this thesis warrants some knowledge of bacterial locomotion, which we briefly discuss next. In particular, we elucidate some aspects of: (i) the physics governing the fluid flow around microorganisms, and, (ii) the basics of bacterial chemotaxis. For greater detail regarding the former topic, the reader is advised to consult ref. [8,9], while for the latter, one can consult ref. [5–7,10].

1.2 Motion of a single microorganism in a Newtonian fluid

1.2.1 Hydrodynamics

The phenomena described in this thesis are mainly concerned with fluid flow around motile microorganisms, i.e., micron sized ‘swimmers’ that are capable of self propulsion in a fluid by converting energy from one form (e.g. chemical) to another

(mechanical). The equations governing the fluid velocity and pressure are the Navier-Stokes and the continuity equations, which, in their dimensionless form, are:

$$\begin{aligned} \frac{\text{Re}}{\text{St}} \frac{\partial \tilde{\mathbf{u}}}{\partial \tilde{t}} + \text{Re} \tilde{\mathbf{u}} \cdot \tilde{\nabla} \tilde{\mathbf{u}} &= -\tilde{\nabla} \tilde{p} + \tilde{\nabla}^2 \tilde{\mathbf{u}} + \tilde{\mathbf{f}}, \\ \tilde{\nabla} \cdot \tilde{\mathbf{u}} &= 0, \end{aligned} \quad (1.1)$$

where $\tilde{\mathbf{u}}$, \tilde{p} and \tilde{t} are the dimensionless fluid velocity, fluid pressure, and time, respectively, and $\tilde{\mathbf{f}}$ is the dimensionless external force (per unit volume) acting on the fluid. The non-dimensionalization is done by using u_{ref} , l_{ref} , t_{ref} and $\mu u_{ref}/l_{ref}$ as the reference velocity, length, time and pressure scales, respectively. $\text{Re} = \rho u_{ref} l_{ref} / \mu$ is the Reynolds number, where ρ and μ are the fluid's density and viscosity, respectively. It is a measure of the relative magnitudes of the inertial forces to that of the viscous forces acting on the fluid. $\text{St} = u_{ref} t_{ref} / l_{ref}$ is the Strouhal number, which compares the characteristic time scale t_{ref} to the flow time scale l_{ref}/u_{ref} .

The typical sizes ($l_{ref} = 1-100 \mu\text{m}$) and swimming speeds ($u_{ref} = 10-1000 \mu\text{m/s}$) of microorganisms, combined with the density ($\rho \sim 1000 \text{ kg/m}^3$) and viscosity ($\mu \sim 0.001 \text{ Pa}\cdot\text{s}$) of the media in which they swim (mostly water), render the Reynolds number of these systems to be $O(10^{-5} - 0.1)$. As a result, fluid inertia is negligible, and if $\text{St} \geq O(1)$, then the eqn. 1.1 simplify to:

$$\begin{aligned} -\nabla p + \mu \nabla^2 \mathbf{u} &= \mathbf{f}, \\ \nabla \cdot \mathbf{u} &= 0, \end{aligned} \quad (1.2)$$

i.e., the Stokes equation and the continuity equation. This simplification leads to two very important properties: (i) time independence, and, (ii) linearity. Time independence lends instantaneity to the fluid velocity and pressure, which means that they 'adjust instantaneously' to any time-dependent changes in the flow conditions [11], e.g, moving boundaries like the locomotory appendages of microorganisms. Linearity is an extremely important property, as it allows the development of Stokes flow solutions via methods of superposition, and makes it possible to obtain solutions to eqn. 1.2 analytically. In the context of microorganism locomotion, the aforementioned properties make it imperative for a microorganism to swim by deforming its body in

a time-*irreversible* fashion (such that the time lapse of its body geometry does *not* appear identical when viewed forward and backward in time). This idea is referred to as Purcell’s ‘scallop theorem’ [12].

When the force in eqn. 1.2 is concentrated at a single point, say at \mathbf{x}_0 , it can be written as $\mathbf{f} = (f\mathbf{e})\delta(\mathbf{x} - \mathbf{x}_0)$, where \mathbf{e} is the direction along which the force is acting. The corresponding solution of the flow field \mathbf{u}_S , is called a Stokeslet, and it is a fundamental, singular solution of the Stokes equations:

$$\begin{aligned}\mathbf{u}_S(\mathbf{x}) &= \frac{\mathbf{f}}{8\pi\mu} \cdot \left(\frac{\mathbf{I}}{r} + \frac{(\mathbf{x} - \mathbf{x}_0)(\mathbf{x} - \mathbf{x}_0)}{r^3} \right), \\ &= \frac{\mathbf{f}}{8\pi\mu} \cdot \mathbf{G}(\mathbf{x}, \mathbf{x}_0)\end{aligned}\tag{1.3}$$

where $r = |\mathbf{x} - \mathbf{x}_0|$. Moreover, because the Stokes equations are linear, one can obtain higher order singular solutions by taking derivatives of eqn. 1.3 (see ref. [13, 14] for details). Of special interest, is the solution obtained via the operation $\mathbf{e} \cdot \frac{\partial \mathbf{G}}{\partial \mathbf{x}_0}$, which is called an ‘axisymmetric Stokeslet dipole’ or a force dipole:

$$\mathbf{u}_D(\mathbf{x}) = \kappa \left(-\frac{(\mathbf{x} - \mathbf{x}_0)}{r^3} + \frac{3}{r^3}((\mathbf{x} - \mathbf{x}_0) \cdot \mathbf{e})^2 (\mathbf{x} - \mathbf{x}_0) \right),\tag{1.4}$$

where κ is called the dipole strength and has units of m^3/s . Eqn. 1.4 represents the flow field due to an axisymmetric force dipole located at \mathbf{x}_0 . We call it *axisymmetric* because it was obtained by taking the derivative of the Stokeslet along the direction in which the force \mathbf{f} is acting, i.e., along \mathbf{e} . Physically, eqn. 1.4 is the flow induced by two equal and opposite, collinear forces (directed along \mathbf{e} and $-\mathbf{e}$) with an infinitesimal separation between them. It is also important to note that the force dipole strength scales as $\kappa \sim fb/(8\pi\mu)$, where b is a measure of the separation between the collinear forces’ points of application. If these forces are assumed to originate due to a microorganism’s appendages exerting a propulsive force and its cell body exerting a drag force on the fluid, then b represents the characteristic size of the microorganism. The force dipole thus acts as a leading order approximation of the flow generated by a microorganism exerting an axisymmetric forcing (about the direction \mathbf{e}) on the ambient fluid. Higher order approximations of the microorganism’s effect on the ambient fluid

flow can be obtained by performing a multipole expansion of the Stokeslet solution, about the direction \mathbf{e} [14, 15]. These higher order approximations account for: (i) the finite size of the microorganism, (ii) the asymmetry in its structure (e.g., the relative sizes of the cell-body and the flagellum), and, (iii) the equal and opposite torques that its body and flagellum exert on the surrounding fluid. The singularities representing these three effects are called: (i) the source dipole, (ii) the force quadrupole, and, (iii) the rotlet dipole, respectively. We now provided the expressions for the fluid flow caused by these three singularities, in an unbounded fluid. The source dipolar flow is given by:

$$\mathbf{u}_{SD}(\mathbf{x}) = \sigma \left(-\frac{\mathbf{e}}{r^3} + \frac{3}{r^5} ((\mathbf{x} - \mathbf{x}_0) \cdot \mathbf{e})(\mathbf{x} - \mathbf{x}_0) \right), \quad (1.5)$$

where σ is the source dipole strength. The force quadrupolar flow is given by:

$$\begin{aligned} \mathbf{u}_Q(\mathbf{x}) = & \nu \left[\frac{\mathbf{e}}{r^3} - \frac{3}{r^5} \{ 3(\mathbf{x} - \mathbf{x}_0) ((\mathbf{x} - \mathbf{x}_0) \cdot \mathbf{e}) + ((\mathbf{x} - \mathbf{x}_0) \cdot \mathbf{e})^2 \mathbf{e} \} \right] \\ & + \nu \left[\frac{15}{r^7} ((\mathbf{x} - \mathbf{x}_0) \cdot \mathbf{e})^3 (\mathbf{x} - \mathbf{x}_0) \right], \end{aligned} \quad (1.6)$$

where ν is the force quadrupole strength. Finally, the rotlet dipolar flow is given by:

$$\mathbf{u}_{RD}(\mathbf{x}) = \frac{3\tau}{r^5} ((\mathbf{x} - \mathbf{x}_0) \cdot \mathbf{e})(\mathbf{e} \times (\mathbf{x} - \mathbf{x}_0)), \quad (1.7)$$

where τ is the rotlet dipole strength. The units of σ, ν, τ are m^4/s , as can be deduced from a simple dimensional analysis. It is important to note that while the force dipole (eqn. 1.4) and the source dipole (eqn. 1.5) contributions are expected to be non-zero for most microorganisms, the same cannot be said for the force quadrupole (eqn. 1.6) and the rotlet dipole (eqn. 1.7) contributions. In particular the force quadrupolar contributions are significant only for microorganisms that display sufficient fore-aft asymmetry (e.g., most flagellated bacteria, spermatozoa), while the rotlet dipole contributions are significant only for microorganisms that propel themselves either via a single rotating flagellum (e.g., *V. alginolyticus*), or via a rotating flagellar bundle (e.g., *E. coli*). The key point to note is that a rotlet dipole can only be ‘generated’ if the microorganism exerts equal and opposite torques on the ambient fluid.

The most important point to take from the above discussion is that the analysis of fluid flow at large distances from a microorganism can be done by ‘replacing’ it with a combination of the singularities, whose flows are represented by eqns. 1.4 to eqn. 1.7. By tuning the singularity strengths ($\kappa, \sigma, \nu, \tau$), one can model a host of microorganisms. Fig. 1.1 lists the signs of these singularities for typical microorganisms studied by researchers in this field [14, 16–18].

Microorganism	Force dipole (κ)	Source dipole (σ)	Force quadrupole (ν)	Rotlet dipole (τ)
<i>E. coli</i>	> 0	< 0	> 0	> 0
<i>C. reinhardtii</i>	< 0	< 0	N.A.	≈ 0
<i>V. carteri</i>	≈ 0	> 0	≈ 0	≈ 0
<i>V. cholera</i>	> 0	< 0	< 0	N.A.
<i>P. aeruginosa</i>	> 0	< 0	> 0	N.A.

Figure 1.1. : Signs of the multipole strengths for different microorganisms, based on the flow-fields generated by them and their morphologies/geometries. ‘N.A.’ denotes that the sign is not decipherable based on the geometry alone. More details about the significance of these signs can be found in Chapter 6.

It must be emphasized that the presence of bounding surfaces/interfaces drastically changes the form of the flow fields $\mathbf{u}_D(\mathbf{x})$, $\mathbf{u}_{SD}(\mathbf{x})$, $\mathbf{u}_Q(\mathbf{x})$, $\mathbf{u}_{RD}(\mathbf{x})$. This is because in an unbounded fluid, the flow due to these singularities decays to zero as $r \rightarrow \infty$, but the same would not be true always if there were to exist, say, a wall at some $r = R_w < \infty$. In the latter case, the fluid velocity would need to satisfy certain boundary conditions based on the type of confinement [11]. These restrictions in the decay rate of the velocity due to a force dipole, and the fact that the microorganism experiences zero force and torque at all times—because its inertia is negligible—lead to interesting dynamical changes in its motion. They result in hydrodynamically induced linear and angular velocities in the motion of the microorganism, which is responsible for many interesting swimming behaviors displayed by them [19–30] (see the introduction to Chapter 6 for extensive details). The incorporation of bound-

ary conditions onto the singularity solutions and the calculation of hydrodynamically induced velocities is a non-trivial process, and requires knowledge of solution methodologies beyond the scope of the present Chapter [13]. At this point, it suffices to say that when the need to do so arises, we resort to previously published literature in this field and cite the appropriate references for the interested reader. Although this somewhat simplistic representation hides the intricate details of fluid flow in the immediate vicinity of the microorganism, it is still able to predict experimentally observed phenomena like: (i) attraction of the bacteria *E. coli* to plane [21, 29] and curved [26] solid surfaces, (ii) attraction of bacteria to air-fluid interfaces [27, 30], (iii) circular swimming of bacteria near rigid surfaces [20] and air-fluid interfaces [24], and, (iv) swimming of bacteria and spermatozoa parallel to rigid surfaces, at a fixed separation [19, 22–25, 28, 31]. The last of these points has been discussed in detail in this thesis in Chapter 6.

In Chapters 3 to 5 of this thesis, we use the ideas discussed above to model the hydrodynamic interaction of a microorganism (modeled as a force dipole, eqn. 1.4) with a spherical nutrient source (marine snow or oil drop) that is either stationary (Chapters 3, 4) or moving under the influence of gravity (Chapter 5). In Chapter 6 we explore the effects of the higher order singularities (eqn. 1.4 to eqn. 1.6) on the motion of microorganisms near fluid-fluid interfaces. Hydrodynamic interactions can alter the swimming characteristics of microorganisms in non-trivial ways (see ref. [8]) and are a passive mechanism of motility alteration. In addition, microorganisms themselves have various propulsion strategies that enable them to make the most of their surroundings. One of these is chemotaxis, which is the focus of our next section.

1.2.2 Chemotaxis

Chemotaxis can be defined as the ability of microorganisms (primarily bacteria) to detect gradients in ambient chemical concentrations, and then tune their motility in accordance with their needs, so as to ‘climb’ up or down these gradients. The

chemical responsible for chemotaxis is termed as a chemo-attractant/-repellant, or more generally, a chemoeffector. In essence, it can be thought of as being the nutrient that the bacteria seek. The chemoeffector molecules bind to chemoreceptors on a bacterium’s cell membrane, and the ensuing chemical reactions enable the bacterium to ‘sense’ ambient chemoeffector concentrations and react accordingly (see ref. [5] for details). Bacteria rely on temporal sensing—their ability to continuously compare the concentrations in their immediate vicinity as they swim—to gauge chemoeffector gradients in three-dimensional space [32]. In rare cases, they may even compare the concentrations at the two ends of their cell-body and thus directly sense spatial gradients, though still at length scales of the order of a few microns [33]. Bacteria utilize an intricate chemosensory apparatus to alter their swimming metrics based on the feedback they receive from gradient-sensing [34–38].

Typical bacterial motion comprises of bursts of straight ‘runs’ interspersed with sudden changes in the swimming direction, called ‘tumbles’. Chemotaxis induced deviation from this behavior can be of different types, e.g., a change in the frequency of tumbling as a function of ambient nutrient/chemoeffector concentration, or even a shift in the regime of swimming from ‘run-and-tumble’ to ‘run-and-reverse’ [39]. These changes aim to prolong a bacterium’s stay in a desired region, e.g., bacteria are known to tumble (or reverse) less often in nutrient-rich environments, to increase their average nutrient exposure and fulfill their energetic requirements. Therefore, the tumbling frequency is an important metric for quantifying a bacterium’s ability to find nutrition. The pioneering work by Macnab and Koshland [32], and Berg and Brown [5, 10, 40, 41], and subsequent studies [42, 43] have proposed models relating a bacterium’s tumbling frequency to the rate of change of chemoeffector concentration experienced by the bacterium, say $\dot{C}h$. The main idea is the same in all cases: whenever $\dot{C}h > 0$ (bacterium is experiencing progressively higher nutrient concentrations) the fractional amount of chemoreceptor reacting with the chemoeffector increases, and the subsequent cellular processes suppress tumbling. Thus, a bacterium in a nutrient rich region is less likely to leave it abruptly on account of a tumble.

In Chapter 4 of this thesis, we show how the intricacies of chemotaxis summarized above are incorporated into a simple mathematical formulation describing the locomotion of a chemotactic bacterium near nutrient effusing sources like marine snow particles or crude oil drops. Combined with the ideas of the previous section, this enables us to understand the colonization of nutrient sources by motile, chemotactic microorganisms; and the importance of different hydrodynamic and chemotactic parameters in this process. In Chapter 5, we extend the studies of Chapters 3 and 4 to study the problem of hydrodynamics- and chemotaxis-mediated accumulation of marine microorganisms around sinking (resp. rising) nutrient sources like marine snow (resp. oil drops). Thus, in totality, Chapters 3 to 5 answer many questions pertaining to the effects of: (i) hydrodynamics alone, and, (ii) hydrodynamics *and* chemotaxis on the colonization of stationary and translating (rising/settling) nutrient sources by microorganisms.

1.3 Motion of a suspension of microorganisms in a Newtonian fluid

So far, we have discussed how fluid flow and motility of a single microorganism affect each other. A natural extension is the study of a number of microorganisms in a fluid, or an active suspension. From a first principles perspective, this would involve solving for the fluid flow around finite (micron sized) immersed bodies while accounting for the specifics of the locomotion of each one of them. A number of studies have been carried out based on this idea and variations thereof; details can be found in ref. [44–46]. This approach is extremely useful when interactions between microorganisms may not be ignored, and the fluid flow occurs primarily because of forces exerted by the microorganisms. In many cases however, microbes are found in reasonably dilute concentrations in preexisting background flows that are generally stronger than the ‘dipole flows’ of Section 1.2.1. The effect of microbes on the flow can then be neglected altogether, and we have a ‘one-way coupling’ wherein one only considers the effect of the flow on the microbes. Although these situations can be

treated using the first principles approach, it sometimes makes more sense to use reduced order models like continuum theories for active suspensions. This is because the latter offer crucial simplifications in the desired analysis, e.g., the possibility of analytical derivations, reduction in computational costs etc.

Continuum theories of microorganism suspensions model them as a scalar field that is being advected by some background fluid flow, and more crucially, by a ‘flow’ that arises from the microorganisms’ motility. A very general continuum field equation for the concentration n of an active suspension would look like:

$$\frac{\partial n}{\partial t} + \nabla \cdot (n\mathbf{u}) + \nabla \cdot (n\mathbf{V}) = \nabla \cdot (\mathbf{D}_n \cdot \nabla n), \quad (1.8)$$

where the intrinsic motility is codified in the advective and diffusive flux terms, $(n\mathbf{V})$ and $(\mathbf{D}_n \cdot \nabla n)$, respectively. The success of continuum theories is contingent on how accurately are these terms represented. We will discuss one such representation, and guide the reader interested in extensive details to ref. [47–51]. We will try to answer the question: how can a collective reaction—to chemical cues—by a suspension of chemotactic bacteria be incorporated into the paradigm of eqn. 1.8? The answer lies in the fact that when length scales of observation are large enough, then (i) individual ‘gradient climbing’ of multiple chemotactic bacteria can be lumped together as a collective flux \mathbf{V} , and, (ii) randomness associated with swimming can be represented by a diffusion tensor \mathbf{D}_n , in eqn. 1.8. As an example, consider the equation:

$$\frac{\partial n}{\partial t} + \nabla \cdot (n\mathbf{u}) + \nabla \cdot \left(n\chi \frac{\nabla C}{|\nabla C|} \right) = \nabla \cdot (\mathbf{D}_n \cdot \nabla n), \quad (1.9)$$

which states that in addition to advection by a (background) fluid velocity \mathbf{u} , a suspension of bacteria will tend to swim along the direction of increasing chemoeffector concentration (denoted by C) at a rate χ , and at the same time, diffuse in space with mean squared displacement proportional to $\|\mathbf{D}_n\|$. This idea was first proposed by Keller and Segel in 1970, who stated that “*even though a cell may not be capable of making an accurate assessment of the gradient to which it is exposed at a given time, its average behavior can nevertheless reflect the gradient with arbitrary accuracy*” [52].

The idea of eqn. 1.9, as simple as it is, has been used in the past to successfully explain a number of observable phenomena like, oxytaxis/chemotaxis driven plume dynamics [53–57], bioconvection in sessile drops [58,59], chemotaxis driven instability in thin films [60] and chemotactic foraging in the turbulent ocean [61,62]. We will use a variation of this concept in Chapter 2 of the thesis to study the effects of buoyancy-induced multiphase flow on chemotactic foraging in sub-marine nutrient plumes.

1.4 Outline of the thesis

Thus far, we have given a general outline of the overarching goals of this thesis (Section 1.1), and the technical details (Sections 1.2 and 1.3) involved in answering some of the questions that interest us. We now provide motivations behind choosing our problem statements, and briefly list the methodologies adopted to solve them.

- Our study in Chapter 2 is motivated by the process of methane biodegradation in wake of the events of the Gulf of Mexico oil spill. We investigate the consumption of a dissolved chemo-effector by model micro-organisms, in a flow generated by buoyancy driven rise of mono-disperse oil drops. We employ direct numerical simulations to resolve the multiphase flow, chemo-effector transport, and microorganism transport in a swarm of rising oil drops. We quantify the difference in the rate of consumption by motile and non-motile microorganisms, and identify the key biophysical parameters affecting this difference. This work has been published in the International Journal for Multiphase Flow, 2018 [63].
- While Chapter 2 details the influence of oil drops in the consumption of *soluble* hydrocarbons, Chapter 3 investigates the same for *insoluble* hydrocarbons. The central question of this chapter is: through what mechanisms do marine bacteria attach themselves onto the surface of oil drops to begin biodegradation? We focus specifically on the hydrodynamics of this complex process. In particular, we investigate the swimming dynamics of a model microorganism/microswimmer

(a force dipole) in the vicinity of a clean drop, and of a surfactant covered drop. Our results highlight the importance of considering dispersant-addition in oil spills involving insoluble hydrocarbons. This study has been published in *Soft Matter* 2018 [64].

- A key result that emerges from Chapter 3 is that hydrodynamics can act as an effective ‘trap’ only when a microorganism of size $\sim O(10) \mu\text{m}$ is at most $O(20) \mu\text{m}$ away from the surface of a drop. Therefore, the role of chemotaxis becomes very crucial in leading a distant bacterium up to a food source so that the nutrient uptake can commence. In Chapter 4, we study how the interaction between hydrodynamics and chemotaxis affects the colonization of nutrient sources by microorganisms. We use an individual based model and perform probabilistic simulations to ascertain the impact of environmental and motility characteristics on the distribution of microorganisms around a spherical nutrient source. Our study provides an insight onto the interplay of two important mechanisms governing microorganism behavior near nutrient sources, isolates each of their effects, and offers greater predictability of this non-trivial phenomenon. This work has been published in *Physical Review E* [65].
- Nutrient sources aren’t always stationary; in fact, quite often, they are moving under the influence of external forces (e.g., gravity) or flow. This motivates us to generalize the works of Chapters 3, 4 to the motion (and possible accumulation) of microorganisms around *moving* nutrient sources. In Chapter 5, we document hydrodynamics-mediated trapping of microorganisms around a moving spherical nutrient source such as a settling marine snow aggregate. We find that there exists a range of size and excess density of the nutrient source, and motility and morphology of the microorganism under which hydrodynamic interactions enable the passive capture of approaching microorganisms onto a moving nutrient source. We simulate trajectories of chemotactic and non-chemotactic bacteria encountering a sinking marine snow particle effusing soluble nutrients to calcu-

late the average nutrient concentration to which the bacteria are exposed. We thus provide a consistent description of how microorganism motility, fluid flow and nutrient distribution affect foraging by marine microbes, and the formation of biofilms on spherical nutrient sources under the influence of fluid flow. The results from this Chapter have been published in *Frontiers in Microbiology* 2019 [66].

- Chapter 6 deals with a slight variation of the oil-microbe interactions discussed thus far. Instead of studying colonization of oil drops (or marine snow particles), we focus on bacterial accumulation at/near *floating fluid films*. This is important because bioremediation almost invariably involves the interaction of bacteria with planar fluid-fluid interfaces, e.g., hydrocarbon degradation by bacteria at oil-spill sites. “Films of bacteria at interfaces” [67] are formed before the breakdown of heavy oil begins. It is thus necessary to understand the role played by hydrodynamics in biofilm incipience on fluid surfaces. In particular, we study the dynamics and statistics of microorganisms in a ‘floating biofilm’, i.e., a confinement with an air-fluid interface on one side and a fluid-fluid interface on the other. We use an extension of the force dipole model to account for the finer features of bacterial propulsion and geometry (relative sizes of the cell body and the flagellum). We then perform probabilistic simulations to ascertain the spatial distribution of bacteria as a function of their morphology and the viscosity contrast across the fluid-fluid interface.
- In Chapter 7, we summarize our studies in the context of our original goal. In addition, we propose further investigations that can help to improve our fundamental understanding of the relation between hydrodynamics and oil-microbe interactions.

2. NUTRIENT UPTAKE BY CHEMOTACTIC MICROORGANISMS IN PRESENCE OF RISING OIL DROPS

2.1 Introduction

Subsurface hydrocarbon (HC) spills/leaks—both natural and anthropogenic—are a major source of carbon and energy for a plethora of marine microorganisms [2]. In fact, the role of methanotrophs in degrading methane in the Deepwater Horizon spill in 2010 is well documented [3,4,68]. A major portion of this degradation occurred in the presence of a rising swarm of oil drops, i.e., in an inherently unsteady flow environment consisting of at least two distinct fluid phases [69]. Similarly, it is expected that the many *soluble* HCs being leaked into the oceans are also consumed by marine bacteria under the influence of flows that are driven by buoyancy of the *insoluble* oil components (e.g., high-molecular-weight aliphatic hydrocarbons). These flows result in significant three dimensional velocity fluctuations (called ‘pseudo-turbulence’) due to the hydrodynamic interactions between the oil drops [70–73]. The velocity fluctuations in turn drive dispersion of the dissolved HCs via combined diffusive and convective transport. Therefore, pseudo-turbulence ensures that not only is the fluid medium in a state of agitation, but that any concentrated ‘patches’ of dissolved HCs are being continuously stirred (dispersed into thinner or smaller patches, resulting in enhanced HC/nutrient gradients) and mixed (homogenized due to fluid flow and nutrient diffusion).

The aforementioned processes are expected to create a fundamental difference in the nutrient uptake by motile bacteria, as compared to that by the non-motile

⁰This chapter has been reprinted with minor changes, with permission, from the material as it appears in the article “*Nutrient uptake by chemotactic bacteria in presence of rising oil drops*”, by N. Desai, S. Dabiri and A. M. Ardekani, International Journal of Multiphase Flow, vol. **108**, pp. 156, 2018 (DOI: 10.1016/j.ijmultiphaseflow.2018.06.016). Copyright (2018) of Elsevier Ltd.

ones. Central to understanding this difference is a well studied phenotype of bacteria called chemotaxis [40]: the ‘gradient sensing ability’ of a bacterium that allows it to alter its swimming strategy in order to reside in regions of high (low) concentrations of desired (undesired) chemical species called chemoattractants (chemorepellants). The pseudo-turbulence engenders nutrient gradients and drives chemotactic motion of motile microbes. For example, methanotrophic bacteria like *Methylomonas* can chemotax toward methane-rich regions in a HC plume [68]. This directed motion exists only for motile bacteria, which hints at the advantage that they might have over their non-motile counterparts. However, the extent to which chemotaxis can be beneficial is not known *a priori*, and requires detailed investigation of the transport phenomena involved. The way in which these organisms consume nutrients relative to each other, and the factors that influence this competition are unclear, and subject to multifarious bio-physical interactions. In the present work, we unravel the results of these interactions, through mathematical models and direct numerical simulations (DNS).

Our problem statement entails modeling the consumption (uptake) of a dissolved chemoattractant (nutrient) by model bacteria—both motile and non-motile—in a swarm of oil drops rising through a column of fluid. The chemoattractant is present in a patch that gets de-localized into thinner ‘strands’ due to the fluid flow induced by the drops (see Fig. 2.1 (a) and (b)). We investigate the interaction of physical/flow characteristics (oil drop diameter and volume fraction) with biological characteristics (time scale of nutrient consumption by bacteria, sensitivity to nutrient gradients, swimming speed), and the resulting effect on the competitive consumption of the available nutrient. Our aim is to ascertain and quantify the ‘chemotactic advantage’, i.e., the difference between the consumption rates by motile and non-motile bacteria, that arises due to chemotactic ability of the former [61]. An important physical parameter that governs the consumption dynamics is the molecular diffusivity of the nutrient, which eventually smears out any heterogeneities in the nutrient distribution. Nutrient gradients developed by pseudo-turbulence disappear quickly, or slowly, de-

pending on whether the nutrient diffusivity is high, or low, respectively. The typical diffusivity values for nutrients range from 10^{-5} to 10^{-8} cm^2/s [74], which is three orders of magnitude smaller than the momentum diffusivity of water (10^{-2} cm^2/s). A fully resolved DNS for the nutrient distribution with such small diffusivities is very expensive from a computational perspective. This forces us to choose a larger nutrient diffusivity in our simulations: 5×10^{-4} cm^2/s . Thus, the quantification of the chemotactic advantage presented in this paper is conservative due to this choice of nutrient diffusivity. The results presented improve our understanding about the consumption of soluble nutrients in sub-surface hydrocarbon plumes. In the Appendix of our paper, we comment on the sensitivity of the results to the nutrient diffusivity and discuss the possible changes that could transpire for more realistic diffusivity values. Although we are motivated by sub-surface HC degradation, we point out that our study can be easily tailored—by merely changing the values of the dimensionless parameters—to simulate chemotaxis in situations involving chemoeffector/nutrient dispersion in other multi-phase flows. In the next Section, we describe our mathematical model and the governing equations in detail.

2.2 Mathematical model

We numerically solve the equations governing multi-phase flows, i.e., the continuity equation and the Navier-Stokes equation:

$$\nabla \cdot \mathbf{u} = 0, \quad (2.1)$$

$$\begin{aligned} \frac{\partial \mathbf{u}}{\partial t} + \nabla \cdot \mathbf{u}\mathbf{u} = & -\frac{1}{\rho} \nabla p + \left(1 - \frac{\rho_0}{\rho}\right) \mathbf{g} + \frac{1}{\rho} \nabla \cdot (2\mu \mathbf{E}) \\ & + \frac{1}{\rho} \int_{\partial V} \sigma \kappa' \mathbf{n}' \delta^\beta (\mathbf{x} - \mathbf{x}') dA', \end{aligned} \quad (2.2)$$

where $\mathbf{u}(x, y, z, t)$ is the fluid velocity field, t is the time, p is the fluid pressure, ρ and μ are the density and viscosity of the fluid, respectively, ρ_0 is the average

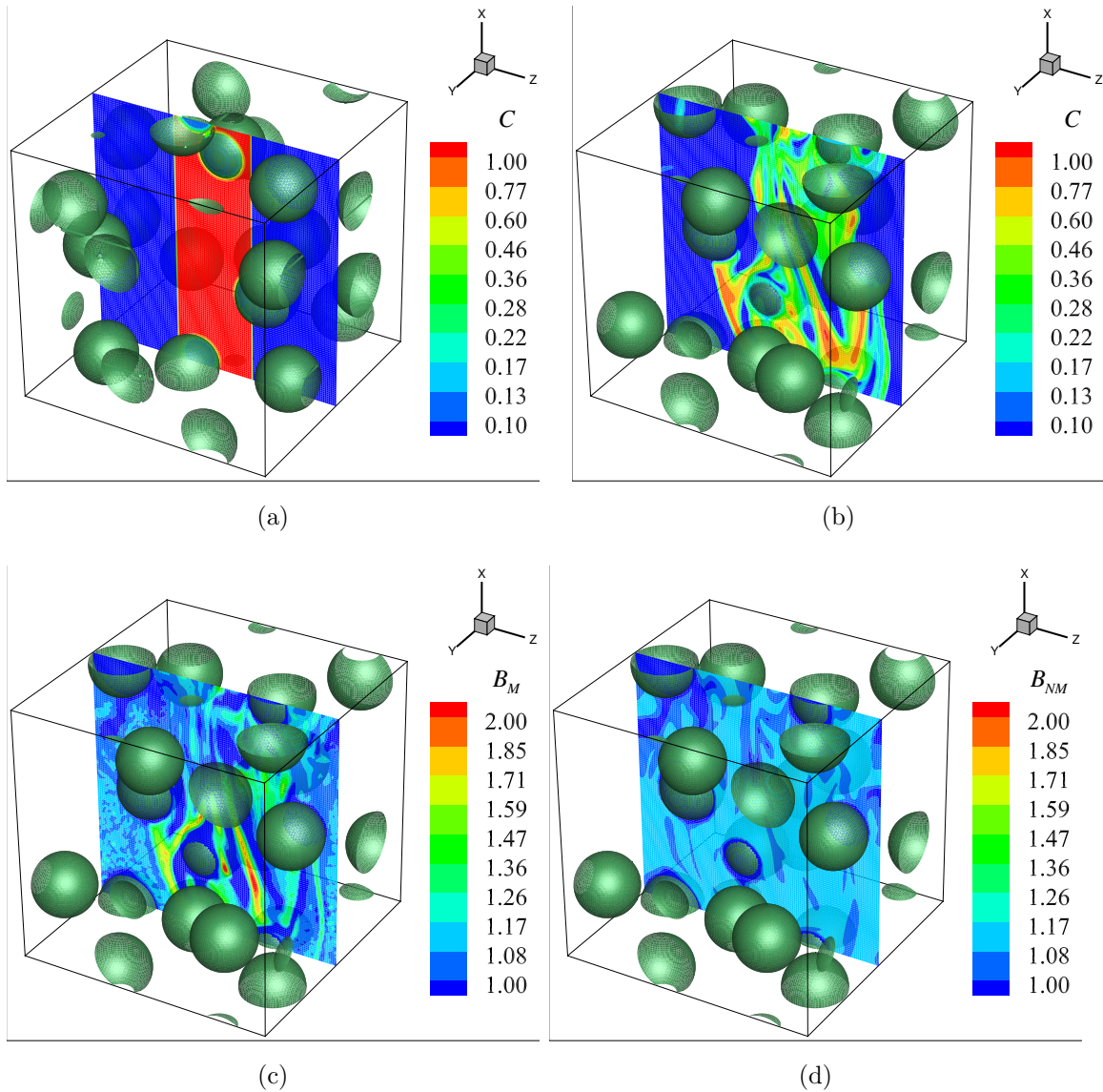


Figure 2.1. : (a) The initial distribution of the chemoattractant/nutrient. (b) The distribution of the nutrient after some time has elapsed in the simulations. (c) The distribution of the motile bacteria at the same instant of time as in (b). Notice higher concentrations of motile bacteria B_M in the nutrient-rich regions, due to chemotaxis. (d) The distribution of the non-motile bacteria at the same instant of time as in (b). Note that the distribution of the non-motile bacteria remains more or less uniform, as there is no bias in their motion.

density of the oil-water system, and σ is the surface tension between oil and water. \mathbf{E} is the rate of strain tensor, defined as $\mathbf{E} = \frac{1}{2} (\nabla \mathbf{u} + \nabla \mathbf{u}^T)$, with T denoting the transpose operator acting on the velocity gradient tensor $\nabla \mathbf{u}$. Equation 2.1 is the condition for incompressibility of a fluid and equation 2.2 is a differential form of the conservation of fluid momentum. The last term in equation 2.2 is the contribution of surface tension forces on the fluid flow, with the area integral carried out over all points on the oil-water interface ∂V ; \mathbf{x} is the point in the fluid domain where we want to evaluate the fluid velocity, κ' is the mean curvature, and \mathbf{n}' is the outward pointing unit vector normal to the interface at the *interface* point \mathbf{x}' , and δ^β is the three-dimensional Dirac-delta function [75, 76]. The interface corresponds to the surface of mono-disperse drops of diameter d , density ρ_g and viscosity μ_g , where the subscript g indicates that the desired properties are of the dispersed phase (in our case, an insoluble oil drop). The fluid flow is governed by the Eötvös number $EO = \frac{\rho_f g d^2}{\sigma}$ (a measure of the relative importance of the buoyancy and surface tension forces), and the Galileo number $Ga = \frac{\rho_f^2 g d^3}{\mu_f^2}$ (a measure of the relative importance of the inertial and viscous forces), where the subscript f indicates that the desired properties of the carrier phase (in our case, water) are being used. The $-(\rho_0/\rho)\mathbf{g}$ term in equation 2.2 is a force that prevents free fall of the fluid and ensures zero momentum flux through the boundaries of our computational domain [70]. The bacteria—both motile (B_M) and non-motile (B_{NM})—are modeled as a continuum, being transported according to the following advection-diffusion equations:

$$\frac{\partial B_M}{\partial t} + \nabla \cdot ((\mathbf{u} + V_s \mathbf{p}) B_M) = \nabla \cdot (D_b \nabla B_M), \quad (2.3)$$

$$\frac{d\mathbf{p}}{dt} = \frac{1}{2} \boldsymbol{\omega} \times \mathbf{p} + \frac{1}{\beta_C} (\mathbf{I} - \mathbf{p}\mathbf{p}) \cdot \nabla C, \quad (2.4)$$

$$\frac{\partial B_{NM}}{\partial t} + \nabla \cdot (B_{NM} \mathbf{u}) = 0. \quad (2.5)$$

The non-motile species act as mere tracers that follow the fluid flow, while the motile bacteria have an additional chemotaxis driven velocity $V_s \mathbf{p}$ with respect to

the fluid (equation 2.3). In addition to deterministic swimming, the motile bacteria can also diffuse with diffusivity D_b . This diffusion is indicative of the stochastic nature of bacterial motion. Equation 2.4—solved only in case of the motile species—is an expression for time evolution of the swimming orientation \mathbf{p} , modified to include the effects of external nutrient gradients. The first term on the right hand side is the influence of the background vorticity $\boldsymbol{\omega}$. In addition to the vorticity, the background strain rate \mathbf{E} also affects the swimming orientation, but only if the bacteria are elongated. As a first approximation, we neglect this latter effect, and assume the bacteria to be nearly spherical in shape. The chemotactic bias in the swimming direction is introduced through the second term on the right hand side of equation 2.4, which models the effect of an external nutrient gradient (∇C , C being the concentration of the nutrient) on the rate of change of swimming orientation. β_C is the inverse of the chemotactic sensitivity, which determines the relative importance of steering by external chemical gradients as compared to that by external vorticity. In their present form, equations 2.3 and 2.4 assume that all cells around a differential volume δV at position \mathbf{x} are oriented along the same direction \mathbf{p} . This is a strong assumption, but it adds considerable simplicity to our numerical simulations. A more complete description would require us to couple our multi-phase DNS procedure with a transport equation for the probability distribution $\psi(\mathbf{x}, \mathbf{p}, t)$ of the bacterial positions and orientations, and then perform appropriate averaging to fully incorporate the effects of randomness in swimming orientations in equation 2.3 (see [50]). This will increase the dimensionality of the system from three to five, and together with the front-tracking method used to fully resolve the evolution of oil-water interface, render the problem computationally unwieldy. A justification of our method is that re-orientations due to flow, and particularly chemotaxis, are strong enough to ensure rapid correction in the swimming direction, over the smallest length scale in our system (≈ 0.03 mm). Therefore, we use the present formulation and integrate equation 2.4 at each time step and position, instead of using averaged ‘equilibrium’ values of the vector \mathbf{p} (see a similar method in the context of gyrotaxis, first proposed by Ped-

ley, Hill and Kessler [77], and recently solved numerically by Karimi and Ardekani in the context of gyrotaxis in stratified media [78]). In addition, equation 2.4 does not contain any rotary diffusive terms, i.e., random, smooth changes in the swimming direction of the bacterium. We chose to neglect this effect based on a simple scaling analysis, towards which we first re-write equation 2.4, with the inclusion of a random orientation de-correlation due to the rotary diffusivity D_R :

$$d\mathbf{p} = \left[\frac{1}{2}\boldsymbol{\omega} \times \mathbf{p} + \frac{1}{\beta_C} (\mathbf{I} - \mathbf{p}\mathbf{p}) \cdot \nabla C \right] dt + \left[\sqrt{4D_R}\boldsymbol{\eta}_R \times \mathbf{p} \right] dt, \quad (2.6)$$

where the rotary diffusion is modeled via a Gaussian white-noise on the unit sphere, $\boldsymbol{\eta}_R$. The vorticity scales as $|\boldsymbol{\omega}| \approx \sqrt{g/d} \approx 44 \text{ s}^{-1}$ to 86 s^{-1} , based on the typical values given in Table 2.1. In comparison, the orientation change due to a rotary diffusivity value $D_R = 0.035$ to $0.45 \text{ rad}^2/\text{s}$ amounts to $\approx \sqrt{4D_R} \cdot O(1) \text{ s}^{-1/2} \approx 0.42 \text{ s}^{-1}$ to 1.34 s^{-1} . Thus, as long as there exists a sufficiently strong background flow, we can safely neglect the effect of rotary diffusion on the bacterial orientation. Fig. 2.9 in the Appendix shows the difference in the results between the instance that considers rotary diffusivity, and one that does not; clearly, the difference is imperceptible. Note that the use of a deterministic, continuum formulation for chemotaxis, as opposed to the classic run-and-tumble formulation, is justified based on the ratio of the characteristic length scale l_{ref} of our problem ($l_{ref} \equiv$ drop diameter $d \approx 1 \text{ mm}$) to the typical run length l_{run} of marine bacteria ($\approx 0.05 \text{ mm}$) being much greater than unity [43, 79]. In such large length scale systems, we can say that equation 2.4 captures the average reorientation tendency of a chemotactic swimmer in response to chemical cues and ambient flows [52]. It can be thought of as a ‘chemotactic torque’, or a means to the ‘spatial sensing’ of nutrient gradients, which is indeed found in some species of microorganisms [33, 80]. Similar models have been used in the absence [81, 82] and presence [83] of external fluid flows to explain phenomena like micro-swimmer clustering and aerotaxis-induced bioconvection plumes, respectively. Lushi *et al.* have performed a study highlighting the similarities between the present model and the run-and-tumble model, in the context of stability and collective mo-

tion of auto-chemotactic suspensions [84]. The chemoeffector distribution, $C(\mathbf{x}, t)$, is governed by the scalar transport equation with a sink term:

$$\frac{\partial C}{\partial t} + \nabla \cdot (C\mathbf{u}) = \nabla \cdot (D_m \nabla C) - \alpha_C B_M C - \alpha_C B_{NM} C, \quad (2.7)$$

where D_m is the diffusivity of nutrient in water and α_C is a constant which quantifies the nutrient uptake rate by the bacteria. The last two terms on the right hand side of equation 2.7 are the reductions in the nutrient concentration due to uptake by the motile and non-motile species, respectively. It is postulated that chemotactic species will ‘climb up’ the gradients, and as a result, will consume higher concentrations. Since our study is motivated by the extent of consumption, the instantaneous motility benefit is defined as the volume averaged difference between the rates of consumption by the motile and the non-motile species, i.e., motility benefit $\Delta U(t) = \dot{C}_M - \dot{C}_{NM}$ [62], where

$$\dot{C} = \frac{\int_V \alpha_C B C dV}{\int_V dV}, \quad (2.8)$$

and $B = B_M$ and B_{NM} , for motile and non-motile species, respectively. A benefit due to motility exists only if $\dot{C}_M > \dot{C}_{NM}$. In our results, we normalize $\Delta U(t)$ by the quantity $\alpha_C B_0 C_0$ —where B_0 is a baseline number density and C_0 is a baseline nutrient concentration—which has the units $\mu\text{M}/\text{s}$, and signifies a reference consumption rate. In addition to the normalized motility benefit $\Delta \bar{U} = \Delta U / (\alpha_C B_0 C_0)$, we present a measure of the relative rates of consumption by motile and non-motile bacteria, called the ‘chemotactic amplification factor’ R_U [62]:

$$R_U = \frac{\dot{C}_M + \dot{C}_{NM}}{2\dot{C}_{NM}}, \quad (2.9)$$

It is clear from the definition that R_U compares the rate of consumption in a region inhabited by both motile and non-motile species, with the scenario where all consumption is assumed to be done by non-motile species alone. It quantifies enhancement in the total uptake rate by a bacterial population due to the chemotactic species. This definition is particularly useful in assessing the chemotactic advantage when the nutrient availability is very low.

We use the finite-volume method on a uniform, structured, staggered grid, combined with the projection method to solve equations 2.1 and 2.2 [85]; and track the interface using the front-tracking method [75, 76]. The validation of the front-tracking method being used in this article can be seen in previous publications by the authors [72, 86]. All terms in equation 2.2 are discretized explicitly using the QUICK scheme for the convective terms [87], central differences for diffusive terms and front-tracking, with second order accurate representation for δ^β [88], for the surface tension contributions. Equations 2.3, 2.5 and 2.7 are also solved explicitly using the finite-volume method, with convective terms discretized using a fifth order accurate WENO scheme [89] and diffusive terms discretized using central differences. A second order accurate predictor-corrector scheme is employed for all time-integrations. The magnitude of \mathbf{p} is preserved at unity by using a post-stabilization approach used in ref. [78] and detailed in ref. [90].

The initial condition for the fluid-velocity is obtained as the statistically steady-state for a rising swarm of drops [70, 71]. The time evolution of the fluctuation Reynolds number for the various background fluid-flows in the simulations is shown in Fig. 2.2; while other quantities pertaining to the pseudo-turbulence are detailed in Table 2.1. It is interesting to note that the energy dissipation rates generated by rising oil drops— $O(10^{-3})$ W/kg—are at least 3 orders of magnitude higher than those corresponding to ‘relatively strong’ marine turbulence ($\sim 10^{-6}$ W/kg) [91]. This allows us to neglect the effects of marine turbulence, and focus solely on the hydrodynamic interactions between rising drops, in our simulations. The initial nutrient-rich region is in the form of a cylinder placed centrally (see Fig. 2.1), occupying $\approx 8\%$ of the domain volume and with its axis along the direction $\mathbf{g}/|\mathbf{g}|$. We note that we have also carried out investigations for different initial shapes of the nutrient-rich region, i.e., for (i) a cylindrical shape perpendicular to the direction of ascent (along the y axis in Fig. 2.1), and, (ii) a spherical shape of same volume as the cylinder (see Fig. 2.11 in the Appendix and the accompanying discussion). The nutrient concentration inside the drops is set to zero. The concentration of the motile and non-motile bacteria is

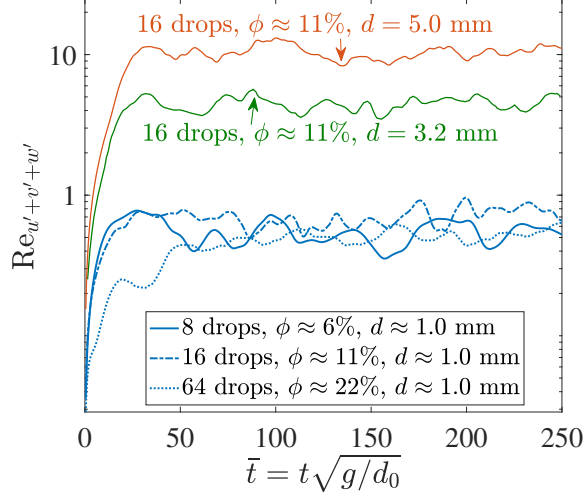


Figure 2.2. : (Color online) Time evolution of the fluctuation Reynolds numbers $\text{Re}_{u'+v'+w'}$ of the drops in the simulations; see the Appendix and the ref. [70, 71] for the definition of the drop fluctuation Reynolds number. The statistical steady states can be easily identified in all 5 cases (at $\bar{t} \approx 50$), the background flow-fields (and drop positions) at these instants are used as the initial condition for the fluid velocity $\mathbf{u}(t = 0)$ in the simulations that are performed to ascertain the chemotactic advantage.

uniform everywhere, except inside the drops (where it is set to zero). Note that the equation 2.5, for the evolution of non-motile bacteria does not have any diffusivity, but there exists some numerical diffusion. We do not expect significant clustering of the non-motile bacteria to take place. This is because of the initially uniform distribution of B_{NM} , combined with absence of a term with non-zero divergence in the convective flux of B_{NM} (see the explanations of microorganism clustering based on the divergence of their velocities, as given in ref. [92]). Thus, $B_{NM}(\mathbf{x}, t)$ is expected to be $\approx B_0$ everywhere in the domain. In our simulations, the value of $|B_{NM} - B_0|/B_0$ stays below $\approx 3\%$ for most of the domain; and therefore numerical diffusion is small. The orientations of the (motile) bacteria are randomly initialized. Periodic boundary conditions are enforced in all directions, for \mathbf{u} , C , B_M and B_{NM} .

In order to elucidate the effects of external flow on nutrient uptake and motility benefit, we solve equations 2.1 to 2.7, subject to parametric sweeps in (i) the important biological parameters at play, i.e., α_C , β_C and V_s , and, (ii) the relevant hydrodynamic parameters, i.e., drop diameter d and volume fraction of the oil phase ϕ , for drop diameters commensurate with those of an oil spill. The values of these parameters are listed in Table 2.1. The fluid properties ($\mu_f, \mu_g, \rho_f, \rho_g, \sigma$) are those of Light Louisiana oil (involved in the Deepwater Horizon oil-spill) and water [93]. The size of the drops was estimated based on previous literature pertaining to droplet size distribution from sub-surface oil-spills [94–96]. The bacterial swimming speed values encompass a range from 50 to 300 $\mu\text{m/s}$. This range is expected to cover a wide variety of bacterial species, with values $> \approx 60 \mu\text{m/s}$ being more appropriate for marine bacteria [6]. The uptake rate constant α_C was estimated based on typical bacteria length-scales and nutrient diffusivities, as done in the first paragraph of Section 2.3.1. An estimate of the inverse chemotactic sensitivity, β_C , as defined by us was not available, and so we decided to cover a broad range for the values of β_C . The bacterial diffusivity was estimated from the scaling $D_b \sim V_s^2 \tau / 3$ [10], where V_s is the swimming speed and τ is the mean bacterial run time. For $V_s \approx 100 \mu\text{m/s}$, and $\tau = 1.5 \text{ s}$, this yields $D_b = 5 \times 10^{-5} \text{ cm}^2/\text{s}$. But once again, numerical constraints force us to choose a larger diffusivity of $D_b = 5 \times 10^{-4} \text{ cm}^2/\text{s}$, this time for the bacteria. The reference nutrient concentration was chosen based on the values reported by Valentine *et al.* [68]. Our computational domain corresponds to a representative fluid volume ($L^3 \approx 0.15 - 9 \text{ cm}^3$) consisting of mono-disperse oil drops of prescribed diameters ($d \approx 0.1 - 0.5 \text{ cm}$), rising in a water column that has a patch of dissolved nutrient, as shown in Fig. 2.1.

2.3 Results and Discussion

We will first discuss some important bio-physical mechanisms at play, which will be visible in the solutions to equations 2.1 to 2.7. The initial nutrient distribution, as shown in Fig. 2.1(a) gets distorted once the drops rise through the fluid column.

Table 2.1. : List of simulation parameters.

Parameter (description)	Value (units)
<u>Flow/physical parameters</u>	
μ_f (viscosity of suspending fluid)	0.01 (poise)
μ_g (viscosity of dispersed phase)	0.12 (poise)
ρ_f (density of suspending fluid)	1.00 (g/cm ³)
ρ_g (density of dispersed phase)	0.85 (g/cm ³)
σ (surface tension)	40 (dyne/cm)
d (diameter of drops)	0.13 - 0.5 (cm)
$Eo = \rho_f g d^2 / \sigma$ (Eötvös number)	0.41 - 6
$Ga = \rho_f^2 g d^3 / \mu_f^2$ (Galileo number)	2.15×10^4 - 1.22×10^6
$Re_{u'+v'+w'}$ (fluctuation Reynolds number)	0.5 - 10
ϵ_f / ρ_f (dissipation rate per unit mass)	2.7×10^{-3} - 1.2×10^{-2} (W/kg, or, m ² s ⁻³)
Re_r (rise Reynolds number)	15 - 400
We (Weber number)	2.8×10^{-3} - 0.54
<u>Bacteria/biological parameters</u>	
V_s (swimming speed)	20 - 300 (μ m/s)
α_C (nutrient uptake rate constant)	10^{-11} - 10^{-7} (cm ³ /s/cell)
β_C (inverse chemotactic sensitivity)	0.4 - 4000.0 (μ Mcm ⁻¹ s)
D_b (diffusivity)	5×10^{-4} (cm ² /s)
B_0 (reference number density)	1.5×10^5 (cells/cm ³)
<u>Nutrient</u>	
C_0 (reference concentration)	25 (μ M)
D_m (diffusivity)	5×10^{-4} (cm ² /s)
$Sc = \mu_f / (\rho_f D_m)$ (Schmidt number)	2, 20
V_p / L^3 (volume fraction of nutrient patch)	2 - 8 (%)
<u>Numerical simulation</u>	
L (computational box length)	0.5325, 1.3564, 2.0833 (cm)
N^3 (number of grid points)	192 ³
N_d (number of drops)	8, 16, 64
$h = L/N$ (smallest length scale resolved)	0.0028, 0.0071, 0.0108 (cm)

As a result, the fairly homogeneous, ‘cylindrical’ nutrient distribution at the vertical mid-plane gets heterogenized, leading to (i) ‘breaking’ or stirring of the nutrient patch into strands of varying thicknesses and concentration, and (ii) subsequent dissipation of these strands—both by the flow, and molecular diffusion—into increasingly uniform concentrations across the entire fluid domain. The chemotactic, motile bacteria forage for nutrient-rich regions, and are also transported and rotated by the flow. The non-motile organisms are simply carried by the flow, and can encounter nutrient rich regions only by chance. This fundamental difference in the ability of motile and non-motile species to access and consume nutrients is expected to yield an instantaneous chemotactic advantage to the former ($\Delta U(t) > 0$ and $R_U(t) > 1$). But this benefit diminishes because as time progresses, the heterogeneities—engendered by mechanisms described in point (i) above—are lost and the nutrient distribution relaxes to a uniform non-zero concentration. Once this relaxation occurs, there aren’t any significant chemoattractant gradients left for chemotaxis to be beneficial and the chemotactic advantage ceases to exist (i.e., $\Delta U(t) \sim 0$ and $R_U(t) \sim 1$). However, nutrient consumption will continue to occur and the volume-averaged nutrient concentration will continue to decrease. Eventually, over a time scale of the order of a few hours or days (depending on the nutrient availability and consumption rate constant), the entire nutrient available will get consumed by the bacteria (both motile and non-motile) and the volume-averaged nutrient concentration will reduce to ~ 0 . But this does not happen in our simulations because the time for which we run them is smaller than the time required to completely consume the entirety of the available nutrient.

The previous paragraph suggests that slower distortion of the initial nutrient field and/or faster detection of the nutrient gradients will provide maximum nutrient exposure to the motile species. Therefore, the time scale of the chemotactic response relative to that of changes in the ambient nutrient concentrations is of utmost importance. The time scale of the chemotactic response is dictated by the inverse sensitivity β_C and the swimming speed V_s , while the ambient nutrient concentration changes over

a time scale governed by the flow. Another important consideration in the following discussions is the characteristic length scale associated with nutrient (and bacterial) heterogeneity l_C , i.e.,

$$l_C^2 \equiv \frac{\overline{(C - C_0)^2}}{|\overline{\nabla C}|^2}, \quad (2.10)$$

and the volume-averaged (denoted by an over-bar) nutrient gradient $|\overline{\nabla C}|$. This latter quantity is a useful measure of the scale of the nutrient gradient being experienced by a bacterium in the flow field. Thus, any comparative analysis of the resulting dynamics is best understood by keeping in mind (i) the chemotactic and hydrodynamic time scales, and (ii) the nutrient gradient length scales. In what follows, we bring out the effect of each relevant biophysical parameter by resorting to a comparison of the above mentioned intrinsic scales of the problem.

2.3.1 Influence of biological parameters, α_C , β_C and V_s

As discussed above, the nutrient strand formation is driven by fluid flow, while the localization of the bacteria in regions of high nutrient concentration is achieved by chemotaxis. This means that the biological parameters primarily govern the speed with which a nutrient ‘hot-spot’ is encountered. We performed simulations for a wide range of these parameters, in order to bring out their effect on the consumption process. We begin by analyzing the influence of the uptake rate constant α_C . A measure of this constant can be obtained by first calculating the uptake rate on a ‘per cell’ basis, which is estimated from the diffusion limited uptake time scale that scales as $\tau_{diff}^{-1} \approx aD_m B_0$, where a is the characteristic size of the bacterium [97]. For a given number density B_0 , α_C then scales as $\approx (B_0 \tau_{diff})^{-1} \approx aD_m$. This gives $\alpha_C \approx O(10^{-8}) \text{ cm}^3\text{s}^{-1}\text{cell}^{-1}$, for $a \approx O(10) \text{ }\mu\text{m}$ and $D_m \approx O(10^{-9}) \text{ m}^2/\text{s}$.

Fig. 2.3(a) shows how the instantaneous motility benefit changes with time for rate constants ranging from $1 \times 10^{-10} \text{ cm}^3\text{s}^{-1}\text{cell}^{-1}$ to $1 \times 10^{-7} \text{ cm}^3\text{s}^{-1}\text{cell}^{-1}$. We notice a monotonic increase in the motility benefit as α_C increases. The results indicate that a faster rate of consumption translates directly to enhanced motility benefit. A

physical reason for the behavior shown in Fig. 2.3(a) can be understood by comparing two time scales pertinent to the problem: the uptake time scale and the time scale for the persistence of nutrient gradients. A faster rate of uptake enables the motile species to profit more from staying in regions of high nutrient concentration. These regions eventually perish due to diffusion and their ephemeral nature is best exploited if the bacteria consume the nutrient rapidly enough. But we must keep in mind that higher α_C means faster consumption by the non-motile species as well. Therefore, the relative rate of consumption, i.e., the chemotactic amplification R_U stays more or less the same for each case—particularly for $\alpha_C = 10^{-10}$ and $10^{-9} \text{ cm}^3\text{s}^{-1}\text{cell}^{-1}$ —as seen in Fig. 2.4(a). In other words, any advantage offered to the motile species by an increase in α_C is offered equally to the non-motile species, resulting in no relative benefit for the former. Our calculations show that, for the parameters of Fig. 2.3, the motile bacteria consume the nutrient $\approx 5\%$ ($\Delta U/\dot{C}_{NM} \approx 0.05$) faster than the non-motile ones, irrespective of the value of α_C .

The next biological parameter we consider is the inverse chemotactic sensitivity β_C (see equation 2.4). This parameter is only relevant for motile bacteria. It is a measure of the time taken by a chemotactic bacterium to reorient towards the direction ∇C , i.e., in the direction of increasing concentration of the chemoeffector C . Lower values of β_C indicate one of the following two scenarios: (i) for a fixed $|\nabla C|$, the bacterium rotates more rapidly to attain a swimming direction along ∇C , or (ii) the bacterium is able to sense subtler spatial gradients in its vicinity, and reorient accordingly. Fig. 2.3(b) shows a series of curves wherein the value of the dimensionless motility benefit, $\Delta\bar{U}(t)$, increases progressively, as β_C is reduced from $4000.0 \mu\text{Mcm}^{-1}\text{s}$ to $0.4 \mu\text{Mcm}^{-1}\text{s}$. This is an implication of the balance between the two reorientation effects in equation 2.4: rotation due to the ambient vorticity ($\boldsymbol{\omega} \times \mathbf{p}$) vs. rotation as a response to local gradients in C ($\beta_C^{-1} (\mathbf{I} - \mathbf{p}\mathbf{p}) \cdot \nabla C$). The rotation due to ambient vorticity dominates for large values of β_C , and although bacteria always tend to rotate towards the direction of increasing nutrient concentration, they are unable to do so quickly enough. This reveals a second balance of time scales inherent in our problem:

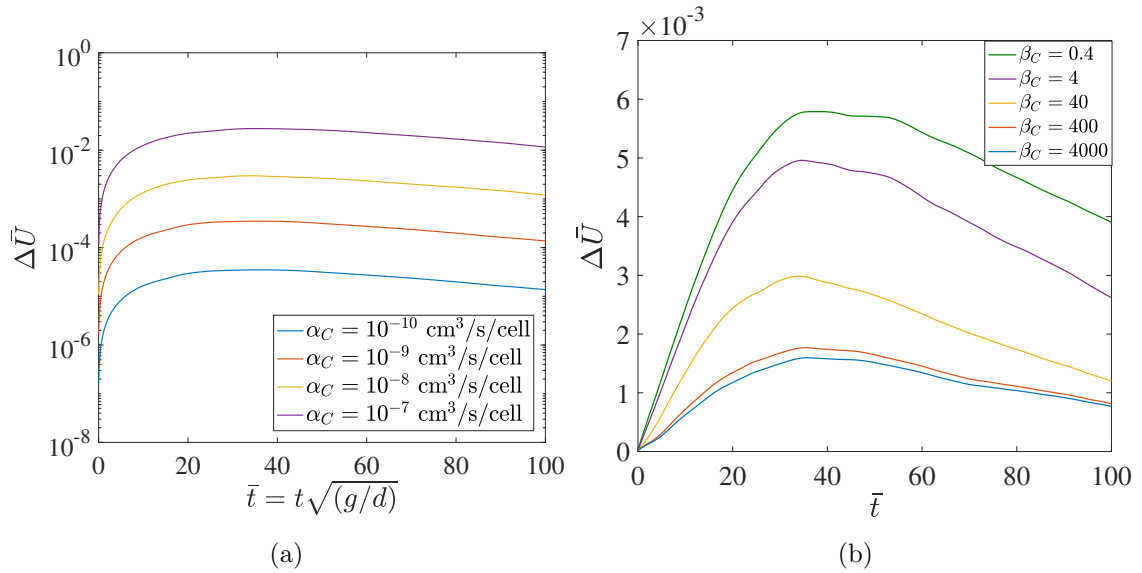


Figure 2.3. : (Color online) (a) Time evolution of the dimensionless motility benefit for different uptake rate constants (α_C). $\beta_C = 40.0 \mu\text{Mcm}^{-1}\text{s}$. (b) Time evolution of the dimensionless motility benefit for different inverse chemotactic sensitivities (β_C); the units of β_C are $\mu\text{Mcm}^{-1}\text{s}$. $\alpha_C = 1 \times 10^{-8} \text{ cm}^3\text{s}^{-1}\text{cell}^{-1}$. The other parameters are: $d = 1.32 \text{ mm}$; $\phi \approx 11\%$; $V_s = 100 \mu\text{ms}^{-1}$; $D_m = D_b = 5 \times 10^{-4} \text{ cm}^2/\text{s}$; $C_0 = 25 \mu\text{M}$; $B_0 = 1.5 \times 10^5 \text{ cells}/\text{cm}^3$; $Eu = 0.40$; $Gr = 2 \times 10^4$.

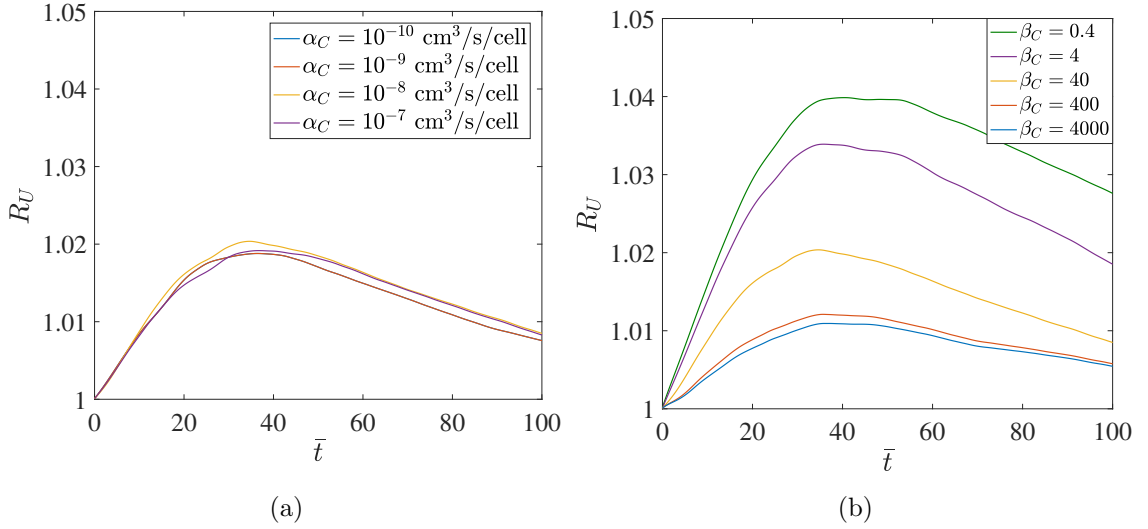


Figure 2.4. : (Color online) (a) Time evolution of the chemotactic amplification factor for different uptake rate constants (α_C). $\beta_C = 40.0 \mu\text{Mcm}^{-1}\text{s}$. Clearly, a change in α_C does not affect the relative consumption rates significantly, because it proportionately enhances the values of \dot{C}_M and \dot{C}_{NM} . (b) Time evolution of the chemotactic amplification factor for different inverse chemotactic sensitivities (β_C); the units of β_C are $\mu\text{Mcm}^{-1}\text{s}$. $\alpha_C = 1 \times 10^{-8} \text{ cm}^3\text{s}^{-1}\text{cell}^{-1}$. The other parameters are: $d = 1.32 \text{ mm}$; $\phi \approx 11\%$; $V_s = 100 \mu\text{ms}^{-1}$; $D_m = D_b = 5 \times 10^{-4} \text{ cm}^2/\text{s}$; $C_0 = 25 \mu\text{M}$; $B_0 = 1.5 \times 10^5 \text{ cells}/\text{cm}^3$; $EO = 0.40$; $Ga = 2 \times 10^4$.

the competition between $|\omega|^{-1}$ (the time scale for reorientation by flow) and $\frac{\beta_C}{|\nabla C|}$ (a chemotactic reorientation time scale). As long as $\frac{\beta_C}{|\nabla C|} > |\omega|^{-1}$, the reorientation will predominantly be due to the local rotation rate of the fluid. In this case, the possibility of chemotaxis being beneficial is contingent on the proximity of motile bacteria to regions of high concentration gradients (large values of $|\nabla C|$), because low values of $|\nabla C|$ prove insufficient to overcome the tendency of hydrodynamics-induced reorientation. Scaling analysis reveals that in order for chemotactic reorientation to be effective, β_C must be $\leq \frac{|\nabla C|}{(u_c/l_{ref})}$; which gives—for parameters used in Fig. 2.3(b)— $\beta_C \leq O(10) \mu\text{Mcm}^{-1}\text{s}$.

Fig. 2.3(b) shows that the increase of motility benefit $\Delta\bar{U}(t)$ is not always commensurate with the increase in β_C^{-1} , particularly when β_C is very large (least sensitive chemotaxis) or small (most sensitive chemotaxis). The rate of increase in $\max.\{\Delta\bar{U}\}$ —with respect to β_C —becomes smaller when β_C reduces. This suggests an upper limit to the chemotactic advantage that can be offered by enhanced sensitivity to gradients in nutrient concentration. This is seen in the reduced difference in the motility benefit curves for $\beta_C = 4.0 \mu\text{Mcm}^{-1}\text{s}$ to $0.4 \mu\text{Mcm}^{-1}\text{s}$, and quantified in Fig. 2.5. It is also apparent that the value of $\Delta\bar{U}(t)$ for $\beta_C = 4000.0 \mu\text{Mcm}^{-1}\text{s}$ to $400.0 \mu\text{Mcm}^{-1}\text{s}$ is not substantial. This observation corresponds to a regime where chemotaxis is not as significant in reorienting the bacteria as hydrodynamics. Thus, we conclude that $\beta_C \geq O(100) \mu\text{Mcm}^{-1}\text{s}$ represents negligible effect of ∇C on the bacteria's orientation, while $\beta_C \leq O(10) \mu\text{Mcm}^{-1}\text{s}$ represents almost instantaneous reorientations to ambient ∇C . A true coupling of the chemotactic and hydrodynamic reorientation effects takes place only for the intermediate values of β_C ($O(10) \mu\text{Mcm}^{-1}\text{s} \leq \beta_C \leq O(100) \mu\text{Mcm}^{-1}\text{s}$). Fig. 2.4(b) shows that higher chemotactic sensitivity (low β_C) enhances the total uptake by 4% for $V_s = 100 \mu\text{m/s}$. This factor increases for higher swimming speeds, which is discussed next.

The swimming speed is another biological factor that allows marine bacteria to exploit gradients in nutrient concentration. Since diffusion tends to smoothen all gradients, it is imperative that the bacteria swim to nutrient-rich regions as fast

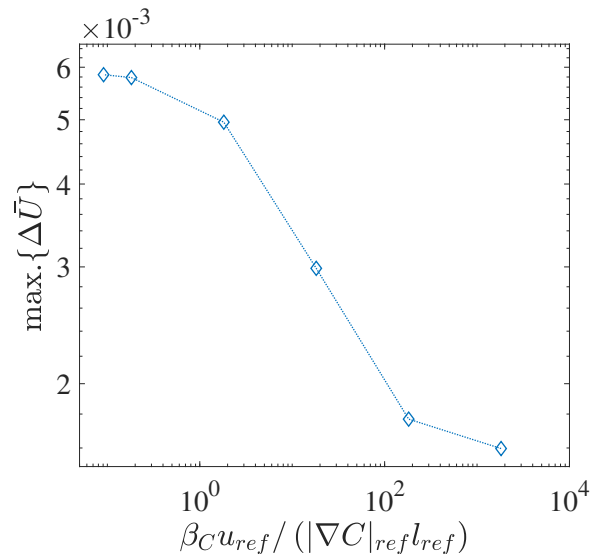


Figure 2.5. : (Color online) Variation of the maximum value of the dimensionless instantaneous motility benefit, $\max.\{\Delta \bar{U}\}$, with β_C scaled by $(|\nabla C|_{ref} l_{ref} / u_{ref})$. The motility benefit increases with the chemotactic sensitivity (inverse of β_C), but not indefinitely; a saturation occurs for $\beta_C < 0.4 \mu\text{Mcm}^{-1}\text{s}$.

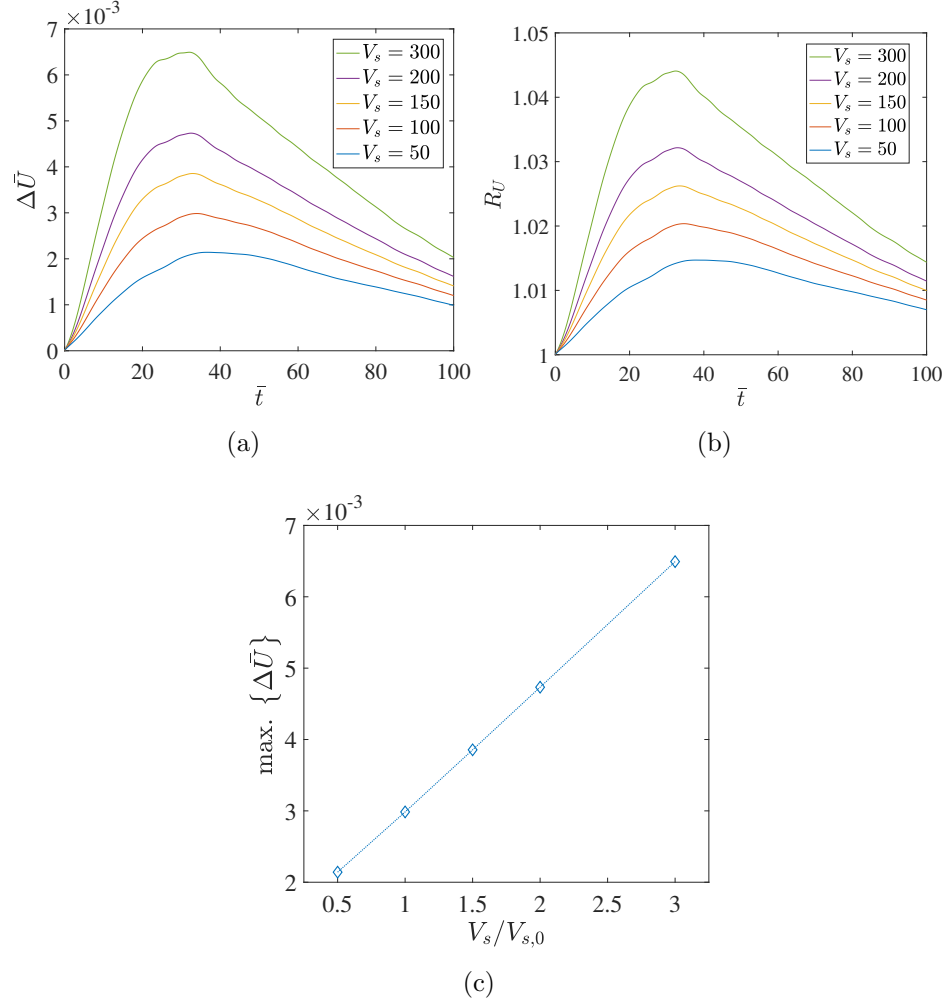


Figure 2.6. : (Color online) (a) Time evolution of the dimensionless motility benefit for different swimming speeds. (b) Time evolution of the chemotactic amplification for different swimming speeds; the units of V_s are $\mu\text{m/s}$. (c) The maximum motility benefit scales linearly with the swimming speed ($V_{s,0} = 100 \mu\text{m/s}$). The other parameters are: $d = 1.32 \text{ mm}$; $\phi \approx 11\%$; $\alpha_C = 1 \times 10^{-8} \text{ cm}^3 \text{ s}^{-1} \text{ cell}^{-1}$; $\beta_C = 40.0 \mu\text{Mcm}^{-1} \text{ s}$; $D_m = D_b = 5 \times 10^{-4} \text{ cm}^2/\text{s}$; $C_0 = 25 \mu\text{M}$; $B_0 = 1.5 \times 10^5 \text{ cells/cm}^3$; $Eo = 0.40$; $Ga = 2 \times 10^4$.

as possible. This balance between the diffusion and the chemotactic time scales is one of the most important factors in determining the extent to which motility can be beneficial in marine environments [61]. Fig. 2.6(a) brings out the effect of swimming speeds on the motility benefit, with speeds ranging from 50 to 300 $\mu\text{m/s}$; a range of values that is typical for marine bacteria. The first feature we observe is that increasing V_s has a fairly monotonous effect on the consumption characteristics: faster bacteria profit considerably. This is a direct consequence of the chemotactic time scale being progressively shorter than the diffusion time scale, as V_s is increased. This means that under identical conditions, a faster bacterium will be able to travel deeper into the nutrient-rich regions as compared to a slower bacterium. Just like β_C , V_s only affects the performance of the motile species, and so higher swimming speeds also lead to an increase in the relative consumption, as shown in Fig. 2.6(b). An interesting observation is the dependence of the maximum motility benefit on the normalized swimming speed $V_s/V_{s,0}$; which is linear for a wide range of swimming speeds, as shown in Fig. 2.6(c). This is an important result because it allows us to estimate the motility benefit at different swimming speeds of the bacterium under more varied conditions set by the other parameters involved. One can estimate the maximum possible enhancement in the consumption rate by noting two things: (i) for the highest chemotactic sensitivity ($\beta_C = 0.4 \mu\text{Mcm}^{-1}\text{s}$), the consumption is enhanced by $\approx 4\%$, and, (ii) the maximum motility benefit scales linearly with the swimming speed V_s . One subtle aspect of higher swimming speeds leading to enhanced consumption is the assumption that the span of nutrient-rich regions is wide enough to ensure that they are not simply bypassed by the faster bacteria. There is a trade-off between reaching nutrient-rich regions faster and staying there for as long as possible [61]. Based on the results of our simulations, the spatial extent of nutrient-rich regions is wide enough for increased V_s to pose significant benefits.

To conclude this Section, we stress on the nature of dependence of $\Delta\bar{U}$ and R_U on each of the biological parameters studied. We saw that a the change in α_C only affects $\Delta\bar{U}$ and not R_U , because increasing α_C increases the consumption rate by *both* motile

and non-motile bacteria. But an increase in β_C and V_s affects *only* the consumption by motile bacteria, and thus results in significant changes in both $\Delta\bar{U}$ and R_U . In case of V_s , the chemotactic advantage is derived from faster gradient climbing, which enables the fast bacteria to seek out proportionately higher nutrient concentrations and increase the uptake rate. Therefore, the maximum motility benefit achieved increases linearly with V_s . The variation of $\Delta\bar{U}$ with β_C is more complex and the response of Fig. 2.3(b) is due to the continuously evolving nature of both ∇C and $|\boldsymbol{\omega}|$, and their interaction via equation 2.4. The apparent saturation in instantaneous $\Delta\bar{U}(\bar{t})$ for low values of β_C is due to purely chemotactic reorientations; while negligible $\Delta\bar{U}(\bar{t})$ for high values of β_C can be attributed to purely hydrodynamic reorientations.

2.3.2 Influence of physical parameters: drop diameter and volume fraction

Biological parameters like the ones discussed above are only one set of properties that can influence the nutrient consumption by motile and non-motile bacteria. Another set of properties comes from the hydrodynamic aspects of oil spill, namely the diameter of the rising drops and their volume fraction. These properties change the background flow field and in this way, fundamentally alter the process of chemotaxis. While there was very little qualitative change in the evolution of the nutrient field in the DNS of the previous set of results, we cannot say the same when the background hydrodynamics—the major cause of nutrient redistribution—itself is different. The size and volume fraction of the rising oil drops can drastically change the length scales of the nutrient strands and the time scales of their transport through the domain. It will also directly affect the transport of the bacteria (see equations 2.3 and 2.4), thus providing us with a wide array of bio-physical effects to investigate. We study these effects systematically by: (a) first varying the diameter of the drops but keeping the volume fraction constant; and then (b) varying the volume fraction of

the oil but keeping the drop diameters constant, in order to facilitate comparisons between the various cases considered.

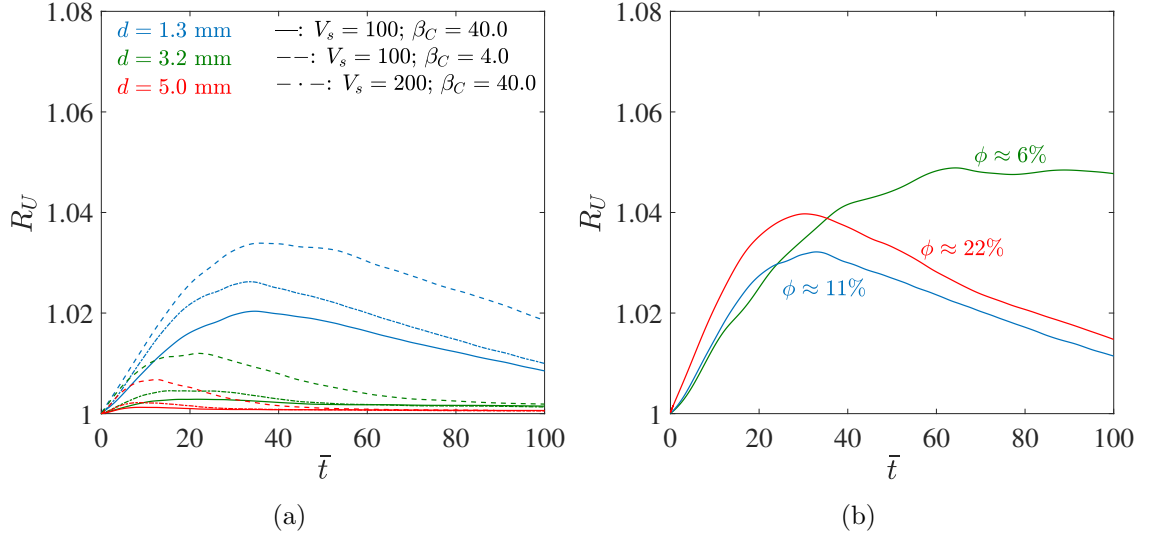


Figure 2.7. : (Color online) (a) Time evolution of the chemotactic amplification factor, for different drop diameters, but same volume fraction in all cases: $\phi \approx 11\%$. The units of V_s are $\mu\text{m/s}$, and of β_C are $\mu\text{Mcm}^{-1}\text{s}$. (b) Time evolution of the chemotactic amplification factor, for different volume fractions, but same drop diameters in all cases. $Eu = 0.40$; $Gr = 2 \times 10^4$. $d \approx 1$ mm. The other parameters are: $\alpha_C = 1 \times 10^{-8} \text{ cm}^3 \text{ s}^{-1} \text{ cell}^{-1}$; $D_m = D_b = 5 \times 10^{-4} \text{ cm}^2/\text{s}$; $C_0 = 25 \mu\text{M}$; $B_0 = 1.5 \times 10^5 \text{ cells/cm}^3$. We would like to emphasize that the motility benefit, $\Delta \bar{U}$, follows an identical trend as the amplification factor, R_U , and therefore is not shown here ($\max \{ \Delta \bar{U} \} = 0.006$).

Fig. 2.7(a) shows evolution of the amplification factor $R_U(t)$ as a function of the diameter of the oil drops. It is to be noted that in all of the cases described, the size of our representative system (i.e., the computational domain) is adjusted such that the volume fraction of the oil phase remains the same. We note that dispersants are often used in oil spill remediation efforts to help break the oil into smaller droplets by reducing the interfacial tension between water and oil. The reduced drop diameters (due to break up) increase the effective surface area of the oil phase, making it easier

for the biodegrading agents to break down the heavier (insoluble) HCs released in the oil spill. Here, we show that this also has an indirect effect on the degradation of the soluble HCs, as the flow field around the rising drops depends heavily on the drop diameter, via the Eötvös and the Galileo numbers. The drop diameters for a surfactant-laden oil phase are typically ≈ 1 mm or smaller, and those for a pure oil phase emanating from a leak are ≈ 5 mm or larger [94–96]. In this Section, we investigate the dependence of the amplification factor on d , for three drop diameters, spanning across a range that includes the aforementioned sizes. We see a marked difference in the values of $R_U(\bar{t})$ for the three cases, as shown in Fig. 2.7(a). The amplification is seen to be the highest for the smallest drop diameters. In fact, for the largest diameters (the red lines in Fig. 2.7(a)) motility doesn't lead to any significant advantage whatsoever, irrespective of changes in the two most important biological parameters— V_s and β_C —governing the sensitivity of motile bacteria to ambient gradients. The advantage offered by high swimming speeds and/or high chemotactic sensitivity seems to get enhanced as the diameter of the oil drops is reduced. The first effect (increased sensitivity to V_s with lower d) is a direct consequence of the length scales traversed by the motile bacteria to reach the high-concentration regions, which scale as l_c (see equation 2.10), and are much shorter for smaller drop diameters. In fact, it is seen that $l_c \approx O(1)$ mm for $d = 1$ mm, and $l_c \approx O(100)$ mm for $d = 5$ mm (see Fig. 2.12 in Appendix). The second effect (increased sensitivity to β_C with lower d) is also directly attributed to a change in the drop diameters; with smaller drops engendering stronger gradients, and faster reorientations. When the characteristic length scale of the problem decreases, it leads to a proportional increment in the magnitude of concentration gradients, making chemotaxis more effective. Thus, even though the spatial extent of heterogeneities increases with increasing drop diameters, the gradients within these heterogeneities are not strong enough to provide sufficient advantage to motile bacteria. We note that larger drop diameters also mean reduced values of the characteristic vorticity ($|\boldsymbol{\omega}| \approx \sqrt{g/d}$), but this just means that bacteria do not change their swimming directions fast enough even due to rotation by the

flow. In such a scenario, the bacteria do not deviate much from their initial swimming direction, and it can be said that their encounter with nutrient-rich regions depends heavily on them simply straying into regions with high enough values of C , or $|\nabla C|$. In light of this discussion, the results presented in Fig. 2.7(a) suggest a potential benefit that may be incurred by motile bacteria if dispersants are used during an oil spill.

Finally, we discuss what happens if the volume fraction ϕ of oil in the oil-water system changes, but the diameter of the drops remains the same. This parameter is a reasonable metric to quantify the intensity of any leak, with higher volume fractions representative of regions of intense dispersive activity by the rising, insoluble HCs. In the DNS, we simply change the number of drops occupying the computational domain to change the volume fraction of the system. We analyze small drop diameters ($d \approx 1$ mm) so as to characterize chemotactic advantages that are significant. Our studies indicate a non-trivial temporal evolution of the chemotactic amplification as a function of the volume fraction. There are significant differences, both in the maximum amplification achieved, the time scale at which said maximum is reached, and the rate of the eventual decay in $R_U(t)$. The maximum value of R_U is higher for $\phi \approx 6\%$ and $\phi \approx 22\%$, than it is for $\phi \approx 11\%$. This increase in the maximum value of R_U either side of $\phi \approx 11\%$ can be explained by examining how the nutrient patch deforms in the two cases. The pseudo-turbulent dissipation rate increases as the volume fraction of the system increases [71]. In our study, the values of the steady state dissipation rates per unit mass (in the suspending fluid) for $\phi \approx 22\%$, 11% and 6% are 9.3×10^{-3} W/kg, 4.3×10^{-3} W/kg and 2.7×10^{-3} W/kg, respectively. Thus, the nutrient dispersion—which increases monotonically with the dissipation rate in the fluid [61]—is fastest for $\phi \approx 22\%$ and slowest for $\phi \approx 6\%$. This results in more intense stirring of the nutrient in the former case, leading to a relatively higher initial availability of the nutrient, and thus an earlier peak in R_U . But high dissipation rate also means faster mixing. The strong gradients that form disappear equally quickly and therefore the chemotactic advantage isn't sustained for long.

The behavior for $\phi \approx 6\%$ is exactly opposite, wherein the initial distribution is not ‘broken’ quickly enough. This can be explained by considering the anisotropy in the fluid velocity fluctuations, or equivalently, the same for the drop velocity fluctuations: $\overline{\text{Re}}_{u'}/\overline{\text{Re}}_{v'+w'}$ [70, 71]. This ratio is a measure of the dispersion of the nutrient in the rise-direction, as compared to the dispersion transverse to the rise-direction. Its values for $\phi \approx 6\%$, 11% , and 22% , are 3.3541, 1.4248 and 1.3403, respectively. Clearly, for the lowest volume fraction, there isn’t appreciable transverse dispersion due to pseudo-turbulence. As a result, the nutrient is not distributed over an appreciable region of the domain early on in the simulations. But this also means that it takes greater time for the nutrient to diffuse away to a uniform background concentration. Therefore, for $\phi \approx 6\%$, the chemotactic species get ample time to populate the nutrient-rich regions, and so a maximum in R_U is reached, but much later than that for $\phi \approx 22\%$. The motile bacteria are afforded more nutrient-rich regions, and importantly, for longer times, if the fluid flow is driven by a lower volume fraction of drops. This prolongation of the chemotactic advantage—and a very gradual decay—is readily seen in Fig. 2.7(b). For $\phi \approx 11\%$, the two effects—initial nutrient stirring and eventual homogenization—balance each other and neither one is dominant enough. Thus, the amplification for $\phi \approx 11\%$ is not stronger than $\phi \approx 6\%$ because of relatively faster homogenization of the nutrient, and is not stronger than $\phi \approx 22\%$ because of relatively slower initial dispersion of the cylindrical nutrient patch. Finally, we emphasize that for the range of parameters considered in Fig. 2.7(b), the average rise Reynolds number of the system does not vary much with the volume fraction ($\text{Re}_r \approx 15 - 35$); leading us to believe that it is solely the aforementioned chemotactic interactions of the bacteria with the nutrient field—and not the specific bacterium-flow interactions—that result in the varied behavior exhibited in this Section.

2.4 Chemotactic amplification vis-à-vis nutrient availability

We have seen how different bio-physical parameters shape the evolution of the motility benefit $\Delta\bar{U}(\bar{t})$ and the chemotactic amplification $R_U(\bar{t})$, in pseudo-turbulent flows generated by a swarm of rising drops. The motility benefit only quantifies the difference between the consumption rates of motile and non-motile bacteria, but does not fully specify the advantages of motility, e.g., even though $\Delta\bar{U}(\bar{t})$ increases with α_C , $R_U(\bar{t})$ remains unchanged, indicating that for the parameter values considered, faster consumption doesn't necessarily help the motile bacteria exclusively. On the other hand, whenever motile bacteria are provided an exclusive advantage (i.e., motility results in higher relative rates of consumption), the nature of the variation of $R_U(\bar{t})$ and $\Delta\bar{U}(\bar{t})$ is almost identical. Therefore, the importance of defining a second metric to quantify chemotactic advantage doesn't become immediately obvious. But whenever the nutrient availability is low, the value of $\Delta\bar{U}(\bar{t})$ is bound to be smaller than the cases where the nutrient availability is high [62]. In such cases it is more instructive to assess the chemotactic advantage in terms of the chemotactic amplification factor.

Fig. 2.8 highlights the importance of measuring the quantity R_U . It can be seen that the absolute motility benefit $\Delta\bar{U}$ is higher when the initial nutrient volume (V_p) is higher, but maximum amplification occurs for the case in which V_p is *lower*. This shows how motile bacteria are expected to profit most from situations where nutrient availability is sparse. It is also seen that the motility benefit and the amplification factor decay to zero and to unity respectively, much faster for lower values of V_p . This is because of the smaller nutrient patch being mixed up faster. Therefore, even though low nutrient availabilities favor consumption by motile species, this advantage doesn't last for long.

In our studies, the chemotactic amplification varies from being negligible ($< 1\%$) for the larger values of d and ϕ , to $\approx 24\%$ for systems where $d \approx 1$ mm, $\phi \approx 6\%$, swimming speeds are particularly high, and nutrient availability $V_p/L^3 = 2\%$, as seen in the inset in Fig. 2.8(b). An important observation is that under suitable

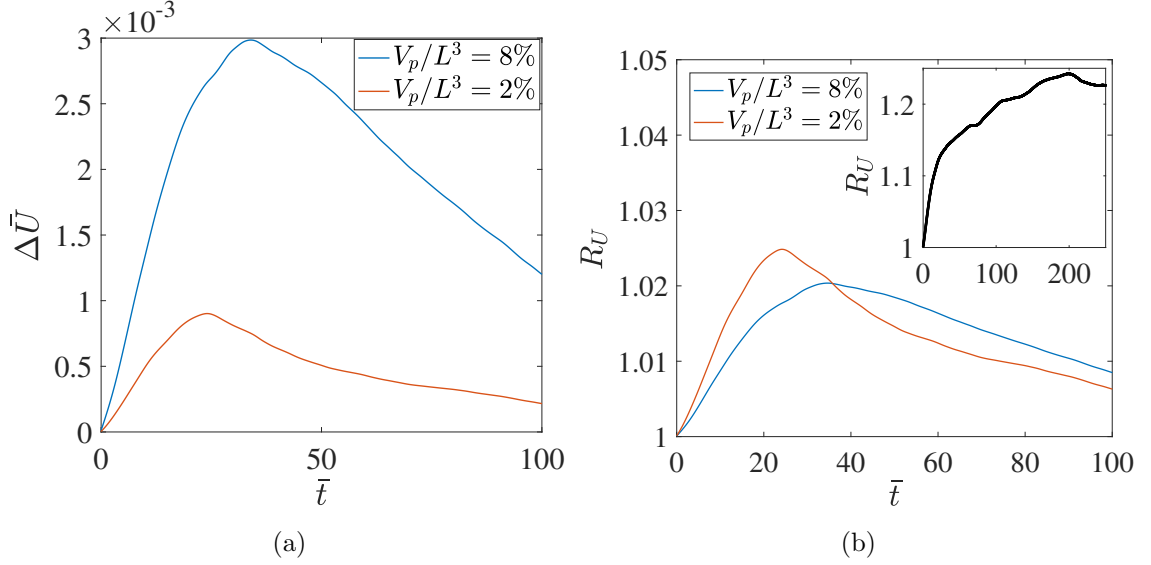


Figure 2.8. : (Color online) (a) Time evolution of the dimensionless motility benefit, for different nutrient availabilities (volume of the nutrient patch V_p , normalized by the volume of the computational domain L^3). (b) Time evolution of the chemotactic amplification factor, for the same nutrient availabilities as in part (a). The inset shows the case of maximum $R_U \approx 24\%$ obtained in our study (for $d \approx 1$ mm, $\phi \approx 6\%$, $V_s = 300$ $\mu\text{m/s}$, $\beta_C = 0.4$ $\mu\text{Mcm}^{-1}\text{s}$, and $V_p/L^3 = 2\%$). Note the significant increase in the time taken to reach a maximum in R_U , and as a consequence, an almost 4-fold prolongation of the motility benefit as compared to the baseline simulations. While the maximum is reached somewhere around $\bar{t} \approx 50$ in the baseline simulations, it takes $\bar{t} \approx 200$ to observe a maximum for the inset. The other parameters for the main figures (a) and (b) are: $Eu = 0.40$; $Ga = 2 \times 10^4$; $d \approx 1$ mm; $\phi = 6\%$; $\alpha_C = 1 \times 10^{-8}$ $\text{cm}^3\text{s}^{-1}\text{cell}^{-1}$; $D_m = D_b = 5 \times 10^{-4}$ cm^2/s ; $C_0 = 25$ μM ; $B_0 = 1.5 \times 10^5$ cells/cm^3 .

conditions, chemotaxis leads to significant prolongation of the motility benefit: up to 4 times longer than the time durations for the baseline simulations. The amplification factor is expected to increase even more if the availability of nutrient is limited to $\approx 1\%$ of the computational domain by volume. We emphasize that due to our choice of a much higher nutrient (and bacteria) diffusivity than usual, the values of R_U and $\Delta\bar{U}$ are under-predicted for the results discussed thus far. An examination of the chemotactic advantage for lower diffusivities, along with $V_p/L^3 = 1\%$, yields an upper limit of chemotactic amplification to be $\approx 45\%$ (see Fig. 2.10 in the Appendix, and the accompanying discussion). This particular scenario is quintessential for any chemotactic species to profit heavily, and represents the case where $\Delta\bar{U}(t)$ is extremely small, yet the nutrient has been consumed almost exclusively by the motile bacteria.

2.5 Conclusion

In this paper, we quantified the chemotaxis driven consumption of a dissolved chemoeffector in the presence of a rising swarm of oil drops, and unraveled the role of motility on the consumption dynamics. The pseudo-turbulence induced by the rising drops causes significant dispersion of the nutrient patches in the water column. The motile bacteria—capable of chemotactic foraging—benefit from local gradients in nutrient concentration to reach nutrient-rich regions. They thus gain an advantage which is unavailable to their non-motile, non-chemotactic counterparts, that rely solely on the ambient flow to carry them towards any nutrient hot-spots. The maximum motility benefit is seen to saturate with enhanced chemotactic sensitivity, and is seen to increase linearly with the swimming speed. Lower volume fractions of the dispersed (oil) phase prove beneficial to the motile bacteria, owing to less vigorous mixing—and consequently greater availability—of nutrient-rich regions. The motility benefit for low volume fractions is seen to extend to much longer times. On the other hand, higher volume fractions also prove advantageous, because they increase the initial availability of the nutrient to the motile bacteria by vigorously dispersing

the nutrient patch. The most important effect of the hydrodynamic factors, however, is the significant difference between the instantaneous values of motility benefit, for larger oil drops versus those for smaller oil drops (that could result due to addition of dispersant). This difference stems from the relatively weaker nutrient gradients formed in the former case, which do not prompt sufficiently strong chemotaxis, thus reducing the disparity between the behaviors of motile and non-motile species. In terms of relative rates of consumption, we find that motility can provide an advantage ranging from a $O(1)\%$ to $\approx 24\%$ faster consumption of the available nutrient, depending on the parameters detailed above and the spatial scale of a nutrient patch. We estimate that lower nutrient diffusivities lead to even more advantageous conditions for chemotactic bacteria, and an amplification of $\approx 45\%$ can be achieved if the chemotaxis is strong enough, the initial nutrient availability is restricted to 1% of the domain, and the fluid flow is driven by a low ($\approx 6\%$) volume fraction of oil drops. Our study provides useful insights, and scope for experimentation, into the role of droplet size on the microbial biodegradation of dissolved HCs in marine environments.

2.6 Appendix

We provide the definitions of the various pseudo-turbulence parameters given in Table 2.1. These definitions are borrowed from the papers by Bunner and Tryggvason [70, 71]. The volume-averaged velocities of the dispersed phase (oil drops) are given by $\mathbf{V}_g = (U_g, V_g, W_g)$, and those of the suspending fluid (water) are given by $\mathbf{V}_f = (U_f, V_f, W_f)$. The slip velocity between the two phases is defined as, $\mathbf{V}_r = \mathbf{V}_g - \mathbf{V}_f$, and the rise Reynolds number as, $\text{Re}_r = \rho_f |\mathbf{V}_r| d / \mu_f$. The velocity of the center of mass of the l^{th} drop, $\mathbf{V}_g^{(l)}$, is obtained by differentiating its position, $\mathbf{r}_g^{(l)}$, with respect to time:

$$\mathbf{V}_g^{(l)}(t) = \frac{d\mathbf{r}_g^{(l)}}{dt}, \quad (2.11)$$

and the instantaneous volume-averaged velocity of the dispersed phase, $\mathbf{V}_g(t)$, is then obtained by averaging $\mathbf{V}_g^{(l)}$ over all the drops:

$$\mathbf{V}_g(t) = \frac{1}{N_d} \sum_{l=1}^{N_d} \mathbf{V}_g^{(l)}(t); \quad (2.12)$$

finally, \mathbf{V}_g is obtained by the following time-averaging:

$$\mathbf{V}_g = \frac{1}{T} \int_T \mathbf{V}_g(t) dt, \quad (2.13)$$

and the Weber number is defined as, $We = \rho_f U_g^2 d / \sigma$. The fluctuation Reynolds number $Re_{u'+v'+w'}$ is defined based on the fluctuation velocities of the dispersed phase, which we define next. The instantaneous fluctuation velocities are defined as:

$$V'_{g_i}(t) = \sqrt{\frac{1}{N_d} \sum_{l=1}^{N_d} \left(V_{g_i}^{(l)}(t) - V_{g_i}(t) \right)^2}, \quad (2.14)$$

where, $i = 1, 2, 3$ refers to the velocities along the x, y, z directions, respectively. The fluctuation Reynolds number is then given by:

$$Re_{u'+v'+w'} = \frac{\rho_g (U'^2 + V'^2 + W'^2)^{1/2} d}{\mu_g}, \quad (2.15)$$

and the *mean* fluctuation Reynolds number by:

$$\overline{Re}_{u'+v'+w'} = \sqrt{\frac{1}{T} \int_{t=0}^T Re_{u'+v'+w'}^2(t) dt}, \quad (2.16)$$

where $U' = V'_{g_1}, V' = V'_{g_2}, W' = V'_{g_3}$, and T is the time for which the simulations are run. The pseudo-turbulent dissipation rate per unit volume of the suspending fluid (water), ϵ_f , is given by:

$$\begin{aligned} \epsilon_{fij} &= \frac{1}{2\Omega_f} \int_{\Omega_f} \mu \left(\frac{\partial u_i}{\partial x_j} + \frac{\partial u_j}{\partial x_i} \right)^2 dV, \\ \epsilon_f &= \sum \epsilon_{fij}, \end{aligned} \quad (2.17)$$

where Ω_f is the total volume of the suspending liquid. The dissipation rate on a per unit mass basis is given by ϵ_f / ρ_f .

Fig. 2.9 shows the time evolution of the dimensionless motility benefit and the chemotactic amplification factor, for two cases: one with $D_R \neq 0$ (dashed lines) and another with $D_R = 0$ (solid lines). All our results have been generated using the latter assumption, and it is clear from the negligible difference between the two cases in Fig. 2.9 that our assumption is justified for the present scenario.

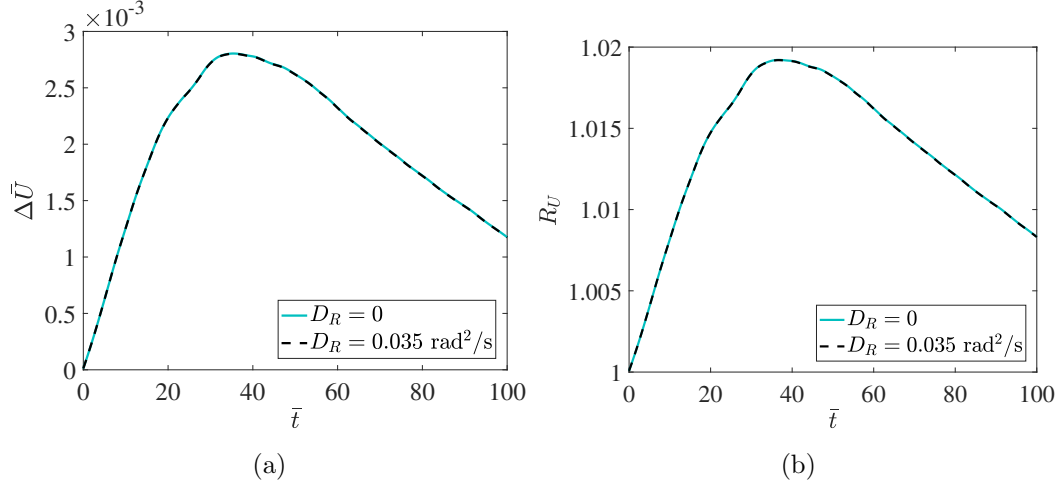


Figure 2.9. : The effect of rotary diffusivity (in the equation governing the orientation of the bacteria, i.e., equation 2.4) on the instantaneous motility benefit $\Delta \bar{U}$ and the chemotactic amplification R_U . We conclude that as long as there exists a background flow that is strong enough, the rotary diffusivity can be safely neglected. The value of D_R is borrowed from a reference calculating the same for the marine bacterium *V. alginolyticus* [98].

Fig. 2.10 details the influence of nutrient diffusivity, D_m , on the chemotactic amplification. A comparison between the plots for $Sc = 2, 20$ and 666 reveals trends that can be used to estimate the consumption dynamics for more realistic nutrient diffusivities ($10^{-5} - 10^{-9} \text{ cm}^2/\text{s}$). Note that for $Sc = 666$, $D_m = 1.5 \times 10^{-5} \text{ cm}^2/\text{s}$; a value that lies on the upper limit of realistic nutrient diffusivities and is indicative of the diffusivity of methane in water [99]. We also stress that the DNS for $Sc = 666$ is not fully resolved: there is a 5% error in the values of volume-averaged consump-

tion rates, and a 15% error in the values of RU , between the highest and the second highest grid resolutions used. Nevertheless, the results of Fig. 2.10, for $Sc = 666$, do provide an approximation of the chemotactic advantage for more realistic diffusivity values. The first observation is that R_U decays faster as nutrient diffusivity increases (Sc decreases); though this effect is most pronounced for the smallest Schmidt number. Secondly, R_U is much less sensitive to the swimming speed for higher nutrient diffusivities. Both these behaviors occur because the time scale for the smearing away of nutrient gradients is faster if the nutrient's diffusivity is large, and thus nutrient hot-spots do not persist long enough to yield greater motility benefit and chemotactic amplification for a given increase in the swimming speed. One can thus say that for nutrient diffusivities lower than that considered in this paper (i.e., for $D_m < 5 \times 10^{-4}$ cm²/s, $Sc > 20$), the chemotactic advantage will extend for longer times and the biological parameters—swimming speed and chemotactic sensitivity—will more significantly affect the magnitude of the motility benefit and the chemotactic amplification. See for example, the inset in Fig. 2.10, wherein a 45% amplification in the overall nutrient consumption is observed, for fairly strong chemotaxis ($V_s = 300$ μ m/s, $\beta_C = 4 \times 10^{-7}$ M \cdot cm⁻¹s), low nutrient availability ($V_p/L^3 = 1\%$), and low volume fraction of oil drops ($\phi \approx 6\%$). In this way, we demonstrate that the results of this study are indeed a conservative estimate of the actual chemotactic advantage that can be derived by marine bacteria in their search for nutrients.

The effect of the shape of the initial nutrient patch on the chemotactic advantage is shown in Fig. 2.11. The initial behavior is identical irrespective of the shape of the nutrient patch and so is the behavior after the attainment of the maximum; but the maximum value of the motility benefit and chemotactic amplification is different in the three cases considered. We find that if the initial shape is a cylinder with axis perpendicular to the direction of gravity—i.e., along the y axis—then the chemotactic advantage is reduced significantly after some time. This behavior can be attributed to the fact that the nutrient patch perpendicular to the drops' average rise direction gets distorted and homogenized much faster than one which is along the direction

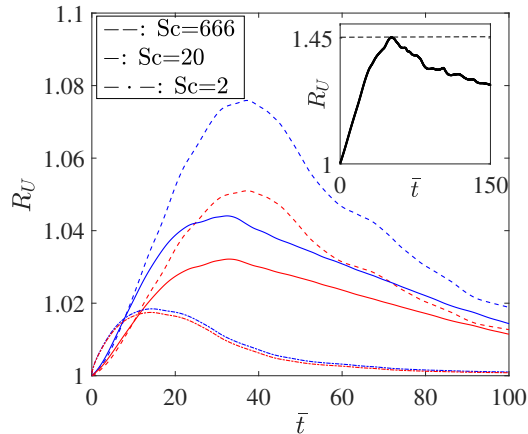


Figure 2.10. : The effect of nutrient diffusivity on the chemotactic amplification R_U . The variation is shown as a function of the swimming speed V_s (200 (red) and 300 $\mu\text{m/s}$ (blue)). As evident from Fig. 2.6, the higher R_U values correspond to the higher swimming speeds. Inset: A significant chemotactic amplification of 45% is observed for $D_m = 1.5 \times 10^{-5} \text{ cm}^2/\text{s}$ ($\text{Sc} = 666$), if the nutrient availability is lowered to $V_p/L^3 = 1\%$. The values of the hydrodynamic parameters for the inset are the same as those for $\phi \approx 6\%$ in Fig. 2.7, and the values of the biological parameters are given in the main text.

in which the drops rise. The same is true for the spherical nutrient patch, although the difference in the maximum is not as significant. A key point is that although there exists a quantitative difference, the qualitative evolution is very similar in all three cases. This leads us to believe that the nature of variation of the chemotactic advantage, with respect different biophysical parameters, should be similar for the three different patch-shapes.

Finally, the length scales used to describe the results of Fig. 2.7(a) in Section 2.3.2 are quantified in Fig. 2.12. We note a direct correlation between low values of \bar{l}_C (or, high values of $|\overline{\nabla C}|$) and high values of $\Delta\bar{U}$.

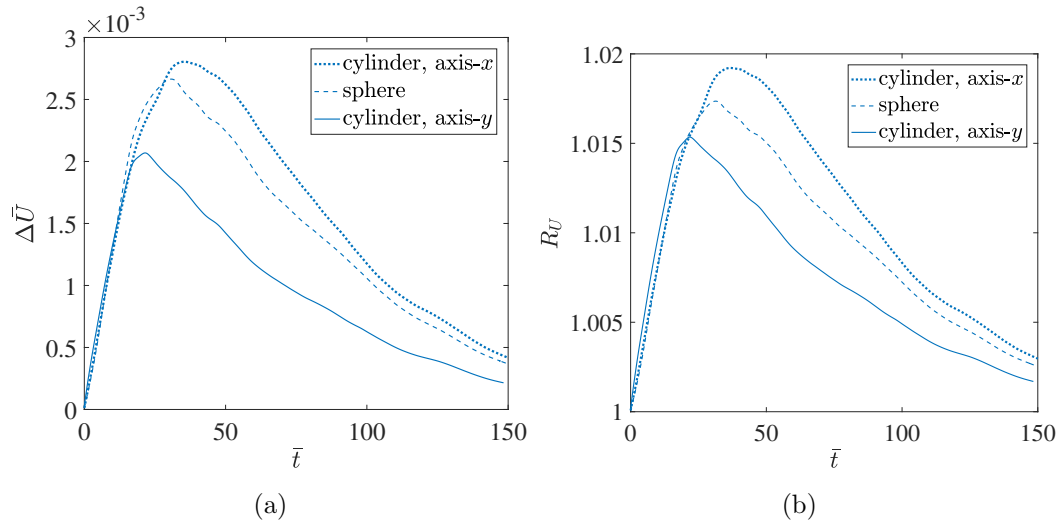


Figure 2.11. : Time evolution of the (a) instantaneous motility benefit $\Delta\bar{U}$, and, (b) amplification factor R_U , as a function of the initial shape of the chemoattractant patch. The spherical patch has the same volume as the cylindrical; ‘axis’ refers to the direction along which the axis of the cylindrical patch is oriented. The other parameters are: $\alpha_C = 1 \times 10^{-8} \text{ cm}^3 \text{ s}^{-1} \text{ cell}^{-1}$; $\beta_C = 40.0 \text{ } \mu\text{Mcm}^{-1} \text{ s}$; $V_s = 100 \text{ } \mu\text{m/s}$; $D_m = D_b = 5 \times 10^{-4} \text{ cm}^2/\text{s}$; $C_0 = 25 \text{ } \mu\text{M}$; $B_0 = 1.5 \times 10^5 \text{ cells/cm}^3$.

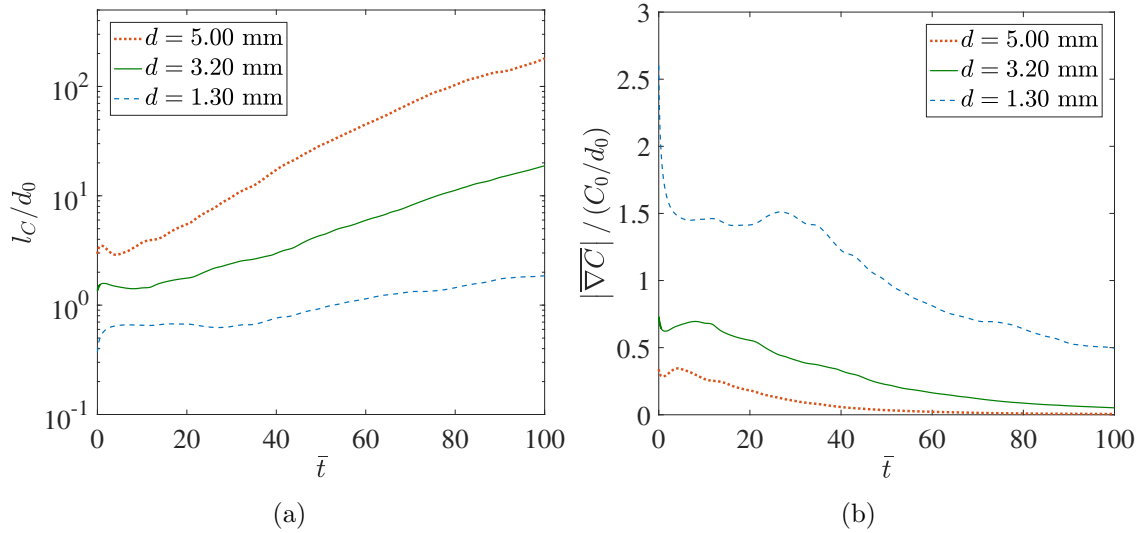


Figure 2.12. : (Color online) (a) Time evolution of the nutrient heterogeneity length-scale l_C normalized by the drop diameter $d_0 = 0.13$ cm, for the background flows corresponding to different drop diameters, d . (b) Time evolution of the volume-averaged nutrient gradient $|\nabla C|$ normalized by a reference gradient C_0/l_{ref} , for the background flows corresponding to different drop diameters, d . The other parameters are: $\alpha_C = 1 \times 10^{-8}$ cm³s⁻¹cell⁻¹; $\beta_C = 40.0$ μ Mcm⁻¹s; $V_s = 100$ μ m/s; $D_m = D_b = 5 \times 10^{-4}$ cm²/s; $C_0 = 25$ μ M; $B_0 = 1.5 \times 10^5$ cells/cm³.

3. HYDRODYNAMICS-MEDIATED TRAPPING OF MICRO-SWIMMERS NEAR DROPS

3.1 Introduction

The ubiquity of micro-organisms coupled with the ever increasing knowledge about their relevance has inspired vast amounts of fundamental research in the field of hydrodynamics of micro-swimmers [7–9, 47, 48, 100–106]. A key feature of micro-swimmer locomotion is their fascinating behavior under the influence of bounding surfaces, with examples including—but not limited to—“swimming on the right-hand side” [107], “swimming in circles”, with the direction of rotation depending on the rigidity [20] or fluidity [23, 24] of the surface, reversal of swimming direction [108] and wall-accumulation [21, 22, 109–111]. These near-surface phenomena are of utmost importance in the comprehension of bio-film formation and evolution [112–114]. In depth understanding of microbial motion in varied environments can also be sought by conducting experiments on artificial micro-swimmers, which provide greater control over their swimming behavior [115–124]. These artificial swimmers have indeed been used to study the intricacies of locomotion near solid boundaries [122, 125, 126]. Takagi *et al.* [125] performed one such study on the locomotion of a Janus micro-rod in the vicinity of inert colloidal particles. Their experiments revealed that the rod got trapped near the surface of a colloid, orbited around it for some time, before escaping and progressing toward similar interactions with other colloids encountered in its path. This behavior was explained using lubrication theory and steric interactions. Later, Spagnolie *et al.* [127] performed a theoretical analysis of a micro-swimmer near

⁰This chapter has been reprinted with minor changes, with permission, from the material as it appears in the article “*Hydrodynamics-mediated trapping of micro-swimmers near drops*”, by N. Desai, V. A. Shaik and A. M. Ardekani, *Soft Matter*, vol. **14**, pp. 264, 2018 (DOI: 10.1039/c7sm01615h). Copyright (2018) of The Royal Society of Chemistry.

a colloid (rigid sphere) based on far-field hydrodynamic approximations, and reported a number of conclusions: (i) the existence of a threshold colloid radius above which swimmers can not escape the colloid via hydrodynamics alone; (ii) the existence of a “basin of attraction” at most 2-3 body lengths in depth; and, (iii) the possibility of a diffusion-induced escape, even off colloids larger than the critical trapping radius.

In this paper, we aim to extend the analysis by Spagnolie *et al.* to locomotion near (spherical) drops that can either be clean, or have a surfactant on the interface. Due to the presence of a surfactant, the fluid-fluid interface can exhibit miscellaneous behavior [128, 129] such as viscous, elastic or viscoelastic properties [128, 129]. To ensure analytical tractability, we assume that the surfactant is insoluble, incompressible and has zero diffusivity, while the interface is assumed to behave as a “Newtonian fluid interface” [130] (possessing only interfacial shear and dilatational viscosities, the latter does not affect the physics due to the incompressible surfactant condition) following the Boussinesq-Scriven constitutive law [130–134]. Our aim is to bring out the variation in trapping characteristics—in the presence and absence of a surfactant—of drops of different sizes, and bulk and interface viscosities. A study of this kind is particularly relevant to the phenomenon of bio-degradation of oil drops by marine microbes in the event of an oil spill [2, 3]. As an example, consider the Deepwater Horizon oil spill in the Gulf of Mexico in 2010 [3]. The role played by marine bacteria in the degradation of the contents of the spill [135] (both water soluble and insoluble) is well known and has been documented [4, 68, 136, 137]. It is also known that huge amounts of dispersant/surfactant was added at the well head to break down the heavier hydrocarbons into tiny droplets, and aid bioremediation [3]. These oil droplets, 10 - 60 μm in diameter, got trapped in the subsurface hydrocarbon plumes [69, 93, 138] and acted as a rich source of carbon for the marine bacterial community. A purely hydrodynamics-driven attraction of swimmers to drops hints at an intriguing *passive* mechanism through which motile marine bacteria may forage for nutrition amongst oil droplets. The influence of surfactants on the aforementioned attraction is also of prime interest, as it offers insight on the efficacy of using dispersant in the aftermath

of an oil spill. Yet another interesting application could be the selective capture, analysis and treatment of bacteria using air bubbles [139–141]; an approach prevalent in the food processing industry [142]. Towards this end, we analyze the locomotion of a micro-swimmer in the vicinity of a drop, and conclude that the addition of surfactant results in a drastic reduction in the critical trapping radius of a drop, as long as the surface viscosity is small. For a given drop size, the surfactant-laden drops are more likely to trap nearby bacteria. We also show that the diffusion-induced escape is delayed by the addition of a surfactant, meaning that a bacterium is likely to be retained on a surfactant-laden drop for longer time, resulting in an increased possibility of bioremediation via other microbiological processes.

The rest of this paper is organized as follows. We first describe our modeling technique, the governing equations of fluid flow and swimmer motion, and the boundary conditions on the surface of a clean and a surfactant covered stationary drop. We then proceed to solve for the translational and rotational dynamics of the swimmer and obtain its swimming trajectories to ascertain quantities of interest, like the critical trapping radius and the basin of attraction. We present a scaling analysis for the critical trapping radius and the depth of the basin of attraction in the case of locomotion around a clean bubble. Finally, we incorporate the effects of randomness in swimming, and estimate the time that a swimmer spends on the surface of the drop (both clean and surfactant-laden). We obtain the probability distribution function (p.d.f.) for the trapping time using our simulation results for 10^4 cases. In all cases, we perform comparative studies to pinpoint the influence of the drop’s bulk and interface viscosities. In the end, we conclude by reiterating our results and discussing them with regards to subsurface bioremediation.

3.2 Mathematical model

The bacteria/swimmer is modeled as a prolate spheroid with aspect ratio γ . In a quiescent fluid in an unbounded domain, it simply swims with a constant swimming

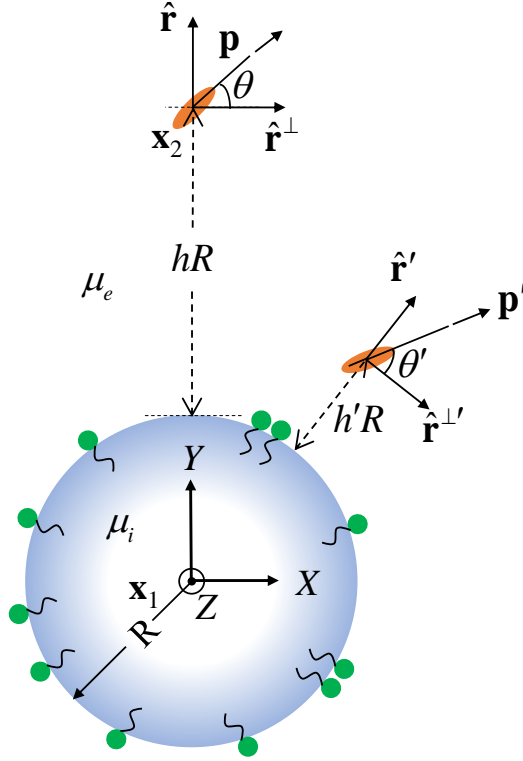


Figure 3.1. : A schematic of the problem being solved, showing a spherical drop covered with surfactant. The origin of a ‘fixed’ coordinate system XYZ lies at the center of the spherical drop. In a quiescent, unbounded, fluid, the swimmer will swim along the direction \mathbf{p} . In cases where the swimmer’s diffusive motion is negligible, the swimming trajectory is restricted to the plane defined by the vectors $\hat{\mathbf{r}}^\perp$ and \mathbf{p} , with the motion governed by eqns. 3.14, and the unit vector $\hat{\mathbf{r}}^\perp \times \hat{\mathbf{r}}$ always directed along \mathbf{e}_Z . Note that h is the *dimensionless* separation of the swimmer from the surface of the drop.

speed V_s along its orientation \mathbf{p} . The fluid-flow far away from the bacteria/swimmer can be approximated by a force dipole (dipole strength is F and its orientation is along \mathbf{p} ; see Fig. 3.1) acting on the fluid. The flow is governed by the conservation of mass (eqns. 3.1 and 3.3) and momentum (eqns. 3.2 and 3.4):

$$\nabla \cdot \mathbf{v}^{(e)} = 0, \quad (3.1)$$

$$-\nabla p^{(e)} + \mu_e \nabla^2 \mathbf{v}^{(e)} = F (\mathbf{p} \cdot \nabla) \{ \mathbf{p} \cdot \boldsymbol{\delta} (\mathbf{x} - \mathbf{x}_2) \}, \quad (3.2)$$

$$\nabla \cdot \mathbf{v}^{(i)} = 0, \quad (3.3)$$

$$-\nabla p^{(i)} + \mu_i \nabla^2 \mathbf{v}^{(i)} = 0. \quad (3.4)$$

Eqns. 3.1 and 3.2 apply to the exterior, while eqns. 3.3 and 3.4 apply to the interior of the drop. $\mathbf{v}^{(k)}$ (\mathbf{x}), $p^{(k)}$ (\mathbf{x}) and μ_k denote the fluid's velocity, pressure and viscosity, respectively ($k = i$ (e) for the region interior (exterior) to the drop).

In addition to the governing equations, the fluid velocity and pressure must also satisfy the following velocity boundary conditions

$$\mathbf{v}^{(e)} \cdot \mathbf{n} = \mathbf{v}^{(i)} \cdot \mathbf{n} = 0 \text{ at } |\mathbf{x}| = R, \quad (3.5)$$

$$(\mathbf{I} - \mathbf{nn}) \cdot \mathbf{v}^{(e)} = (\mathbf{I} - \mathbf{nn}) \cdot \mathbf{v}^{(i)} \text{ at } |\mathbf{x}| = R, \quad (3.6)$$

$$|\mathbf{v}^{(i)}| < \infty, \text{ for } |\mathbf{x}| = 0; \mathbf{v}^{(e)} \rightarrow 0, \text{ for } |\mathbf{x}| \rightarrow \infty, \quad (3.7)$$

The stress boundary conditions written in spherical polar coordinates are given by

$$\mathbf{n} \cdot (\mathbf{T}^{(i)} - \mathbf{T}^{(e)}) \cdot (\mathbf{I} - \mathbf{nn}) = \nabla_S \sigma + \nabla_S \cdot \boldsymbol{\tau}_S \text{ at } |\mathbf{x}| = R,$$

$$\nabla_S \cdot \boldsymbol{\tau}_S = \mu_S \left[\frac{2v_\theta}{r_1^2} + \frac{1}{r_1 \sin(\theta)} \frac{\partial \bar{\omega}}{\partial \phi} \right] \mathbf{e}_\theta + \mu_S \left[\frac{2v_\phi}{r_1^2} - \frac{1}{r_1} \frac{\partial \bar{\omega}}{\partial \theta} \right] \mathbf{e}_\phi, \quad (3.8)$$

$$\text{where } \bar{\omega} = \frac{1}{r_1 \sin(\theta)} \left[\frac{\partial v_\theta}{\partial \phi} - \frac{\partial}{\partial \theta} (\sin(\theta) v_\phi) \right],$$

where r_1 is the distance from the center of the drop. The surfactant-transport equation is given by

$$\nabla_S \cdot \mathbf{v}_S = 0 \text{ at } |\mathbf{x}| = R, \quad (3.9)$$

where R in the above equations is the radius of the drop, \mathbf{n} is the normal vector to the surface, pointing radially outward, $\nabla_S = (\mathbf{I} - \mathbf{nn}) \cdot \nabla$ is the surface gradient operator, $\mathbf{v}_S = (\mathbf{I} - \mathbf{nn}) \cdot \mathbf{v}$, is the tangential fluid velocity on the surface of the drop, $\mathbf{T}^{(e)}$ and $\mathbf{T}^{(i)}$ are the fluid stress tensors in the region external and internal to the drop ($\mathbf{T} = -p\mathbf{I} + \mu(\nabla\mathbf{u} + \nabla\mathbf{u}^T)$). σ is the interfacial tension of the fluid-fluid interface and it can be non-uniform if the drop is covered with a surfactant. Eqn. 3.9 is a reduced form of the surfactant transport equation for the case of an incompressible surfactant [131]. It needs to be satisfied only if we are considering locomotion near a *surfactant-laden* drop; in which case we use the Boussinesq-Scriven constitutive law for the interfacial stress $\boldsymbol{\tau}_S$ [130]. This is shown in the second line of eqn. 3.8, where μ_S is the *interfacial shear viscosity*. The boundary conditions for the case of a *clean* drop can be recovered by disregarding eqn. 3.9, substituting $\boldsymbol{\tau}_S = 0$ in eqn. 3.8, and neglecting $\nabla_S\sigma$ in the stress balance equation.

In deriving the aforementioned boundary conditions, we assume that the drop is not deforming. Drop deformation is negligible when the capillary number (ratio of bulk viscous stress and the capillary stress), $\text{Ca} = \mu_e V_s / \sigma_0$, (σ_0 is the equilibrium interfacial tension) is much smaller than one [11, 143]. In the case of a weakly deforming drop, our analysis, along with the normal stress boundary condition, can be used to determine the leading order drop deformation. Note that the capillary number for a bacterium swimming with a speed [8], $V_s \sim O(10 - 1000) \mu\text{m/s}$ in water, $\mu_e \sim O(10^{-3}) \text{ Pa}\cdot\text{s}$, near oil drops [144], $\sigma_0 \sim O(10) \text{ mN/m}$, lies in the range $O(10^{-6} - 10^{-4})$; this justifies our assumption of a non-deforming drop.

We note that a force dipole cannot move on its own in an unbounded Newtonian fluid, but our model swimmer does swim, due to its intrinsic motility. In presence of surfaces (solid or liquid interface), however, the swimmer interacts hydrodynamically

with the surface and develops a component of locomotion—both translational and rotational—that exists solely due to its proximity to the aforementioned surface, i.e.,

$$\frac{d\mathbf{x}}{dt} = \mathbf{u}_{HI} + V_s \mathbf{p} \quad (3.10)$$

$$\frac{d\mathbf{p}}{dt} = \boldsymbol{\Omega}_{HI} \times \mathbf{p},$$

where \mathbf{u}_{HI} and $\boldsymbol{\Omega}_{HI}$ are the hydrodynamic components of bacteria/swimmer locomotion, obtained after an application of the Faxen's laws for a spheroid using the solution $\mathbf{v}^{(e)}$ [13]. The (dimensionless) expressions for \mathbf{u}_{HI} and $\boldsymbol{\Omega}_{HI}$ are given in the Appendix. In their present forms, eqns. 3.10 do not include the effects of randomness in the motion of the micro-swimmer. These random effects may occur due to Brownian motion and/or other intrinsic random behaviors of the swimmer. The random components of swimmer motility—its linear and angular velocities—are modeled as Gaussian white-noises in three dimensions ($\boldsymbol{\eta}_T$), and on the unit sphere ($\boldsymbol{\eta}_R$), respectively [10, 105, 145]:

$$\mathbf{x}_{n+1} = \mathbf{x}_n + \Delta t(\mathbf{u}_{HI} + V_s \mathbf{p})_n + \sqrt{6D_T \Delta t} \boldsymbol{\eta}_T \quad (3.11)$$

$$\mathbf{p}_{n+1} = \mathbf{p}_n + \Delta t(\boldsymbol{\Omega}_{HI})_n \times \mathbf{p}_n + \sqrt{4D_R \Delta t} \boldsymbol{\eta}_R \times \mathbf{p}_n.$$

We emphasize that the far-field description employed here has been shown to be accurate to distances as small as a few body lengths away from rigid walls [14], and from deformable clean interfaces [146]. In addition, far-field hydrodynamics has also shown qualitative agreement with experimental results on locomotion near plane interfaces that are clean, as well as surfactant-laden [147]. But it is important to note that this far-field description, in spite of its accuracy, does not preclude the swimmer from ‘penetrating’ into the interface; an occurrence which is not physically realized. A more accurate analytical description will involve: (i) the inclusion of higher order singularities (and images) as the swimmer approaches the interface, or (ii) use of the lubrication/thin-film approximation as the swimmer-interface distance reduces beyond a threshold. Both these methods will become extremely unwieldy from a

mathematical standpoint, and therefore, for the sake of simplicity we model the ‘near-field’ dynamics simply as a hardcore repulsion [127], i.e., we set the normal velocity of the swimmer (velocity along the line joining the swimmer center to the drop center) as zero if the swimmer begins to penetrate into the interface. Thus, in addition to eqns. 3.10 (or, 3.11), we need to implement the following constraint/condition, whenever the swimmer touches the interface:

$$\frac{d\mathbf{x}}{dt} = \begin{cases} \mathbf{u}_{HI} + V_s\mathbf{p}, & (\mathbf{u}_{HI} + V_s\mathbf{p}) \cdot \hat{\mathbf{r}} > 0 \\ (\mathbf{u}_{HI} + V_s\mathbf{p}) \cdot \hat{\mathbf{r}}^\perp, & (\mathbf{u}_{HI} + V_s\mathbf{p}) \cdot \hat{\mathbf{r}} \leq 0 \end{cases}, \quad (3.12)$$

where $\hat{\mathbf{r}}$ and $\hat{\mathbf{r}}^\perp$ are unit vectors along, and perpendicular to the line joining the center of the drop to the center of the swimmer, respectively (see Fig. 3.1).

An active swimmer can get trapped or adsorbed onto a liquid-liquid interface due to factors like affinity for one of the two phases comprising the interface (amphiphilicity) [148], chemotaxis driven attachment, or one of the many interfacial phenomena discussed in [67], and references therein. However, this phenomenon will not, in general, occur universally. The details of such an interface-attachment are subject to a wide range of effects like the nature of the bacterial solution, the fluid-fluid interface, the presence/absence of surfactant on the drop surface, the nature of the surfactant, the availability of other compounds and biological material, and the motility traits (tendency of flagellar bundling-unbundling for petrichous organisms, flagellum flicking for mono-flagellates, strength of diffusive motion, etc.) of the micro-swimmers themselves. In particular, we note that the bacterium *C. crescentus* gets trapped onto an air/water interface when swimming in a nutrient-rich growth medium, but not in “minimal salt motility medium” [149]. In fact, the ‘competitive adsorption’ of surfactants can also hinder swimmer adsorption onto drop surfaces [149]. Different strains of bacteria respond differently to oil-water interfaces; with their response depending on motility, stage of colony growth, availability of other nutrients and/or dispersant, nature and composition of the hydrocarbon oil that the bacteria are being exposed to, and other environmental factors [67, 150–153]. Some hydrocarbon degrading bacteria (*P. aeruginosa*) have been observed as showing ‘poor adherence’

to the target hydrocarbon (hexadecane) [154]. Therefore, it is fair to say that a description of swimmer motion near oil drops, that is consistent with all aspects of hydrodynamics and surface chemistry, is quite a formidable task to undertake. With the above discussion in mind, we assume that the conditions (nutrient availability, type of surfactant, micro-swimmer affinity) in our study are ideal for the preclusion of any ‘non-hydrodynamic’ entrapment, and that the repulsive ‘lubrication force’ (and stochastic diffusion [21, 149]) is strong enough to prevent adsorption of micro-swimmers onto the spherical drops. We do acknowledge however, that the exact values of critical trapping radius and the mean trapping time being presented in this paper are subject to change based on the adsorption kinetics of active swimmers near interfaces. These changes though, can be easily incorporated into our present model, if a more comprehensive analysis is desired and the adsorption kinetics are known.

We non-dimensionalize the above equations using the following scales: lengths by the semi-major axis length of the swimmer b , velocities by the swimming speed V_s , time by b/V_s , viscosity by μ_e , and pressure by $\mu_e V_s/b$. The important dimensionless parameters in our study then become: the viscosity ratio, $\lambda = \mu_i/\mu_e$, the dimensionless surface viscosity, $\beta = \mu_s/(\mu_e R)$, the ratio of radius of the drop to the swimmer length scale, $A = R/b$, the dimensionless swimmer dipole strength, $\alpha = F/(8\pi\mu_e b^2 V_s)$, and the dimensionless translational diffusivity, $D = D_T/(bV_s)$.

In the subsequent sections, we integrate eqns. 3.10 and 3.11 numerically and bring out the influence of different viscosity ratios, (dimensionless) surface viscosities, diffusion strengths and drop radii, on the trapping characteristics of a micro-swimmer swimming in the vicinity of a clear or surfactant covered drop. We note that all our results have been obtained for the case of $\alpha > 0$ (equivalently, $F > 0$), i.e., for swimmers called *pushers*, like the well-studied bacterium *E. coli* [8].

Next, we justify the range of parameter values used in this manuscript. We assume the suspending fluid is water. The viscosity ratio of the crude oil drops to water is $\lambda \sim O(0.1 - 100)$ [155], $\lambda \ll 1$, and $\lambda \gg 1$, respectively. To understand the physics associated with the motion of microorganisms near drops of different viscosity,

we vary the viscosity ratio in the range 10^{-3} to 10^3 . Since the dipole moment of *E. coli.*, is $F \approx 0.1 - 1 \text{ pN } \mu\text{m}$ [8, 21]; its swimming speed in an unbounded fluid is [8], $V_s \approx 10 \mu\text{m/s}$ and its length is [8, 21], $b \approx 1 - 10 \mu\text{m}$, we derive the range of its dipole strength $\alpha = \frac{F}{8\pi\mu_e b^2 V_s} \approx 0.004 - 4$. We note that the dimensionless interfacial viscosity depends on both the dimensional interfacial viscosity and the radius of the drop, $\beta = \mu_S/(\mu_e R)$. Since the typical size of a microorganism lies in the range of $b \sim O(1 - 100) \mu\text{m}$ [8], we assume the radius of the drop lies in the range of $R \sim O(10 - 1000) \mu\text{m}$. At an oil-water interface, high molecular weight surfactants such as proteins display large interfacial shear viscosities [156, 157], $\mu_S = 0.1 - 1000 \text{ mN s m}^{-1}$. However, at air-water interface, low molecular weight surfactants like sodium lauryl sulfate or a mixture of sodium lauryl sulfate and lauryl alcohol or decanoic acid or steric acid monolayers show very small surface shear viscosities [158, 159], $\mu_S = O(10^{-4}) \text{ mN s m}^{-1}$. Furthermore, this interfacial shear viscosity of low molecular weight surfactants increases with an increase in the concentration of the surfactant, achieves a maximum value, and then decreases a little. Hence, depending on the surfactant used, the viscosity ratio, the size of the drop and the surfactant concentration, the value of the dimensionless interfacial viscosity can vary in the range $0 \leq \beta < \infty$. The value of $\beta \rightarrow 0$ is achieved for small concentration of low molecular weight surfactant distributed over large bubbles, while the value of $\beta \rightarrow \infty$ is achieved for high molecular weight surfactant distributed over small oil drops.

3.3 Deterministic scattering and trapping

We begin our discussion by analyzing the solution of eqns. 3.10. Firstly, we aim to identify the minimum radius (the “critical trapping radius” [127]) for which a swimmer approaching a drop gets trapped, i.e., begins to orbit the drop (see Fig. 3.2). Next, we proceed toward computing the basin of attraction [127], i.e., the threshold region around the drop within which a tangentially directed swimmer gets attracted to—and trapped onto—the interface (see Fig. 3.6). Finally, we show that

the numerically obtained expressions can also be estimated analytically for the special case of locomotion around a clean (spherical) bubble ($\lambda \rightarrow 0$).

3.3.1 Critical trapping radius, A_c

We emphasize that the trapping of the swimmer results due to a balance between the hardcore repulsion (‘enforced’ to prevent the penetration/ of swimmer into the drop), and the hydrodynamic attraction inherent in eqn. 3.10. Once the latter effect brings the swimmer close enough to the interface (~ 1 swimmer body length), the former effect becomes dominant, thus preventing interface penetration. The subsequent motion of the swimmer is governed by the hydrodynamics induced rotation, which in turn depends acutely on the dimensionless parameters described earlier. Crucially, there exists a critical trapping radius of the drop, below which an approaching swimmer simply skims the drop surface for some time before escaping (see Fig. 3.2(a-c)). This kind of behavior is called scattering [127]. We re-iterate that this scattering behavior is contingent upon the swimmer adsorption being negligible, or, the adsorption time scale being larger than the time taken by the swimmer to traverse the surface of the drop. This is because if the swimmer adsorption is fast enough, then no scattering is likely to occur. For radii larger than the critical trapping radius, the swimmer is unable to escape and becomes hydrodynamically trapped onto the drop surface (see Fig. 3.2(d,e)).

Fig. 3.3 shows how the critical trapping radius for a clean drop, $A_{c, clean}$, varies as a function of the viscosity ratio, (λ), for different values of the dipole strength α . The particular nature of the A_c vs. α variation is explained via scaling analysis, and physically, in a later section. We note that a significant difference in the values of $A_{c, clean}$ occurs only for low values of the dipole strength, with the most viscous drops being more capable of trapping micro-swimmers that approach them directly. A drop is said to be ‘more capable’ if its A_c value is *smaller*. On the other hand, for higher

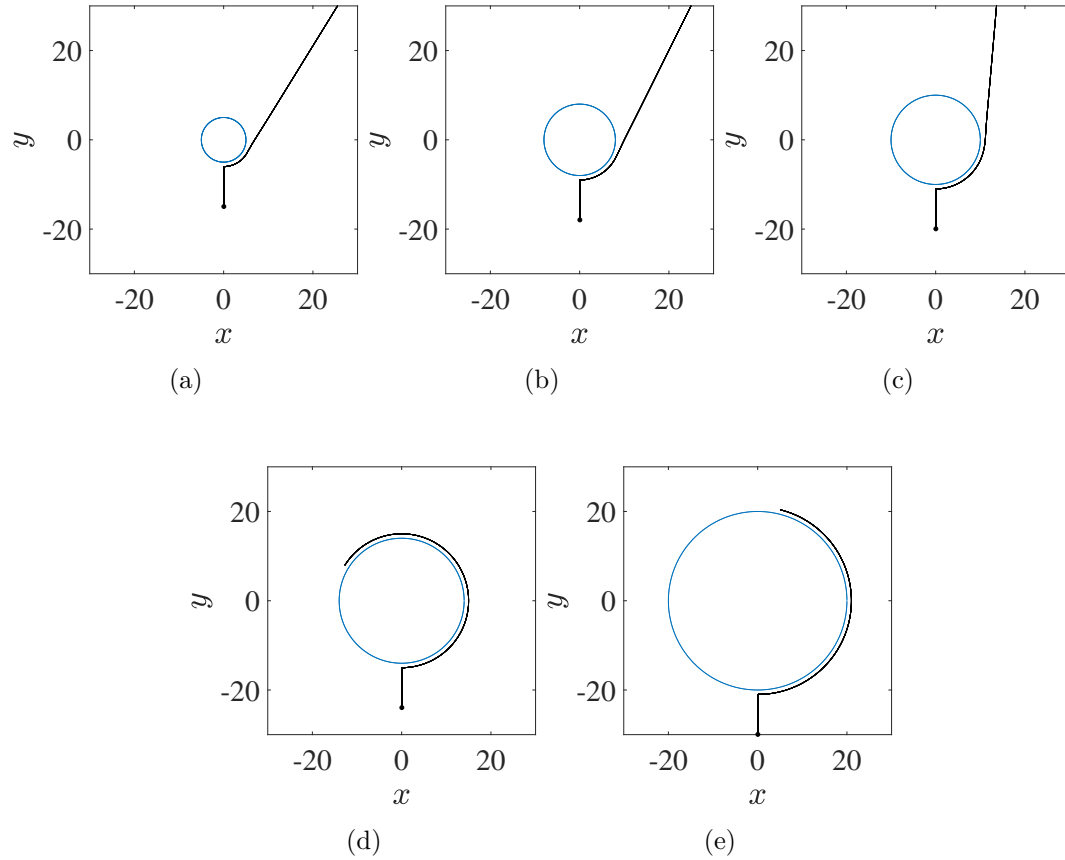


Figure 3.2. : Schematics showing the idea of the critical trapping radius [127]. Notice how the trajectories around smaller drops escape (a-c), while those around drops with radius larger than the critical trapping radius ($A > A_c \sim 10.7$) get trapped, and orbit the surface (d,e).

values of α , the threshold does not vary much, i.e., the viscosity ratio does not dictate the trapping strength for swimmers with high dipole strengths.

Next, we investigate the effect of surface viscosity in Fig. 3.4 (a) and (b). It is clear that the addition of surfactant leads to interesting changes in the trapping characteristics, by rendering the viscosity ratio immaterial for high values of surface viscosities ($\beta \geq 1$), as shown by the more or less coincident curves in Fig. 3.4(b). It is only for negligible surface viscosities, i.e., $\beta \rightarrow 0$, that the viscosity ratio becomes

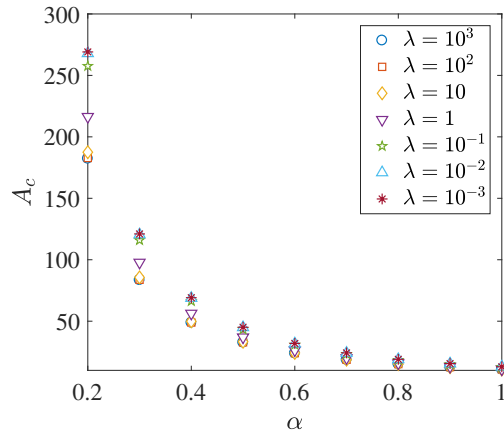


Figure 3.3. : Variation of the critical trapping radius, $A_{c, \text{clean}}$, with the swimmers' dipole strengths, α , for different viscosity ratios, λ . The origin is located at the center of the drop, and the swimmer is initially placed at $(X_0, Y_0, Z_0) = (0.1, -(A + 20.0), 0)$. Eqn. 3.10 are integrated using the explicit-Euler method, with time-interval $\Delta t = 10^{-3}$.

important, and affects the values of the critical trapping radii (Fig. 3.4(a)) for the case of *surfactant-laden* drops.

The surfactant-laden drops exhibit another very interesting behavior: they are more effective in trapping approaching swimmers than even the rigid sphere, particularly for small values of α . This advantage is highest for $\beta \rightarrow 0$ and reduces with increasing β , ultimately resulting in an $A_{c, \text{surf.}}$ vs. α trend that is coincident with the corresponding curve for a rigid sphere (Fig. 3.4(b)). It also means that the effect of λ on A_c is opposite for surfactant-laden drops, when compared to the clean drops. For a clean drop, A_c was seen to decrease as λ was increased; but for surfactant-laden drops, the effect is reversed, i.e., A_c *increases* with an increase in λ . This observation helps us to answer a key question: does the addition of surfactant yield any benefit in terms of the ability of a drop to trap nearby swimmers? To answer this, we refer to Fig. 3.5, where we note that the addition of surfactant does prove extremely useful in cases where the dipole strength of the swimmer is not very high and the surface viscosity (due to presence of surfactant) is negligible. Even for typical values of α

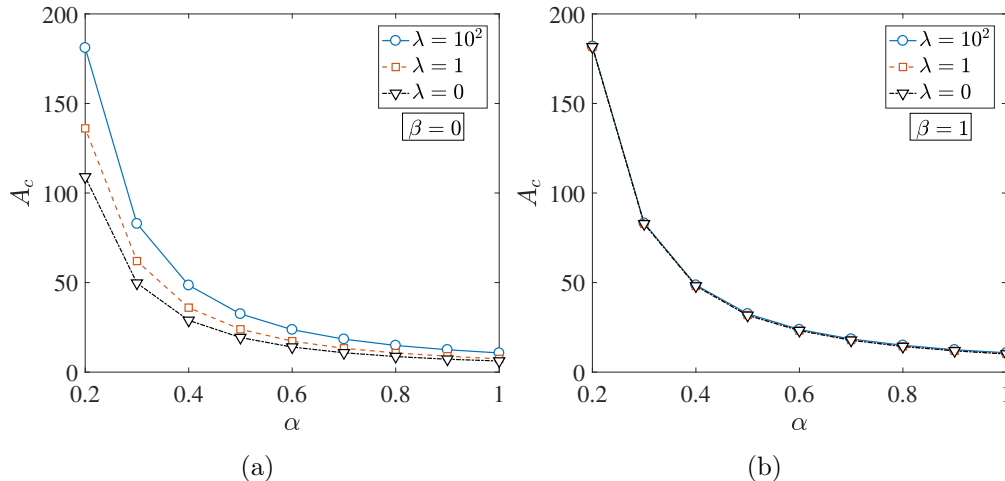


Figure 3.4. : Variation of the critical trapping radius for surfactant-laden drops, $A_{c,surf.}$, with the swimmers' dipole strengths, α , for different viscosity ratios, λ . (a) $\beta = 0$; and (b) $\beta = 1$.

(0.4 - 0.6), the addition of surfactant (with small surface viscosity) can lead to a $\sim 30\%$ reduction in the critical trapping radius. It must be noted that this difference increases even more if the viscosity ratio is below unity, with the most beneficial scenario for surfactant addition being when $\lambda \rightarrow 0$, i.e., for micro-organism locomotion around drops with negligible viscosity as compared to the suspending fluid. The above discussions hint at a potential benefit that may be gained by using dispersant in oil spills as it would result in disintegration into smaller oil drops that could still passively attract bio-degrading bacteria, while simultaneously increasing the surface area to carry out the bio-degradation.

3.3.2 Basin of attraction, h^*

Fig. 3.6 shows an example of two swimming trajectories—one just inside the basin, and another just outside—and their different evolutions with time, depending on their proximity to the interface. The swimmer that started inside the basin of

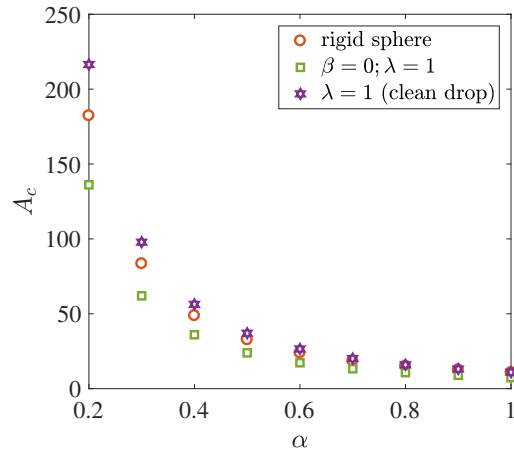


Figure 3.5. : A comparison between the critical trapping radii for three cases: the rigid sphere, a surfactant-laden drop ($\beta = 0; \lambda = 1$), and a clean drop ($\lambda = 1$). It is seen that surfactant-laden drops with negligible surface viscosities have the smallest critical trapping radius.

attraction gets hydrodynamically trapped, while the one that started outside the basin escapes. This shows that a true indication of a swimmer's entrapment is dictated not only by the critical trapping radius, but also by the basin of attraction, because hydrodynamic effects on their own are not strong enough to attract distant swimmers onto surfaces/interfaces. We emphasize here that unlike the critical trapping radius, which may change depending on the adsorption kinetics of the system, the concept of the basin of attraction remains valid even in cases where the micro-swimmer can get easily adsorbed onto the drop surface.

In what follows, we define the 'basin depth' h^* as the maximum distance from the surface of the drop, for which a swimmer released tangentially ($\theta(0) = 0$) gets attracted to, and begins to orbit, the drop. It should be noted that such a basin of attraction exists only if the drop radius is larger than the critical trapping radius. Fig. 3.7 shows the depth of the basin of attraction of a clean, spherical drop, for a range of dipole strengths and viscosity ratios. In each of the sub-figures, we see that the basin's extent (h^*) increases with the viscosity ratio, which is expected based on our earlier

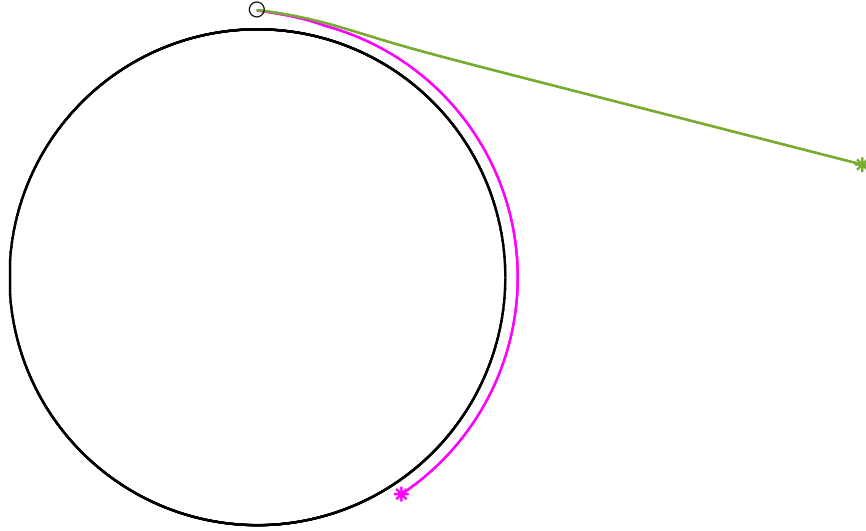


Figure 3.6. : An example of the basin of attraction: the magenta trajectory falls just inside the basin of attraction h^* and so begins to orbit the interface; the green trajectory on the other hand, falls outside h^* , and hence escapes the interface. Note that the radius of the drop is large enough to trap any directly impacting swimmers, and the escape in this case is only because of an increased initial separation, i.e., $h > h^*$.

discussion, where we saw that the clean drop's ability to trap swimmers enhances as the viscosity ratio increases. Another important observation is the reduced role of the viscosity ratio in dictating entrapment, as the swimmer's dipole strength increases. For higher dipole strengths (α), the curves for the three viscosity ratios are seen to almost collapse onto each other, i.e., h^* has a weaker dependence on λ . Thus, the swimmers with larger values of α get attracted to the interface, regardless of it being a low-viscosity fluid-sphere ($\lambda < 1$), or a high viscosity one ($\lambda > 1$). In contrast, swimmers with low values of α are trapped better by the more viscous drops.

Finally, Fig. 3.8 depicts these variations for a surfactant-laden drop. In this case, the effects of changing λ , A and α , are qualitatively the same as those for a clean drop; while an increase in the surface viscosity leads to a reduction in the depth of the basin. We notice a correlation between the basin depth and the critical trapping

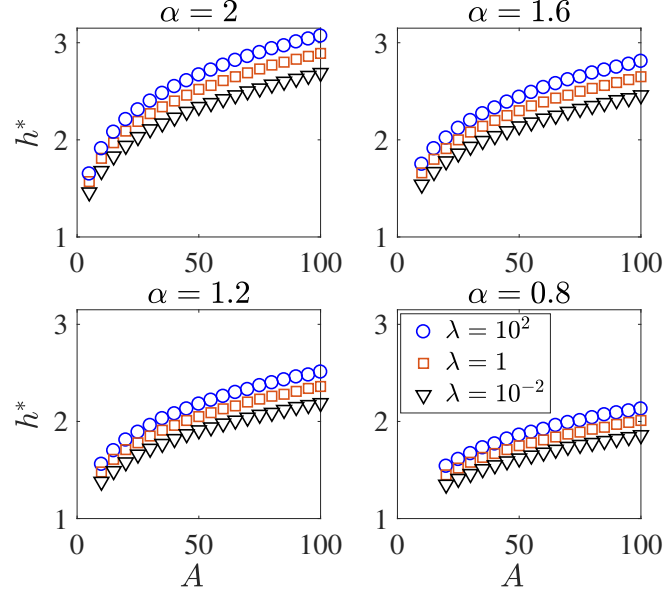


Figure 3.7. : Variation of the basin of attraction for a clean drop, as a function of the swimmer's dipole strength (α), the drop radius (A), and the viscosity ratio (λ).

radius, in that the drops having lower values of A_c have higher values of h^* . Therefore, we conclude that drops with lower values of β are more successful in trapping nearby swimmers, owing to their smaller critical trapping radii.

Based on the above results, we conclude that the radius of the basin of attraction ($A_{basin} = A + h^*$), is at best, only about three body-lengths larger than the radius of the drop (for the case of $A \sim 80$, $\alpha = 2.0$, $\beta = 0$, $\lambda = 10^2$). This means that the swimmer must be at most $O(10)$ μm off the interface, in order to get trapped. In all other cases, the swimmer will most definitely escape the hydrodynamic attraction of the drop.

3.3.3 Swimming dynamics: $h(t) - \theta(t)$ phase space analysis

In this section, we discuss the solution to eqns. 3.10 from a dynamical system perspective. In the deterministic case, given an initial condition, the position and orientation of the swimmer are determined uniquely by the evolution equations for

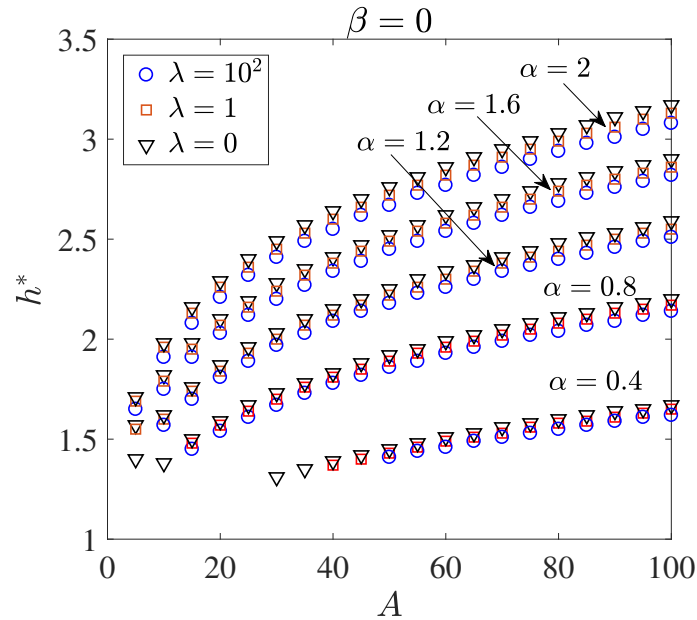


Figure 3.8. : Variation of the basin of attraction for a surfactant-laden drop, as a function of the swimmer's dipole strength (α), the drop radius (A), and the viscosity ratio (λ). The dimensionless surface viscosity $\beta = 0$.

$h(t)$ and $\theta(t)$. It is therefore instructive to look at the vector field/phase space of $h(t)$ vs. $\theta(t)$ to gain an insight into the various kinds of behaviors that are possible. The nature of such a vector field is governed by parameters A , α , λ and β . Fig. 3.9 shows the vector field for two different cases: $A = 10$, $\alpha = 0.8$ and $A = 90$, $\alpha = 2.0$, with λ and β being the same in both cases. We can immediately see that in Fig. 3.9(a), there are no initial points, $h(0)$ and $\theta(0)$, that correspond to a trajectory which, after a sufficiently long time, ends up on the surface of the drop ($h(t_{end}) \sim 1$). This is because of the radius in that case being smaller than the corresponding critical trapping radius. On the other hand, Fig. 3.9(b) shows several initial points in the phase space with trajectories that lead to swimmer capture. Notably, the concept of the basin of attraction is quite clear when we see how increasing $h(0)$ (while keeping $\theta(0) = 0$) first leads to swimmer entrapment, and then to escape, as $h(0)$ increases beyond the depth of the basin of attraction, h^* (see the curves in Fig. 3.9(b) that

are colored and marked by symbols). Interestingly, all phase spaces for $A > A_c$ are characterized by a saddle point, as shown by the diamond symbol for Fig. 3.9(b), that divides the phase space into ‘trapping’ and ‘escaping’ regions. In Fig. 3.9(b), the regions marked ‘T₁’ and ‘T₂’ are the trapping regions, while those marked ‘E₁’ and ‘E₂’ are the escaping regions of the phase space.

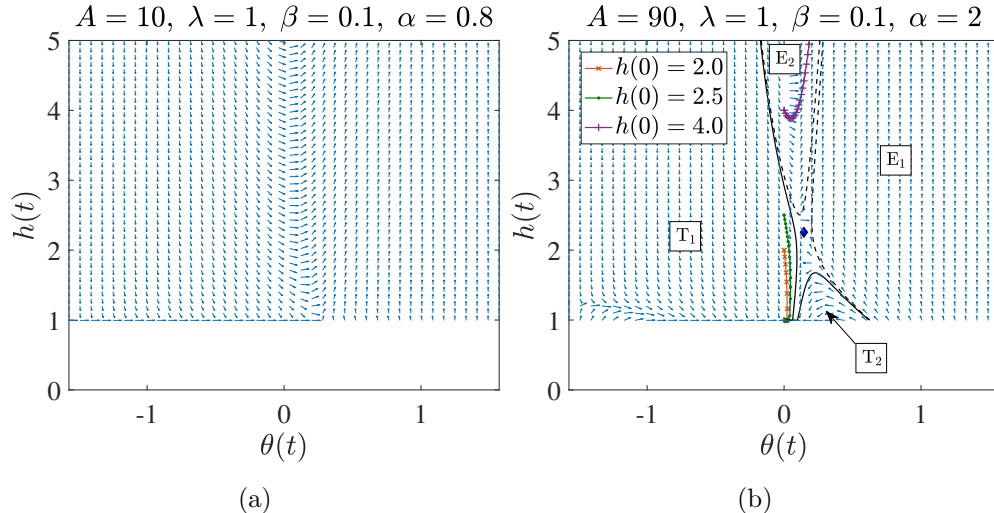


Figure 3.9. : Phase space plots for, (a) a surfactant-laden drop with radius less than the corresponding A_c , and, (b) one with radius larger than A_c . There are no trajectories that eventually get trapped at $h = 1$ in (a), while in (b) there are a host of such trajectories, most notably the ones marked with symbols. The $h = 1$ region can easily be discerned by the bottom-most row of vectors. The dashed lines bound the regions in the $h - \theta$ space that we term as ‘escaping’ regions, while the solid lines bound all initial (h, θ) pairs that will eventually get trapped onto the surface of the drop, or the ‘trapping’ region. For the lines in the legend, $\theta(0) = 0$; these correspond to the tangential release used to define the basin of attraction (see Fig. 3.6). Notice the change in the swimmer dynamics (from trapping to escape) as $h(0)$ increases beyond h^* (~ 3 in the case shown).

The idea behind the critical trapping radius becomes clearer, when we note that reducing the value of the drop radius leads to a “loss of the saddle point” into the surface of the drop, an idea explained in detail by Ishimoto and Gaffney in the context of swimming motion near plane walls/interfaces [160].

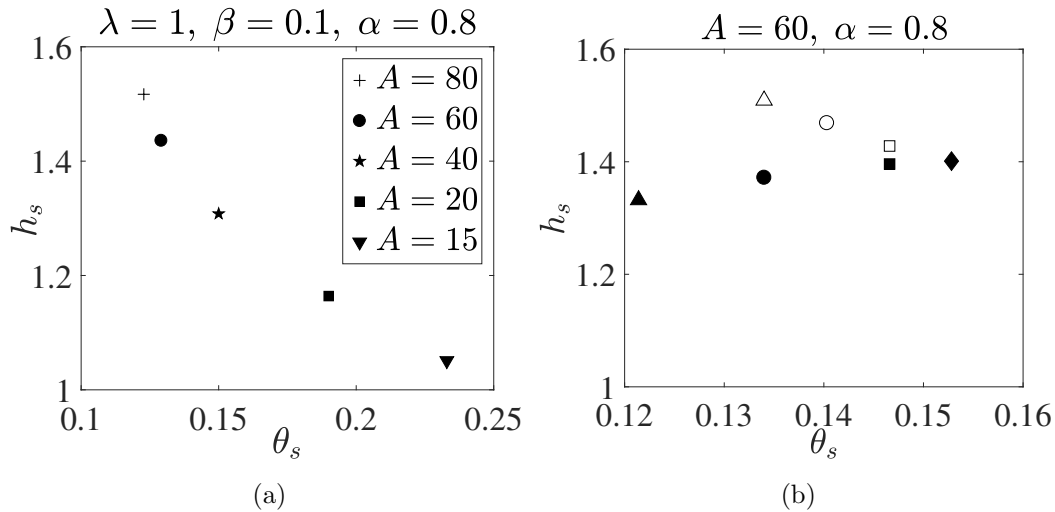


Figure 3.10. : (a) Variation of the saddle point location (h_s, θ_s) as a function of the drop radius, for a surfactant covered drop. Similar behavior is also seen for all other cases, i.e., for clean drops, and for a rigid sphere (not shown here). (b) Variation of the saddle point location (h_s, θ_s) as a function of the viscosity ratio, for a clean drop (filled symbols), and a surfactant covered drop (hollow symbols, $\beta = 0.01$). The meaning of the symbols is: triangles $\rightarrow \lambda = 0.1$, circles $\rightarrow \lambda = 1.0$, squares $\rightarrow \lambda = 10.0$, diamond \rightarrow rigid sphere, i.e., eqn. 3.13.

In our case, we see from Fig. 3.10(a) that reducing the value of A brings the saddle point closer and closer to $h = 1$, and this in turn reduces the area of the ‘trapping’ region. We note that although in Fig. 3.10(a) we show this ‘loss of saddle point’ for one set of parameters, it is a general occurrence for all parametric ranges in our study. Another interesting aspect of this section is the sensitivity of the saddle point (of course, for cases when $A > A_c$) to variations in λ and β . This is shown in Fig.

3.10(b). We notice straight away that the behavior for λ and/or $\beta \rightarrow \infty$ matches that for a rigid sphere [127]:

$$\begin{aligned} h_s &= \frac{(9\alpha^2 A/2)^{1/5}}{2} \\ \theta_s &= \left(\frac{3\alpha}{8A^2}\right)^{1/5}. \end{aligned} \tag{3.13}$$

Secondly, we see once again, the opposite effects of changing the viscosity ratio for a clean drop, and a surfactant-laden drop. For a given surfactant (fixed β), reducing λ moves the saddle point to *higher* values of h , and lower values of θ . The extent of this shift is determined by the value of β (it is not very significant, so it has not been shown in the manuscript). In case of a clean drop however, reducing λ moves the saddle point to *lower* values of h , and lower values of θ . These changes in the saddle point location, although significant from a qualitative aspect, are quite minor in a quantitative sense; thus highlighting the utility of our discussions in the previous sections towards gaining a more physical understanding of the system dynamics.

3.3.4 Scaling laws for A_c and h^* , as $\lambda \rightarrow 0$

In this section, we derive analytical expressions for the critical trapping radius and the size of the basin of attraction, for the case of locomotion around a clean bubble, i.e., when the viscosity ratio, $\lambda \rightarrow 0$. In cases where the diffusivities are negligible, the motion of the swimmer is restricted to two dimensions: in a plane that is defined by the unit vectors $\hat{\mathbf{r}}$ and \mathbf{p} . This two-dimensional motion can be completely specified by the following (dimensionless) dynamic equations for the swimmer separation h and its in-plane orientation θ [127](see Fig. 3.1):

$$\frac{dh}{dt} = \sin \theta + \mathbf{u}_{HI} \cdot \hat{\mathbf{r}}, \tag{3.14}$$

$$\frac{d\theta}{dt} = \frac{1}{A+h} (\cos \theta + \mathbf{u}_{HI} \cdot \hat{\mathbf{r}}^\perp) + (\hat{\mathbf{r}}^\perp \times \hat{\mathbf{r}}) \cdot \boldsymbol{\Omega}_{HI},$$

along with the repulsion condition (when $h \sim 1$, for a spherical swimmer) of eqn. 3.12, written as:

$$\frac{dh}{dt} = \max \{(\sin \theta + \mathbf{u}_{HI} \cdot \hat{\mathbf{r}}), 0\}. \quad (3.15)$$

To make analytical progress, we expand the expressions for \mathbf{u}_{HI} and $\boldsymbol{\Omega}_{HI}$ (see Appendix) in terms of the small parameter $h/A \ll 1$, and then linearize the system of equations about $\theta = 0$ [127], thus obtaining:

$$\begin{aligned} \frac{dh}{dt} &= \theta - \frac{\alpha}{4h^2} + O(\theta^2), \\ \frac{d\theta}{dt} &= \frac{1}{A} - \frac{3\alpha}{8h^3}\theta + O(\theta^2). \end{aligned} \quad (3.16)$$

In order for the swimmer to be trapped at the bubble surface, we need to find the equilibrium solutions to eqn. 3.16, i.e., set $d\theta/dt = 0$, to obtain:

$$\theta_{eqb.} = \frac{8h_{eqb.}^3}{3A\alpha}. \quad (3.17)$$

We now require that for $\theta = \theta_{eqb.}$, dh/dt , given by:

$$\frac{dh}{dt} = \frac{8h_{eqb.}^3}{3A\alpha} - \frac{\alpha}{4h_{eqb.}^2}, \quad (3.18)$$

stays non-positive (or alternatively, zero, as constrained by eqn. 3.12), which immediately yields (upon setting $h_{eqb.} = 1$)

$$A_{c,bubble} \geq 32/(3\alpha^2), \quad (3.19)$$

for a spherical (pusher) swimmer. A comparison with the full numerical simulations, in Fig. 3.11 shows that our theoretical prediction is an excellent approximation for the critical trapping radius. While bubbles with $A \geq A_{c,bubble}$ trap the micro-swimmers on their surface, the ones with $A < A_{c,bubble}$ can only scatter the micro-swimmers (like the trajectories in Fig. 3.2(a-c)). The reason behind this is easily understood upon examining $d\theta/dt$ from eqn. 3.16. If $A \geq A_{c,bubble}$, then θ continues to decrease with time and dh/dt continues to become more and more negative, thus precluding any escape. However, for $A < A_{c,bubble}$, θ will *increase* with time, until it reaches an ‘escape value’

$$\theta_{esc.} = \frac{4h^2}{\alpha}, \quad (3.20)$$

after which dh/dt becomes positive and the swimmer is able to escape the hydrodynamic attraction of the bubble. Eqn. 3.18 is also instructive in physically understanding the variation of A_c with the dipole strength α , as shown in Fig. 3.3 to 3.5. Although the derivation presented in this section holds for locomotion around a spherical bubble, it can still be used to get a mechanistic description of the more general cases. While the monotonic reduction in A_c with increasing values of α is explicitly seen in eqn. 3.11, we can also interpret this in terms of the swimming speed V_s . Clearly, lower swimming speeds correspond to higher (dimensionless) dipole strengths ($\alpha \propto V_s^{-1}$), which in turn results in lower values of dh/dt at $\theta = \theta_{eqb}$. (see eqn. 3.18). This means that deterministically, slower swimmers will struggle to escape from the hydrodynamic attraction of drops. Thus, the drops as small as even 10-15 swimmer body lengths, can hydrodynamically capture swimmers that are slow enough, e.g., for typical values discussed in Section 3.2, we see that bubbles as small as 30 μm in diameter can trap microbes ($\sim 2 \mu\text{m}$ in length) with swimming speeds less than $\sim 10 \mu\text{m/s}$. Thus, based on the motility characteristics of bacterial strains, the methodology discussed herein can help estimate bubble sizes for bacterial removal applications.

Eqns. 3.16 can also be used to estimate the size of the basin of attraction around a bubble, for small times. We proceed, in the vein of Spagnolie *et al.*, and expand h and θ in a polynomial series in time t :

$$h(t) = h_0 + h_1 t + h_2 t^2 + \dots, \quad (3.21)$$

$$\theta(t) = \theta_1 t + \theta_2 t^2 + \dots$$

Next, we make use of the definitions of dh/dt and $d\theta/dt$ from eqn. 3.16, along with the time derivative of the polynomials in eqn. 3.21, to get the relation:

$$(h_1 + 2h_2 t) = (\theta_1 t + \theta_2 t^2) - \frac{a}{4(h_0 + h_1 t + h_2 t^2 + \dots)^2}, \quad (3.22)$$

$$(\theta_1 + 2\theta_2 t) = \frac{1}{A} - \frac{3\alpha}{8(h_0 + h_1 t + h_2 t^2 + \dots)^3} (\theta_1 t + \theta_2 t^2 + \dots),$$

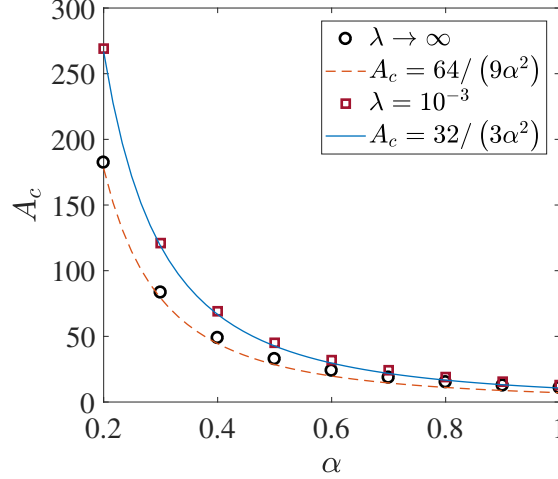


Figure 3.11. : A comparison between the scaling for the critical trapping radius of a clean bubble, as derived in eqn. 3.19 (solid line), and by the numerical solution to eqns. 3.10 (asterisks). Also shown is the comparison between numerics (circles) and scaling analysis (dashed lines) for a rigid sphere, as derived by Spagnolie *et al.* [127].

which can be solved by comparing terms of same order in t . This yields:

$$h(t) = h_0 - \underbrace{\frac{\alpha}{4h_0^2}}_{h_1} t + \underbrace{\left(\frac{1}{2A} - \frac{\alpha^2}{16h_0^5} \right)}_{h_2} t^2, \quad (3.23)$$

$$\theta(t) = \underbrace{\frac{1}{A}}_{\theta_1} t - \underbrace{\frac{3}{16} \frac{\alpha}{Ah_0^3}}_{\theta_2} t^2,$$

where $h_0 = h(0)$ is the initial separation, the limiting case of which will correspond to the depth of the basin of attraction. Minimization of $h(t)$ in the top line of eqn. 3.23 gives,

$$t_{min} = -\frac{h_1}{2h_2} = \frac{2\alpha Ah_0^3}{(8h_0^5 - A\alpha^2)}. \quad (3.24)$$

Evaluating $\theta_{esc.}(t_{min})$ from eqn. 3.20, and then using the bottom line of eqn. 3.23 to set $\theta(t_{min}) \leq \theta_{esc.}(t_{min})$ (see eqn. 3.20), gives us an equation in h_0 . Substituting

$h_0 = (\alpha^2 A \rho)^{1/5}$ in this equation for h_0 , we obtain a cubic equation in ρ with only one real root, $1024\rho^3 - 1024\rho^2 + 237\rho - 16 = 0$. Hence the basin of attraction is given by

$$h^* = \rho^{(1/5)} (\alpha^2 A)^{(1/5)}, \quad (3.25)$$

where $\rho^{(1/5)} = 0.93$. As seen in Fig. 3.12, this result does not match accurately with the numerics. Instead, we note that the scaling given by $(\alpha^2 A)^{1/5}$ is still correct, and so we use the numerical results to obtain a satisfactory fit to an expression with the form of eqn. 3.25. This method yields a value of $\rho^{(1/5)} \sim 0.8$. This results in excellent agreement between our numerical simulations and the scaling analysis (see Fig. 3.12). It is very interesting to note that the $(\alpha^2 A)^{1/5}$ scaling law for h^* for the case of a clean bubble is the same as the one derived by Spagnolie *et al.* for the case of a rigid sphere [127].

An important aside to our present study could be the analysis of locomotion near a drop that is acted upon by a prescribed force, e.g., due to its weight and buoyancy. We would like to point out that we have also performed similar simulations (not shown here) for this particular scenario. We found that for very low values of the force acting on the drop, a swimmer does get hydrodynamically trapped to the drop's surface, much like our results in this paper; but it tends to escape (as seen from the drop's frame of reference) once the force acting on the drop becomes large. A drop rising/sinking with a speed much larger than the speed of the swimmer may never trap a swimmer.

3.4 Effects of diffusive motion

We now move on to the discussion of randomness in swimming, i.e., the translational and rotational diffusive motion, modeled using the Gaussian white-noise terms in eqn. 3.11. The results discussed up until now were obtained for a deterministic swimmer, where diffusivity is zero and swimmer behavior can be exactly predicted, based on the swimmer's dipole strength (α), the size of the drop (A), and nature of the interface (β, λ). In reality however, swimming is far from deterministic, and ran-

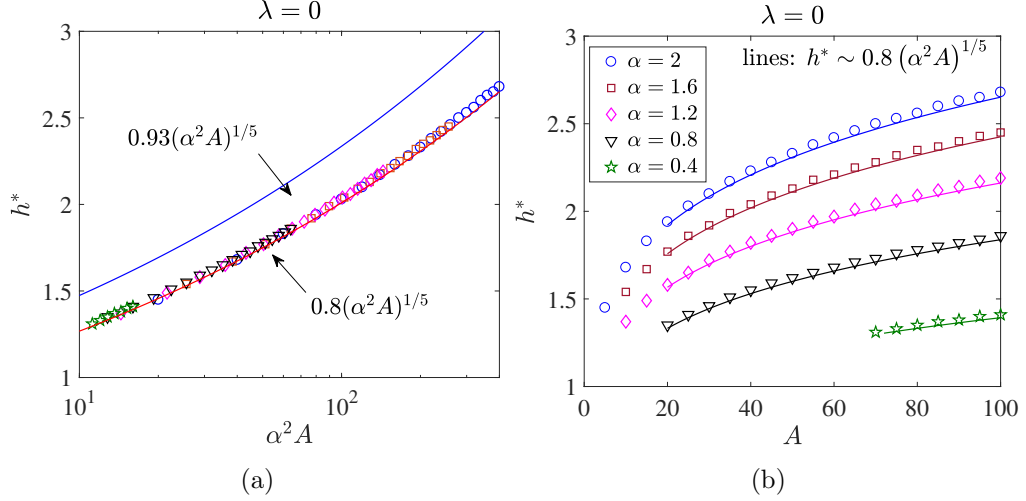


Figure 3.12. : Variation of the basin of attraction (h^*) with (a) the product of the square of swimmer's dipole strength and drop radius ($\alpha^2 A$) and (b) the drop radius (A) for the motion of swimmer near a clean bubble ($\lambda = 0$). Symbols denote the numerical results while the lines indicate the scaling laws. For $h^* = 0.8(\alpha^2 A)^{1/5}$, the numerical results match with the scaling laws.

domness is a key component of the swimmer dynamics. The randomness we study in this section accounts both for the stochasticity of swimmer motion, and the inherent variabilities that will always be observed across different swimmers in an The randomness in swimmer motion can have a thermal origin, or it can stem from factors like flagellar imperfections, or ciliary sensitivity to the availability of ATP molecules [105]. Note that we are not modeling the 'run-and-tumble' nature of bacteria, because it is debatable that bacteria employ the same motility traits near interfaces as they do in a 'free solution' [23, 24, 105, 110]. Moreover, for an isotropic tumbling—implemented using the method described in [161, 162]—the swimmer escapes in most of the cases for all drop radii, due to the (tumble induced) sudden increase in the angle θ to a value beyond the 'escape angle' θ_{esc} . (see eqn. 3.20). For spherical swimmers, we assume the rotational diffusivity, $D_R = 3D_T/4$. Note that this is a simplification, and is derived for the case of motion of a spherical swimmer in an infinite fluid; for flow near confine-

ments, or other general configurations, the diffusivity tensors need to be calculated by making use of the Stokes-Einstein equations, and the mobility matrices particular to the system [8]. The most striking contrast offered by the inclusion of randomness effects is that the swimmer is no longer guaranteed to be trapped whenever it gets hydrodynamically attracted to a drop larger than the critical trapping radius [127]. If we assume that the swimmers are unlikely to be adsorbed onto the interface, then the diffusive motion can allow them to reorient away from the interface, and in the process even escape the hydrodynamic trap. This escape can happen at any instant of time, and is not dictated deterministically. Therefore, we need to quantify it using the underlying p.d.f. for the trapping characteristics. A natural option is to quantify the time the swimmer spends orbiting the interface before it escapes (if at all such an escape occurs). Towards this end, we perform multiple simulations and record the ‘interface-retention time’, or trapping time, in each case, and finally report the p.d.f. We also report the mean trapping time and its variation with the dimensionless quantities of interest.

Fig. 3.13 shows, qualitatively, the difference between the diffusion-based swimming behavior around a surfactant laden drop and a clean drop. It is clear that all other parameters remaining the same, a swimmer is more likely to escape a clean drop earlier than it does a surfactant-laden one. This trend shows how advantageous is the use of dispersant in enabling hydrodynamics-induced trapping around oil drops.

To quantify our observations, we performed 10^4 numerical simulations for different λ and β and aimed to extract underlying p.d.f. of the trapping time. In each of the simulations the swimmer is released tangentially, from an initial separation of $h(0) = 1.001$. We define the trapping time as the time spent by the swimmer at a separation less than or equal to $h = 1.5$ from the drop surface; before it exceeds this threshold for the first time, i.e., $T_h = \min_t \{t : h \geq 1.5\}$ [127]. These results are shown in Fig. 3.14. All probability distribution functions follow the inverse Gaussian distribution when the simulations are run for times as large as $t_{end} = 400$. We see that a swimmer spends more time orbiting a drop if the interface is a surfactant

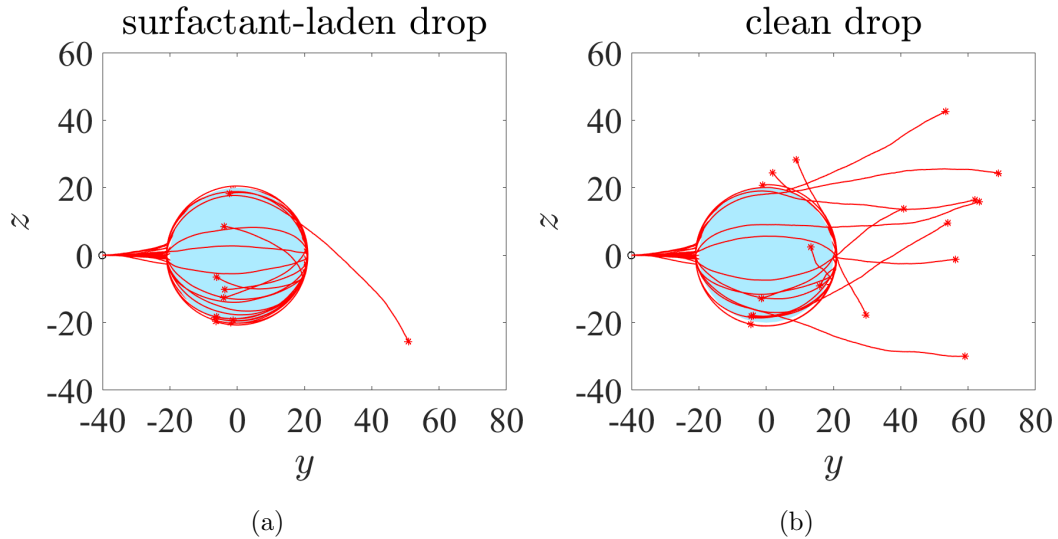


Figure 3.13. : Trajectories of 20 instances of direct impact on to a (a) surfactant-laden drop with $\beta = 0.1$ and $\lambda = 1.0$, and, (b) clean drop with $\lambda = 1.0$. The radius $A = 20$ and the dimensionless translational diffusivity $D = 5 \times 10^{-4}$. Notice that in the former case, there is only one swimmer that escapes the hydrodynamic attraction, which might be due to the low value of D [127]. In the latter case, a greater number of swimmers are able to escape the confinements of the drop, even for low diffusivities.

covered drop, and that this time is inversely related to the dimensionless surface viscosity β . In case of a clean drop, the mean trapping time is less than that of a rigid sphere, but just by adding surfactants one can get a drastic enhancement in swimmer-retention near interfaces. Even here, the behavior of the trapping time (T_h) with respect to the viscosity ratio (λ) depends acutely on whether the drop is clean, or surfactant-laden. For a clean drop, the mean trapping time is seen to decrease as λ increases (Fig. 3.14(a)); but for a surfactant-laden drop, a comparison across Fig. 3.14(b-d) reveals that the mean trapping time actually *increases* as λ increases. It is also clear that the limiting cases of large β and λ tend toward the behavior observed for locomotion around a rigid sphere. However, β and λ need not be several

orders of magnitude larger than $O(1)$, in order to replicate the results obtained for a rigid sphere. Finally, just like in the study of the critical trapping radius, we see the occurrence of a saturation in the trapping dynamics as β increases beyond a threshold value of ~ 10 .

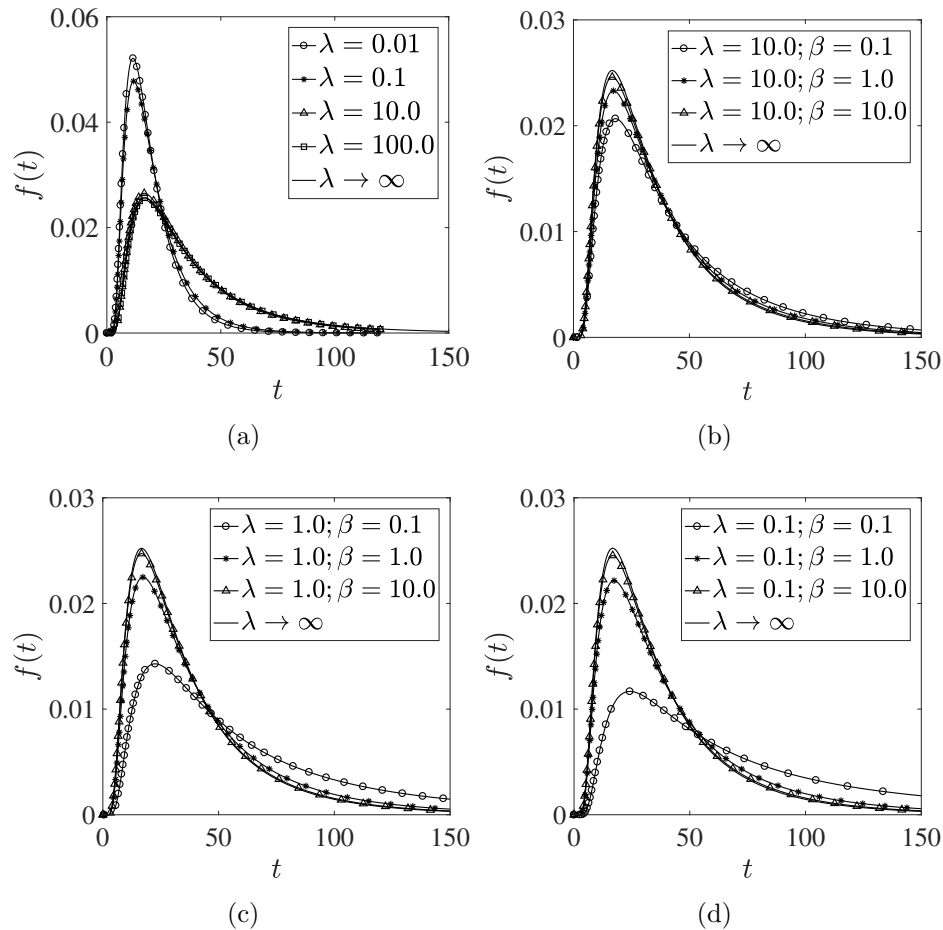


Figure 3.14. : Probability distributions $f(t)$ for the case of tangential release of microswimmer from an initial separation, $h(0) = 1.001$, from the drop's surface, for (a) a clean drop at different viscosity ratios (simulations run until $t_{end} = 120$); and surfactant-laden drop with: (b) $\lambda = 10.0$ ($t_{end} = 200$), (c) $\lambda = 1.0$ ($t_{end} = 200$), (d) $\lambda = 0.1$ ($t_{end} = 200$; except for the case when $\beta = 0.1$, where $t_{end} = 400$), and different surface viscosities. The other parameters are: $A = 20$, $\alpha = 0.8$, $D = 2 \times 10^{-3}$.

Next, we investigate the variation of trapping times of swimmers having different diffusivities, that are swimming around clean drops (surfactant-covered drops) of different radii, but all having fixed viscosity ratios (a fixed viscosity ratio and a fixed dimensionless surface viscosity). Physically speaking, the diffusive motion will dominate when directed motion due to a swimmer's intrinsic motility is not significant enough ($D \propto V_s^{-1}$). Therefore, even though slower swimmers are more likely to get hydrodynamically trapped near fluid-fluid interfaces (see discussion in Section 3.3.4), they are also more capable of escaping. This idea further highlights the necessity for a detailed analysis of locomotion around spherical surfaces. This variation is shown in the contour plots in Fig. 3.15. It can be seen that in certain cases ($A = 25$, $D = 0.006$), the mean trapping time for surfactant-laden drops is as much as $\sim 25\%$ higher than that for clean drops. The trends of reduction in the mean trapping times with increasing diffusivities, and decreasing interface radii are also apparent in Fig. 3.15. We also performed parametric sweeps in λ and β (for surfactant-laden drops), for different values of A and D , but the results in those cases were seen to be in line with our observations thus far, i.e., an attainment of saturation in the trapping behavior as $\beta \geq O(1)$ so they are not included.

3.5 Conclusion

We investigated the locomotion of micro-swimmers (modeled as a force dipole) near stationary, clean and surfactant-laden drops. In our analysis, it was assumed that the swimmer does not get adsorbed onto the (liquid-liquid) interface. The surfactant was considered incompressible, and its presence imparted an interfacial viscosity to the drop. This was incorporated using the Boussinesq-Scriven constitutive law for surface stresses in the shear stress boundary condition. A combination of hydrodynamic interaction and near-surface steric repulsion results in the swimmer orbiting the drop. Straight swimmers (no random component of motility) are seen to react in a binary way: they either orbit the drop endlessly, or are scattered, with the re-

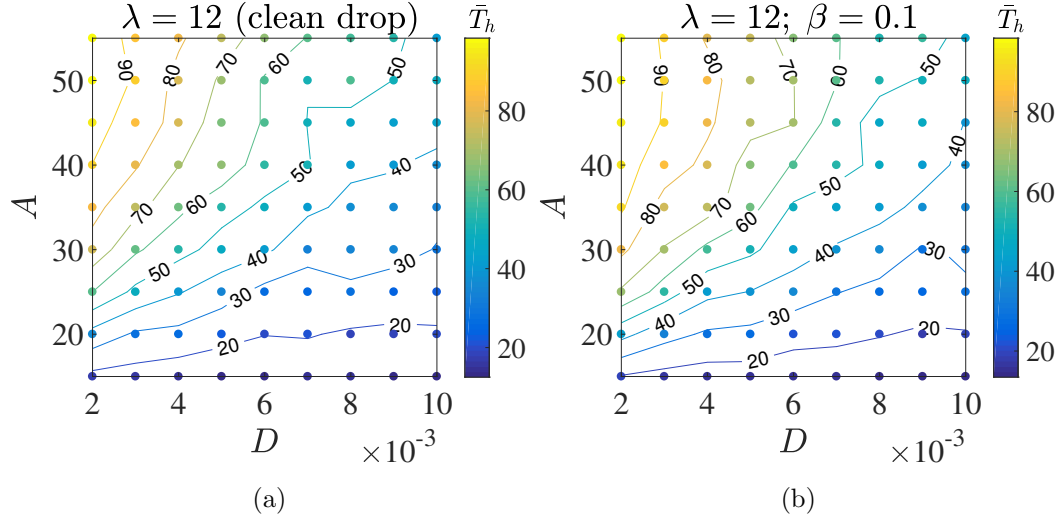


Figure 3.15. : Mean trapping times (\bar{T}_h) as a function of diffusivity D and radius of drop A , for (a) a clean drop ($\lambda = 12$), (b) surfactant-laden drop with λ same as (a), and $\beta = 0.1$. Results have been obtained from 100 trials, with simulations running until $t = 100$. The other parameters are: $\alpha = 0.8$.

sponse contingent upon the drop radius. The former effect is seen only if the drop size exceeds a threshold called the critical trapping radius. This radius is the least for drops that are covered with surfactants of low interface viscosity; signifying the ease with which such drops may attract nearby swimmers—particularly those that are not fast enough—compared to clean drops. Moreover, this disparity (between clean and surfactant-laden drops) in the ‘ability’ to trap micro-swimmers only increases as the viscosity ratio of the drops *decreases*; thus highlighting a particularly non-trivial aspect of surfactant addition. We were able to obtain a scaling for the critical trapping radius for the case of a clean bubble ($\lambda \rightarrow 0$), and our analytical result matches very well with full numerical simulations. Next, we showed that even for the strongest-attraction case—of low surface viscosities—the influence of hydrodynamic attraction does not extend beyond a region that is about 3 swimmer body lengths larger, radius wise, than the drop itself. This means that in order for hydrodynamics-based attachment to occur, a bacterium must somehow reach within an $O(1)$ body length from the

drop-surface. The mechanism for this initial approach could either be a chance encounter, or directed motion in the form of chemotaxis. We also analyzed the swimmer dynamics, in the deterministic case, by careful consideration of the $h(t) - \theta(t)$ phase space. We found that there exists a saddle point in the system dynamics in all cases where the drop radius is larger than the corresponding critical trapping radius. The sensitivity of the critical trapping radius and the depth of the basin of attraction—to λ and β —was explained in terms of the change in the saddle point location as one or more of the said parameters were varied.

In another set of simulations (Section 3.4), which included Brownian/athermal diffusive effects, we observed that a swimmer could escape from the drop surface, even when the drop radius was larger than the corresponding critical trapping radius. This escape also occurs due to other orientation decorrelation mechanisms such as run and tumble reorientation. We first carried out numerical simulations for multiple (10^4) instances to obtain the underlying probability distribution of the trapping times. It was seen that even in cases where the behavior of the drop departed from that of the rigid sphere [127] ($\beta, \lambda < O(10)$), the inverse Gaussian distribution was a reasonable match for our empirical distributions. Ultimately, we analyzed the variation of the mean trapping time with the viscosity ratio and dimensionless surface viscosity and concluded that in general, a surfactant-laden drop retains a swimmer at its surface longer than a clean drop. We noticed how addition of surfactant leads to opposite effects as the viscosity ratio of the drop changes. Clean (surfactant-laden) drops tend to trap the micro-swimmer for shorter (longer) times as their viscosities, with respect to background fluid, decrease. This result is important from the perspective of dispersant addition in oil spills. We stress that in all cases, the influence of surfactant is seen to saturate rapidly with increasing surface viscosity, which makes it imperative to perform validating experiments in the regime of very small surface viscosities. We believe it will be an exciting venture to experimentally test our results, and build upon them to include more sophisticated biophysical mechanisms that can then be used to explain oil-microbe interactions in lab-on-a-chip setups or marine ecosystems.

3.6 Appendix A: Velocity of a swimmer outside a clean/surfactant laden drop

The expressions for dimensional translational and rotational velocity of a swimmer (modeled as a force dipole) outside a clean/surfactant laden drop have been derived in [134]. We utilize the characteristic scales mentioned in the main text to non-dimensionalize these expressions. A general expression for the translational velocity of a swimmer outside a drop is given by

$$\mathbf{u}_{HI} = \sin^2(\theta) \mathbf{u}_{HI,1} - \sin(\theta) \cos(\theta) \mathbf{u}_{HI,2} + \cos^2(\theta) \mathbf{u}_{HI,3}. \quad (3.26)$$

The expressions for $\mathbf{u}_{HI,1}$, $\mathbf{u}_{HI,2}$ and $\mathbf{u}_{HI,3}$ for a drop covered with incompressible surfactant are given as

$$\begin{aligned} \mathbf{u}_{HI,1} &= \frac{\alpha}{\bar{R}^2} \frac{3y}{(-1+y)^2(y+1)^2} \hat{\mathbf{r}}, \\ \mathbf{u}_{HI,2} &= -\frac{\alpha}{\bar{R}^2} \hat{\mathbf{r}}^\perp \sum_{n=0}^{\infty} \frac{3(2n+3) \left[1 + \beta n^2 + \left(3\beta + \lambda + \frac{1}{3}\right)n\right] y^{2n+3}}{6 + 2\beta n^2 + (6\beta + 2\lambda + 2)n}, \\ \mathbf{u}_{HI,3} &= -\frac{3\alpha}{2\bar{R}^2} \frac{y}{(-1+y)^2(y+1)^2} \hat{\mathbf{r}}, \end{aligned} \quad (3.27)$$

while those for a clean drop without any interfacial viscosity are given as

$$\begin{aligned} \mathbf{u}_{HI,1} &= \frac{\alpha}{\bar{R}^2} \frac{(\Lambda + 2)y}{(-1+y)^2(y+1)^2} \hat{\mathbf{r}}, \\ \mathbf{u}_{HI,2} &= -\frac{\alpha}{\bar{R}^2} \hat{\mathbf{r}}^\perp \sum_{n=0}^{\infty} \frac{3\Lambda(n - \Lambda + 1)(2n + 3)}{2n + 6 - 6\Lambda} y^{2n+3}, \\ \mathbf{u}_{HI,3} &= -\frac{\alpha}{2\bar{R}^2} \frac{(\Lambda + 2)y}{(-1+y)^2(y+1)^2} \hat{\mathbf{r}}. \end{aligned} \quad (3.28)$$

Here $\Lambda = \lambda/(\lambda + 1)$, $y = A/(A + h)$, $\bar{R} = A + h$, and A is the dimensionless radius of the drop. Similarly, the expression for the dimensionless angular velocity of a swimmer outside a drop, $\boldsymbol{\Omega}_{HI} = \Omega_{HI}(\hat{\mathbf{r}}^\perp \times \hat{\mathbf{r}})$ is given as

$$\Omega_{HI} = \Omega_{HI,1} + \Gamma \Omega_{HI,2}, \quad (3.29)$$

where $\Gamma = \gamma/(\gamma + 1)$, γ is the aspect ratio of the swimmer. $\gamma = 0$ for a spherical swimmer and $\gamma \rightarrow \infty$ for a rod shaped swimmer. Here, the expressions for $\Omega_{HI,1}$ and $\Omega_{HI,2}$ for a drop covered with incompressible surfactant are given as

$$\Omega_{HI,1} = -\frac{3\alpha \sin(2\theta)}{4\bar{R}^3} \sum_{n=0}^{\infty} \frac{n(n+2) [\beta n^2 + (\beta + \lambda + \frac{5}{3})n - 2\beta - \lambda + \frac{7}{3}]}{\beta n^2 + (\beta + \lambda + 1)n - 2\beta - \lambda + 2} y^{2n+1},$$

$$\Omega_{HI,2} = \frac{\alpha \sin(2\theta)}{2\bar{R}^3} \left(\tilde{\Omega} \cos^2(\theta) + \hat{\Omega} \right); \quad (3.30)$$

where,

$$\begin{aligned} \tilde{\Omega} &= \frac{9(6\beta + 3\lambda - 2)}{8(2\beta + \lambda - 2)} y \\ &+ \frac{3}{4} \sum_{n=0}^{\infty} \frac{n^3\beta + (\frac{5}{2}\beta + \lambda + 3)n^2 + (-\frac{1}{2}\beta + \frac{1}{2}\lambda + \frac{17}{2})n - 3\beta - \frac{3}{2}\lambda + 5}{\beta n^2 + (\beta + \lambda + 1)n - 2\beta - \lambda + 2} \\ &\times (n+3) y^{2n+1}, \\ \hat{\Omega} &= -\frac{1(6\beta + 3\lambda - 2)}{2(2\beta + \lambda - 2)} y \\ &- \frac{3}{2} \sum_{n=0}^{\infty} \frac{n^3\beta + (2\beta + \lambda + \frac{5}{3})n^2 + (-\beta + \frac{14}{3})n - 2\beta - \lambda + \frac{8}{3}}{\beta n^2 + (\beta + \lambda + 1)n - 2\beta - \lambda + 2} \\ &\times (n+2) y^{2n+1}. \end{aligned}$$

Finally, the expressions for $\Omega_{HI,1}$ and $\Omega_{HI,2}$ for a clean drop without any interfacial viscosity are given as

$$\Omega_{HI,1} = -\frac{3\alpha \sin(2\theta)}{4\bar{R}^3} \sum_{n=0}^{\infty} \frac{n(n+2)(-2\Lambda^2 + n + 1)}{n + 2 - 3\Lambda} y^{2n+1}, \quad (3.31)$$

$$\Omega_{HI,2} = \frac{\alpha \sin(2\theta)}{2\bar{R}^3} \left(\tilde{\Omega} \cos^2(\theta) + \hat{\Omega} \right);$$

where,

$$\begin{aligned}\tilde{\Omega} &= \frac{27}{8} \frac{\Lambda^2 x}{(-2 + 3\Lambda)} \\ &\quad - \frac{3}{4} \sum_{n=0}^{\infty} \frac{(\Lambda - 2)n^2 + (3\Lambda^2 + \frac{5}{2}\Lambda - 6)n + \frac{3}{2}\Lambda^2 + 4\Lambda - 4}{(n + 2 - 3\Lambda)} (n + 3) y^{2n+1}, \\ \hat{\Omega} &= -\frac{3}{2} \frac{\Lambda^2 x}{(-2 + 3\Lambda)} \\ &\quad - \frac{3}{2} \sum_{n=0}^{\infty} \frac{n^2 + (-2\Lambda^2 - \Lambda + 3)n - \Lambda^2 - 2\Lambda + 2}{(n + 2 - 3\Lambda)} (n + 2) y^{2n+1}.\end{aligned}$$

3.7 Appendix B: Velocity of a swimmer outside a clean bubble

A simplified expression for the translational velocity of a swimmer outside a clean bubble is given as follows

$$\mathbf{u}_{HI} = -\frac{\alpha A (A + h)}{h^2 (2A + h)^2} (1 - 3\sin^2(\theta)) \hat{\mathbf{r}} \quad (3.32)$$

while the angular velocity of a swimmer outside a clean bubble, $\mathbf{\Omega}_{HI} = \Omega_{HI} (\hat{\mathbf{r}}^\perp \times \hat{\mathbf{r}})$ is given as

$$\Omega_{HI} = \frac{3A\alpha \cos(\theta) \sin(\theta)}{h^3 (2A + h)^3} \left[\begin{aligned} &\Gamma (A^2 + 3Ah + \frac{3}{2}h^2) \cos^2(\theta) \\ &+ (-\Gamma - 1) A^2 - 2A\Gamma h - \Gamma h^2 \end{aligned} \right] \quad (3.33)$$

For $h/A \ll 1$, we can write the above expressions for velocities as a series in h/A . The leading order term in this expansion gives the velocity of the swimmer near a plane stress-free interface. This expansion is given by

$$\mathbf{u}_{HI} = \frac{1}{16} \frac{(1 - 3\sin^2(\theta)) \alpha}{h^2} \left(\frac{h^2}{A^2} - 4 \right) \hat{\mathbf{r}} + O\left(\frac{\alpha}{h^2} \left(\frac{h}{A} \right)^3 \right) \quad (3.34)$$

$$\begin{aligned}\Omega_{HI} &= -\frac{9\alpha \sin(\theta) \cos(\theta)}{16h^3} \left[\begin{aligned} &\Gamma \left(\frac{h^2}{A^2} - \frac{h}{A} - \frac{2}{3} \right) \cos^2(\theta) \\ &+ \frac{(-\Gamma/3+1)h^2}{A^2} + \frac{(\Gamma/3-1)h}{A} + \frac{2}{3}\Gamma + \frac{2}{3} \end{aligned} \right] \\ &\quad + O\left(\frac{\alpha}{h^3} \left(\frac{h}{A} \right)^3 \right)\end{aligned} \quad (3.35)$$

Since the position and orientation of the swimmer are governed by eqns. 3.14, we substitute the above expansion for the velocity of the swimmer in these equations to obtain the following simple equations, valid for $h/A \ll 1$,

$$\begin{aligned}\frac{dh}{dt} &= \sin(\theta) - \frac{\alpha}{4h^2} (1 - 3\sin^2(\theta)) \\ \frac{d\theta}{dt} &= \frac{1}{A} \cos(\theta) - \frac{3\alpha}{32h^3} [\Gamma(1 - \cos(2\theta)) + 2] \sin(2\theta)\end{aligned}\tag{3.36}$$

Furthermore, we pursue a small θ expansion of the above equations, given as

$$\begin{aligned}\frac{dh}{dt} &= \theta - \frac{\alpha}{4h^2} + O(\theta^2) \\ \frac{d\theta}{dt} &= \frac{1}{A} - \frac{3\alpha}{8h^3} \theta + O(\theta^2)\end{aligned}\tag{3.37}$$

4. COMBINED INFLUENCE OF HYDRODYNAMICS AND CHEMOTAXIS IN THE DISTRIBUTION OF MICROORGANISMS AROUND SPHERICAL NUTRIENT SOURCES

4.1 Introduction

Chemotaxis can be defined as the ability of bacteria to perceive gradients in ambient nutrient/chemical concentrations and adjust their motility so as to ‘climb’ up or down these gradients. It is one of the most widely studied properties of bacteria, particularly for the enteric bacterium *E. coli* [5, 10, 40, 41]. The nutrient/chemical responsible for chemotaxis is called the chemoeffector. The motion of *E. coli* is termed ‘run-and-tumble’ because it consists of almost straight runs separated by sudden tumbles, i.e., abrupt changes in the swimming direction [5, 10, 40, 41]. Bacteria rely on temporal comparison of ambient nutrient concentrations to gauge chemoeffector gradients, and refine their motion as required [34–38]. Based on the feedback, a variety of changes can take place to alter bacterial motion, e.g., a change in swimming speed as a function of ambient concentration (chemokinesis), a change in the frequency of tumbling, or even a shift in the regime of swimming from run-and-tumble to ‘run-reverse-and-flick’ [163]. The cumulative effect of the above sequence of actions is to prolong the bacterium’s stay in any desired region. For example, chemokinesis can either slow bacteria down in regions of high nutrient concentration, or it can speed them up so as to have proportionately faster gradient-climbing. Similarly, bacteria are known to increase their average exposure to nutrients and thus fulfill their energetic re-

⁰This chapter has been reprinted with minor changes, with permission, from the material as it appears in the article “*Combined influence of hydrodynamics and chemotaxis in the distribution of microorganisms around spherical nutrient sources*”, by N. Desai and A. M. Ardekani, Physical Review E, vol. **98**, pp. 012419, 2018 (DOI: 10.1103/PhysRevE.98.012419). Copyright (2018) of The American Physical Society.

quirements, by tumbling (or reversing) less often in nutrient hot-spots. In addition to chemotaxis—which is an ‘active response’ by a bacterium to ambient physico-chemical stimuli—a bacterium’s motility can also get altered ‘passively’ via hydrodynamic interactions (H.I.) with nearby boundaries [8]. Some examples are “swimming on the right-hand side” [107], “swimming in circles” [20,23,24,149,160], reversal of swimming direction [108] and wall-attraction/accumulation [14,21,64,109–111,127,164]. These near surface phenomena, coupled with bacterial chemotaxis, are of utmost importance in the comprehension of bio-film formation and evolution [112–114]. While studies focusing solely on H.I. (ref. [107]- [64]), on chemotaxis without H.I. [6,79,165–171], or on chemotaxis and H.I. due to self-generated bacterial flows in infinite domains [172,173] abound; the combined effect of chemotaxis and H.I. on the locomotion of microorganisms near a boundary that is also a source of a chemoattractant, has not been studied. The studies that do consider the effects of fluid flow on bacterial motion (chemotactic or otherwise) near surfaces have been mostly limited to the cases where the bacterial cell is translated and rotated by a pre-existing background flow [79,166–170]. In absence of any background flows, a consistent description of H.I.s should involve fluid-flow that is generated on account of bacterial swimming and its proximity to surfaces.

In this paper, we aim to understand the combined/competitive effects of hydrodynamic and chemotactic attraction of model microorganisms to spherical nutrient sources. We study the motion of a bacterium that can run-and-tumble, near a stationary, spherical surface which acts as a source of the chemoeffector. Therefore, the motion is dictated by three different mechanisms: (i) translation due to inherent motility as well as hydrodynamic interaction (attraction) with the nutrient source (which can be a rigid sphere or a drop), (ii) rotation due to hydrodynamic interaction and random effects like thermal/athermal diffusion, and, (iii) chemotactic re-orientation due to the spatial distribution of a chemoeffector having a prescribed concentration on the surface of the source [165].

The fluid flow far from a bacterium can be modeled as that due to a force dipole, i.e., two equal and opposite, collinear forces with an infinitesimal separation between them [14]. A force dipole that lies within a few (1-3) body lengths from the surface of a rigid sphere (which, in an experiment, can be a colloid [125] or an isolated nutrient source like a marine snow particle) is prone to getting ‘hydrodynamically trapped’ onto the surface of the sphere [64, 127]. Beyond this separation, hydrodynamics alone cannot lead to attachment of microorganisms onto nutrient sources. In fact, Drescher *et al.* performed experiments and concluded that hydrodynamics becomes important only when a bacterium reaches “within a few microns” from a surface, and that hydrodynamic interactions successfully explain the “long residence times” of *E. coli* near no-slip surfaces [17]. This means that in order for hydrodynamics-based capture to occur, a bacterium must reach within an $O(1)$ body length from the spherical surface. This ‘initial approach’ could either be a chance encounter, or directed motion in the form of chemotaxis. It is this idea that motivates our study to understand how effective chemotaxis is, in conjunction with hydrodynamics, in the ‘capture’ of microorganisms around a spherical nutrient source with prescribed surface concentration of the chemoattractant.

A study of this type has been carried out in the past by Jackson [165], but without accounting for any hydrodynamic interactions. Another related work is by Bearon [169] where they quantify the rate at which motile bacteria colonize sinking aggregates like marine snow, phytoplankton, etc [6]. This study neglects H.I.s and considers the effect of the background flow (generated due to a sphere settling at zero Reynolds number [11]) on the bacterium’s position and orientation, but does not consider biased tumbling due to chemotaxis. In a similar fashion, Locsei and Pedley [170], studied the motion of a bacterium tracking an alga wherein they evaluate a background flow field due to a model algal cell. They then use this flow to translate and rotate the bacterial cell and neglect other H.I.s between the algal and the bacterial cell. In addition, they model chemotaxis in an empirical fashion based on experimental observations [174];

where the chemotactic re-orientation involves just a reversal in the swimming direction whenever the separation between the algal and bacterial cells exceeds a threshold.

In this paper, we wish to provide a mathematical model that consistently accounts for chemotaxis and hydrodynamic interactions, in situations where no other background flow exists. Towards this, it is essential to include, (i) chemotactic bias in bacterial motion stemming from the temporal comparison of nutrient concentrations by a bacterium, and, (ii) the fluid-flow (and concomitant bacterial motion) that stems solely from the interaction between the bacterium and the surface or boundary. Our objective is to obtain the spatial distribution (in the form of a probability distribution function, or, p.d.f.) of non-interacting chemotactic microorganisms ‘released’ at a given separation from the (nutrient) source, and with an arbitrary initial orientation. This p.d.f. will, in general, be a function of: (i) hydrodynamic parameters like the size (diameter) of the source, the swimming speed of the microorganism and the thrust force it exerts on the fluid, i.e., its dipole strength; and, (ii) chemotactic parameters like the chemoeffector concentration on the surface of the source and the tumbling frequency of the microorganism. A thorough understanding of these functional dependencies is warranted to successfully isolate the effects of chemotaxis from those of hydrodynamics; and in the process, better understand the dynamics of microorganism locomotion and colonization in the context of lab-on-a-chip setups or marine ecosystems.

The rest of the paper is organized as follows. We first describe the governing equations of fluid flow and the boundary conditions on the surface of a rigid, stationary sphere (which, in our case, represents the source of chemoattractant). This enables us to discuss the hydrodynamics induced locomotion of the model microorganism. We then describe the randomness in the microorganism motion, the chemoattractant distribution and the modeling of run-and-tumble chemotaxis for a single microorganism. We also comment on the near field effects and how they are expected to alter our model. Once the mathematical model is laid out, we present the results of the probabilistic simulations for the translational and rotational dynamics of the

microorganism. In all cases, we perform relevant comparative studies and discussion of the results, to pinpoint the influence of different parameters involved. Finally, we end by making some concluding remarks.

4.2 Mathematical modeling and methodology

4.2.1 Hydrodynamic Interaction

The contribution of the microorganism to the fluid flow is modeled as a pusher force dipole (dipole strength F oriented along \mathbf{p} ; see Fig. 4.1). Even though the force dipole representation is most accurate when the flow field is being analyzed far away from the microorganism, we note that such representations have been shown to be accurate at distances as small as a few body lengths away from rigid walls [14, 21], and interfaces [146, 147]. These have also been used to study the locomotion, and hydrodynamic trapping, of microswimmers around rigid spherical obstacles [127] and spherical drops [64]. To model the bacterial motion in the unbounded case (when it is far away from any surface), we make two additions: (i) we allow the force dipole to have swimming velocity $V_s \mathbf{p}$ in an unbounded fluid, where V_s is the swimming speed of the microorganism; (ii) we assume that in an unbounded fluid, the dipole orientation can ‘tumble’ with a characteristic tumbling frequency τ_0^{-1} and diffuse over the unit sphere with a (rotary) diffusivity D_r , this part is discussed in detail in Section 4.2.2.

The effect of a solid boundary near the bacterium, i.e., the hydrodynamic interaction (H.I.), is incorporated by first solving the governing equations for fluid-flow with appropriate boundary conditions. These include the differential forms of the conservation of mass,

$$\nabla \cdot \mathbf{v} = 0, \quad (4.1)$$

and momentum,

$$-\nabla P + \mu \nabla^2 \mathbf{v} = -F (\mathbf{p} \cdot \nabla) \{ \mathbf{p} \cdot \boldsymbol{\delta}(\mathbf{x} - \mathbf{x}_2) \}, \quad (4.2)$$

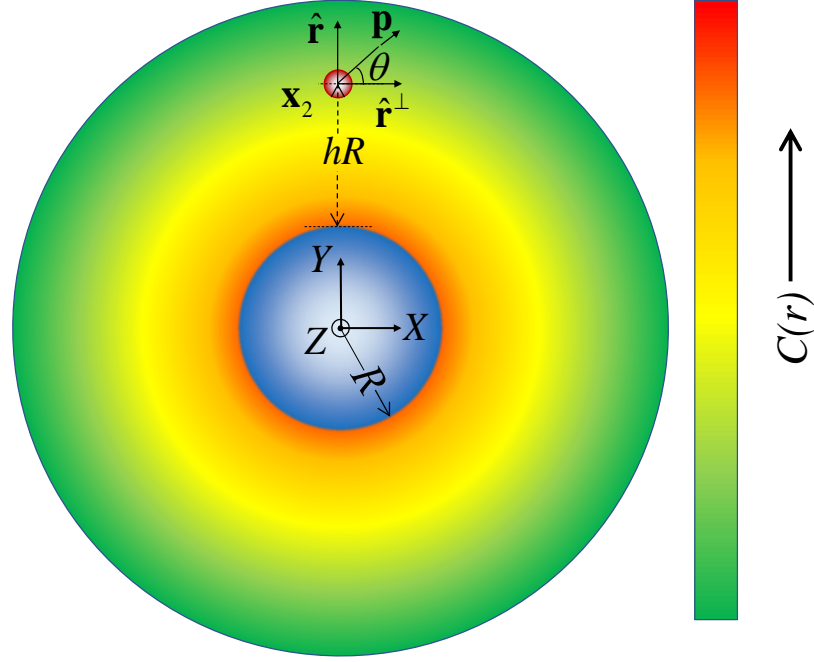


Figure 4.1. : (Color online) A schematic of the problem being solved, showing a spherical nutrient source of radius R , a spherical swimming microorganism of radius b oriented along the unit vector \mathbf{p} , and the spherically symmetric chemoattractant distribution around it $C(r)$. The origin of a ‘fixed’ coordinate system XYZ lies at the center of the source. The coordinate system defined by the unit vectors $\hat{\mathbf{r}}$, $\hat{\mathbf{r}}^\perp$ and $\hat{\mathbf{r}}^\perp \times \hat{\mathbf{r}}$ can rotate and translate with respect to the fixed coordinate system, as the microorganism moves through the fluid. In a quiescent, unbounded, fluid ($h \rightarrow \infty$), the microorganism will swim along the direction \mathbf{p} . The hydrodynamic interaction induced translational velocity, \mathbf{u}_{HI} , and rotational velocity, $\boldsymbol{\Omega}_{HI}$, of the microorganism is expressed as functions of the microorganism separation from the surface h , and its in-plane orientation θ (see equations 4.4 and 4.5). Note that h is the dimensionless separation of the microorganism from the source.

in the Stokes flow regime, because for the length scales involved in our problem, the flow inertia is negligible. Equations 4.1 and 4.2 need to be solved subject to the boundary conditions:

$$\begin{aligned} \mathbf{v}(|\mathbf{x}| = R) &= 0, \\ \mathbf{v}(|\mathbf{x}| \rightarrow \infty) &= 0 \end{aligned} \tag{4.3}$$

In the above equations, \mathbf{v} , P and μ are the fluid's velocity, pressure and dynamic viscosity, respectively. R is the radius of the spherical nutrient source. \mathbf{x} is the position at which the velocity needs to be evaluated, \mathbf{x}_2 is the position vector from the origin of the coordinate system to the center of the microorganism (see Fig. 4.1), and $\delta(\mathbf{x})$ is the three-dimensional Dirac-delta function. Equations 4.1 - 4.3 can be solved for $\mathbf{v}(\mathbf{x})$ and $P(\mathbf{x})$, by using the method of images as shown in ref. [13]. Thereafter, an application of the Faxen's law for a sphere, by treating the image flow field as an ambient flow and utilizing the force free and torque free conditions, yields the linear (\mathbf{u}_{HI}) and angular ($\boldsymbol{\Omega}_{HI}$) velocity of the force dipole, due to the hydrodynamic influence of the nearby particle (see ref. [64, 127]):

$$\begin{aligned} \frac{\mathbf{u}_{HI}}{V_s} &= -\frac{3A\alpha_D(1-3\sin^2\theta)(A+h)}{2h^2(2A+h)^2}\hat{\mathbf{r}} \\ &+ \frac{3A^3\alpha_D(2A^2+6Ah+3h^2)\sin 2\theta}{4h^2(2A+h)^2(A+h)^3}\hat{\mathbf{r}}^\perp, \end{aligned} \quad (4.4)$$

$$\frac{\boldsymbol{\Omega}_{HI}}{V_s/b} = -\frac{3A^3\alpha_D(2A^2+6Ah+3h^2)\sin 2\theta}{4h^3(2A+h)^3(A+h)^2}(\hat{\mathbf{r}}^\perp \times \hat{\mathbf{r}}). \quad (4.5)$$

In equations 4.4 and 4.5, b is a measure of the microorganism size (if the microorganism is assumed to be spherical, then b is its radius), $h = (|\mathbf{x}_2| - R)/b$ is the dimensionless separation of the microorganism from the surface of the source, $A = R/b$ is the dimensionless radius of the source, θ is the in-plane orientation of the microorganism (see Fig. 4.1), and $\alpha_D = F/(8\pi\mu b^2 V_s)$ is the dimensionless dipole strength of the microorganism. Before proceeding, we make an important note regarding the generality of the hydrodynamic aspect of our study. Equations 4.4 and 4.5 describe the swimming dynamics of a model microorganism near a rigid spherical nutrient source. It is also possible to derive the same for motion around spherical drops by using appropriate boundary conditions in place of 4.3, as done by Shaik and Ardekani [134]. In this study, we restrict ourselves to the analysis of motion around rigid, spherical nutrient sources (e.g., marine snow particles). However, a similar analysis can be performed for a nutrient source like an oil drop (i.e., for a spherical fluid-fluid interface); for details see ref. [64] and the Appendix. For a viscosity ratio corresponding

to crude oil, there is only a minor quantitative change in the final results of interest (see Fig. 4.12 in the Appendix). Therefore, we note that our study also reflects the accumulation trends around crude oil drops that are the sole source of carbon for a wide class of marine bacteria [2]. Thus, the results of this study can be used to understand bioremediation in an oil spill.

Once \mathbf{u}_{HI} and $\boldsymbol{\Omega}_{HI}$ are known, the motion of the microorganism can be defined in terms of the evolution equations for its position $\mathbf{x}_2(t)$ and orientation $\mathbf{p}(t)$, where t is the time. The former is given by,

$$\frac{d\mathbf{x}_2}{dt} = \mathbf{u}_{HI} + V_s \mathbf{p}, \quad (4.6)$$

while the *hydrodynamic component* of the latter is,

$$\left. \frac{d\mathbf{p}}{dt} \right|_{\text{hydrodynamic}} = \boldsymbol{\Omega}_{HI} \times \mathbf{p}. \quad (4.7)$$

Equation 4.7 is not complete yet because we haven't accounted for two important randomness effects in the motion of any bacterium: the run-and-tumble motion and thermal/athermal diffusion. We now turn our attention to modeling these effects.

4.2.2 Chemotactic Re-orientation

The motion of a bacterium in an unbounded, quiescent fluid is characterized by run-and-tumble, i.e., nearly straight swimming (runs) interspersed with abrupt re-orientations (tumbles) due to certain flagellar mechanisms [175–177]. The runs themselves are not perfectly straight due to various reasons (Brownian rotation, flagellar imperfections, ATP availability) and the bacterium is seen to undergo rotary diffusion during the course of each run [105]. In this Section, we discuss the incorporation and implementation of these re-orientations into our model. The rotary diffusion is straightforward and just adds a random component to the right-hand-side of equation 4.7; written as a stochastic differential equation, this yields:

$$\mathbf{p}_{n+1} = \mathbf{p}_n + \Delta t (\boldsymbol{\Omega}_{HI})_n \times \mathbf{p}_n + \sqrt{4D_r \Delta t} \boldsymbol{\eta}_r \times \mathbf{p}_n, \quad (4.8)$$

where D_r is the rotary diffusivity of the bacterium, $\boldsymbol{\eta}_r$ is the Gaussian white noise on the unit sphere [10, 105, 145], and the subscripts n and $n + 1$ refer to the values of the variables at the current, and the next time step, respectively. In general, the rotary diffusivity is obtained by using the Stokes-Einstein relations along with the mobility matrices of the system under consideration [8]. Due to the changing geometry of the problem, the mobility matrices will be a function of the position and the orientation of the microorganism, and the effect of Brownian rotation will be a more involved stochastic differential equation (see ref. [178, 179] for details) instead of eqn. 4.8. Also, the magnitude of the fluctuations will be a function of the microorganism's distance from the source. For the sake of simplicity however, we assume the mobility matrix to be constant and isotropic, in which case eqn. 4.8 holds. We emphasize that this does not alter the essential physics that we observe in our study. We discuss this idea in detail in the Appendix. The tumbling of the bacterial cell is a probabilistic event, modeled as a Poisson process with rate τ_0^{-1} [10]. This means that in an unbounded fluid, the probability of a tumble to occur after an infinitesimal interval dt is constant and is given by,

$$P_{t,0} = dt/\tau_0. \quad (4.9)$$

Therefore, $1/\tau_0$ is the mean tumbling frequency for a bacterium, and a tumble is effected by the following ‘rule’ [180, 181]:

$$\begin{aligned} \mathbf{p}_{n+1} &= \phi \mathbf{p}_n + (1 - \phi) \mathbf{p}', \\ \phi &\equiv H(\mathfrak{R}_{n+1} - P_{t,0}), \end{aligned} \quad (4.10)$$

where H is the Heaviside function [182], and \mathfrak{R}_{n+1} is a random number chosen from a uniform distribution on $[0, 1]$. Therefore, during a run (if $P_{t,0} < \mathfrak{R}_{n+1}$), the bacterium re-orientes ‘smoothly’ via equation 4.8, but in case of a tumble (if $P_{t,0} > \mathfrak{R}_{n+1}$) it changes its orientation instantaneously to a new orientation \mathbf{p}' . This post-tumble orientation could either be one from a uniform distribution on the unit sphere (an isotropic tumble); or, it could be biased, i.e., correlated in some way to the pre-tumble orientation (anisotropic tumble). In this study, we use a probability distribution $g(\beta)$, of the angle β between the pre- and post-tumble orientations which has been observed

experimentally for the bacterium *E. coli* [40], and a succinct mathematical expression is provided in ref. [43]: $g(\beta) = (1 + \cos \beta) / 2$. Note that in reality, a tumble is not instantaneous (it takes around 0.1s) but we assume it to be so for the current work.

The run-and-tumble described thus far enables a bacterium to perform a ‘random walk’ through its environment, just like Brownian/diffusive motion. The effective diffusivity of this random walk is given by $D_{eff} = V_s^2 \tau_0 / 3$ [183]. The true utility of this motility feature however, is observed when a bacterium forages for nutrients. An intricate mechanism [110,177] allows the bacterium to alter its tumbling frequency—or equivalently, its run time—in such a way that it spends more (resp. less) time in a desired (resp. undesired) region, e.g., in a region that is rich (resp. poor) in nutrients. As a result, the rate of the Poisson process (or, equivalently, the tumbling frequency) is no longer a constant τ_0^{-1} , but it changes depending on the nutrient exposure of the bacterium. If the organism finds itself in regions of progressively increasing nutrient concentration, then its tumbling frequency reduces ($\tau > \tau_0$); and if the organism moves to regions of declining nutrient concentrations, then the tumbling frequency stays unaltered at $\tau = \tau_0$. It is therefore imperative to have an idea about the nutrient distribution, before proceeding on to model bacterial chemotaxis. The concentration C of the nutrient/chemoeffector is governed by the following conservation equation:

$$\frac{\partial C}{\partial t} + \nabla \cdot (C\mathbf{v}) = D_C \nabla^2 C, \quad (4.11)$$

subject to the boundary conditions:

$$\begin{aligned} C(|\mathbf{x}| = R) &= C_0, \\ C(|\mathbf{x}| \rightarrow \infty) &= 0. \end{aligned} \quad (4.12)$$

D_C in eqn. 4.11 is the nutrient diffusivity. We now proceed to make two simplifications to equation 4.11. Firstly, we consider steady-state nutrient distribution, thus dropping the first term on the left hand side of equation 4.11. Next, we note that the characteristic Peclet number for the problem is very small, which allows us to neglect the advection terms in eqn. 4.11. The Peclet number is,

$$\text{Pe} = \frac{V_s l_{ref}}{D_C}, \quad (4.13)$$

where $V_s \approx 10 \mu\text{m/s}$ is the reference velocity scale (the bacterium's swimming speed) and l_{ref} is a reference length scale (for phytoplankton, $l_{ref} \approx 10 \mu\text{m}$; for oil drops, $l_{ref} \approx 20 - 60 \mu\text{m}$ [94–96]). The value of D_C for some typical nutrients—like C_6 sugar, or hydrocarbons like CH_4 —is $\approx 10^{-5} \text{ cm}^2/\text{s}$ [74, 99]. For the above mentioned parameters, we see that the Pe is $O(0.1)$, and thus advection can be neglected as a first approximation [170, 184]. As a result, we obtain the very simple diffusion equation for the chemoeffector concentration,

$$D_C \nabla^2 C = 0, \quad (4.14)$$

which can be solved using the boundary conditions 4.12 to get:

$$C(r) = \frac{C_0 R}{r}, \quad (4.15)$$

here $r = |\mathbf{x}_2|$ is the radial distance from the origin of the coordinate system (see Fig. 4.1). We can now define the chemotactic motion of the bacterium by relating its tumbling frequency to the temporal evolution of the nutrient concentration C in the bacterial reference frame. Towards this, we employ the ‘bi-phasic tumbling frequency’ model developed by Brown and Berg for *E. coli* [41], but without the ‘memory effect’, i.e.,

$$\tau = \begin{cases} \tau_0 \exp\left(\alpha_C \frac{K_D}{(K_D + C)^2} \frac{DC}{Dt}\right), & \frac{DC}{Dt} > 0 \\ \tau_0, & \frac{DC}{Dt} \leq 0 \end{cases} \quad (4.16)$$

where K_D is a measure of how well the chemoattractant binds to the chemoreceptor, and α_C is a time scale characteristic to the system being studied. A lack of the ‘memory effect’ means that τ depends only on the *instantaneous* rate of change (material derivative) of C (i.e., DC/Dt) with respect to the bacterial motion, and not on the averaged time history of nutrient concentration [32]. It is clear that if the material derivative is positive, then the run-time $\tau > \tau_0$; if the material derivative is negative, then the run-time does not change, as observed in experiments with *E. coli* [41]. Equation 4.16 thus provides us with a framework that explains how tumbles assist a microorganism in foraging for desired chemical species. As the organism swims

through its environment, it ‘senses’ the changes in the ambient nutrient concentration and alters its tumbling statistics according to equation 4.16 [185,186]. Therefore, in the presence of a chemoeffector, a tumble occurs within an infinitesimal time interval dt , if $P_t = dt/\tau > \mathfrak{R}_{n+1}$; notice how P_t can be lesser than $P_{t,0}$ (equation 4.9) if a chemoeffector is involved. We note that although the above model was developed for the enteric *E. coli*, a judicious choice of the quantity α_C and slight changes in the type of re-orientation can enable us to mimic chemotactic responses that are not of the ‘run-and-tumble’ type, e.g., see the recent work by Son *et al.* [39].

4.2.3 Near wall Effects

So far, we have described the effect of H.I. and chemotaxis on the locomotion of a microorganism modelled as a force dipole. These descriptions are apt in situations when the microorganism is a few (> 2) body-lengths away from the source. What happens when the microorganism drifts to within 2 body lengths from the solid surface? In such a scenario, the far field force dipole assumption can lead to the microorganism penetrating into the solid surface; an occurrence which is clearly aphysical. This could be prevented by: (i) the inclusion of higher order singularities (and images) in equation 4.2; or (ii) use of the lubrication/thin-film approximation, as the microorganism-surface distance becomes very small. Both these methods are unwieldy, and so, for the sake of simplicity, we model the ‘near field’ hydrodynamics as a hard-core repulsion [109,127,164], i.e., we set the normal velocity of the microorganism to be zero if the microorganism distance becomes less than 1 body-length from the surface:

$$\frac{d\mathbf{x}_2}{dt} = \begin{cases} \mathbf{u}_{HI} + V_s\mathbf{p}; & |\mathbf{x}_2| \leq (R + b), (\mathbf{u}_{HI} + V_s\mathbf{p}) \cdot \hat{\mathbf{r}} > 0 \\ (\mathbf{u}_{HI} + V_s\mathbf{p}) \cdot \hat{\mathbf{r}}^\perp; & |\mathbf{x}_2| \leq (R + b), (\mathbf{u}_{HI} + V_s\mathbf{p}) \cdot \hat{\mathbf{r}} \leq 0 \end{cases}, \quad (4.17)$$

where b is a characteristic microorganism dimension. While the evolution of the microorganism position \mathbf{x}_2 , is clear from the relation 4.17, we still need to ascertain the evolution of the microorganism orientation \mathbf{p} , when it is close to the surface. The

microorganism orientation is affected deterministically by Ω_{HI} , and randomly via the Gaussian white-noise (rotary diffusion, D_r) and the Poisson process (tumbling, equation 4.10). It is the third behavior that we need to treat carefully, keeping in mind how surfaces affect bacterial tumbling. As stated by Elgeti *et al.* in a recent review article, “The swimming behavior of bacteria close to surfaces differs from the run-and-tumble motion in free solution” [105]. This difference in swimming behavior is well-documented in prior experimental studies [20, 23, 24, 107, 110, 187]. Specifically, it is known that tumbling of the bacterium *E. coli* is reduced by as much as $\approx 50\%$ in the proximity of solid surfaces [110, 187]; and that *E. coli* can escape these surfaces not by tumbling away, but by diffusing their orientation away from the surface and then swimming away [109, 164]. Even in the event that a tumble does occur, the post-tumble orientations are mostly restricted to the tangent plane at the location of the bacterium. The near interface behavior of marine bacteria—that do not necessarily utilize the run-and-tumble motion of *E. coli*—has not been investigated in detail. Therefore, we take an empirical approach to near surface tumbling and postulate that the microorganism ceases to tumble at distances from the solid surface that are less than twice its body-length. The rotary diffusion of a bacterium on the other hand, is independent of its ability to tumble, or display other motility traits [10]. It is a well known behavior of most bacterial species, both enteric and marine, and is attributed to thermal fluctuations and/or intrinsic irregularities. Therefore, the ‘ D_r term’ influences the orientation \mathbf{p} of the microorganism irrespective of its distance from the surface. In summary, the microorganism motion in the bulk (> 2 body-lengths separation) is governed by equations 4.6, 4.8, 4.10, 4.15 and 4.16; while that near the surface (< 2 body-lengths separation) is governed by 4.8 and 4.17. In what follows, we numerically solve these equations for sufficiently large number of instances, to get statistically meaningful results and deduce the effect of the various mechanisms (see Table 4.1) on the distribution of microorganisms around spherical nutrient sources.

4.3 Results and Discussion

4.3.1 Interplay between hydrodynamic interaction and chemotaxis

We select the following scales to non-dimensionalize the various quantities of interest: lengths by the characteristic microorganism dimension b ($1 \mu\text{m}$), speeds by the swimming speed V_s ($10 \mu\text{m/s}$), time by b/V_s (0.1 s), dipole strength by $\mu b^2 V_s$ ($0.01 \text{ pN}\cdot\mu\text{m}$), nutrient concentration by K_D , and rotary diffusivity by V_s/b (10 s^{-1}). This yields the important dimensionless parameters, along with their orders of magnitude, in our study to be: radius of the source $A = R/b \approx 20 - 60$, dipole strength $\alpha_D = F/(8\pi\mu b^2 V_s) \approx 0.1 - 2.0$ ($F \approx 0.1 - 10 \text{ pN}\cdot\mu\text{m}$), diffusivity $D = D_r b/V_s \approx 10^{-5} - 10^{-3}$, surface concentration (representative nutrient availability) $C_0/K_D \approx 10^{-2} - 10^2$, and run-time (or equivalently, inverse of tumbling frequency) $\tau^* = \tau_0 V_s/b \approx 4 - 12$.

Table 4.1. : Summary of various mechanisms dictating swimming behavior near a rigid, spherical surface exuding a chemoattractant with a specified concentration at the surface of the source.

Mechanism: dimensionless parameter	Contribution
Hydrodynamic interaction (H.I.): α_D and A	Attraction of nearby microorganisms leading to scattering/trapping
Chemotaxis: C_0/K_D and τ^*	Initial attraction of distant bacteria towards the nutrient source
Hard-core repulsion: $ \mathbf{x}_2 /(R+b) \leq 1$	Balance with H.I. leads to orbiting/entrapment
Rotary diffusion: D	Orientational fluctuations may cause the microorganism to escape from surface

In our simulations, the baseline parameters are: $\alpha_C = 300$ s, $C_0/K_D = 1.0$, $\tau^* = 6$, $\alpha_D = 0.8$ or 10^{-3} , $A = 20$, $D = 7.5 \times 10^{-4}$ (or, $D \approx 0$, when rotary diffusion is neglected). The swimming dynamics is solved for 10000 instances, each running up to 200 dimensionless time units ($t_{end} = 200$). In each case, the initial position of the microorganism is 20 body-lengths away from the source ($|\mathbf{x}_2(0)| = 40$), and the initial orientation is randomly assigned. The final result that we investigate is the distribution of the microorganisms' locations $r(= |\mathbf{x}_2|)$ at the end of the simulations. We compute two different quantities of interest: (i) a 'surface concentration' C_s , and, (ii) a radial distribution function $f(r)$. C_s is the fraction of the total microorganisms that get trapped at the surface, i.e., those whose trajectory end-point lies within a separation of 1.5 body-lengths from the source. It is a measure of the surface colonization by the bacteria. $f(r)$ is a distribution function such that the fraction of microorganisms that lie in a thin spherical shell of radius dr is equal to $4\pi r^2 f(r) dr$. In other words, the probability of finding a microorganism between r and $r + dr$ is proportional to $4\pi r^2 f(r) dr$. $f(r)$ is normalized such that together with C_s , it satisfies

$$C_s + \int_{r=A}^{\infty} 4\pi r^2 f(r) dr = 1. \quad (4.18)$$

A confluence of chemotaxis, hydrodynamics, 'hard-core repulsion' and rotational diffusion shapes the behavior, and subsequent distribution of the swimming microorganisms around the source. Before proceeding to isolate the effects of each of these, we provide a qualitative description of the important physico-chemical interactions taking place. Spagnolie *et al.* used solely hydrodynamics based arguments to show that if the radius of a spherical obstacle is larger than a 'critical trapping radius', then it can hydrodynamically capture or trap swimmers that directly impinge upon it (see Fig. 4.2(a)). Alternatively, swimmers with dipole strengths larger than a critical value can get hydrodynamically trapped around spherical obstacles (see Fig. 4.2(b)). In addition, for all cases where hydrodynamic trapping is expected to occur, there exists a 'basin of attraction' such that tangentially directed pusher swimmers

that lie within the basin get trapped and travel along the surface of the sphere (see Fig. 4.2(c)). The ‘depth’ of this basin varies with the sphere radius A , and the dipole strength α_D . It is at most 2.5 body-lengths for A as large as 200 and $\alpha_D = 0.8$. At such small separations, Molaei *et al.* have shown the inability of an *E. coli* cell to tumble, or even escape the solid surface [110, 187]. Therefore, hydrodynamics is strongest, and tumbling weakest, when the microorganism is located very close to the source. Conversely, when the microorganism is far from the source, the hydrodynamics becomes negligible and chemotaxis is the dominant factor in dictating its motion.

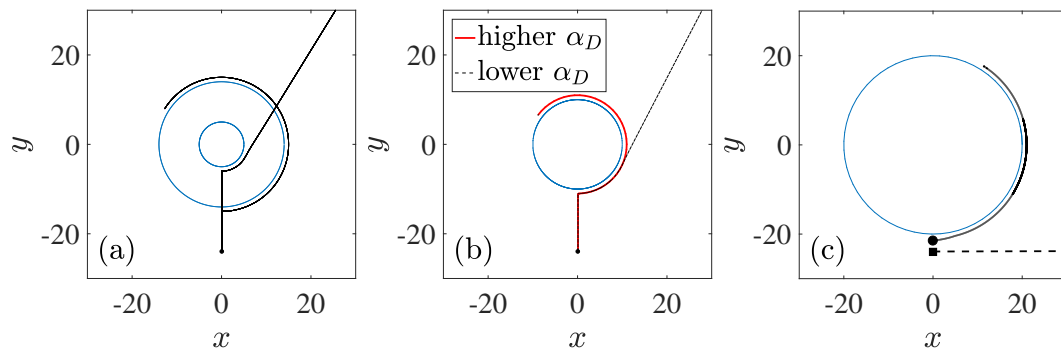


Figure 4.2. : (a) The concept of the critical trapping radius [127]: the swimmer trajectory around the smaller sphere escapes, while that around the larger sphere (whose radius is greater than a critical trapping radius) gets trapped. The swimmers’ initial orientation, $\mathbf{p}(0) = \mathbf{e}_Y$. (b) Alternatively, for a fixed radius, only the swimmer with α_D larger than a ‘critical dipole strength’ will get trapped around the sphere. (c) The concept of the basin of attraction [127]: the swimmer whose initial location is marked by a circle (resp. square) and whose trajectory is shown by a solid line (resp. by a dashed line), starts inside (resp. outside) the basin of hydrodynamic attraction, and thus it gets trapped onto (resp. escapes) the surface. The swimmers’ initial orientation, $\mathbf{p}(0) = \mathbf{e}_X$. It is important to note that the basin of attraction is defined only in cases when hydrodynamic trapping is ensured.

Thus, a bacterium located far away from the source can get attracted to, and even trapped onto, it via the following sequence of events: (i) chemotaxis, i.e., biased tumbling causing the bacterium to come within 2-3 body lengths from the source, followed by (ii) hydrodynamic attraction on account of the theory detailed in Sections 4.2.1 and 4.2.3. Once the bacterium reaches the nutrient, its behavior is governed by the interplay of: (i) hydrodynamics, (ii) hard-core repulsion, and (iii) rotary diffusion. The interaction between the first two may result in the trapping of the microorganism, depending on its dipole strength and the radius of the source. If the radius is larger than the critical trapping radius (corresponding to the bacterium's dipole strength), then the bacterium will be trapped at the surface—due to a balance between hydrodynamic attraction and hard-core repulsion—and will orbit around the source. The third effect contributes toward probable escape of any bacterium that would get trapped onto the surface based purely on hydrodynamics. The escape can occur due to a reorientation that turns the bacterium to an extent that $(\mathbf{u}_{HI} + V_s \mathbf{p}) \cdot \hat{\mathbf{r}} > 0$ (see equation 4.17), thus allowing it to swim away from the surface. This three-way coupling has been explained schematically in Fig. 4.3, and discussed in greater detail in ref. [64, 127]. Note also that rotary diffusion causing escape (for a variety of microorganisms) from solid surfaces has been observed experimentally in ref. [17, 109, 164].

Quantitatively, it suffices to remember that hydrodynamic trapping is most favored for high values of α_D and low values of D . This is because large α_D results in stronger hydrodynamic attraction, and small D reduces the influence of rotary diffusion. We further explain this idea in the next Section. Table 4.1 summarizes the influence of the mechanisms discussed above, on the fate of a microorganism located initially at some arbitrary distance from the source, and oriented along any arbitrary direction. Fig. 4.4 shows typical trajectories and provides an understanding of microorganism distribution around the source for the case of strong and weak chemotaxis; in the subsequent sections we quantify these results.

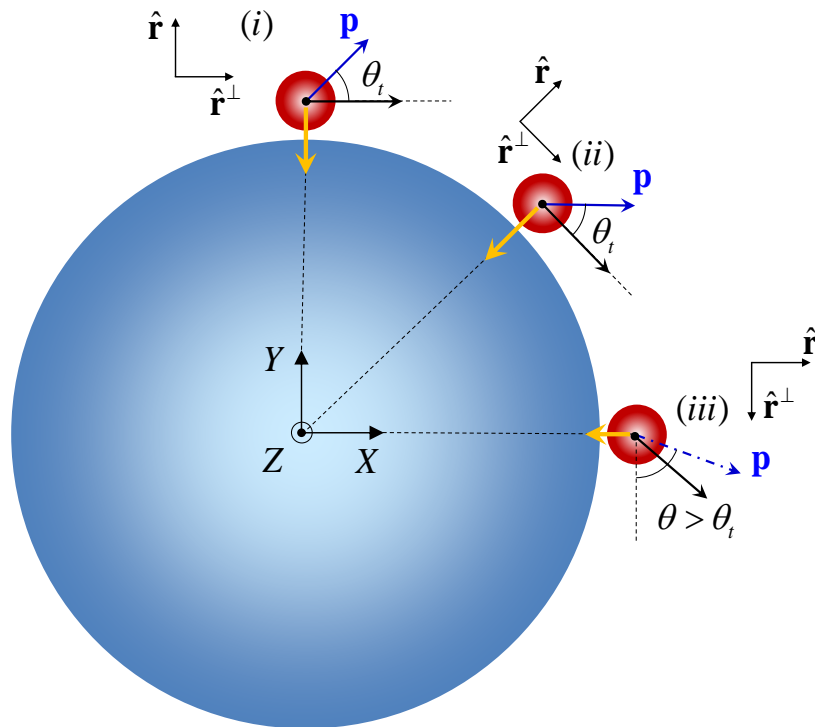


Figure 4.3. : (Color online) An illustration of the effect of hydrodynamics on the motion of the microorganism as it gets trapped onto the surface of the nutrient source. The thin blue arrows are the microorganism's intrinsic motility $V_s \mathbf{p}$, the thick orange arrows are the hydrodynamic component of microorganism's motion toward the center of the nutrient ($\mathbf{u}_{HI} \cdot \hat{\mathbf{r}}$), and the black arrows are the instantaneous velocity $d\mathbf{x}_2/dt$ (eqn. 4.17). (i-ii) Hydrodynamics—if strong enough—rotates the microorganism such that it always maintains a constant separation $h_t (\approx 1)$ and in-plane angle θ_t , and such that $(\mathbf{u}_{HI} + V_s \mathbf{p}) \cdot \hat{\mathbf{r}} \leq 0$. As a result, the microorganism swims tangentially along the surface and stays trapped. (iii) Rotary diffusion—if significant—can cause the microorganism to rotate to an in-plane angle greater than θ_t which reduces the hydrodynamic attraction, causes $(\mathbf{u}_{HI} + V_s \mathbf{p}) \cdot \hat{\mathbf{r}} > 0$, and thus leads to escape.

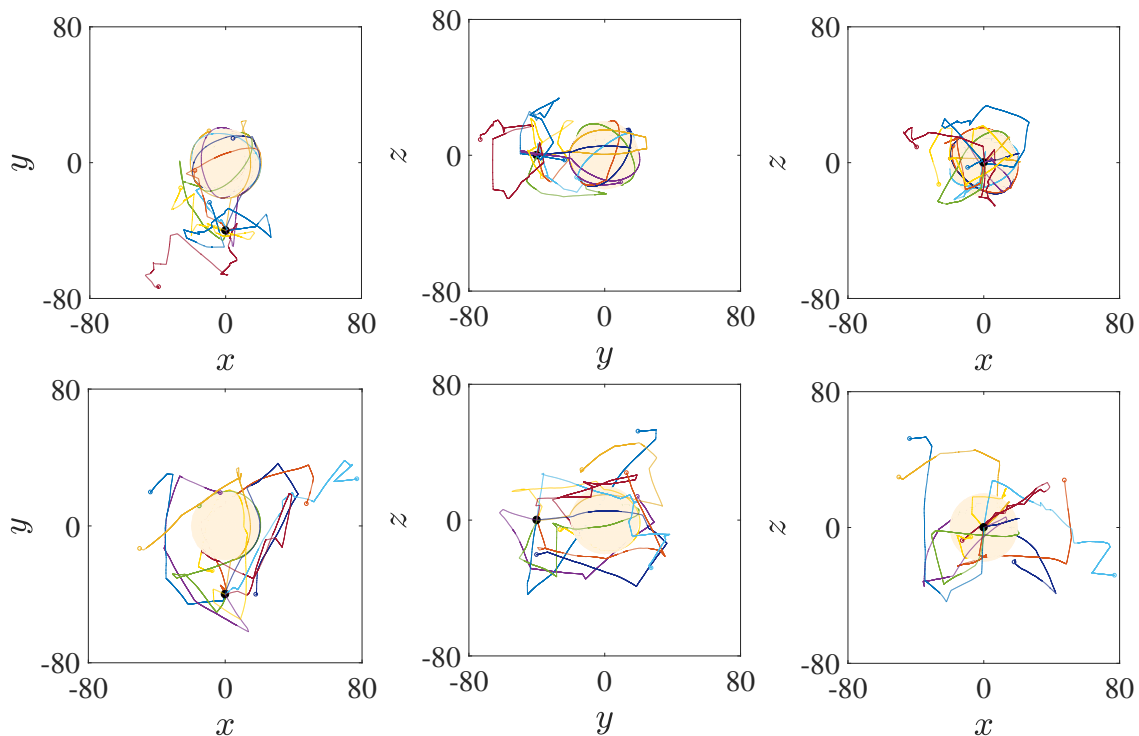


Figure 4.4. : (Color online) A schematic of the effect of chemotaxis strength on the accumulation around the nutrient source. The left, central and right columns show the x - y , y - z and x - z projections, respectively, of the microorganisms' trajectories. The microorganisms are located initially at $(x(0), y(0), z(0)) = (0, -40, 0)$, and oriented arbitrarily. It is important to note that in the absence of chemotaxis, most of the microorganisms would just 'swim away' from the source without appreciably changing their orientations. The upper (resp. lower) row represents strong (resp. weak) chemotaxis, which could either be due to $C_0/K_D = 1.0$ (resp. $C_0/K_D \ll 1.0$), or a small (resp. large) value of τ^* . Clearly, strong (resp. weak) chemotaxis leads to the microorganisms being, in general, closer to (resp. further from) the nutrient.

4.3.2 Types of behaviors

Fig. 4.5 provides us with an intuition about the different physical mechanisms dictating microorganism attraction and entrapment onto nutrient sources. It contains

features of run-and-tumble chemotaxis as well as hydrodynamic trapping. We see that chemotaxis doesn't always succeed in bringing the microorganism to the source (red trajectory); or that chemotaxis can lead the microorganism close enough to the source but still outside its basin of attraction (blue trajectory). In the case shown by the magenta trajectory, we see how chemotaxis allows a microorganism to make 'contact' with the source but it later gets scattered instead of being trapped. Finally, we also see how chemotaxis and hydrodynamics enable the microorganism to make 'contact' with the source and then glide along its surface due to hydrodynamic entrapment (green trajectory). This rich variety of trajectories emerges due to an interplay involving varying strengths of one or all of the mechanisms detailed in Table 4.1. It is clear that the phenomena being investigated is very non-trivial in all its complexity. A better understanding can be obtained by first considering limiting values of certain parameters, and then moving on to more general parametric regimes. In particular, an understanding of the limiting scenarios $D \approx 0$ and/or $\alpha_D \approx 0$ is warranted. We will see that both these parameters play an important role in the extent of surface colonization C_s , and the nature of the distribution function $f(r)$.

4.3.3 Influence of the dipole strength α_D and the rotary diffusivity D

Fig. 4.6(a) shows the variation in C_s with α_D for $D \approx 0$ and $D = 7.5 \times 10^{-4}$. The corresponding bulk distributions $f(r)$ are shown in Fig. 4.6(b). The other parameters are kept at their baseline values, such that chemotactic approach is guaranteed in most cases. The bulk concentration is highest near the surface and reduces monotonically to zero as r increases. This shows that chemotaxis, on average, helps the microorganisms to locate nutrient rich regions in their surroundings.

We note that for $D \approx 0$, the response is binary, i.e., C_s is either ≈ 0.155 or ≈ 0.60 and $f(r)$ varies as one of the two discernible curves in the main plot of Fig. 4.6(b). This is because in the absence of orientational fluctuations, bacteria that enter the basin of attraction (through chemotaxis) behave deterministically: they either get

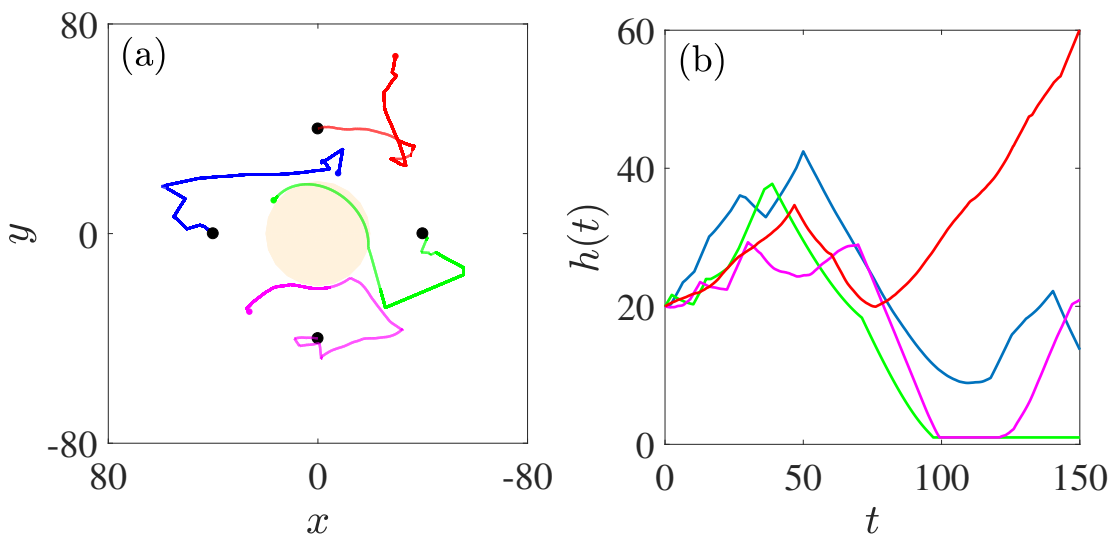


Figure 4.5. : (Color online) (a) Visualization of the different behaviors elicited by the mechanisms discussed in Table 4.1. The starting positions are shown by black dots. Red: this microorganism is unable to locate the source in the time for which the simulations were run. Blue: this microorganism ‘chemotaxes’ close enough to the source, but does not enter the basin of hydrodynamic attraction. Magenta: in this case, the microorganism does make contact with the source, but the hydrodynamic attraction is not strong enough for trapping to occur. Green: an example of a successful trapping wherein chemotaxis and hydrodynamics work in conjunction to bring and trap a microorganism onto the source. See main text for details about the regimes in which such behaviors occur. (b) The time evolution of the distance from the source, $h(t)$, of trajectories in panel (a).

trapped or they escape. For a given size of the source ($A = 20$ in all our results), the type of behavior—both qualitative *and* quantitative—depends only on the value of α_D : (i) for large enough α_D , a majority of microorganisms get trapped at $r \approx 20$; while, (ii) for smaller α_D , a majority is distributed in the bulk fluid (recall Fig. 4.2(b)). This behavior can be understood by considering the dependence of hydrodynamic interactions on the dipole strength and on the distance of the microorganism from

the source. At large distances, hydrodynamics has a negligible impact on reorienting the bacteria, and they behave more or less similarly, irrespective of their α_D values. However, once inside the basin, the fate of a bacterium (trap or escape) depends acutely on α_D ; and for a given size A , any bacterium with α_D above (resp. below) a critical value gets hydrodynamically trapped (resp. escapes). In fact, for a fixed A , purely hydrodynamics based trapping occurs above a critical $\alpha_D \geq 8/(3A^{1/2})$ [127]. Therefore, for $A = 20$, trapping should occur for $\alpha_D \geq 0.65$, as evident in Fig. 4.6. Even then, the randomness of the initial approach means that $C_s < 1$, i.e., not all microorganisms get trapped (recall the red and the blue trajectories in Fig. 4.5).

Another feature of the results in this Section is that higher C_s values imply a lower average value of $f(r)$. This allows us to identify the regions where most of the microorganisms accumulate. In all scenarios when $C_s < 0.2$, the nature of $f(r)$ is such that $\int_A^{2A} 4\pi r^2 f(r) dr \approx 0.5$. This can be interpreted as an ‘off-surface’ accumulation. It occurs due to an efficient chemotactic approach combined with weak hydrodynamic attraction; causing most microorganisms to gather within one (source) radius from the surface.

As a microorganism with $\alpha_D \geq 0.65$ comes in contact with the source, it begins to travel along the surface due to the mechanisms explained in Fig. 4.3. The only mechanism that can get such a trapped microorganism to escape is its own rotary diffusivity. This idea was explained schematically in Fig. 4.3 and an example of such an escape can be seen in the magenta trajectory of Fig. 4.5. Fig. 4.6(a) shows (blue line marked with squares) the variation of C_s with α_D for $D = 7.5 \times 10^{-4}$. It can be seen that rotary diffusivity markedly affects the tendency of the microorganism to accumulate at the surface and consequently, results in more microorganisms in the fluid surrounding the source (inset in Fig. 4.6(b)). For example, for $\alpha_D = 0.7$ there is $\approx 60\%$ reduction (resp. increment) in surface colonization (resp. average bulk distribution) for a modest rotary diffusivity. As the strength of hydrodynamic attraction grows (α_D increases) a greater fraction of the microorganisms get trapped at the surface, in spite of orientational fluctuations. Therefore, the near-field hydrody-

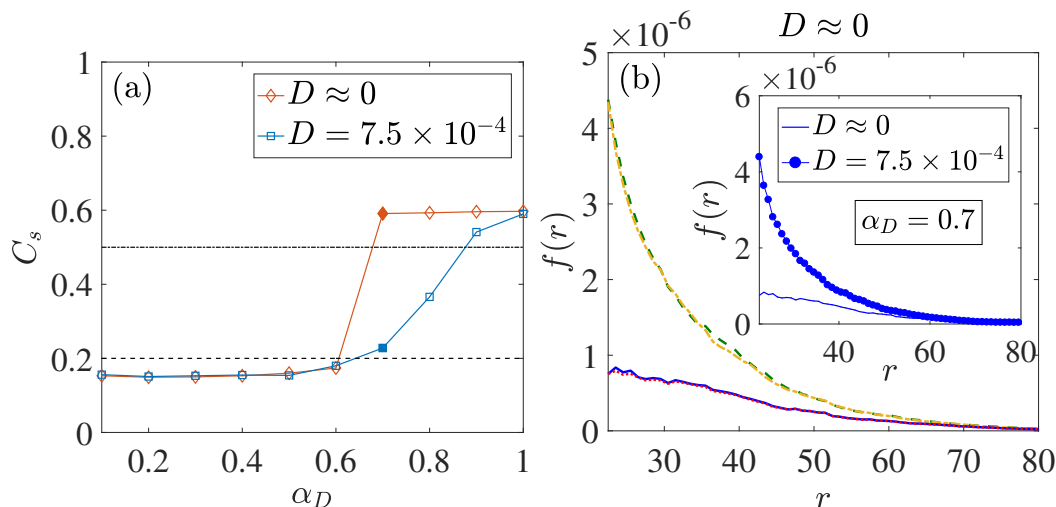


Figure 4.6. : (Color online) (a) Variation of the surface concentration, C_s , with the dipole strength α_D for $D \approx 0$ (negligible rotary diffusion), and $D = 7.5 \times 10^{-4}$ (moderate rotary diffusion). (b) Main figure: The distribution $f(r)$ for $D \approx 0$, and $\alpha_D = 0.1$ (green dashed line), $\alpha_D = 0.6$ (orange dash-dotted line), $\alpha_D = 0.7$ (blue solid line), $\alpha_D = 1.0$ (red dotted line). Inset: The distribution $f(r)$ for $\alpha_D = 0.7$ for $D \approx 0$ and 7.5×10^{-4} (corresponding surface concentrations are shown in panel (a) by filled symbols). Notice the drastic difference in the values of C_s and $f(r)$ for the two different values of rotary diffusivities.

dynamic attraction acts as a crucial mechanism that allows microorganisms to colonize nutrient sources.

Finally, whenever hydrodynamic attraction is weak ($\alpha_D < 0.65$), the rotary diffusivity does not affect the surface concentration at all (values of C_s for $D \approx 0$ and $D > 0$ are coincident for $\alpha_D < 0.65$, for a wide range of D). This is understandable because if hydrodynamic interactions are weak, the microorganism just doesn't rotate fast enough to stay trapped onto the surface, and thus its escape is guaranteed regardless of other influences (see Fig. 4.3). The very weak dependence on D comes from the fact that far away from the source—where the microorganisms predominantly reside—orientational changes due to rotary diffusivity are negligible as

compared to those due to a tumble; as also seen for collective motion of active suspensions [188]. Fig. 4.10 in the Appendix shows that the bulk distributions are also practically identical in this case.

4.3.4 Variability in chemotactic factors: C_0/K_D and τ^*

In Section 4.3.3, we saw the importance of hydrodynamics in trapping chemotactic microorganisms onto the source. We also explained how rotary diffusivity of the microorganisms reduces surface colonization. The main question that we aim to answer in this Section is: how does chemotaxis-based initial approach affect the colonization of nutrient sources by bacteria? There are two factors that we need to consider: (i) nutrient availability in the form of a prescribed background concentration, and, (ii) the microorganism's intrinsic response to gradients in nutrient concentration. The nutrient availability—which is an environmental factor—is quantified by the ratio C_0/K_D . Thus, it could be an indication of the actual concentration of a given chemoattractant at the source (e.g., the amount of soluble hydrocarbons in a drop of crude oil), or the affinity of the chemoreceptor to the chemoattractant [79]. The intrinsic chemotactic response—which is a motility trait of individual bacteria—depends on the mean tumbling frequency τ_0^{-1} .

Does greater nutrient availability enhance the colonization of nutrient sources by bacteria? Fig. 4.7(a) shows that this is not necessarily the case, irrespective of the hydrodynamic influences. The C_s vs. C_0/K_D trend for all combinations (high/low) of α_D and D is the same: an approximately two-fold initial increase, followed by little change for a wide range of C_0/K_D , and then a reduction. There isn't much difference in the surface concentration (and the bulk distribution; see Fig. 4.8(a)) between $C_0/K_D = 0.1, 1.0, 10.0$. This behavior is explained by the scaling of the run-time τ with C_0/K_D , which can be easily assessed by examining equation 4.16. If $C_0 \ll K_D$, then $\tau/\tau_0 \sim \exp(DC/Dt)$; if $C_0 \sim K_D$, then $\tau/\tau_0 \sim \exp(C^{-1}DC/Dt)$; and if $C_0 \gg K_D$, then $\tau/\tau_0 \sim \exp(C^{-2}DC/Dt)$ [41]. This means that higher nutrient availability

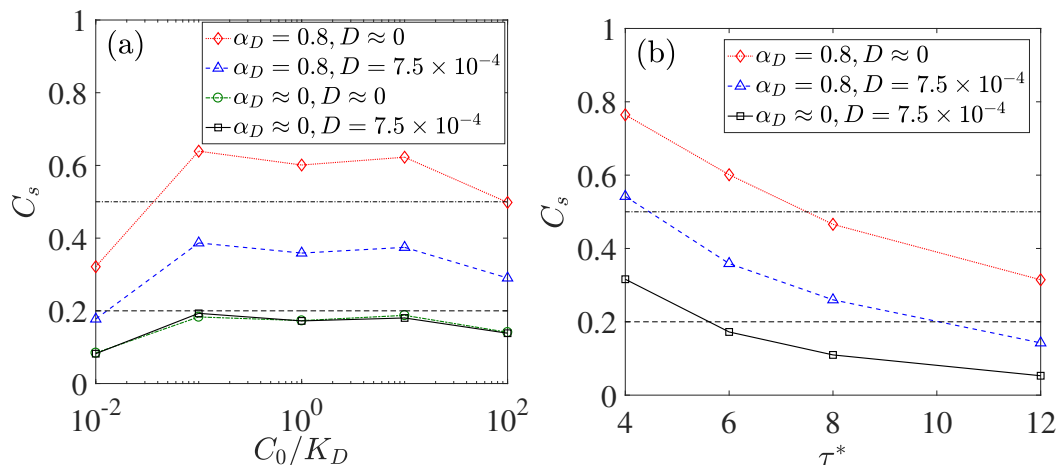


Figure 4.7. : (Color online) Variation of the surface concentration C_s with (a) C_0/K_D , and, (b) τ^* . In each case, C_s is highest when $\alpha_D > 0.65$ and D is negligible, as expected based on the discussion in Section 4.3.3. Also, the results are independent of D for $\alpha_D \approx 0$. For small τ^* , C_s varies almost linearly with τ^* .

doesn't always result in a proportionate increase in the run-time τ in nutrient-rich regions, and so, it doesn't necessarily translate to improved chemotactic performance. In fact, if C_0/K_D is increased even further to 100.0, then we observe a decline in C_s as compared to the previous three cases, due to the dominant contribution of the C^{-2} term, as described above. Physically, $C_0 \ll K_D$ would mean that the ambient nutrient concentration is not high enough to prompt rapid chemotaxis, while the other extreme $C_0 \gg K_D$ is equivalent to a nutrient abundance that makes 'chemotactic foraging' unnecessary.

The chemotactic response of bacteria is much more sensitive to τ^* (dimensionless run time), than it is to C_0/K_D . The variation of C_s with respect to τ^* is monotonic, and bacteria with lower mean run-lengths are much more effective in colonizing nutrient sources. Fig. 4.7(b) shows that surface colonization can be as high as 80 % for $\tau^* = 4$. The green trajectory of Fig. 4.5 is a good example of such strong surface colonization, wherein chemotaxis enables the microorganism to make contact with the

source and strong hydrodynamic attraction keeps it trapped at the surface. Owing to their random initial orientations, it is essential for the distant bacteria to tumble more frequently in order to ‘locate’ the source. This is why bacteria with smaller τ^* values are able to orient themselves along ∇C —and ultimately enter the basin of hydrodynamic attraction—faster than those with larger τ^* , and high C_s values for the former are just a consequence of this rapid chemotactic response.

An inspection of Fig. 4.8 in the context of Fig. 4.7 enables us to draw useful conclusions about the bacterial distribution in the bulk for different values of C_0/K_D and τ^* . A general observation from Fig. 4.7 is that chemotaxis can be considered ‘strong’ (resp. ‘weak’) whenever $C_0/K_D \approx O(1)$ (resp. $C_0/K_D \ll 1$) and/or $\tau^* < 8$ (resp. $\tau^* > 8$). We see that the value of $f(r = 20)$ and the subsequent decline of $f(r)$ is much more gradual for weak chemotaxis (Fig. 4.8(a) and 4.8(c)), with $\int_A^{4A} 4\pi r^2 f(r) dr \approx 0.5$. This suggests insignificant accumulation at any particular location because the chemotactic bias isn’t strong enough. The curves for $C_0/K_D = 0.01, 100$ in Fig. 4.8(b), and for $\tau^* = 12$ in Fig. 4.8(d) exemplify the scenarios when hydrodynamic attraction is strong enough to promote surface-aggregation, but the initial approach toward the source is highly hindered. As opposed to all other cases, these distributions exhibit a gentle maximum at a distance $r \approx 30$. This is an interesting aspect of the present study: the existence of a ‘depletion zone’ in the bulk distribution of microorganism positions for all scenarios involving strong hydrodynamics and weak chemotaxis. In spite of the latter effect, some microorganisms *do* encounter the source and get trapped onto it; while others move in an almost random fashion. The depletion zone spatially demarcates these two extremes.

4.4 Conclusion

We formulated a mathematical model and performed probabilistic simulations to ascertain the distribution of microorganisms around a spherical nutrient source. The model was based on, and the distribution was mediated by, a combination of (i) hy-

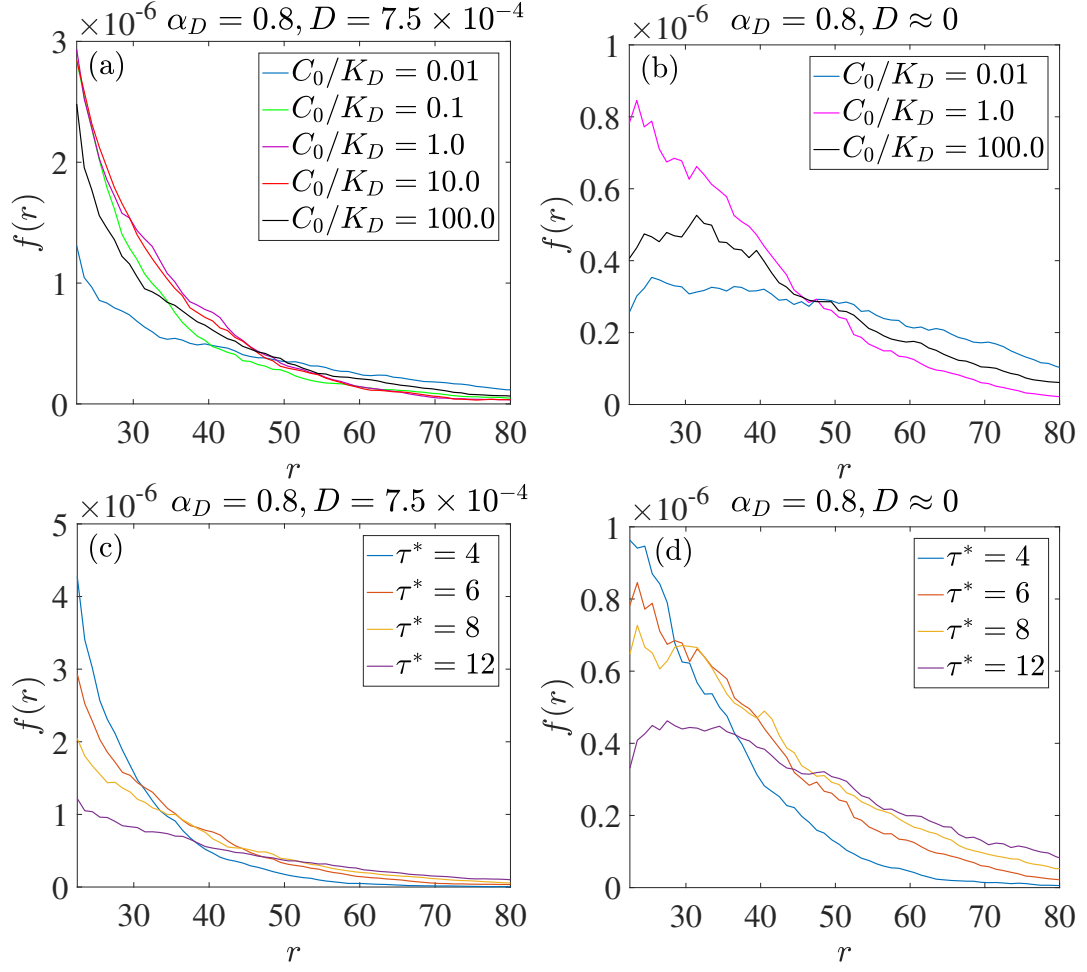


Figure 4.8. : (Color online) The bulk distribution $f(r)$ as a function of (a-b) C_0/K_D , and, (c-d) τ^* . Note the almost similar distributions for $C_0/K_D = 0.1, 1.0, 10.0$, just like the corresponding C_s values in Fig. 4.7. In conjunction with Fig. 4.7, it is evident how rotary diffusion causes more microorganisms to stay in the bulk. For weak chemotaxis, there is no appreciable accumulation anywhere in the bulk. $f(r)$ increases to a maximum and then decays to zero for weak chemotaxis in the panels (b) and (d). See main text for details.

drodynamic interaction (H.I.) with the source, and, (ii) chemotaxis (Ch.) toward the nutrient/chemoeffector emanating from the source. In our model, we assumed that hydrodynamic interactions and rotary diffusion dominate in the near-field of the nu-

trient source, while chemotaxis dominates when the microorganism is far away. This distinction stems from the fact that bacterial tumbling is hindered in the proximity of solid surfaces (thus precluding run-and-tumble chemotaxis and surface-escape via tumbling) [110], and so near surface bacterial behavior is governed by hydrodynamics in conjunction with rotary diffusion [109, 127, 164]. Hydrodynamic interactions can be strong or weak, depending on the value of the microorganism's dipole strength and the radius of the source. Chemotaxis too, can be strong or weak, depending on the microorganism's mean tumbling frequency, and the nutrient availability in its surroundings. Therefore, the distribution is affected by environmental (source size and nutrient availability) factors, as well as by the microorganism's intrinsic motility features (dipole strength, tumbling frequency, etc.). Although both hydrodynamics and chemotaxis attract a bacterium toward the source, their separate 'domains of influence' and relative strengths can lead to interesting changes in the spatial distribution of microorganisms around the surface from which the nutrient diffuses out into the environment. Towards this, we performed a systematic parametric study and revealed different surface colonization and bulk distribution features, highlighted in Fig. 4.9.

We see that stronger H.I. always leads to greater surface colonization (i.e., the quantity C_s), irrespective of the strength of the chemotactic influence. Similarly, stronger chemotaxis always leads to greater surface colonization, irrespective of the strength of the hydrodynamic influence. Understandably, C_s is greatest when both the influences are strong, because this scenario corresponds to a more effective 'initial approach' (toward the source) due to chemotaxis, followed by a strong hydrodynamic attraction. On the other hand, it is the least when both chemotaxis and H.I. are weak. The surface colonization is also not substantial ($C_s < 0.5$) whenever chemotaxis or H.I. is weak. Strong chemotaxis, but weak H.I. leads to an off-surface accumulation with majority of microorganisms collecting in the bulk within a distance of one (source) radius from the surface. Finally, we find an interesting bulk distribution for the case of weak chemotaxis and strong H.I., which leads to the formation of a de-

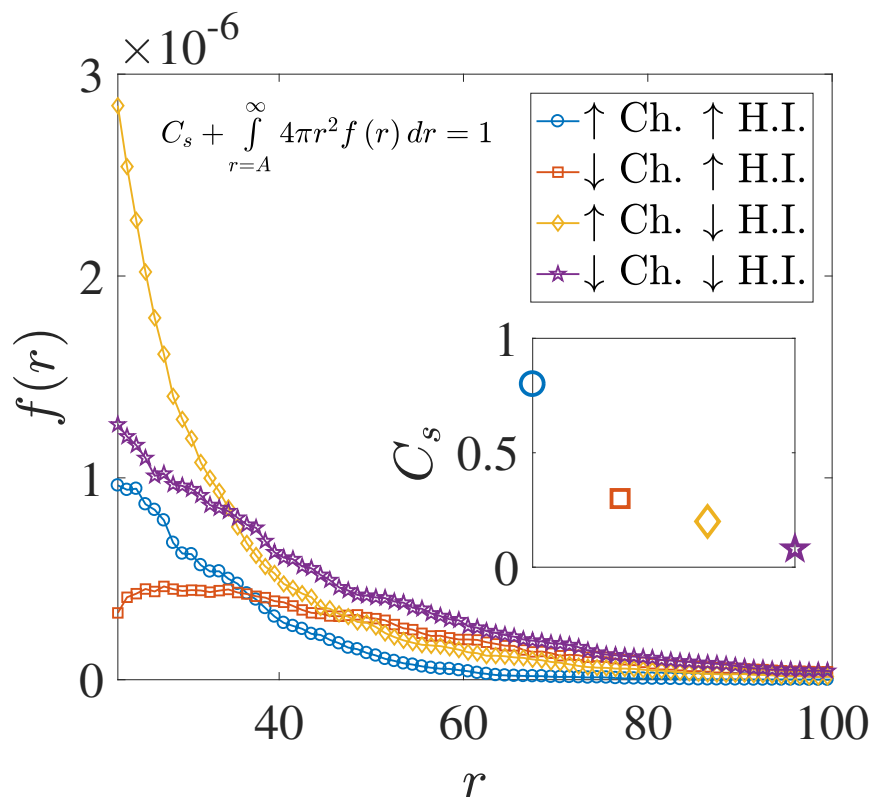


Figure 4.9. : (Color online) The four qualitatively different behaviors, or spatial distributions $f(r)$, that can be realized due to the combined influence of hydrodynamics (abbreviated in the legend as H.I.) and chemotaxis (abbreviated in the legend as Ch.) on the locomotion of microorganisms around a spherical nutrient source. \uparrow (resp. \downarrow) denotes a strong (resp. weak) influence. The inset shows the surface colonization C_s for each of the four behaviors, with correspondence based on marker type.

pletion zone in the microorganism distribution, characterized by a gentle maximum in the value of $f(r)$ at $r \approx 30$. This is because weak chemotaxis does not enable enough bacteria to come close to the source, but those that do come close enough, get trapped due to strong hydrodynamic attraction. These sufficiently general trends help establish the importance of chemotaxis and hydrodynamics in our problem. From them, we conclude that strong chemotaxis is essential to obtain greater aggregation of microorganisms near nutrient sources, and strong hydrodynamic interactions enable

surface colonization. In addition to these generalities, we also find that higher nutrient availability—reflected in the value of the dimensionless parameter C_0/K_D —doesn't lead to proportionate increase in surface colonization (see Fig. 4.7(a)). This is because the bacterium's run-length τ depends on both its ambient nutrient concentration, C , and the instantaneous rate at which this concentration changes, DC/Dt , via eqn. 4.16. However, strong chemotaxis on account of lesser mean run time τ_0 is much more effective in enhancing the surface colonization (see Fig. 4.7(b)). In this way, our study yields a qualitative and quantitative insight into the process of bacterial attraction to, and aggregation around, nutrient sources under the combined influence of the two major factors dictating microorganism locomotion: passive response via hydrodynamics and active response via chemotaxis.

An important assumption in our study is that tumbling, and hence chemotaxis, is suppressed when the bacterium is at a distance less than or equal to two body-lengths from the source. The basis of this assumption is the experimental work by Molaei *et al.* which confirmed tumbling suppression near rigid walls [110,187]. In addition, we use the model proposed by Brown and Berg to incorporate bacterial chemotaxis [41], and neglect any 'memory effects' when calculating the run time in presence of a chemoeffector (see equation 4.16). We emphasize that the finer aspects of chemotaxis can be easily incorporated into our study, like tumbling anisotropy enforced due to proximity to surfaces and/or due to altogether different foraging tactics like reversals and flicks. It would be interesting to see the extent to which these influences affect the results of our study. Equally interesting is the possibility of studying hydrodynamic interactions between microorganisms in the semi-dilute regime, and how it would affect their spatial distribution around nutrient sources. A more complex mathematical model—one which includes some, or all, of the aforementioned effects—would require experiments to ascertain tumbling alteration close to curved surfaces, and predict bacterial re-orientations differing from the archetypal tumble. The present study improves our understanding of bacterial colonization of surfaces, and is expected to

have far reaching consequences in bioremediation, selective microorganism capture, lab-on-a-chip assays and investigations on bacteria in porous media.

4.5 Appendix

In Fig. 4.7 we saw that rotary diffusivity has no effect on the surface colonization when hydrodynamic effects are negligible, i.e., $\alpha_D \approx 0$. Fig. 4.10 shows that even the bulk distribution is not affected significantly in this case. This is because for $\alpha_D \approx 0$, the microorganisms execute a biased random walk and get reflected from the surface irrespective of the magnitude of rotary diffusion, as explained in Section 4.3.3.

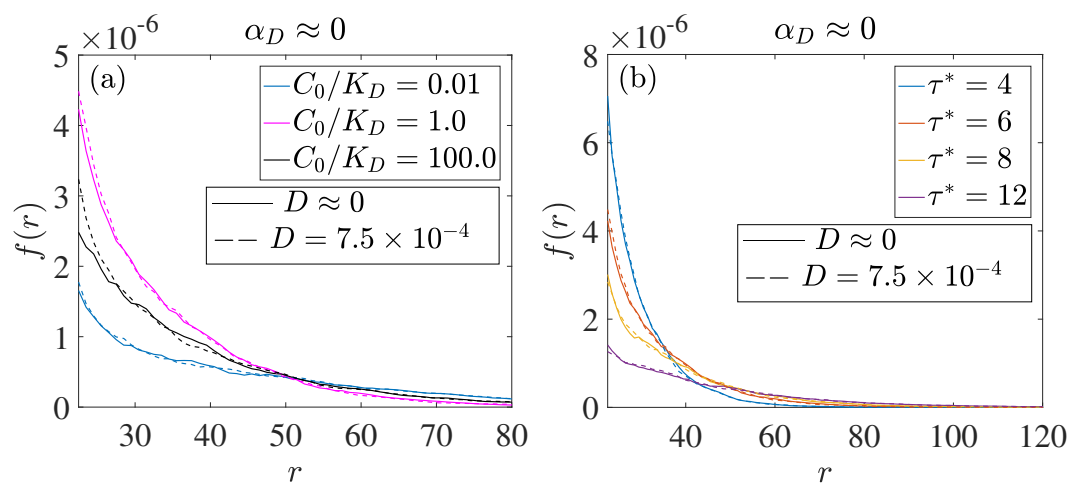


Figure 4.10. : (Color online) The bulk distribution $f(r)$ as a function of (a) C_0/K_D , and, (b) τ^* , for negligibly small hydrodynamic attraction ($\alpha_D \approx 0$) and $D \approx 0$, $D = 7.5 \times 10^{-4}$.

In Section 4.2.2 we mentioned that the effect of rotary diffusion as given by eqn. 4.8 is strictly correct only if the rotary diffusion tensor—say $\mathbf{D}_{\mathbf{R}}$ —is isotropic, i.e., when $\mathbf{D}_{\mathbf{R}} = D_r \mathbf{I}$. In reality, the presence of a surface and the approach of bacterium to the spherical source imparts anisotropy and time dependence, respectively, to $\mathbf{D}_{\mathbf{R}}$. The stochastic effects become considerably involved when the diffusivities evolve with time (see eqns. (13) and (14) in ref. [179]). However, in our problem, fluctuations in

the bacterial orientation are only important in the near-field, i.e., when a bacterium orbits around the source (see Fig. 4.5, Table 4.1 and the discussion in the last paragraph of Section 4.3.3 in relation to Fig. 4.6(a) and Fig. 4.10). Also, the change in $\|\mathbf{D}_R\|$ for a sphere is most significant when it is very close to a solid wall [189–191]. In fact, using the mobility expressions given by Cichocki and Jones [190] we can estimate that $\|\mathbf{D}_R\|$ is halved when a sphere almost makes contact with the wall (assuming, of course, that their results can be reasonably used for our configuration of two spheres—the source and the bacterium—because $R/b \gg 1$). Therefore, the D_r in eqn. 4.8 can be considered as the ‘reduced’ rotary diffusivity due to close proximity to a surface. In other words, if the rotary diffusivity in the unbounded fluid is D_{r0} , then that near the source will be $D_r = kD_{r0}$, where $k \approx 1/2$. Note that using two different values of D_r :

$$D_r = \begin{cases} D_{r0}, & |\mathbf{x}_2| \gg (R + b) \\ \frac{D_{r0}}{2}, & |\mathbf{x}_2| \approx (R + b) \end{cases}, \quad (4.19)$$

instead of using only $D_r = (D_{r0}/2)$ everywhere in the domain, will not change our results appreciably, once again because of the near-field significance of rotary diffusion (see Fig. 4.11).

The methodology outlined in Section 4.2 also enables us to compute the distribution of microorganisms around more general surfaces, for example, that near fluid-fluid interfaces. The fundamental difference in this case is that the boundary conditions change from those given in eqn. 4.3, to the more general form of continuity of fluid velocity and stress [11]. As a result, for microorganism motion around clean drops, the viscosity ratio of the drop with respect to the suspending fluid—denoted by λ —appears as an extra parameter that can dictate the distribution function $f(r)$. This change is reflected in the expressions for \mathbf{u}_{HI} and $\mathbf{\Omega}_{HI}$, which were derived recently by Shaik and Ardekani [134]. If we assume that the near field hydrodynamic and tumbling characteristics remain the same as those in Section 4.2.3, and that the microorganism does not simply adsorb onto the drop’s surface, we can estimate the distribution of chemotactic bacteria around drops as well. Fig. 4.12 shows the spatial

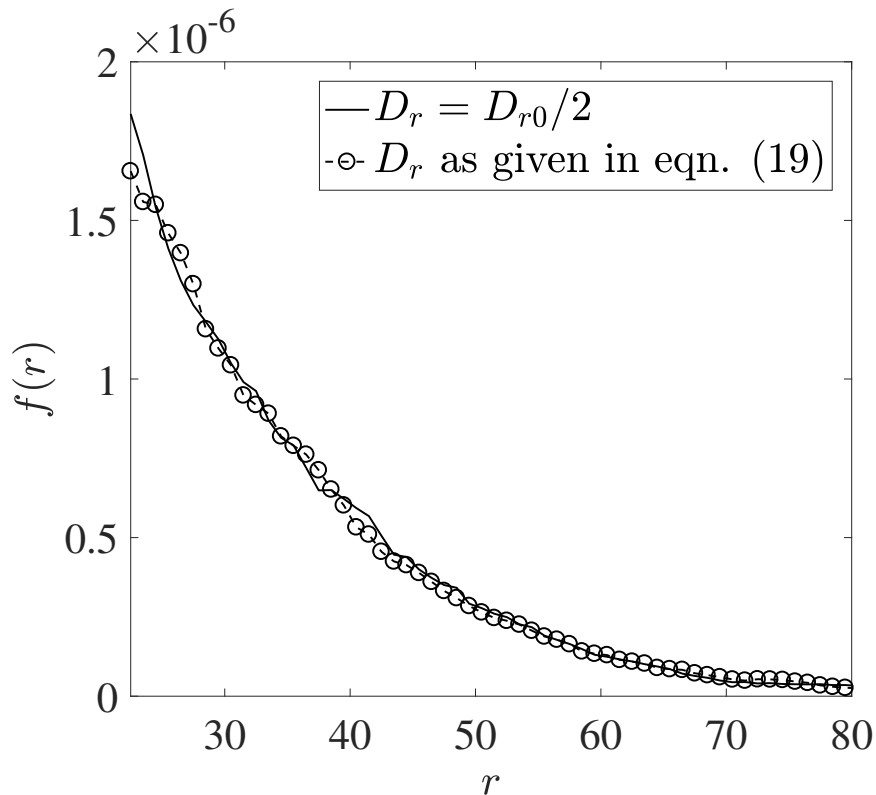


Figure 4.11. : (Color online) The bulk distribution $f(r)$ for two different cases: (i) when the value of D_r in eqn. 4.8 is taken to be half of the rotary diffusivity in an unbounded fluid, D_{r0} , in the *entire* domain (solid line), and, (ii) when eqn. 4.19 is used to assign bacterial rotary diffusivities based on separation of the microorganism from the source (dashed line marked with circles). The surface colonization values are within 1.25% of each other. The value of the dimensionless rotary diffusivity in unbounded fluid is 7.5×10^{-4} , i.e., $D_{r0}b/V_s = 7.5 \times 10^{-4}$.

distribution of chemotactic microorganisms around a stationary drop with viscosity ratio 10, which is indicative of crude oil [192]. The distribution is almost the same as that around a rigid, spherical nutrient source (limiting case of $\lambda \rightarrow \infty$); thus suggesting the utility of our results in the analysis of biodegradation of hydrocarbon effusing crude oil drops.

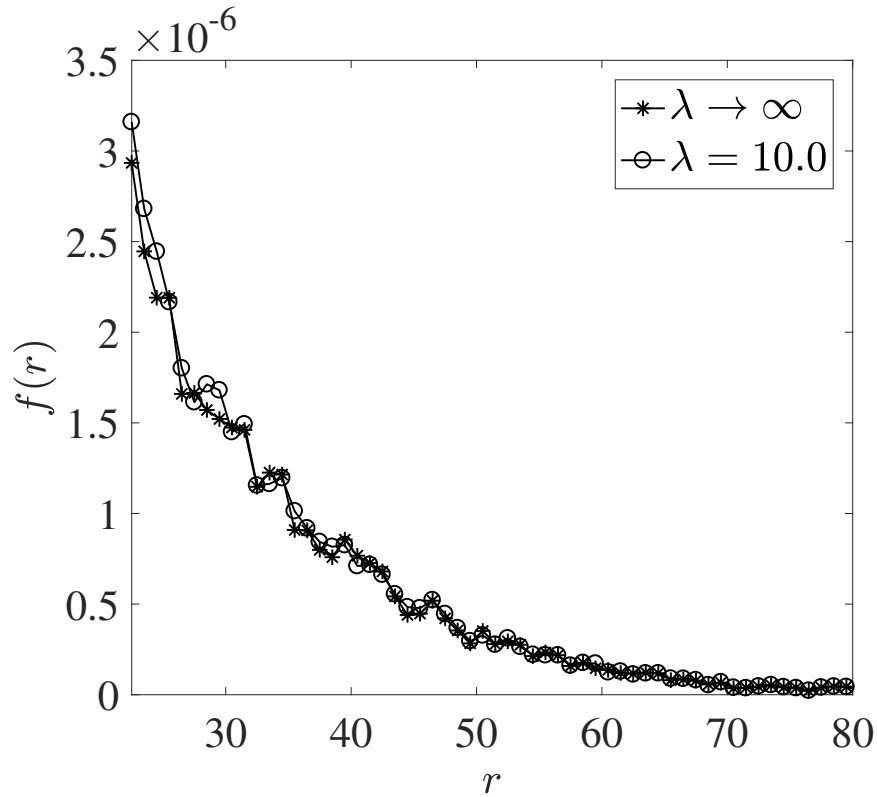


Figure 4.12. : Comparison of the bulk distribution $f(r)$ for combined chemotactic and hydrodynamic attraction to (i) a rigid sphere (asterisks), and, (ii) a clean drop with viscosity ratio $\lambda = 10$ corresponding to crude oil (circles), for the baseline simulation parameters given in Section 4.3.1. The difference between the two cases is not very significant. The surface colonization for the rigid sphere ($C_{s,\text{rigid}} = 0.3589$) is 4 % larger than that for the drop ($C_{s,\text{drop}} = 0.3446$). For motion around the drop, the hydrodynamics induced linear and angular velocities are taken from ref. [134].

5. HYDRODYNAMIC INTERACTION ENHANCES COLONIZATION OF SINKING NUTRIENT SOURCES BY MOTILE MICROORGANISMS

5.1 Introduction

Chemotaxis—the directed motion of bacteria along favorable gradients in chemical concentration—is one of the primary mechanisms through which marine bacteria locate nutrition, from sources like phytoplankton, marine snow and oil drops [6]. In the past, researchers have studied how chemotaxis helps in the colonization of settling particles [193], and of the nutrient plumes that trail these particles [166, 167, 194]. Besides, chemotaxis is also vital in following nutrient sources with inherent motility, e.g., the tracking of the motile algae *Pavlova lutheri* by the marine bacteria *Pseudoalteromonas haloplanktis* [174]. Bacteria utilize a number of strategies, like ‘run-and-tumble’ or ‘run-reverse-flick’, to bias their motion to chemical cues, and find and populate nutrient-rich regions in their environment [5, 39, 51, 194]. These strategies are actively regulated on the level of an individual cell, via chemosensing, i.e., feedback mechanisms involving membrane receptors and intracellular signals [37].

In addition to external chemical cues, microorganism locomotion is also affected by the ambient fluid flow. Microorganisms are translated and rotated by background flows and they undergo changes in their swimming motion by ‘interacting hydrodynamically’ with their surroundings [8, 195]. As a bacterium swims, its appendages disturb the fluid around it, setting up a flow. The presence of bounding surfaces and/or obstacles—especially within a few body-lengths from the bacterium—affects

⁰This chapter has been reprinted with minor changes, with permission, from the material as it appears in the article “*Hydrodynamic Interaction Enhances Colonization of Sinking Nutrient Sources by Motile Microorganisms*”, by N. Desai, V. A. Shaik and A. M. Ardekani, *Frontiers in Microbiology*, vol. **10**, article 289, 2018 (DOI: 10.3389/fmicb.2019.00289). Copyright (2019) of Desai, Shaik and Ardekani.

this flow, which in turn affects the motion of the microorganism itself. This mechanism, wherein an alteration of the fluid flow around a microorganism—due to nearby surfaces/interfaces, or even other microorganisms—changes its motion, is called a hydrodynamic interaction. Hydrodynamic interactions have been used to successfully describe a number of non-trivial phenomena, like the circular trajectories of *E. coli* in the vicinity of plane walls [20,107] and air-fluid or fluid-fluid interfaces [23,24,147]; the tendency of microorganisms to be attracted to and accumulate near walls [21,196]; the enhanced residence time of bacteria and microswimmers near plane and curved solid surfaces [17,125,127]. Examination of the flow fields around bacteria reveals that hydrodynamic interactions are most important at *small* cell-surface separations [17], which suggests that they can affect the trajectories of bacteria that encounter sinking particles either by chance or through chemotaxis.

The influence of near-surface hydrodynamic interactions on foraging by marine bacteria is thus an interesting topic, which has not been considered in detail in prior studies on chemotaxis toward settling particles. Recently, Desai and Ardekani analyzed the influence of hydrodynamic interactions in the motion and distribution of chemotactic bacteria around stationary, spherical nutrient sources, and concluded that hydrodynamic interactions greatly assist in the colonization of nutrient sources [64]. This significance of hydrodynamic interactions in the accumulation around fixed nutrient sources motivates us to examine the combined effects of hydrodynamic interactions and chemotaxis on the distribution of marine microbes around moving (due to gravity) nutrient sources. Our study is particularly relevant in the context of microbial colonization of sinking marine snow particles, and of rising oil drops emanating from natural or anthropogenic oil spills [3]. We wish to identify the factors affecting a bacterium's average nutrient exposure under these conditions. This is pivotal in determining the overall uptake rates by marine bacteria and the subsequent microbiological processes dictating bacterial populations in particular, and the marine biogeochemistry in general [197]. We formulate, and solve, a mathematical model which incorporates the essential features of the mechanisms governing bacterial

motion: (i) run-and-tumble chemotaxis toward a nutrient/chemoattractant emanating from a spherical, sinking nutrient source (e.g., an aggregate like marine snow), (ii) fluid flow caused by the source, and, (iii) hydrodynamic interactions caused by proximity to the nutrient source (a rigid obstacle). We emphasize here that the first response is an active motility trait of most bacteria, and the latter two are passive, i.e., driven solely by hydrodynamics. While the chemotactic response may be specific to bacterial species, the hydrodynamic effects are more generally valid. Through our analysis, we identify the effect of hydrodynamic interactions on the average nutrient exposure of marine bacteria swimming close to sinking nutrient sources. We quantify it as a function of important environmental (size of nutrient source and the diffusivity of the nutrient) and biological factors (mean run-time of the bacterium and magnitude of the force its appendages exert on the surrounding fluid).

5.2 Influence of Hydrodynamics and Chemotaxis

We consider a spherical aggregate or marine snow particle of radius a (shown in Fig. 5.1), which also acts as the source of a chemoattractant/nutrient, sinking under the influence of gravity with a force $\mathbf{F}_{ext} = \Delta\rho V_p \mathbf{g}$ acting on it; where, $\Delta\rho$ is the excess density of marine snow [ranging from 10^{-5} g/cm³ to 10^{-3} g/cm³; [198]], $V_p = \frac{4}{3}\pi a^3$ is its volume and \mathbf{g} is the acceleration due to gravity. The nutrient diffusing out of the source is carried by the fluid and forms a downstream plume as shown. At a position \mathbf{x}_2 with respect to the center of this particle, lies a microorganism of size b . The fluid flow is affected by both the sinking particle and the microorganism. The presence of the particle is expected to affect the swimming motion of the microorganism through hydrodynamic interactions, and vice-versa. As the aggregate sinks, it encounters bacteria either because they lie in its path, or because they are attracted, via chemotaxis, to its surface. Once the bacterium-aggregate separation reduces to within a few bacterial body-lengths, chemotaxis becomes less important and hydrodynamic interactions become significant. On the other hand, bacterial motion *far*

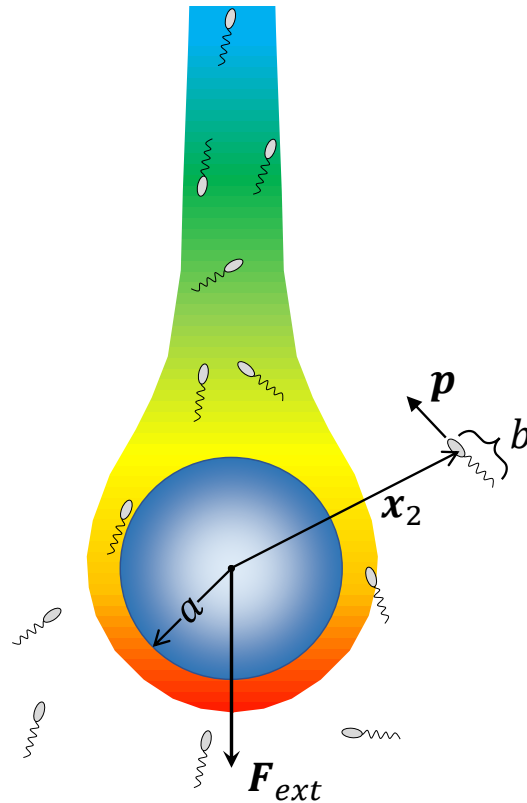


Figure 5.1. : A schematic of the problem being solved. A marine snow aggregate of radius a sinks under the influence of an external force (gravity) \mathbf{F}_{ext} . A chemoattractant emanates from the surface of marine snow, and forms a plume ‘behind’ the marine snow. We consider a system of N_b bacteria (of size b) that are not interacting with each other but can perform chemotaxis toward nutrient hot-spots (the concentration boundary layer and the plume around the aggregate), and interact hydrodynamically with the aggregate upon encountering it. We consider the motion of each bacterium by simulating its trajectory, i.e., the time evolution of its position with respect to the aggregate \mathbf{x}_2 , and its orientation \mathbf{p} , as dictated by hydrodynamic and chemotactic effects.

from the marine snow is affected primarily by chemotaxis. We, thus, first consider the motion of bacteria due to hydrodynamics and chemotaxis separately, and then get the complete description obtained by combining the two effects.

5.2.1 Bacterium as a force dipole

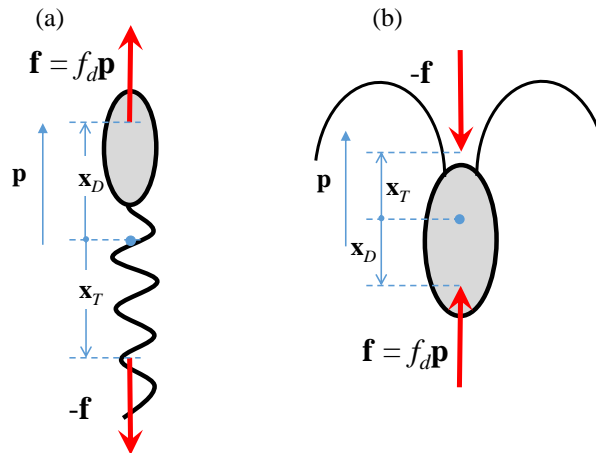


Figure 5.2. : The drag, $f_d \mathbf{p}$, and thrust, $-\mathbf{f}$, exerted by a (a) pusher, and, (b) puller, on the surrounding fluid. \mathbf{p} is the direction in which the microorganism swims in an unbounded, quiescent fluid.

Fig. 5.1 shows the bacterium's location \mathbf{x}_2 with respect to the center of the marine snow, and its orientation \mathbf{p} . These govern the bacterium's trajectory and evolve in time according to

$$\frac{d\mathbf{x}_2}{dt} = \mathbf{u}_{HI} - \mathbf{U}_p + V_s \mathbf{p}, \quad \frac{d\mathbf{p}}{dt} = \boldsymbol{\Omega}_{HI} \times \mathbf{p}, \quad (5.1)$$

where \mathbf{u}_{HI} and $\boldsymbol{\Omega}_{HI}$ are the hydrodynamically induced linear and angular velocities of the bacterium, respectively; \mathbf{U}_p is the velocity of the marine snow particle; and V_s is the swimming speed of the bacterium. Eqn. 5.1 shows that in the absence of hydrodynamic interactions—say, in an unbounded quiescent fluid—the bacterium simply swims along its instantaneous direction \mathbf{p} . In order to calculate \mathbf{u}_{HI} , $\boldsymbol{\Omega}_{HI}$ and \mathbf{U}_p , we need knowledge of the fluid flow around the bacterium. The typical size of marine bacteria ranges from 1-10 μm ; for these length scales, the Reynolds number—which is the ratio of inertial forces to viscous forces—associated with fluid flow is exceedingly small. In addition, we only consider marine snow particles of

diameter d and settling speed U_p such that their associated Reynolds number, $Re_{ms} = \rho U_p d / \mu \ll 1$, where ρ and μ are the density and viscosity of the suspending fluid, respectively. This allows us to safely neglect the effect of fluid inertia in our analysis.

The fluid flow is governed by the equations describing the conservation of mass and momentum. We incorporate the effect of the bacterium on the fluid flow by considering it as a ‘force dipole’, i.e., two equal and opposite forces being exerted on the fluid by the bacterium’s cell body and its flagellum/flagella [17]. The force exerted by the cell body is called the drag (say $\mathbf{f} = f_d \mathbf{p}$), and that by the flagellum is called the thrust ($-\mathbf{f}$). The force dipole representation arises because of the small separation between the points of application of the drag and the thrust. An important parameter in our study is the ‘dipole strength’ of the bacterium, denoted by F_D . Physically, it is the scalar product of the drag force exerted by the bacterium on the fluid, $f_d \mathbf{p}$, and the position of the point of application of the drag, with respect to the center of the bacterium, i.e. , $F_D \approx f_d \mathbf{p} \cdot \mathbf{x}_D$ (see Fig. 5.2). The magnitude of F_D ranges from 0.1-1 pN- μm , for a wide range of bacterial species, e.g., *Escherichia coli*, *Pseudomonas aeruginosa*, *Vibrio cholerae*, *Salmonella typhimurium*, *Vibrio alginolyticus* [17,21,199]. A stronger influence of the microbe on the flow, and thus a stronger hydrodynamic interaction, occurs for larger values of F_D . From Fig. 5.2 and the definition of F_D , it is clear that $F_D > 0$ for microorganisms that exert thrust near their tail (called pushers, e.g., most bacteria) and $F_D < 0$ for microorganisms that exert thrust near their head (called pullers, e.g., algae); in this work, we consider the former case. The details of the mathematical formulation are given in Appendix A, and the expressions for the various hydrodynamically induced velocities are given in Appendix B.

The dynamics described by eqns. 5.1 is most accurate when the separation between the bacterium and the aggregate is large; as this separation reduces, the accuracy of the model deteriorates. Specifically, [21] measured the distribution of *E. coli* in a suspension confined by parallel glass plates and concluded that the force dipole model ceases to be a valid approximation at distances of around 10 body lengths

(i.e., at $(|\mathbf{x}_2| - a) \approx 10b$) from the surface. For $(|\mathbf{x}_2| - a) < 10b$, the effects of finite size of the bacterium, its shape asymmetry and flagellar rotation become important and these are not captured by a force dipole. As the bacterium approaches to within touching distance from the aggregate the force dipole model results in unrealistic effects like the penetration of the bacterium through the rigid surface of the aggregate. This can be remedied using more involved hydrodynamics but for the sake of simplicity we model the near-field interaction between the bacterium and the aggregate as a hardcore repulsion. This means that upon contact, we ensure that the bacterium doesn't penetrate into the aggregate, but moves tangentially along its surface while being free to rotate. Thus, the bacterium cannot penetrate into the aggregate but can still rotate away and escape from it after spending some time on its surface. Such rigid-body or steric interactions are not uncommon and have indeed been observed for a number of microorganisms in contact with rigid surfaces [27, 164].

The force dipole model just described has been used in the past to explain the hydrodynamic trapping of microswimmers/bacteria impinging on stationary rigid spheres [127] and drops [64]. This trapping phenomena has been observed experimentally as well, for both artificial micro-swimmers [125] and for the bacterium *E. coli* and its predator *Bdellovibrio bacteriovorus* [26]. In this study, we show that such trapping can also occur when a bacterium encounters a sinking sphere (see Section 5.3.1).

5.2.2 Bulk nutrient distribution and chemotaxis

Many bacteria follow a run-and-tumble behavior, wherein their orientation, \mathbf{p} , can change abruptly depending on the instantaneous rate of change of chemoattractant concentration in their vicinity. In our case, the chemoattractant concentration, C , satisfies the steady-state convection-diffusion equation

$$\nabla \cdot (\mathbf{v}_{St}C) = D_C \nabla^2 C, \quad (5.2)$$

where D_C is the nutrient diffusivity, and \mathbf{v}_{St} is the flow field due to a sphere sedimenting under gravity, in an unbounded fluid. This is a simplification, because we are not accounting for the effects of the hydrodynamic interactions on the convection-diffusion equation. In reality, hydrodynamic interactions would cause the sphere to rotate as it settles and the presence of the bacterium would disturb the fluid flow, making it different from \mathbf{v}_{St} . Thus, the fluid flow—and through it, the nutrient transport—will be affected by both the rotation of the marine snow and by the bacterium. But for the parameter range of our study (see Table 5.1), the fluid flow associated with the marine snow particle's rotation, and also with the bacterium's locomotion, is negligible in comparison to that associated with the marine snow particle's gravitational settling (see eqns. 5.25 to 5.28 in Appendix). Therefore, we can justify the simplification made in eqn. 5.2. We solve eqn. 5.2 subject to the conditions that $C = C_0$ at the sphere surface, and $C \rightarrow 0$ at large distances away from the sphere. Note that a fixed surface concentration of the nutrient corresponds to transport limited nutrient transfer [91].

Once the concentration C is known, the run-and-tumble chemotaxis is implemented by prescribing the run-time τ of the bacterium as a function of DC/Dt , i.e., the instantaneous rate of change of the chemoattractant concentration as seen by the bacterium. This is done by providing a bias to the mean run-time of the bacterium in absence of chemoattractant, τ_0 , according to the relation (see Appendix C for details):

$$\tau = \tau_0 \exp\left(\alpha_C \frac{K_D}{(K_D + C)^2} \frac{DC}{Dt}\right), \frac{DC}{Dt} > 0; \text{ and, } \tau = \tau_0, \frac{DC}{Dt} \leq 0, \quad (5.3)$$

where α_C is a time-constant and K_D is the half-saturation constant of the receptors that bind to the chemoattractant. Eqn. 5.3 shows how chemotactic bacteria can climb up nutrient gradients: by increasing their run-time whenever they swim along regions with increasing ambient nutrient concentration. One important point is that bacterial tumbling is significantly hindered when they are near solid surfaces and most tumbles are limited to the tangent plane at the surface [110]. Therefore, we restrict near-surface tumbling, and any bacterium that comes into contact with the nutrient

source cannot simply tumble away and escape. Finally, we introduce stochasticity to the bacterium's orientation—stemming from flagellar imperfections and other inherent fluctuations—in between tumbles (when its orientation is governed by the second equation in eqn. 5.1) by allowing for rotational diffusion of the orientation \mathbf{p} with a diffusivity D_r . This changes the second equation in eqn. 5.1 to:

$$\mathbf{p}(t + \Delta t) - \mathbf{p}(t) = \Delta t (\boldsymbol{\Omega}_{HI}(t) \times \mathbf{p}(t)) + \sqrt{4D_r \Delta t} \boldsymbol{\eta}_R \times \mathbf{p}(t), \quad (5.4)$$

where $\boldsymbol{\eta}_R$ is a Gaussian white noise term over the unit-sphere.

5.3 Results

The major bio-physical parameters, and their respective dimensionless representations in our study are: the bacterial dipole strength, $\alpha_D = F_D/(8\pi\mu b^2 V_s)$; the mean run-time of the bacterium, $\tau^* = \tau_0 V_s/b$; the rotational diffusivity of the bacterium, $D = D_r b/V_s$; the nutrient's molecular diffusivity D_C , represented by the Schmidt number, $Sc = \nu/D_C$, where ν is the kinematic viscosity of the surrounding fluid (water); the radius of the settling aggregate $R = a/b$; and the excess density $K_{\Delta\rho} = 2\Delta\rho g b^2/(9\mu V_s)$. Another important parameter is the Péclet number $Pe = U_p a/D_C$, which is the ratio of advective transport of the nutrient to its diffusion. The values of all these parameters are calculated by using the corresponding dimensional values listed in Table 5.1.

5.3.1 Hydrodynamic trapping: with and without orientational diffusion

We first discuss how hydrodynamics affects a bacterium's behavior in close proximity to sinking marine snow, in the absence of tumbling (and hence, chemotaxis), and rotational diffusion ($D_r = 0$ in eqn. 5.4). The idea is that fluid flow caused by a bacterium, if strong enough, causes it to rotate toward a nearby rigid surface and approach it. This 'hydrodynamic attraction' is balanced by hardcore repulsion,

which results in the bacterium swimming tangentially to the surface. In the following discussion, the dimensionless radii (of spherical marine snow) are represented by ‘ R ’.

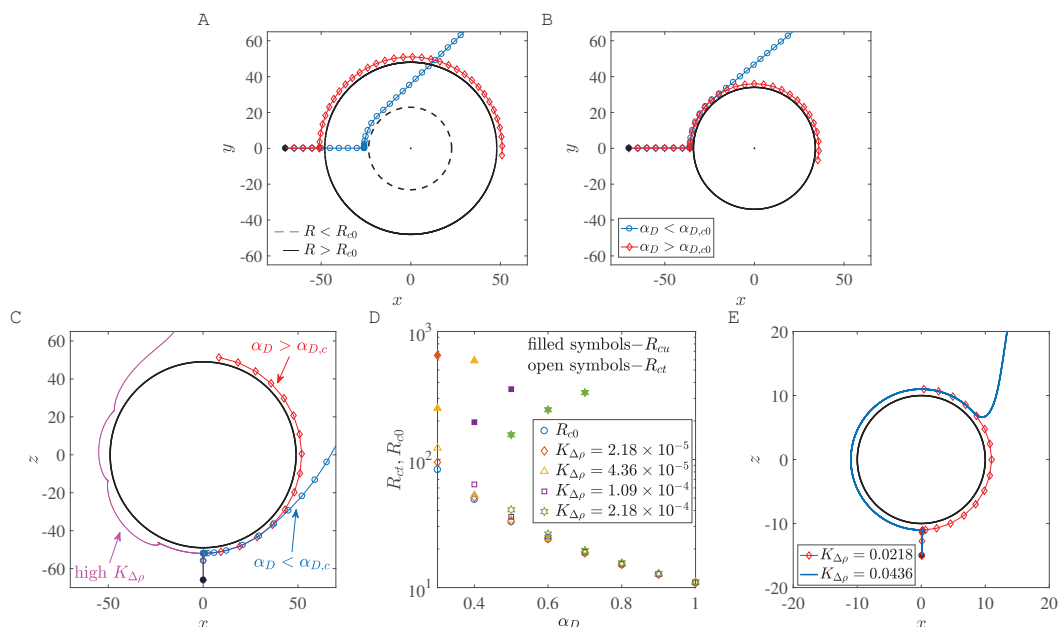


Figure 5.3. : (a) The critical trapping radius for a stationary sphere: a bacterium gets trapped (resp. escapes) if the radius of the sphere being encountered is larger (resp. smaller) than a critical value. (b) Bacterium with dipole strength larger (resp. smaller) than the critical dipole strength, $\alpha_{D,c0}$ is trapped (resp. escapes) around a sphere of given radius R . (c) Trapping around a settling sphere: the trajectories are plotted in the frame of reference moving with the sphere and gravity acts along the $-z$ direction; $\alpha_{D,c}$ is the critical dipole strength above which hydrodynamic trapping occurs (for a settling sphere). (d) Variation of the critical trapping radius of a sphere settling under gravity, R_{ct} , with the bacterium’s dipole strength, for different values of dimensionless excess density $K_{\Delta\rho}$. R_{c0} is the value of the critical trapping radius for a stationary sphere. (e) An illustration of the fact that hydrodynamic capture fails to occur if the dimensionless excess density $K_{\Delta\rho}$ exceeds 4×10^{-2} .

Microswimmers/bacteria encountering stationary spherical obstacles—like rigid spheres or liquid drops—can get trapped onto their surface due to hydrodynamic interactions, if the obstacle radius is larger than a critical radius, say R_{c0} [127]. This is shown in the trajectories in Fig. 5.3(a). The dipole strength is the same for the bacterium trajectory marked by diamonds and the one by circles; in the former, the radius of the sphere is larger than R_{c0} , while in the latter, it is smaller than R_{c0} . Recent experiments on the motion of *B. bacteriovorus* near beads also observed this interesting dependence of hydrodynamic trapping on sphere radius [26]. A different interpretation is that spherical obstacles of a prescribed radius can (hydrodynamically) trap bacteria with dipole strengths larger than a critical value, say $\alpha_{D,c0}$. Therefore, a bacterium with dipole strength less than $\alpha_{D,c0}$, does not get trapped around a sphere [the blue trajectory marked by circles in Fig. 5.3(b)], while one with dipole strength greater than $\alpha_{D,c0}$ does get trapped [the red trajectory marked by diamonds in Fig. 5.3(b)]. For a stationary liquid drop, the dimensionless critical trapping radius can be estimated as,

$$R_{c,drop} \approx \frac{64}{3\alpha_D^2} \frac{\lambda + 1}{3\lambda + 2}, \quad (5.5)$$

where λ is the ratio of the drop's viscosity to the viscosity of its surrounding fluid. Eqn. 5.5 has been obtained from numerical calculations of the critical trapping radius for clean drops, reported in [64]. The critical trapping radius for a stationary rigid sphere, R_{c0} , can be obtained by taking the limit $\lambda \rightarrow \infty$ in eqn. 5.5, which yields $R_{c0} \approx 64/(9\alpha_D^2)$ [127]. This variation is shown by the circles in Fig. 5.3(d). Alternatively, one can also evaluate the critical dipole strength for which a bacterium will trap around a rigid sphere of radius R by inverting the previous expression, i.e., $\alpha_{D,c0} \approx 8/(3R^{1/2})$. If we use the diameters of marine snow particles (0.4 - 100 μm) as a reference, we obtain the corresponding critical dipole strength values in the range $0.05 < \alpha_{D,c0} < 0.6$. Measurements and calculations for *E. coli* estimate a wide range of dipole strengths, $0.01 < \alpha_D < 2$ [17, 177], owing to heterogeneities among different cells [200]. The same is also true for other genera, like the unflagellated marine bacterium *V. alginolyticus* [39, 199]. Therefore, one can conclude that there do exist

scenarios under which most motile bacteria can get hydrodynamically trapped around stationary, rigid spherical obstacles.

Does hydrodynamic trapping occur if the obstacle encountered by the bacterium is moving, instead of being fixed? To answer this, we numerically simulated (without tumbling and rotary diffusion) the dynamics of a bacterium located initially at $\mathbf{x}(0) = (0.1, 0, -R - 15)$, and orientated along the direction opposite gravity, i.e., $\mathbf{p}(0) = (0, 0, 1)$, as shown in Fig. 5.3(c). Thus, the bacterium lies directly in the path of the sinking aggregate and eventually collides with it, after which its motion is dictated by hydrodynamic interactions with, and hardcore repulsion from the aggregate surface. In addition to dipole strength and the sphere radius, we have a third factor that governs the bacterial dynamics when the sphere is settling under gravity: the density difference between the sphere and the ambient fluid, denoted, in dimensionless form, by $K_{\Delta\rho}$. A major difference due to gravitational settling is that if the settling speed is very large (due to large aggregate radius and/or excess density), then the bacterium cannot ‘keep up’ with the sphere and thus cannot be trapped, as seen in the magenta trajectory in Fig. 5.3(c). This is particularly true for low dipole strengths, i.e., when the hydrodynamic interactions between the bacterium and the sphere are weak. But there exists a range of sizes ($0.2 \text{ mm} < a < 0.65 \text{ mm}$) and excess densities ($10^{-4} \text{ g/cm}^3 < \Delta\rho < 10^{-3} \text{ g/cm}^3$) of marine snow for which hydrodynamic trapping occurs [198], specifically if the bacterium’s dipole strengths are large. Fig. 5.3(d) shows that for excess density values that are representative of our system, substantial differences between the critical trapping radii of the stationary (R_{c0}) and the translating (R_{ct}) case occur only for small bacterial dipole strengths. In this regime [$\alpha_D < 0.6$ in Fig. 5.3(d)], the critical trapping radius for the case of a sinking aggregate increases as the excess density of the aggregate increases. However, there is no R_{ct} shown corresponding to $\alpha_D = 0.3$ for $K_{\Delta\rho} = 1.09 \times 10^{-4}$, and corresponding to $\alpha_D = 0.3, 0.4$ for $K_{\Delta\rho} = 2.18 \times 10^{-4}$. For these parameter values, trapping does occur at larger values of R , but the Reynolds number of the aggregate corresponding to these large values is $\sim O(1)$, and so our theory is not valid in those regimes. It

is interesting that even though larger spheres settle faster, they also have a greater ‘hydrodynamic pull’ on a bacterium with large enough dipole strength. Intuitively, one would expect larger spheres/aggregates to be less effective hydrodynamic traps as they settle faster and so an approaching bacterium might not be able to keep up with the settling sphere. But for the range of excess density considered (10^{-4} g/cm³ to 10^{-3} g/cm³), our analysis shows that an increase in aggregate radius also strengthens the hydrodynamic interaction between the aggregate and the bacterium. This enables larger aggregates to act as more effective traps for nearby bacteria. In this way, a sphere of radius less than the critical trapping radius sinks slowly but still doesn’t trap an approaching bacterium (as the hydrodynamic interaction effects are weak), while one with radius larger than the critical trapping radius sinks more rapidly yet it manages to trap oncoming bacteria with large enough dipole strength (due to stronger hydrodynamic interactions). But this effect of larger aggregate radii being more conducive to trapping might not extend indefinitely, as eventually the aggregate Reynolds number will become $\sim O(1)$, and the ideas presented here will become inapplicable. In the low Reynolds number regime discussed here, there is an upper limit of aggregate radii—albeit in a few cases—above which bacteria with smaller dipole strengths fail to remain hydrodynamically bound to the aggregate. This upper limit, R_{cu} , is shown whenever it exists, via filled symbols in Fig. 5.3(d). This upper limit of aggregate radius exists because the hydrodynamic trapping effect competes with the settling rate of the sphere, and there does exist some threshold settling speed above which the sphere’s fast settling precludes hydrodynamic capture altogether. In accordance with this idea, we also see that if the excess density is too high ($K_{\Delta\rho} > 4 \times 10^{-2}$) then hydrodynamic trapping does not occur for realistic values of the bacterium dipole strength and marine snow radius. This upper limit of $K_{\Delta\rho}$ was computed by simulating the encounter of a bacterium of dipole strength $\alpha_D = 2$ (which is the maximum value used in our work), with an aggregate of radius $R = 10$ (which is the minimum value used in our work). As the value of $K_{\Delta\rho}$ was increased from 2.18×10^{-5} , the bacterium got trapped until $K_{\Delta\rho} = 4.36 \times 10^{-2}$

[see Fig. 5.3(e)]. Thus, when $K_{\Delta\rho} \geq 4.36 \times 10^{-2}$, even the bacterium with highest dipole strength considered will fail to get trapped to any aggregate that we have considered in this study. An increase in the sphere size at this value of the excess density also does not favor trapping, because it further increases the sphere's settling speed, without yielding greater advantages for hydrodynamics based trapping. Since even intra-species bacterial dipole strengths can span a wide range—owing to their dependence on cell size, shape and swimming speed—one can expect a multitude of behaviors in reality. The conclusion therefore is that hydrodynamic trapping around a sinking sphere depends acutely on the sphere's excess density and the bacterium's dipole strength.

The above behavior is deterministic because we have neglected the bacterium's rotational diffusivity. In the deterministic case, a bacterium encountering a sinking obstacle is either trapped, or it escapes, depending on the sphere's radius, its excess density and the bacterium's dipole strength. But stochasticity is introduced because of noise/rotational diffusion in the bacterium's orientation, quantified by the dimensionless parameter $D = D_r b / V_s$, where D_r is the rotary diffusivity of the bacterium. If the bacterium's rotary diffusivity is large, then its escape is possible even if the radius of the spherical obstacle is larger than the critical values shown in Fig. 5.3. A large enough rotary diffusion may overpower the fluid-flow induced rotation of the bacterium toward the aggregate. This can cause it to reorient away from the surface of the nutrient source, and simply swim away to escape the hydrodynamic entrapment (see [127] and [64] for details). In presence of noise, the bacterium's interaction with the aggregate is no longer binary (i.e., either trap or escape), and the time a bacterium spends at the surface of the aggregate is a random variable which we call the 'trapping time', shown qualitatively by the trajectories in Fig. 5.4(a).

The distribution of the trapping time, T_h , depends on the size and excess density of the aggregate, and the dipole strength and rotational diffusivity of the bacterium. We use it to quantify the trapping fraction, \mathcal{F}_{trap} , defined as the mean trapping time in a simulation of 1000 bacteria divided by the total simulation time, i.e., $\mathcal{F}_{trap} = \bar{T}_h / T_{end}$,

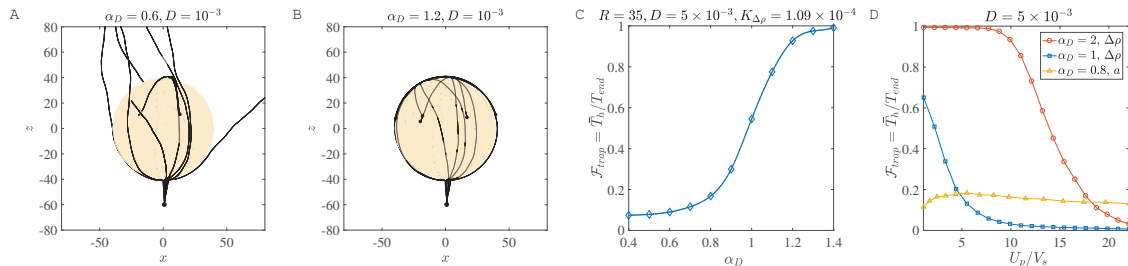


Figure 5.4. : (a) Ten trajectories of bacteria/micro-swimmers (dipole strength $\alpha_D = 0.6$, dimensionless rotary diffusivity $D = 10^{-3}$) encountering a sinking sphere of radius $R = 40$, $K_{\Delta\rho} = 4.36 \times 10^{-4}$. (b) Ten trajectories of micro-swimmers with a higher dipole strength ($\alpha_D = 1.2$) than case (a), but same dimensionless rotary diffusivity ($D = 10^{-3}$) encountering the same sinking sphere as in (a). (c) The trapping fraction \mathcal{F}_{trap} as a function of the dipole strength for parameter values given in the title, with $T_{end} = 500$. Clearly, $\mathcal{F}_{trap} \rightarrow 1$ if the swimmer's dipole strength is large enough. (d) The trapping fraction as a function of the aggregate's settling speed (U_p) normalized by the bacterium's swimming speed (V_s). The legend contains values of the dipole strength, along with the parameter that was varied (to vary U_p) in each case. In the plots marked by circles and squares, $T_{end} = 500$; U_p is changed by changing the excess density ($\Delta\rho$) of the aggregate from 10^{-4} g/cm³ to 2×10^{-3} g/cm³, and aggregate radius is fixed at $a = 45$ μm . In the plots marked by triangles, $T_{end} = 3000$; U_p is changed by changing the aggregate radius from 20 μm to 450 μm , and excess density is fixed at 5×10^{-4} g/cm³.

where \bar{T}_h is the mean over all trial simulations. Fig. 5.4(c) shows that for typical values of the bacterial rotational diffusivity, hydrodynamic trapping is still very likely for $\alpha_D > 1$; thus suggesting that the trapping mechanism is quite robust to noise [see also Fig. 5.4(b)]. As an example of bacteria with $\alpha_D > 1$, consider *E. coli* cells (in water) of size $b \approx 1$ μm , swimming speed 22 ± 5 $\mu\text{m/s}$, and dipole strength $F_D \approx 0.4\text{--}0.6$ pN- μm [17], or *V. alginolyticus* cells of similar size but under conditions where the availability of sodium (Na^+) is somehow inhibited [199]. This is because the

flagellar motor of *V. alginolyticus* is driven by transmembrane Na^+ gradients, so Na^+ deficient conditions reduce its swimming speed from $\approx 100 \mu\text{m/s}$ to $\approx 20 \mu\text{m/s}$, thus increasing the value of α_D [6, 199]. In Fig. 5.4(d), we plot the trapping fraction as a function of U_p/V_s , i.e., the aggregate's sinking speed in an unbounded fluid, divided by the bacterium's swimming speed. The aggregate's speed depends on its excess density $\Delta\rho$ and radius a ; and we have plotted \mathcal{F}_{trap} for the cases where $\Delta\rho$ or a is varied independently. An increase in $\Delta\rho$ increases the settling speed and weakens the hydrodynamic attraction effect, therefore \mathcal{F}_{trap} reduces monotonically with U_p/V_s . Noticeably, if the bacterium's dipole strength is large then hydrodynamic trapping is quite likely ($\mathcal{F}_{trap} \approx 0.8$) even when $U_p/V_s \approx 10$. The nature of \mathcal{F}_{trap} vs. a is non-monotonic because an increased aggregate radius affects both the settling speed and the hydrodynamic interactions (as seen in Fig. 5.3). Higher settling speeds on account of larger aggregate radii do not necessarily diminish hydrodynamic capture, reflected in the gradual initial increase of \mathcal{F}_{trap} as U_p/V_s increases from ≈ 1 to ≈ 6 . This was also apparent in the results shown in Fig. 5.3(d), and is attributed to the fact that hydrodynamic attraction is enhanced for larger radii. But this enhancement does not last indefinitely and as the aggregate's radius increases further [i.e., when $U_p/V_s > 6$ in Fig. 5.4(d)] we begin to see a decline in the trapping fraction. This is because hydrodynamic attraction is now being overpowered by the more rapid settling of the aggregate and the rotary diffusion, making it exceedingly difficult for the bacterium to be retained on the surface of the sinking aggregate.

It is to be noted that the trapping behavior discussed above depends on whether a 'direct encounter' takes place between the bacterium and the sphere. The most common way such an encounter may happen is if the bacterium lies in the swept volume below a settling marine snow particle. Another possibility is chemotaxis toward the surface of the nutrient-effusing marine snow, although this will depend strongly on the relative speeds and on the strength of chemotaxis. Irrespective of the mechanism of the initial contact, hydrodynamic interaction plays a crucial role in

enhancing the nutrient exposure of marine bacteria. In the subsequent sections, we demonstrate this enhancement and explain the factors affecting it.

5.3.2 Average nutrient exposure and the hydrodynamic amplification

In this section, we combine the hydrodynamic and chemotactic effects described in Sections 5.2.1 and 5.2.2 to simulate the trajectories of marine bacteria encountering a sinking nutrient source. The complete details of the simulation methodology are given in Appendix C. In case of a stationary source, the nutrient concentration is spatially symmetric and the solution to eqn. 5.2 (with $\mathbf{v} = 0$) is just $C/C_0 = a/r$; thus there is abundant nutrient availability all around the source. This changes as the source settles under gravity because the nutrient which diffuses out of its surface gets convected downstream as a plume [see Fig. 5.6(a)]. The width of this plume can be thought of as a measure of the spatial ‘nutrient availability’, with wider plumes being more amenable to location and population by bacteria via chemotaxis. An equivalent metric is the concentration boundary layer thickness, denoted by δ_C . It is defined roughly as the (small) radial distance from the source, transverse to the settling direction, within which the nutrient concentration C drops from C_0 to within 1% of C_0 . This boundary layer thickness depends on the nutrient’s Péclet number as $\delta_C \sim aPe^{-1/3}$, for $Pe \gg 1$, and Reynolds number, $Re_{ms} \ll 1$ [11]. Fig. 5.6 shows how the boundary layer thickness reduces as Pe increases due to reducing nutrient diffusivity.

In our simulations, as the bacteria swim past the sinking source they either (i) encounter it (via chemotaxis or otherwise), (ii) enter the boundary layer but do not come into contact with the source, (iii) swim past the sphere but into the plume, or, (iv) just swim past the sphere with minimal hydrodynamic interaction and/or nutrient exposure. The behaviors are shown in Figs. 5.5 and 5.9. Chemotaxis is key for cases (i) through (iii), while hydrodynamics is most important for the case (i). Our aim is to compute the bacteria’s nutrient exposure as a function of vari-

ous bio-physical parameters governing the problem's hydrodynamic and chemotactic influences. Towards this, we define the average nutrient exposure as:

$$\bar{C} = \frac{\sum_{i=1}^{N_b} \int_0^{T_{end}} C_i(t) dt / C_0 T_{end}}{N_b}, \quad (5.6)$$

where $C_i(t)$ is the nutrient history of the i -th bacterium and T_{end} is the simulation-time for it. We use the subscripts *Ch.* and *N.Ch.* to refer to the average nutrient concentrations for chemotactic and non-chemotactic bacteria, respectively. We simulate the system for four different 'bacteria types': either chemotactic or non-chemotactic, with either high or low dipole strengths [see the legend description of Fig. 5.6(b)]. Next, we define a term called the 'hydrodynamic amplification', i.e., the (possible) increase in the nutrient exposure, attributable to hydrodynamic interactions:

$$A_C = \frac{(\bar{C}_H - \bar{C}_L)}{\bar{C}_L} \times 100, \quad (5.7)$$

where the sub-scripts H and L refer, respectively, to the cases in which the hydrodynamic interactions are high/strong and low/weak. The varying strengths of these hydrodynamic interactions could be due to the aggregate's size and excess density, or the bacterium's motility characteristics represented via the dipole strength α_D . In our study we focus on the amplification stemming from the dipole strength, and use $\alpha_D = 2$ (resp. $\alpha_D = 0.1$) for the case of strong (resp. weak) hydrodynamic interactions. Thus the value of A_C will be indicative of whether hydrodynamics is of significant nutritional benefit or not. We postulate that near-surface hydrodynamic interaction significantly increases nutrient exposure as it affects colonization of moving nutrient sources, particularly by the bacteria having large dipole strengths. As explained in Section 5.3.1, this is because strong hydrodynamic attraction results in the bacteria getting trapped on the surface of the nutrient source, instead of just glancing the surface and getting swept away [recall the trajectories in Fig. 5.3(c)].

Fig. 5.5 shows that there is indeed a gentle increase in the value of \bar{C} as the (dimensionless) dipole strength, α_D , increases from 0.1 to 2, both for chemotactic ($\bar{C}_{Ch.}$) and non-chemotactic ($\bar{C}_{N.Ch.}$) bacteria. Naturally, chemotaxis enables the

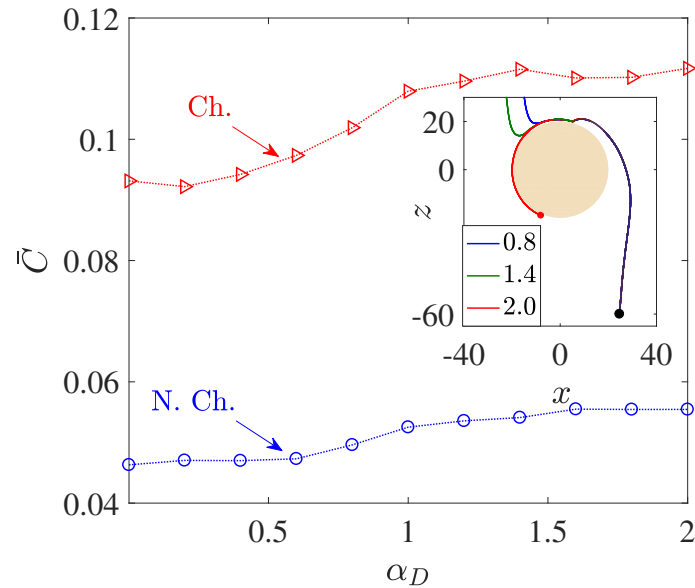


Figure 5.5. : Variation in average nutrient exposure, \bar{C} , as a function of the dimensionless bacterial dipole strength α_D , for chemotactic (Ch.) and non-chemotactic (N.Ch.) bacteria. Inset: The trajectories of three chemotactic bacteria with different α_D values (these are given in the legend). It can be seen that all three trajectories begin just outside the aggregate's swept volume but are able to 'chemotax' onto the surface. The amount of time each bacterium spends on the surface of the source depends on their dipole strengths. The other parameters are: $R = 45$, $K_{\Delta\rho} = 0.0109$, $Sc = 1000$, $\tau^* = 1$.

former to have more than two-folds higher average nutrient exposure, as also remarked by [166]. It is the reinforcing effect of the hydrodynamic interactions with an increase in the dimensionless dipole strength which is of major significance. The increment is not exactly monotonic and most of it occurs over the range $0.5 < \alpha_D < 1.5$. There are upper (resp. lower) limits beyond which an increased (resp. reduced) dipole strength doesn't yield proportionate increments (resp. reductions) in \bar{C} . The reason simply is that for very low dipole strengths, any bacterium encountering the source just doesn't spend enough time swimming along its surface. In fact, the time a bacterium

spends on the source increases as the dimensionless dipole strength increases, to an upper limit after which the bacterium gets trapped and does not escape. This can be seen in the inset of Fig. 5.5: the dipole strength is highest for the red (trapped) trajectory, followed by that for the green and then the blue trajectory. Clearly, the time spent in contact with the source—and thus in a region of maximum nutrient concentration—is directly related to the dipole strength. Therefore, $\alpha_D < 0.5$ (resp. $\alpha_D > 1.5$) represents very weak (resp. strong) hydrodynamic interactions, leading to negligible changes in \bar{C} in those regimes. In the former case, the bacterial residence time (on surface) is not long enough, and in the latter case there is a saturation due to sufficiently strong hydrodynamic interactions. The intermediate region reflects the non-trivial balance between deterministic trapping and stochasticity, as explained in Section 5.3.1.

We saw that hydrodynamic interactions indeed enhance the average nutrient exposure for both chemotactic and non-chemotactic bacteria. More precisely, the hydrodynamic amplification, A_C , as defined in eqn. 5.7 is $\approx 20\%$ for both chemotactic and non-chemotactic bacteria, when comparing the \bar{C} values in Fig. 5.5 for the weakest and the strongest hydrodynamic interactions. Next, we analyze the dependence of the average nutrient exposure on the nutrient's diffusivity, quantified in our simulations by the Schmidt number, Sc . Note that lower values of nutrient diffusivity mean higher values of Sc .

Fig. 5.6(a) shows how the nutrient is restricted to a narrower region around the source as its diffusivity decreases, and the effect of this is seen in the reduction of the average nutrient exposure with increasing values of the Schmidt number for all combinations of chemotactic/non-chemotactic bacteria with strong/weak hydrodynamic interactions in Fig. 5.6(b). This is to be expected though, as in general, a reduction in nutrient diffusivity will reduce the number of bacteria that encounter the source due to chemotaxis, and will also reduce the likelihood of most bacteria in the bulk—chemotactic or otherwise—to populate the nutrient-rich plume. The more interesting aspect can be seen in the inset, wherein stronger hydrodynamic interac-

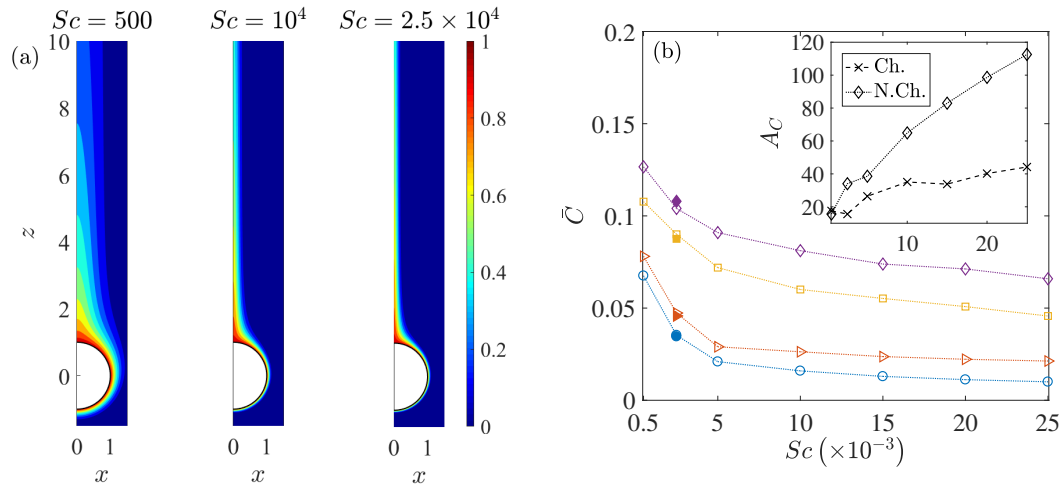


Figure 5.6. : (a) Spatial variation of the nutrient's (normalized) concentration around the sinking sphere. The thickness of the concentration boundary layer, δ_C , reduces as the nutrient diffusivity reduces. The corresponding values of the Péclet number are 100, 2000, 5000. (b) The variation in the average nutrient exposure, \bar{C} , for chemotactic and non-chemotactic bacteria, with strong and weak hydrodynamic interactions, as a function of the Schmidt number. The legends in the main figure are as follows: Diamonds - chemotactic, $\alpha_D = 2$; Boxes - chemotactic, $\alpha_D = 0.1$; Triangles - non-chemotactic, $\alpha_D = 2$; Circles - non-chemotactic, $\alpha_D = 0.1$. The filled symbols (for $Sc = 2500$) correspond to simulation results with $N_b = 5000$ bacteria. Inset: The hydrodynamic amplification, A_C , as a function of Sc , comparing separately the percentage increase in nutrient exposures for chemotactic and non-chemotactic bacteria (recall the definition of A_C from eqn. 5.7). The other parameters are: $R = 45$, $K_{\Delta\rho} = 0.0109$, $\tau^* = 1$.

tions become much more beneficial as the nutrient availability reduces; particularly for the non-chemotactic bacteria wherein they experience more than double the nutrient exposure if hydrodynamic interactions are strong enough. The reason is that hydrodynamic interactions, being a purely passive phenomenon, do not depend on the nature of the nutrient that bacteria seek. They are influenced only by the mor-

phology of the bacteria (via dipole strength, rotational diffusivity) and the size of the sinking nutrient source. Non-chemotactic bacteria can experience nutrient-rich regions in the bulk only by chance. If they do encounter the nutrient source, then the bacteria with low dipole strengths spend very little time on the aggregate surface. In essence, non-chemotactic bacteria with low dipole strengths have no way to maximize their nutrient exposure. Non-chemotactic bacteria with high dipole strengths on the other hand, get trapped onto the nutrient source whenever they encounter it, which greatly benefits them, particularly when nutrients are scarce (high values of Sc). The same explanation applies to chemotactic bacteria as well, but the amplification is not as high. This is because chemotaxis, if reasonably strong, enables chemotactic bacteria with lower dipole strengths to remain in the proximity of the source or in the nutrient-rich plume behind the source. This somewhat reduces their nutrient deficit as compared to their counterparts with higher dipole strengths.

We saw through Fig. 5.6 that thicker concentration boundary layers around sinking aggregates favor foraging. This was because bacteria could easily enter the boundary layer and increase nutrient availability. This idea can be succinctly explained by considering the system of N_b non-interacting bacteria as a continuum with ‘self-diffusion coefficient’ D_b , which scales as $\sim V_s^2 \tau_0$, and then defining a bacterial Péclet number $Pe_b = U_p a / D_b$ (see [201] and [169] for details and applicability of such a simplification). Now, because the ‘bacterial boundary layer’ around the nutrient source scales as $\delta_B \sim a Pe_b^{-1/3}$, and the nutrient boundary layer scales as $\delta_C \sim a Pe^{-1/3}$, the ratio $\delta_B / \delta_C = (Pe / Pe_b)^{1/3}$ decides whether bacteria can effectively colonize the nutrient hot-spots. In the present study, Pe_b ranges from 50 to 40000. As long as $Pe_b > Pe$, the bacteria can form a boundary layer thinner than the nutrient boundary layer, i.e., $\delta_B < \delta_C$ and so chemotaxis will be profitable. As Pe_b reduces, so does the bacterial accumulation around the nutrient source and thus the average nutrient exposure should decline. This concept is borne out in our simulations too—especially for the chemotactic bacteria—as the plots of \bar{C} versus the dimensionless mean runtime τ^* show in Fig. 5.7. For non-chemotactic bacteria with $\alpha_D = 2$, the variation

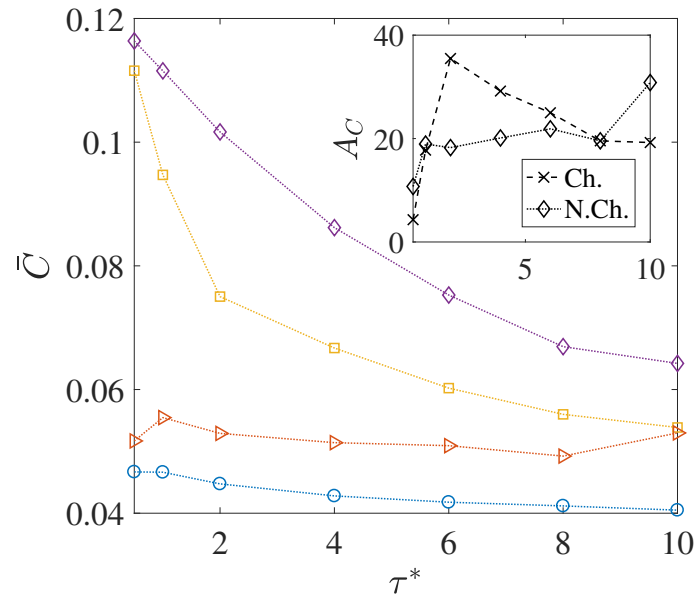


Figure 5.7. : The variation in the average nutrient exposure, \bar{C} , for chemotactic and non-chemotactic bacteria, with strong and weak hydrodynamic interactions, as a function of the (dimensionless) mean run-time τ^* . The legends in the main figure are as follows: Diamonds - chemotactic, $\alpha_D = 2$; Boxes - chemotactic, $\alpha_D = 0.1$; Triangles - non-chemotactic, $\alpha_D = 2$; Circles - non-chemotactic, $\alpha_D = 0.1$. Inset: The hydrodynamic amplification, A_C , as a function of τ^* . The other parameters are: $R = 45$, $K_{\Delta\rho} = 0.0109$, $Sc = 1000$.

is fairly non-monotonic because there is no ‘directionality’ to their motion. Their nutrient exposure depends mostly on their direct encounter with the aggregate. [169] predicted that the encounter rate E_r of non-chemotactic bacteria with the aggregate varies non-monotonically with τ_0 via a scaling $E_r \sim \tau_0^{2/3} I(\tau_0)$. The function $I(\tau_0)$ decreases as τ_0 increases, thus leading to non-monotonic variation of the encounter rate, E_r ; based on the results for smaller τ_0 values, this is also reflected in our simulations. The inset in Fig. 5.7 shows that the hydrodynamic amplification, for chemotactic bacteria, varies non-monotonically as τ^* increases and a maximum of $A_{C,max} \approx 35\%$ is reached at $\tau_{0,opt}^* \approx 2$. A physical interpretation is that chemotaxis is too strong

for $\tau_0 < \tau_{0,opt}$, and thus even weak hydrodynamic interactions cannot prevent the bacteria with the smallest mean run-times from either locating nutrient-rich regions in the bulk (the concentration boundary layer), or from staying close enough to the sinking nutrient source. As a result, the amplification is only $\approx 5\%$ for the lowest self-diffusion coefficient of bacteria ($D_{b,min.} = 5 \times 10^{-7} \text{ cm}^2/\text{s}$) being considered in our study. On the other hand, for the larger mean run-times of $\tau_0 > \tau_{0,opt}$, the reduction in the hydrodynamic amplification can be explained by the weaker chemotaxis leading to lesser colonization of the aggregate surface by bacteria with high dipole strengths. Due to this, hydrodynamics is unable to affect the nutrient exposure as severely as it does for $\tau_0 < \tau_{0,opt}$, resulting in obtained reduction in the values of A_C .

In the foregoing discussions, the size of the sinking aggregate, and thus its sinking speed, was fixed. The effect of hydrodynamic interactions entered the discussion via the different dipole strengths of the bacteria, with trapping (resp. escaping) being favored by high (resp. low) dipole strengths. Fig. 5.8 details the changes in the nutrient exposure and the corresponding hydrodynamic amplifications as a function of the aggregate size. A change in the aggregate size has two implications: the first is that larger aggregates sink more rapidly and thus it becomes difficult for chemotactic bacteria to ‘catch up’ and get trapped onto them. Therefore, even though higher aggregate radius is suitable for hydrodynamic trapping (Section 5.3.1), it doesn’t help because of the large initial separations between the bacteria and the aggregate in our simulations. On the other hand, smaller aggregates sink slowly, giving plenty of time for chemotactic bacteria with high dipole strengths to locate the nutrient source and get trapped onto it. This is why the hydrodynamic amplification reduces as the size of the aggregate increases: the significance of hydrodynamic interactions diminishes and so does the difference between the behaviors of bacteria based on their dipole strengths.

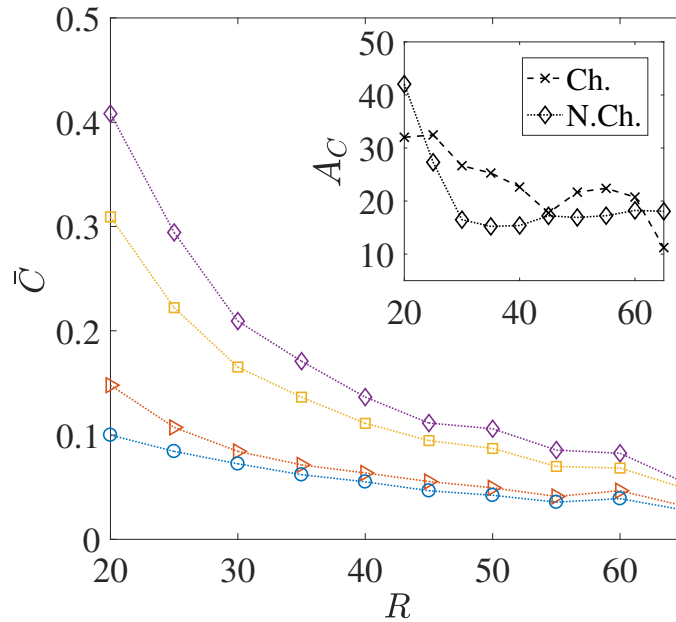


Figure 5.8. : The variation in the average nutrient exposure, \bar{C} , for chemotactic and non-chemotactic bacteria, with strong and weak hydrodynamic interactions, as a function of the (dimensionless) radius of the marine snow particle R . The legends in the main figure are as follows: Diamonds - chemotactic, $\alpha_D = 2$; Boxes - chemotactic, $\alpha_D = 0.1$; Triangles - non-chemotactic, $\alpha_D = 2$; Circles - non-chemotactic, $\alpha_D = 0.1$. Inset: The hydrodynamic amplification, A_C , as a function of R . The other parameters are: $K_{\Delta\rho} = 0.0109$, $\tau^* = 1$, $S_C = 2000$.

5.3.3 Motile, non-chemotactic bacteria versus non-motile bacteria

The locomotion of motile bacteria—both chemotactic and non-chemotactic—was discussed in detail in Sections 5.2.1, 5.2.2 and the Appendix. In comparison, the motion of non-motile bacteria in the ocean is fairly simple: they just act as passive tracers being carried by the fluid flow. It has been shown in the past that the nutrient exposure is more or less the same for motile, non-chemotactic bacteria when compared to non-motile bacteria, over a wide range of initial conditions and Péclet numbers [166]. This is indeed accurate if hydrodynamic interactions are negligible, as seen in

the comparison between the pentagrams and circles in Fig. 5.9(a). In fact, for our simulations, \bar{C}_{NM} was slightly larger than $\bar{C}_{N.Ch.}$ for a wide range of marine snow radii, when hydrodynamic interactions were particularly weak [see Fig. 5.9(b)]. But stronger hydrodynamic interactions greatly improve the nutrient exposure for the non-chemotactic bacteria with the percentage increase

$$A_{C2} = \frac{(\bar{C}_{N.Ch.} - \bar{C}_{NM})}{\bar{C}_{NM}} \times 100, \quad (5.8)$$

being even greater than 100% (i.e., more than two-fold increase) for the case of the scarcest nutrient availability ($Sc = 2.5 \times 10^4$, $Pe = 5000$). The amplification is a little less drastic as a function of aggregate size though, with enhanced hydrodynamic interactions enabling the non-chemotactic bacteria to profit by $A_{C2} \approx 40\%$ for the highest aggregate size, and by $\approx 20\%$ for the lowest. This is a significant contribution and hints at potential motility induced advantage, irrespective of the chemotactic nature of marine microorganisms. Needless to say, the (motile) chemotactic bacteria are always at an advantage with respect to the non-motile bacteria and therefore we do not discuss their comparison in this section.

5.4 Conclusion

In this paper, we investigated the combined influence of hydrodynamics and chemotaxis on the colonization of sinking nutrient sources by marine bacteria. We first developed and simulated a comprehensive mathematical model incorporating bacterial swimming as influenced by: (i) fluid flow, and, (ii) chemotaxis toward the nutrient-rich regions surrounding and trailing a sedimenting marine snow aggregate. In addition to swimming with respect to the ambient fluid, bacteria are rotated and translated due to hydrodynamic interactions with nearby surfaces, such as the sinking aggregate in our case. These interactions, if sufficiently strong, can passively trap bacteria that stray too close to the aggregate and thus play a major role in enhancing a bacterium's stay in the nutrient hot-spots in marine ecosystems. We quantified the critical value of aggregate radius above which oncoming bacteria are

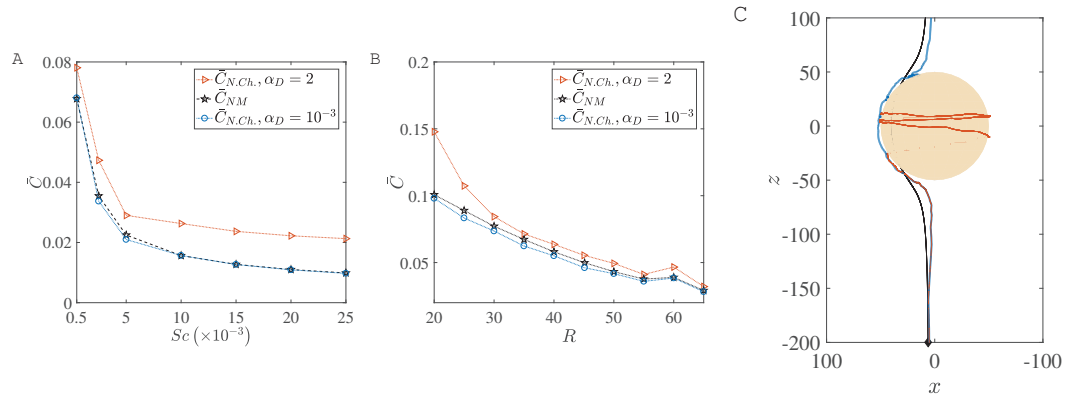


Figure 5.9. : A comparison of the average nutrient exposure, \bar{C} , between motile but non-chemotactic bacteria and non-motile bacteria, as a function of (a) the nutrient diffusivity, and (b) the (dimensionless) radius of the marine snow particle, R . (c) Sample trajectories for the three cases whose nutrient exposures are plotted in panels (a-b), with correspondence based on line colors. The blue and brown trajectories are indistinguishable until they near the aggregate, and the latter gets trapped. Notice the ‘smoothness’ of the non-motile trajectory (black) versus that of the non-chemotactic trajectory of bacterium with weak hydrodynamic interaction (blue). The nutrient exposure for motile, non-chemotactic bacteria has been evaluated for both strong ($\alpha_D = 2$) and weak ($\alpha_D = 10^{-3}$) hydrodynamic interactions. The other parameters are: $K_{\Delta\rho} = 0.0109$, $\tau^* = 1$.

trapped, and its dependence on the aggregate’s excess density and the bacterial dipole strength (dimensionless propulsive force exerted by a bacterium on the fluid). The critical trapping radius was lowest for the smallest excess densities and largest dipole strengths. We note however, that the analysis of the critical trapping radius was carried out in absence of noise/rotational diffusion of the bacterium. In presence of noise, the bacterium’s interaction with the aggregate was quantified via a trapping fraction, \mathcal{F}_{trap} . This is a measure of the likelihood of a bacterium being captured onto the aggregate surface, when its orientation is affected by thermal and/or athermal

fluctuations. We showed that the phenomenon of hydrodynamic trapping is robust to noise, and discussed how factors such as the aggregate's radius and excess density can affect the trapping fraction.

Even though the attractive nature of the hydrodynamic interactions is restricted to within a few body-lengths from the aggregate, we showed that it can drastically alter a marine bacterium's nutrient exposure. For example, chemotactic bacteria with higher dipole strengths had $\approx 40\%$ greater nutrient exposure, as compared to chemotactic bacteria with relatively lower dipole strengths. A quintessential scenario when such large amplifications could occur is the bacterial encounter of sinking phytoplankton cells ($d \approx 100\mu\text{m}$) exuding low molecular weight glycolates [74, 202]. Interestingly, this advantage is not restricted to chemotactic bacteria alone. Due to the purely hydrodynamic nature of the trapping phenomenon, any motile bacteria lying downstream in an aggregate's swept volume can potentially get trapped onto its surface. Hydrodynamics therefore, can yield substantial nutritional benefit even to *non-chemotactic, but motile* bacteria, when compared to the non-motile bacteria. These benefits depend on a variety of environmental conditions and biological parameters, like the size of the marine snow, the molecular diffusivity of the nutrient under consideration and the average run-length of bacterial species. We systematically studied these variations and provided an explanation for the obtained trends based on the influence of hydrodynamic and/or chemotactic effects. In particular, we demonstrated that hydrodynamics becomes progressively more important as the bulk nutrient availability—quantified by a concentration boundary layer thickness—declines, especially for non-chemotactic bacteria. This is particularly significant because the diffusion coefficients of the nutrients consumed by marine bacteria vary over a few orders of magnitude ($10^{-8} \text{ cm}^2/\text{s} < D_C < 10^{-5} \text{ cm}^2/\text{s}$). Our results thus suggest that bacteria can accrue substantial nutritional gains due to motility, particularly when foraging for high molecular weight (thus low diffusion coefficient) solutes which form a major part of available dissolved organic matter in oceans [203]. In contrast, we showed that larger aggregates (marine snow particles with radii greater than 1 mm)

proved too fast for the bacteria to get trapped onto, thus diminishing the role played by hydrodynamics in those regimes. An implication of the nutrient source’s speed being very high is that rising crude oil drops are not amenable to hydrodynamic trapping. Their ‘excess’ densities are quite large ($\Delta\rho \approx -0.15 \text{ g/cm}^3$), thus preventing hydrodynamic trapping to occur at all, even for the smallest drops of diameter ≈ 1 mm. We performed simulations like those discussed before, for rising oil drops and found that the amplification is practically non-existent, irrespective of bacteria being chemotactic or non-chemotactic. Therefore, bacteria must attach onto the rising oil drops via interfacial phenomena other than near-surface hydrodynamics, possibly via adsorption after a random encounter [67, 153]. However, surfactant addition breaks down larger oil drops into droplets ranging from 20-60 μm in diameter [3], which are almost neutrally buoyant and get trapped in sub-surface hydrocarbon plumes [69, 138] or pycnoclines [93]. In these cases, hydrodynamics does affect the accumulation of bacteria around oil drops. Specifically, hydrodynamics enables surfactant-laden drops to trap bacteria more effectively than surfactant-free drops [64], and strong hydrodynamic interactions increase the bacterial colonization of oil drops by $\approx 60\%$ [in comparison to weak hydrodynamic interactions; [65]].

Our study reveals a passive, non-trivial mechanism that can enable marine bacteria to reside on, and populate, moving nutrient sources in the ocean. A key insight is the generality of the hydrodynamic aspects of the results, which do not depend heavily on the details of the bacteria involved. This enables one to use the derivations presented here in combination with different active behaviors—chemotactic or otherwise—to investigate a variety of phenomena involving motile bacteria in fluid flows past nutrient sources. The present work reveals some intricacies of the initial stages of microbial colonization of nutrient sources, and extensions can be developed over the framework presented here. If the rate of aggregate consumption is slow, then our analysis can be extended to the case of time-varying aggregate size by simply replacing the constant \mathbf{F}_{ext} by some time-dependent $\mathbf{F}_{ext}(t)$. The number of bacteria in the simulation would have to be continuously updated over such longer time

scales, with possible alterations to their surface motility, e.g., a change from near-surface swimming/swarming to surface twitching/gliding [204]. Other details in the bacterium’s intrinsic motility—like chemokinesis, near-surface tumbling—are also easy to add in the present study, given the availability of experimental data [39, 110, 187]. In this way, the model described can be extended, in conjunction with observations, to incorporate finer details like evolution of microbial demographics based on surface accumulation and substrate consumption. We thus envision rich applications of this study toward analyzing complex processes involving close association of fluid flow and active motility, e.g., bioremediation, microswimmer sorting/isolation, predator-prey interactions at the micron scale.

5.5 Appendix

Appendix A: Equations governing fluid flow

The fluid velocity, \mathbf{v} , and pressure, P , are governed by the conservation of mass,

$$\nabla \cdot \mathbf{v} = 0, \quad (5.9)$$

and the conservation of momentum under negligible inertia (Stokes equations),

$$-\nabla P + \mu \nabla^2 \mathbf{v} + \mathbf{F}_D = 0, \quad (5.10)$$

where, μ is the dynamic viscosity of the suspending fluid. \mathbf{F}_D is the contribution of the bacterium to the fluid flow, which is well approximated by a force dipole. Mathematically it can be represented as a difference between two point forces separated by a distance b (which is the characteristic size of the microorganism):

$$\mathbf{F}_D = f_a \mathbf{p} \delta \{ \mathbf{x} - (\mathbf{x}_2 + b\mathbf{p}/2) \} - f_a \mathbf{p} \delta \{ \mathbf{x} - (\mathbf{x}_2 - b\mathbf{p}/2) \}, \quad (5.11)$$

where δ is the three dimensional Dirac delta function, \mathbf{x}_2 is the location of the bacterium’s center and \mathbf{p} is the bacterium’s orientation. More formally, a Taylor series

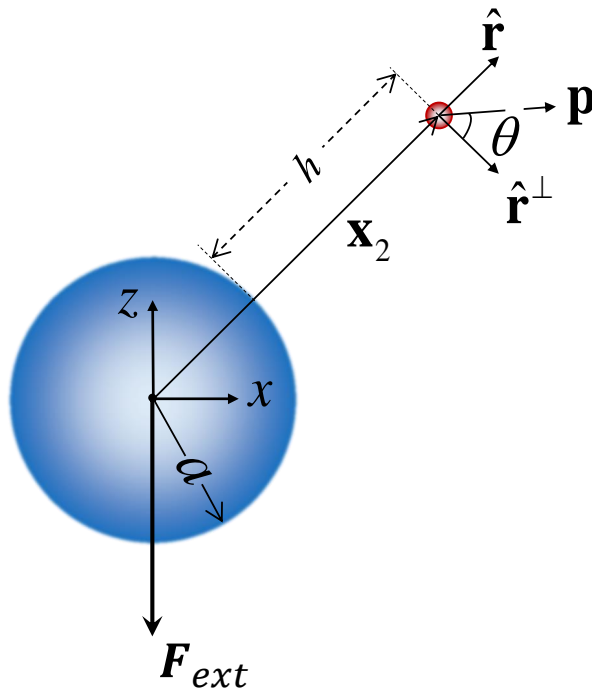


Figure 5.10. : Schematic depicting the coordinate systems, the vectors and the symbols used to describe the linear and angular velocities of the aggregate and the bacterium. The simulations are performed in the coordinate system xyz , which is fixed to the center of the marine snow particle, with the y axis pointing into the plane of the figure. The coordinate system defined by the orthogonal vectors $\hat{\mathbf{r}}$, $\hat{\mathbf{r}}^\perp$ and $\hat{\mathbf{r}}^\perp \times \hat{\mathbf{r}}$ can translate and rotate with respect to xyz . Note that h is the dimensionless separation of the bacterium (assumed to be spherical in our analysis) from the aggregate and θ is the in-plane angle, i.e., the angle between the bacterium's orientation \mathbf{p} and the unit vector $\hat{\mathbf{r}}^\perp$.

expansion of the two terms in eqn. 5.11 yields the force dipole to be the gradient of a point force along \mathbf{p} , taken in the direction of \mathbf{p} itself,

$$\mathbf{F}_D = F_D (\mathbf{p} \cdot \nabla) \{ \mathbf{p} \delta(\mathbf{x} - \mathbf{x}_2) \}, \quad (5.12)$$

the quantity $F_D \approx f_d b$ is called the dipole strength of the microorganism.

Eqns. 5.9 and 5.10 need to be solved subject to the boundary condition

$$\mathbf{v}(\mathbf{x}_s) = \mathbf{U}_p + \boldsymbol{\Omega}_p \times \mathbf{x}_s, \quad (5.13)$$

where \mathbf{x}_s corresponds to the surface of the marine snow particle, \mathbf{U}_p is the velocity with which the particle is sinking and $\boldsymbol{\Omega}_p$ is its angular velocity. Note that if the bacterium is not present (i.e., $F_D = 0$), then $\boldsymbol{\Omega}_p = \mathbf{0}$, and \mathbf{U}_p is given by the Stokes settling velocity $\mathbf{F}_{ext}/(6\pi\mu a)$. But the presence of the bacterium, and concomitant hydrodynamic interactions, mean that \mathbf{U}_p and $\boldsymbol{\Omega}_p$ are not known *a priori*. So, we utilize a well-known technique called the ‘method of reflections’ [13] to obtain \mathbf{u}_{HI} , $\boldsymbol{\Omega}_{HI}$, \mathbf{U}_p and $\boldsymbol{\Omega}_p$. The resulting expressions are provided in Appendix B [eqns. 5.14 to 5.21]. It is very important to note the dependence of these expressions on the quantity α_D , which is the dimensionless dipole strength.

Appendix B: Expressions for hydrodynamically induced translational and angular velocities

The relevant expressions on the right-hand-side of eqn. 5.1 are obtained after the application of the ‘method of reflections’ and Faxén laws for the marine snow particle and the bacterium [13]. They are represented in terms of the unit vectors $\hat{\mathbf{r}}$ and $\hat{\mathbf{r}}^\perp$. $\hat{\mathbf{r}}$ is directed along the line joining the center of the aggregate to the bacterium, and $\hat{\mathbf{r}}^\perp$ is perpendicular to $\hat{\mathbf{r}}$, as shown in Fig. 5.10. The coordinate system defined by the unit vectors $\hat{\mathbf{r}}$, $\hat{\mathbf{r}}^\perp$ and $\hat{\mathbf{r}}^\perp \times \hat{\mathbf{r}}$ can rotate and translate with respect to the body-fixed coordinate system xyz . The expression for \mathbf{u}_{HI} is:

$$\frac{\mathbf{u}_{HI}}{V_s} = \mathbf{u}_{HI,1} + \mathbf{u}_{HI,2} + \mathbf{u}_{HI,3}, \quad (5.14)$$

with,

$$\mathbf{u}_{HI,1} = \frac{3}{4} \frac{R}{R+h} \left[\bar{\mathbf{F}}_{ext} \left\{ 1 + \frac{1}{3} \left(\frac{R}{R+h} \right)^2 \right\} + (\bar{\mathbf{F}}_{ext} \cdot \hat{\mathbf{r}}) \hat{\mathbf{r}} \left\{ 1 - \left(\frac{R}{R+h} \right)^2 \right\} \right], \quad (5.15)$$

$$\mathbf{u}_{HI,2} = -\frac{3R\alpha_D(1-3\sin^2\theta)(R+h)}{2h^2(2R+h)^2}\hat{\mathbf{r}} + \frac{3R^3\alpha_D(2R^2+6Rh+3h^2)\sin 2\theta}{4h^2(2R+h)^2(R+h)^3}\hat{\mathbf{r}}^\perp, \quad (5.16)$$

and

$$\mathbf{u}_{HI,3} = \frac{3}{4}\frac{\alpha_D R}{(R+h)^3} \left[\begin{array}{l} \left(\frac{R}{R+h}\right)^2 \left\{3 + \frac{1}{3}\left(\frac{R}{R+h}\right)^2\right\} \sin(2\theta) \hat{\mathbf{r}}^\perp \\ -2(1-3\sin^2\theta) \left\{1 - \frac{4}{3}\left(\frac{R}{R+h}\right)^2 + \frac{1}{3}\left(\frac{R}{R+h}\right)^4\right\} \hat{\mathbf{r}} \end{array} \right]. \quad (5.17)$$

The expression for $\boldsymbol{\Omega}_{HI}$ is:

$$\frac{\boldsymbol{\Omega}_{HI}}{V_s/b} = \boldsymbol{\Omega}_{HI,1} + \boldsymbol{\Omega}_{HI,2} + \boldsymbol{\Omega}_{HI,3}, \quad (5.18)$$

with

$$\boldsymbol{\Omega}_{HI,1} = \frac{3}{4}\frac{R}{(R+h)^2}(\bar{\mathbf{F}}_{ext} \times \hat{\mathbf{r}}), \quad (5.19)$$

$$\boldsymbol{\Omega}_{HI,2} = -\frac{3R^3\alpha_D(2R^2+6Rh+3h^2)\sin 2\theta}{4h^3(2R+h)^3(R+h)^2}(\hat{\mathbf{r}}^\perp \times \hat{\mathbf{r}}), \quad (5.20)$$

and

$$\boldsymbol{\Omega}_{HI,3} = \frac{3}{2}\alpha_D \left\{ \frac{R}{(R+h)^2} \right\}^3 \sin(2\theta) (\hat{\mathbf{r}}^\perp \times \hat{\mathbf{r}}). \quad (5.21)$$

All the terms in the right-hand-side of eqns. 5.15 to 5.17, 5.19 to 5.21 are dimensionless, and are given by:

$$R = \frac{a}{b}, \quad h = \frac{(|\mathbf{x}_2| - a)}{b}, \quad \alpha_D = \frac{F_D}{8\pi\mu b^2 V_s}, \quad \bar{\mathbf{F}}_{ext} = \frac{\mathbf{F}_{ext}}{6\pi\mu a V_s}. \quad (5.22)$$

In the above equations, h is the dimensionless separation of the microorganism from the surface of the marine snow, and the θ is the angle between the bacterium's orientation \mathbf{p} and the unit vector $\hat{\mathbf{r}}^\perp$ (see Fig. 5.10). The terms given by eqns. 5.16, 5.17, 5.20 and 5.21 arise due to the flow generated by the bacterium (hence the contribution of α_D); while those given by eqns. 5.15 and 5.19 arise due to the fluid flow cause by the settling sphere. Although the latter terms dominate when $|\mathbf{x}_2|$ is large, the former terms can become significant as $|\mathbf{x}_2|$ reduces, i.e., as the bacterium approaches the sphere/aggregate.

The velocity of the settling marine snow particle, as altered by the presence of the microorganism, is given by:

$$\frac{\mathbf{U}_p}{V_s} = \frac{\mathbf{F}_{ext}}{6\pi\mu a V_s} + \frac{\alpha_D}{|\mathbf{x}_2|^2/b^2} \left[\frac{a^2}{|\mathbf{x}_2|^2} \sin(2\theta) \hat{\mathbf{r}}^\perp - (1 - 3\sin^2\theta) \left\{ 1 - \frac{a^2}{|\mathbf{x}_2|^2} \right\} \hat{\mathbf{r}} \right], \quad (5.23)$$

and the angular velocity induced due to hydrodynamic interactions is:

$$\frac{\boldsymbol{\Omega}_p}{V_s/b} = -\frac{3\alpha_D}{2(|\mathbf{x}_2|^3/b^3)} \sin(2\theta) (\hat{\mathbf{r}}^\perp \times \hat{\mathbf{r}}). \quad (5.24)$$

The second term on the right hand side of eqn. 5.23 is the correction to the Stokes settling speed due to the presence of the microorganism. The quantity $|\mathbf{x}_2| \geq a$, and thus the effect of the microorganism on the marine snow's settling speed (and consequently, on the fluid flow and nutrient distribution) can be neglected if

$$\frac{|\mathbf{F}_{ext}|}{6\pi\mu a V_s} \gg \frac{\alpha_D}{R^2}, \quad (5.25)$$

where, recall from eqn. 5.22 that $R = a/b$. Now, considering $\mathbf{F}_{ext} = 4/3\pi a^3 \Delta\rho \mathbf{g}$ (the marine snow particle is sinking under gravity), we have,

$$\frac{16\pi}{9} \frac{\Delta\rho g a^4}{F_D} \gg 1, \quad (5.26)$$

which is typically satisfied for the parameter values listed in Table 5.1. Similarly, the effect of rotation of the marine snow on the nutrient transport can be neglected based on the inequality $|\mathbf{U}_p| \gg |\boldsymbol{\Omega}_p \times a\hat{\mathbf{r}}|$, or,

$$\frac{|\mathbf{F}_{ext}|}{6\pi\mu a V_s} \gg \frac{3\alpha_D}{2R^2}, \quad (5.27)$$

which yields,

$$\frac{32\pi}{27} \frac{\Delta\rho g a^4}{F_D} \gg 1. \quad (5.28)$$

Eqns. 5.26 and 5.28 allow us to neglect the effect of aggregate-bacterium hydrodynamic interactions on the nutrient transport (eqn. 5.2). In addition, the Reynolds number corresponding to the marine snow aggregates considered in this work, $Re_{ms} \ll 1$; hence, we use,

$$\mathbf{v}_{St} = -\mathbf{U}_{p,0} + \left(\frac{3a}{4r} + \frac{a^3}{4r^3} \right) \mathbf{U}_{p,0} + \left(\frac{3a}{4r^3} - \frac{3a^3}{4r^5} \right) \mathbf{x} (\mathbf{U}_{p,0} \cdot \mathbf{x}), \quad (5.29)$$

in eqn. 5.2. Eqn. 5.29 is the flow field due to a sphere being acted upon by an external force \mathbf{F}_{ext} , in the regime of negligible inertia. In eqn. 5.29, $r = |\mathbf{x}|$ and $\mathbf{U}_{p,0} = \mathbf{F}_{ext}/(6\pi\mu a)$ is the velocity of a sphere of radius a in presence of an external force \mathbf{F}_{ext} and negligible inertia, obtained by substituting $\alpha_D = 0$ in eqn. 5.23, hence the sub-script ‘0’.

Appendix C: Simulation details

Nutrient concentration

We solved eqn. 5.2 using a finite element method, and validated our code by comparing the value of the Sherwood number (as a function of Péclet number) with analytical and numerical predictions (see Fig. 5.11 in the Appendix).

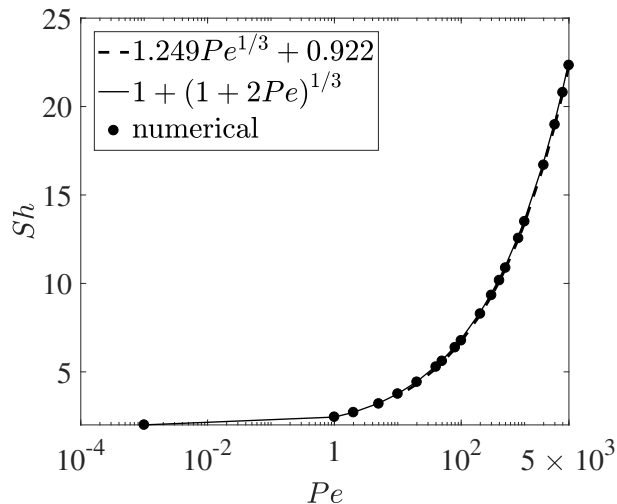


Figure 5.11. : The Sherwood number—a dimensionless measure of the mass transfer rate at the sphere surface—as a function of the Péclet number evaluated using numerical simulations and compared against analytical predictions for $Pe \gg 1$ [dashed line, by [205]] and numerical predictions valid for all Péclet numbers [solid line, by [206]].

Bacteria trajectories

We simulate the mathematical model described in Sections 5.2.1 and 5.2.2, for a system containing $N_b = 1000$ non-interacting bacteria, placed uniformly within a disk of radius $2a$ at a vertical separation $5a$ below the sinking marine snow particle. The simulations are run until either the bacteria are at separations greater than $r_{lim} = 50a$ from the center of the marine snow, or the maximum simulation time is reached. As we are only considering bacteria upstream from the settling marine snow and from within the disc, we are actually neglecting any bacteria that could drift in from above the marine snow, or from ‘the side’. However, as long as the aggregate settles at a rate much faster than the bacterial swimming speed, we can safely neglect the drifting in of any bacteria from above the marine snow. Also, the time taken by a bacterium to diffuse in from the sides via a random walk is $t_d \sim a^2/(V_s^2\tau_0/6)$. Therefore, as long as the aggregate falls a distance greater than a in this time, i.e., as long as $U_p t_d \gg a$, the diffusion of bacteria from the sides can also be neglected. In our case, the minimum value of the ratio $U_p t_d/a$ is ≈ 50 , and so bacteria diffusing in from the sides would not get ample time to locate the nutrient source [167].

We emphasize that the value of the threshold bacteria-aggregate separation above which the simulations are stopped (i.e., r_{lim}), has a minor quantitative effect on the final results, with all our descriptions of the possible qualitative behaviors staying the same. Fig. 5.12 shows that increasing r_{lim} by a factor of two is seen to affect the \bar{C} values of chemotactic bacteria most acutely—by almost 10%—for the case of strongest hydrodynamic interaction. The values of \bar{C} for chemotactic bacteria with weak hydrodynamic interaction, and those for non-chemotactic bacteria do not change appreciably. The maximum change in the values of A_C for chemotactic bacteria is by only 3%, suggesting that our predictions are robust against changes to r_{lim} . It can also be seen that using larger number of bacteria, say, $N_b = 5000$, does not have a very significant quantitative effect on our results (see Fig. 5.6(b) in Section 5.3.2).

We march the equations governing $\mathbf{x}_2(t)$ and $\mathbf{p}(t)$ in time using an explicit Euler method, and track the position and the nutrient concentration to which the bacteria are exposed. We compute DC/Dt for the bacteria at each time-step Δt , and effect a tumble if the quantity $\Delta t/\tau > \mathcal{R}$, where τ is given by eqn. 5.3, and \mathcal{R} is a uniformly chosen random number from $[0,1]$ [161,180]. The tumble is implemented by changing the bacterium's orientation from \mathbf{p} to \mathbf{p}' , with there being no correlation between \mathbf{p} and \mathbf{p}' (isotropic tumbles). The implementation of correlated tumbles, including the 'run-reverse-flick' strategy, is straightforward in that the angle between \mathbf{p}' and \mathbf{p} must be chosen from a prescribed, non-uniform distribution. We also assume that the tumbles are instantaneous. It is easy to see that whenever $DC/Dt > 0$, the tumbling probability $\Delta t/\tau$ is smaller than the unbiased tumbling probability $\Delta t/\tau_0$, and so a bacterium moving up a nutrient gradient is less likely to veer off in a different direction.

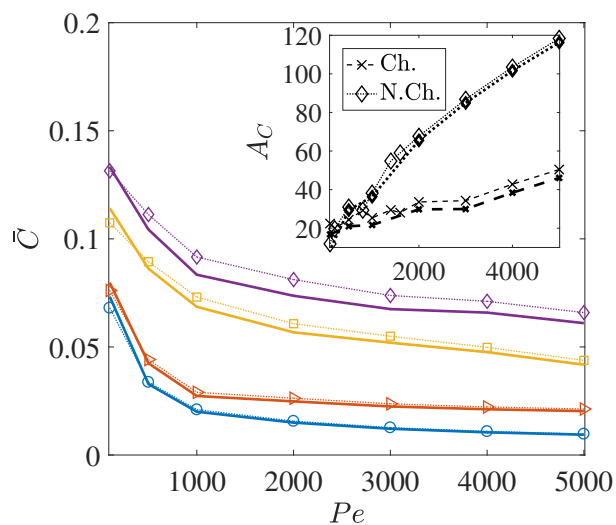


Figure 5.12. : The variation in the average nutrient exposure, \bar{C} , for chemotactic and non-chemotactic bacteria, with $r_{lim} = 25$ (thick lines) and $r_{lim} = 50$ (thin lines). The legends in the main figure are as follows: Diamonds - chemotactic, $\alpha_D = 2$; Boxes - chemotactic, $\alpha_D = 0.1$; Triangles - non-chemotactic, $\alpha_D = 2$; Circles - non-chemotactic, $\alpha_D = 0.1$. Note how r_{lim} affects \bar{C} the most for chemotactic bacteria with $\alpha_D = 2$: this is because the bacteria that get hydrodynamically trapped contribute the same amount to the overall mean nutrient exposure irrespective of the value of r_{lim} .

Table 5.1. : List of parameters and their values used in the numerical simulations.

Symbol	Description	Value range (units)
Flow		
μ	Viscosity of suspending fluid	0.01 (poise)
ρ	Density of suspending fluid	1.00 (g/cm ³)
$d = 2a$	Diameter of marine snow	0.04 - 0.13 (cm)
$\Delta\rho$	Excess density of marine snow	10 ⁻⁴ - 10 ⁻³ (g/cm ³)
$U_p = (2/9)\Delta\rho ga^2/\mu$	Settling speed of marine snow	0.004–0.046 (cm/s)
$Re_b = \rho V_s b/\mu$	Reynolds number for bacterium	10 ⁻⁵ - 10 ⁻⁴
$Re_{ms} = \rho U_p d/\mu$	Reynolds number for marine snow	0.02 - 0.6
Bacteria		
V_s	Swimming speed	10 - 50 ($\mu\text{m/s}$)
b	Size	1 - 10 (μm)
α_C	Chemotactic time constant	1200 (s)
τ_0	Mean run-time	0.4 - 10 (s)
D_r	Brownian rotational diffusivity	10 ⁻³ - 10 ⁻² (s ⁻¹)
F_D	Bacterial dipole strength	0.1 - 1 (pN- μm)
$\alpha_D = F_D/(8\pi\mu b^2 V_s)$	Dimensionless dipole strength	0.1-2
Nutrient		
C_0	Reference concentration	25 (μM)
K_D	Half-saturation constant of chemoreceptor	2.5 - 250 (μM)
D_C	Diffusivity	4×10^{-7} - 2×10^{-5} cm ² /s
$Sc = \nu/D_C$	Schmidt number	500 - 25000
$Pe = U_p a/D_C$	Péclet number	100 - 5000
$Pe_b = U_p a/(V_s^2 \tau_0/6)$	bacterial Péclet number	50 - 40000
$\delta_C \approx (9\mu D_C/2\Delta\rho g)^{1/3}$	Concentration boundary layer thickness	0.0026–0.0132 (cm)
Simulation		
Δt	Dimensionless time step	10 ⁻³
N_b	Number of bacteria in simulation	1000 - 5000
$L_{up} = 5a$	Upstream bacteria starting distance	0.1 - 0.38 (cm)
$R_{disk} = 2a$	Radius of disk of bacteria's initial positions	0.04 - 0.13 (cm)

6. BIOFILMS AT INTERFACES: MICROBIAL DISTRIBUTION IN FLOATING FILMS

6.1 Introduction

Hydrodynamics of swimming microorganisms—a branch of physical sciences with ever-expanding frontiers—has seen intense research from a host of perspectives, an important one being the study of motility near rigid/fluid surfaces [8, 105, 207]. The fluid flow around a microorganism swimming near a surface is fundamentally different than that in an unbounded domain. This difference stems from the fluid dynamic constraints (boundary conditions) imposed by ambient surfaces which result in a ‘hydrodynamic interaction’ of the microorganism with the surface. It can cause: (i) a change in the organism’s swimming speed, or, (ii) a change in its swimming trajectory due to an induced rotation, or, (iii) a drift toward the surface causing surface-accumulation. These physical effects have important consequences on the near-surface functions of microorganisms, e.g., navigation through confinements, foraging, host invasion, stress evasion, and nutrient-source-colonization [204, 208]. Knowledge of microbial locomotion near surfaces can thus drive discovery and inform developments in applications like mammalian fertilisation, control of infectious diseases, membrane anti-fouling and bacterial bioremediation.

In light of these motivations, a large number of analytical, numerical and experimental studies have been conducted on the motion of microorganisms near surfaces. These focus on the motion of micro-swimmers near: (i) a single rigid surface [14, 19, 20, 22, 27, 29–31, 107, 160, 195, 209–214]; (ii) a single plane [23, 24, 30, 147, 215, 216], or deforming [146, 217, 218] fluid-fluid interface; (iii) under confinement by two rigid

⁰This chapter, with additions and/or changes, will be eventually submitted to a peer-reviewed journal, to be considered for publication.

surfaces [21, 109, 196, 219, 220]; or, (iv) under confinement by a rigid surface and a free surface (also called in a film) [28, 221]. Together, these investigations have revealed a fascinating array of swimming behavior displayed by micro-swimmers in the vicinity of surfaces. Motion near a single rigid/fluid surface has been categorized as: (i) attraction to rigid walls [14, 21, 22, 27, 31, 160], (ii) attraction to non-deforming [30, 147, 160, 216] and deforming [146, 217] interfaces; (iii) swimming in circles with the directionality (clockwise vs. counter-clockwise when seen from the ‘microorganism side’) being determined by the rigidity/fluidity of the nearby surface [20, 23, 24, 30]; (iv) scattering away from a rigid [14] or a free surface [160]; and, (v) swimming at a fixed distance from a nearby rigid surface [19, 30, 31, 212–214], a plane, surfactant-laden free surface [23, 24, 30] or deforming free surface [218]. The swimming behavior within a fluid film is generally a combination of the above effects, depending on the swimmer’s proximity to either confining surface, and is useful in predicting microorganism distribution in biofilms [28, 221]. In addition, an imposed external flow can yield rich swimming dynamics of confined microorganisms, depending on the strength of the external flow and the swimmer-surface hydrodynamic interactions [222], e.g., (i) ‘trapping’ in high-shear regions [223, 224], (ii) oscillating across the width of a parallel-plate channel [225, 226], and, (iii) detachment of ‘hydrodynamically attached’ swimmers from a wall due to high external shear [18].

While hydrodynamics-mediated microbial distribution in biofilms resting on rigid substrates has received some attention [18, 28, 221], there are relatively fewer works which focus on *floating* biofilms. A floating biofilm is a unique configuration wherein microorganisms populate a fluid surface instead of a rigid one. It can be idealized as a suspension of microorganisms in a confinement with an air-fluid interface on one side and a fluid-fluid interface on the other. These systems, called “films of bacteria at interfaces” [67], are becoming exceedingly relevant in applications like bioremediation of oil spills [3], emulsion stabilization [227, 228], pathogen control [229] and more fundamental processes like transfer of organic matter between the surface, the bulk and the substratum in lakes and oceans [204, 230]. Motivated by these applications,

we wish to understand how hydrodynamics influences the distribution of microorganisms in floating films. Specifically, under what scenarios does hydrodynamics cause the microorganisms to preferentially reside at/near one of the two (air-fluid or fluid-fluid) confining interfaces? How is this preference affected if the film is flowing? The answer to these questions will depend on the microorganism's geometry (shape and propulsion mechanism) and the physical properties of its surroundings (viscosities of its suspending and underlying fluids, external fluid-flow rates). Our aim is to develop a mathematical model that allows quantification of microorganism distribution across the height of the floating film, with consistent treatment of the flow-physics affecting microorganism dynamics. Towards this, we formulate a problem based on far-field hydrodynamics, stochastic simulation of microorganism trajectories and computation of their time-averaged spatial distributions. Section 6.2 introduces the mathematical model, followed by a description of the solution methodology employed. In Section 6.3.1 we describe the procedure used to obtain the main results in this manuscript, with Sections 6.3.2 and 6.3.3 discussing microbial dynamics in biofilms that are stagnant and flowing, respectively. Finally, Section 6.4 summarizes the main results, suggests many useful extensions of the present work and concludes this study.

6.2 Mathematical model

The Reynolds number corresponding to microorganism swimming is small enough to neglect the effects of inertia on fluid flow and on the motion of the microorganism. The fluid flow is thus governed by the continuity and the Stokes flow equations. This also allows us to use a multipole expansion representation for the swimmer, i.e., we model the swimmer as a collection of Stokes flow singularities located at its centroid, and use them to evaluate any ensuing hydrodynamic interactions. The geometry of our problem is explained in Fig. 6.1. A microorganism of characteristic size a is contained in a fluid of viscosity μ_1 (henceforth called fluid-1), which floats on another fluid of viscosity μ_2 (fluid-2). Any point of interest in the domain is

identified by the coordinate $\mathbf{x} \equiv (x_1, x_2, x_3)$. The height of the fluid-1 film is H . The air-fluid (resp. fluid-fluid) interface at $x_3 = H$ (resp. $x_3 = 0$) is referred to as A-F (resp. F-F). The microbe's configuration is uniquely identified by its height above the $F - F$, z , and its in-plane orientation, θ . We must note that the system described above is an idealization of a biofilm in that the fluid-1 is treated as a Newtonian fluid, and biofilms are generally complex structures characterized by a non-Newtonian environment. However, in this first exploration, we focus on films of bacteria in a Newtonian fluid, which is indeed an appropriate assumption in some instances [204, 231]. We emphasize that complex interfacial and bulk fluid behavior can be systematically incorporated into our mathematical model and comment further on this aspect in Section 6.4.

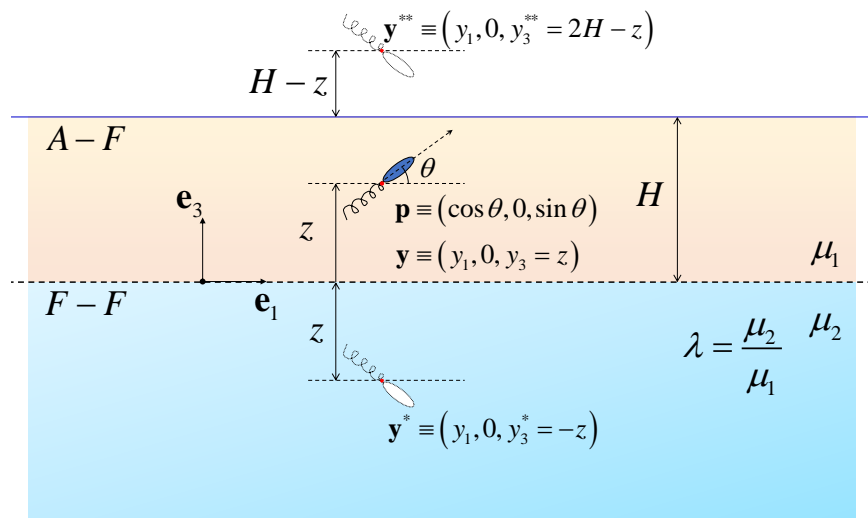


Figure 6.1. : A schematic of the problem being solved. Shown here is the microorganism located at $\mathbf{x} = \mathbf{y}$, along with its ‘images’ at \mathbf{y}^* (w.r.t. the fluid-fluid interface) and at \mathbf{y}^{**} (w.r.t. the air-fluid interface). $A - F$ (resp. $F - F$) refers to the air-fluid (fluid-fluid) interface. Note that the \mathbf{e}_2 component of the swimmer’s orientation has been set to zero without loss of generality. The vertical distribution of a suspension of non-interacting microorganisms depends on the morphology of the microorganisms and the viscosity ratio, $\lambda \equiv \mu_2/\mu_1$, of the fluids involved.

6.2.1 Stokeslet in a floating film

A formal solution procedure for our model of swimmer dynamics in a floating film begins with the fundamental solution to the Stokes equations (in fluid-1) perturbed by a point force (called a Stokeslet) at a prescribed position \mathbf{y} :

$$\nabla \cdot \mathbf{u}^{(1)} = 0, \quad (6.1a)$$

$$\nabla \cdot \mathbf{T}^{(1)} + \mathbf{f}\delta(\mathbf{x} - \mathbf{y}) = \mathbf{0}, \quad (6.1b)$$

$$\mathbf{u}^{(1)}(|\mathbf{x}| \rightarrow \infty) = \mathbf{0}, \quad (6.1c)$$

where, $\mathbf{T}^{(1)}$ is the stress tensor in a Newtonian fluid, given by,

$$\mathbf{T}^{(1)} = -P^{(1)}\mathbf{I} + \mu_1 (\nabla\mathbf{u}^{(1)} + \nabla\mathbf{u}^{(1),T}), \quad (6.2)$$

with $P^{(1)}$ being the fluid pressure, \mathbf{I} the identity matrix, the super-script ' T ' denoting transposition and μ_1 is the fluid viscosity. The linearity of the Stokes flow equations allow us to write the solution of eqn. 6.1 as:

$$\mathbf{u}^{(1)}(\mathbf{x}) = \mathcal{G}^{Os}(\mathbf{x} - \mathbf{y}) \cdot \mathbf{f}, \quad (6.3)$$

where \mathcal{G}^{Os} is the free-space Green's function for the problem, the well-known Oseen tensor,

$$\mathcal{G}^{Os}(\mathbf{x} - \mathbf{y}) = \frac{1}{8\pi\mu_1} \left(\frac{\mathbf{I}}{|\mathbf{x} - \mathbf{y}|} + \frac{(\mathbf{x} - \mathbf{y})(\mathbf{x} - \mathbf{y})}{|\mathbf{x} - \mathbf{y}|^3} \right). \quad (6.4)$$

Now, if instead of being in an unbounded homogeneous fluid-1, the point-force is exerted at a distance z from fluid-2, then one must also solve for the Stoke flow equations in fluid-2 (without the forcing term), subject to the boundary conditions of continuity of velocity and shear stress at the fluid-fluid interface (F-F):

$$\mathbf{u}^{(1)} = \mathbf{u}^{(2)}, \text{ at } x_3 = 0, \quad (6.5a)$$

$$\mathbf{e}_3 \cdot \{\Delta\mathbf{T}\} \cdot \mathbf{e}_1 = \mathbf{e}_3 \cdot \{\Delta\mathbf{T}\} \cdot \mathbf{e}_2 = 0, \text{ at } x_3 = 0, \quad (6.5b)$$

where, $\Delta\mathbf{T} = \mathbf{T}^{(1)} - \mathbf{T}^{(2)}$. This problem (eqns. 6.1 and 6.5) was solved by Aderogba and Blake in ref. [232]. $\mathbf{u}^{(1)}(\mathbf{x})$ can be represented as a superposition of the original

force singularity with a system of ‘image singularities’ placed at the ‘image point’ $\mathbf{y}^* = \mathbf{y} - 2(\mathbf{e}_3 \cdot \mathbf{y})\mathbf{e}_3$ (see Fig. 6.1). One can write

$$\mathbf{u}^{(1)}(\mathbf{x}) = \mathcal{G}_1^{FF}(\mathbf{x}, \mathbf{y}, \mathbf{y}^*; \lambda) \cdot \mathbf{f}, \quad (6.6)$$

with,

$$\begin{aligned} \mathcal{G}_1^{FF}(\mathbf{x}, \mathbf{y}, \mathbf{y}^*; \lambda) &= G^{Os}(\mathbf{x} - \mathbf{y}) - \mathbf{N}^\lambda \cdot G^{Os}(\mathbf{x} - \mathbf{y}^*) \\ &+ \{2\Lambda_1 z (\mathbf{e}_3 \cdot \nabla_0) + \Lambda_1 z^2 \mathbf{M} \cdot \nabla_0^2\} G^{Os}(\mathbf{x} - \mathbf{y}^*), \end{aligned} \quad (6.7)$$

where $\nabla_0 \equiv \partial/\partial\mathbf{y}$, $\mathbf{N}^\lambda \equiv \text{diag.}(\Lambda_2, \Lambda_2, 1)$, with $\Lambda_2 = (\lambda - 1)/(\lambda + 1)$; $\Lambda_1 = \lambda/(\lambda + 1)$; and, $\mathbf{M} \equiv \text{diag.}(1, 1, -1)$. The first term on the right hand side of eqn. 6.7 represents the effect of the force singularity in fluid-1, while the other terms are contributions from the image. Similarly, the flow-field in fluid-2 can also be represented as contributions from singularities placed at \mathbf{y} , as $\mathbf{u}^{(2)}(\mathbf{x}) = \mathcal{G}_2^{FF}(\mathbf{x}, \mathbf{y}; \lambda) \cdot \mathbf{f}$, with,

$$\begin{aligned} \mathcal{G}_2^{FF}(\mathbf{x}, \mathbf{y}; \lambda) &= \frac{2}{1 + \lambda} \mathbf{R} \cdot \mathcal{G}^{Os}(\mathbf{x} - \mathbf{y}) + \\ &\frac{2}{1 + \lambda} \left\{ z (\mathbf{e}_3 \cdot \nabla_0) - \frac{z^2}{2} \nabla_0^2 \right\} \mathcal{G}^{Os}(\mathbf{x} - \mathbf{y}), \end{aligned} \quad (6.8)$$

where $\mathbf{R} \equiv \text{diag.}(1, 1, 0)$. Therefore, flow-fields given by $\mathbf{u}^{(1)}(\mathbf{x}) = \mathcal{G}_1^{FF} \cdot \mathbf{f}$ and $\mathbf{u}^{(2)}(\mathbf{x}) = \mathcal{G}_2^{FF} \cdot \mathbf{f}$ will satisfy the Stokes equations and the boundary conditions in eqns. 6.5.

One special case of the aforementioned discussion is when the point-force acts near an air-fluid interface (A-F). Consider now the presence of an A-F at $x_3 = H$, which requires $\mathbf{u}^{(1)}(\mathbf{x})$ to satisfy the boundary conditions:

$$\mathbf{e}_3 \cdot \mathbf{u}^{(1)} = 0, \text{ at } x_3 = H, \quad (6.9a)$$

$$\mathbf{e}_3 \cdot \mathbf{T}^{(1)} \cdot \mathbf{e}_1 = \mathbf{e}_3 \cdot \mathbf{T}^{(1)} \cdot \mathbf{e}_2 = 0, \text{ at } x_3 = H. \quad (6.9b)$$

The boundary conditions in eqns. 6.9 are indicative of vanishing normal velocity and shear stresses. The solution to eqns. 6.1 and 6.9 is obtained easily by a slight adjustment and reinterpretation of eqns. 6.6 and 6.7. We just need to substitute

$\lambda = 0$ in eqn. 6.7 and note that now the image singularities must lie at $\mathbf{y}^{**} = \mathbf{y} + 2\{H - (\mathbf{e}_3 \cdot \mathbf{y})\} \mathbf{e}_3$ (see Fig. 6.1). This yields

$$\mathbf{u}^{(1)}(\mathbf{x}) = \mathcal{G}_1^{AF}(\mathbf{x}, \mathbf{y}, \mathbf{y}^{**}) \cdot \mathbf{f}, \quad (6.10)$$

with,

$$\mathcal{G}_1^{AF}(\mathbf{x}, \mathbf{y}, \mathbf{y}^{**}) = G^{Os}(\mathbf{x} - \mathbf{y}) + \mathbf{M} \cdot G^{Os}(\mathbf{x} - \mathbf{y}^{**}), \quad (6.11)$$

The solutions discussed thus far—for a point force near a F-F or an A-F—are exact in terms of satisfying the governing equations and the appropriate boundary conditions. However, errors are introduced when *both* these interfaces exist, the configuration of interest in this work. The errors stem from the fact that the fluid velocity in eqn. 6.6 does not satisfy the boundary conditions given in eqn. 6.9, and the fluid velocity in eqn. 6.10 does not satisfy the boundary conditions given in eqn. 6.5. Therefore, an accurate calculation of $\mathbf{u}^{(1)}(\mathbf{x})$ for a Stokeslet under confinement by two interfaces would require us to obtain successive ‘images of images’ an infinite number of times [221, 233]. However, for the evaluation of a microorganism’s hydrodynamically induced translational and rotational velocities, we can neglect the effect of the higher order images as a first approximation; this is discussed in the next section.

6.2.2 Hydrodynamic interactions: Higher order multipoles

Once the image system for a Stokeslet in a floating film is known, we can take its appropriate derivatives to construct the image systems for more complex force distributions. This is important because we are modeling the microorganism—and its hydrodynamic interactions with the interfaces—as a distribution of forces that its appendages exert on the fluid. These can be recovered by writing the multipole expansion form of the flow induced by the microorganism’s motion [15]. For this, we assume the microorganism to be an axisymmetric prolate spheroid of major axis length $2a$ and minor axis length $2b$. At a given instant, it is located at $\mathbf{x} = \mathbf{y}$, and oriented along the direction \mathbf{p} . The multipole expansion of the flow due to the microorganism

can be represented in terms of its contributions in an unbounded fluid, which involve gradients of the Oseen tensor $\mathcal{G}^{Os}(\mathbf{x} - \mathbf{y})$, plus correction terms—encoded in a tensor, say \mathcal{H} —stemming from the planar interfaces:

$$\mathbf{u}^{(1)}(\mathbf{x}) = \mathbf{u}^D(\mathbf{x}) + \mathbf{u}^{SD}(\mathbf{x}) + \mathbf{u}^Q(\mathbf{x}) + \mathbf{u}^R(\mathbf{x}) + \dots, \quad (6.12)$$

where,

$$\frac{\mathbf{u}^D}{8\pi\mu_1} = \kappa(\mathbf{p} \cdot \nabla_0) \{(\mathcal{G}^{Os} + \mathcal{H}) \cdot \mathbf{p}\}, \quad (6.13a)$$

$$\frac{\mathbf{u}^{SD}}{8\pi\mu_1} = -\frac{\sigma}{2} \nabla_0^2 \{(\mathcal{G}^{Os} + \mathcal{H}) \cdot \mathbf{p}\}, \quad (6.13b)$$

$$\frac{\mathbf{u}^Q}{8\pi\mu_1} = \nu(\mathbf{p}\mathbf{p} : \nabla_0 \nabla_0) \{(\mathcal{G}^{Os} + \mathcal{H}) \cdot \mathbf{p}\}, \quad (6.13c)$$

$$\frac{\mathbf{u}^R}{8\pi\mu_1} = \tau(\mathbf{p} \cdot \nabla_0) \nabla_0 \times \{(\mathcal{G}^{Os} + \mathcal{H}) \cdot \mathbf{p}\}. \quad (6.13d)$$

Note that all directional gradients in eqn. 6.13 have been taken with respect to \mathbf{p} , which is a manifestation of the microorganism's axisymmetry [15]. The absence of any terms proportional to $\{(\mathcal{G}^{Os} + \mathcal{H}) \cdot \mathbf{p}\}$ signify that the microorganism does not exert any *net* force or torque on the fluid. The terms in eqns. 6.13a to 6.13d are called the force dipole, the source dipole, the force quadrupole and the rotlet dipole respectively, and each has its own physical meaning. The force dipole represents the equal and opposite forces the microorganism exerts on the fluid, the source dipole represents the finite size of the microorganism, the force quadrupole represents the first effects of asymmetric forcing—stemming from asymmetry in microbial shape—by the microorganism and the rotlet dipole represents the equal and opposite torques that a (helically flagellated) microorganism exerts on the fluid [14, 221]. The coefficients $\kappa, \sigma, \nu, \tau$ are called the strengths of each of these singularities. Dimensional consistency requires their dimensions to be: $[\kappa] = [\text{velocity} \times \text{length}^2]$ and $[\sigma, \nu, \tau] = [\text{velocity} \times \text{length}^3]$. It is very important to note that in principle, the multipole expansion is a valid description of the flow in the far-field of a swimmer, but remarkably, experiments (see ref. [21]) and numerical simulations (see ref. [14]) have shown that it is accurate up to swimmer-boundary separations as small as one body-length. Also, one could extend

the multipole expansion of eqn. 6.12 even further, but we restrict ourselves to 4 terms for simplicity, and also because these terms capture the essential swimmer dynamics and have easily realizable physical significance. In fact, because we are eventually interested in swimmer distributions transverse to the floating film, we do not discuss the hydrodynamic effects of the rotlet dipole (eqn. 6.13d) as it does not yield any swimmer motion in the \mathbf{e}_3 direction [14, 160, 221].

The ‘ \mathcal{H} terms’ in eqn. 6.13, by definition, denote the hydrodynamic influence of the confinement (F-F and A-F) on the swimmer-generated flow. This influence results in the swimmer’s translation and rotation. It is quantified by the Faxén laws for a force-free and torque-free spheroidal particle:

$$\begin{aligned} \mathbf{u}_{HI}(\mathbf{y}, \mathbf{p}) &= \mathbf{u}^{\mathcal{H}}(\mathbf{x} = \mathbf{y}) + O(a^2/H^2), \\ \boldsymbol{\Omega}_{HI}(\mathbf{y}, \mathbf{p}) &= \left[\frac{1}{2} \nabla \times \mathbf{u}^{\mathcal{H}}(\mathbf{x}) + \frac{\gamma^2 - 1}{\gamma^2 + 1} \mathbf{p} \times (\mathbf{E}^{\mathcal{H}}(\mathbf{x}) \cdot \mathbf{p}) \right] \Big|_{\mathbf{x}=\mathbf{y}} \\ &\quad + O(a^2/H^2), \end{aligned} \quad (6.14)$$

where a/H is the characteristic microorganism size normalized by the height of the film, the super-script ‘ \mathcal{H} ’ denotes contributions to $\mathbf{u}^{(1)}(\mathbf{x})$ from the images of the swimmer’s singularity representation, $\gamma = a/b$ is the aspect ratio of the microorganism and $\mathbf{E}^{\mathcal{H}}$ is the rate-of-strain tensor derived from the $\mathbf{u}^{\mathcal{H}}$ flow.

An explicit expression for \mathcal{H} will complete our quantification of the swimmer-interface hydrodynamic interactions. Based on the discussion in Section 6.2.1, one would require to take infinite images to accurately satisfy the boundary conditions on both A-F and F-F. However, in the present problem, our aim is to use the above-described method of images to obtain the hydrodynamically induced translational and rotational velocities of a model swimmer. This requires evaluation of $\mathbf{u}^{\mathcal{H}}(\mathbf{y})$, i.e., the flow due to the image system evaluated *at* the microorganism’s location (see Faxén laws given in eqns. 6.14). The major contribution to $\mathbf{u}^{\mathcal{H}}(\mathbf{y})$ comes from the first two images: (i) the image at \mathbf{y}^* , taken with respect to the fluid-fluid interface (eqns. 6.6 and 6.7), and, (ii) the image at \mathbf{y}^{**} , taken with respect to the air-fluid interface (eqns. 6.10 and 6.11). The contributions due to any other ‘image of image’

will be of a higher order in a/H . So as a first approximation, they can be neglected in comparison to the contributions due to the images at \mathbf{y}^* and \mathbf{y}^{**} . In addition, the higher order images will always be further from the microorganism than the images at either \mathbf{y}^* or \mathbf{y}^{**} , so the dominant contribution to the hydrodynamic interactions will always stem from one of the two images shown in Fig. 6.1. This is especially true when considering thick fluid films, i.e., when $a/H \ll 1$. Therefore, we approximate the ‘film correction’ as that due to the first two images of the Stokeslet,

$$\begin{aligned} \mathcal{H}(\mathbf{x}, \mathbf{y}, \mathbf{y}^*, \mathbf{y}^{**}; \lambda) &\approx \mathcal{G}_1^{FF}(\mathbf{x}, \mathbf{y}, \mathbf{y}^*; \lambda) \\ &+ \mathcal{G}_1^{AF}(\mathbf{x}, \mathbf{y}, \mathbf{y}^{**}) - 2\mathcal{G}^{Os}(\mathbf{x} - \mathbf{y}), \end{aligned} \quad (6.15)$$

where \mathcal{G}_1^{FF} and \mathcal{G}_1^{AF} are given in eqns. 6.7 and 6.11, respectively. Along with the hydrodynamics-induced drift and reorientation, a microorganism has its own active motility, can interact sterically with either interface and has a tendency to reorient itself randomly due to structural imperfections. Therefore, the motion of the microorganism is described by the following coupled, non-linear ordinary differential equations:

$$\begin{aligned} \frac{d\mathbf{y}}{dt} &= V_s \mathbf{p} + \mathbf{u}_{HI}(\mathbf{y}, \mathbf{p}) + \mathbf{V}_{st}, \\ d\mathbf{p} &= \left\{ \boldsymbol{\Omega}_{HI}(\mathbf{y}, \mathbf{p}) \times \mathbf{p} + \sqrt{4D_r/dt} d\mathbf{W} \right\} dt, \end{aligned} \quad (6.16)$$

where D_r is the rotational diffusivity of the microorganism and $d\mathbf{W}$ is a random variable chosen from a normal distribution with zero mean and unit variance. The expressions for the \mathbf{e}_3 component of $\mathbf{u}_{HI}(\mathbf{y}, \mathbf{p})$, and the \mathbf{e}_2 component of $\boldsymbol{\Omega}_{HI}(\mathbf{y}, \mathbf{p})$ have been provided, singularity-wise, in the Appendix (see eqns. 6.25 to 6.30). These are the only hydrodynamic components responsible for altering the vertical distribution of the swimmers. \mathbf{V}_{st} is the steric-interaction-induced velocity of the microorganism which prevents it from penetrating into the interface; it is implemented as a hard-core repulsion. Finally, note that swimmer elongation will result in steric torques upon contact with the interface, but we neglect them in this study as their influence on the swimmers’ spatial distribution is not very significant.

We conclude this section with a physical discussion of the microorganism's behavior within the floating film. The hydrodynamic-interaction-effects will be strongest at swimmer-interface separations corresponding to ~ 1 swimmer body-length [17,21]; beyond these the swimmer motion will be dictated by self-propulsion and rotary diffusion [109,207,226]. Thus, in the present configuration, a swimmer near the center of the film is expected to swim toward one of the two interfaces, reach close enough to be affected by hydrodynamic interactions and then translate and/or rotate in a fashion acutely dictated by the type of interface: A-F or F-F, and the morphology of the swimmer: the parameters γ and κ, σ, ν . The near-interface hydrodynamic interactions can lead to various behaviors which we identify, one singularity at a time, in the subsequent sections.

6.3 Results

6.3.1 Dimensionless parameters and simulation methodology

We render the equations dimensionless by scaling lengths with the film height H and velocities with the swimming speed V_s . The key dimensionless parameters in our study are the viscosity ratio, $\lambda = \mu_2/\mu_1$; the swimmer elongation γ ; and the dimensionless force dipole, $\kappa' = \kappa/(H^2V_s)$; source dipole, $\sigma' = \sigma/(H^3V_s)$; and force quadrupole, $\nu' = \nu/(H^3V_s)$ strengths. We note that by definition, higher values of λ correspond to a less viscous fluid-film floating on a more viscous underlying fluid. The symmetry about the azimuthal angle (ϕ) and along the \mathbf{e}_1 and \mathbf{e}_2 directions allows us to study the swimmer motion in terms of only two degrees of freedom: its separation from the F-F, $z' = z/H$, and its orientation $\mathbf{p} = (\cos \theta, 0, \sin \theta)$. We perform probabilistic simulations by integrating eqns. 6.16 using the explicit Euler method, for $N_b = 1000$ swimmers whose initial positions (resp. orientations) are assigned from a uniformly random distribution between $[a/H, 1-a/H]$ (resp. $[0, 2\pi]$). The simulations run until $t_{end} = 100H/V_s$, after which we extract the probability

distribution of the time-averaged swimmer position and orientation, $\Psi(\bar{z}, \bar{\theta})$, where the over-bars denote time-averages:

$$\bar{z} = \frac{1}{t_{end}} \int_0^{t_{end}} \frac{z(t')}{H} dt', \quad \bar{\theta} = \frac{1}{t_{end}} \int_0^{t_{end}} \theta(t') dt'. \quad (6.17)$$

The distribution function is normalized such that,

$$\frac{1}{2\pi} \int_0^1 \int_0^{2\pi} \Psi(\bar{z}, \bar{\theta}) d\theta d\bar{z} = 1, \quad (6.18)$$

i.e., $\Psi(\bar{z}_i, \bar{\theta}_j) d\bar{z}d\theta \times N_b/(2\pi)$ yields the number of swimmers within the bin $[\bar{z}_i \pm d\bar{z}, \bar{\theta}_j \pm d\bar{\theta}]$. Our main objective is to ascertain the time-averaged swimmer distribution as a function of film height, $\mathcal{F}(\bar{z})$, toward which we integrate eqn. 6.18 over $\bar{\theta}$, to obtain,

$$\mathcal{F}(\bar{z}) = \frac{1}{2\pi} \int_0^{2\pi} \Psi(\bar{z}, \theta) d\theta. \quad (6.19)$$

We also define the ‘fraction’ of swimmers at the F-F (resp. A-F) as \mathcal{F}^0 (resp. \mathcal{F}^1), given by,

$$\mathcal{F}^0 = \int_0^{1.1\bar{a}} \mathcal{F}(\bar{z}) d\bar{z}, \quad (6.20a)$$

$$\mathcal{F}^1 = \int_{1-1.1\bar{a}}^1 \mathcal{F}(\bar{z}) d\bar{z}, \quad (6.20b)$$

where $\bar{a} = a/H$ [18]. The quantities mentioned above act as useful indicators of the spatial distribution of swimmers as mediated by hydrodynamic interactions, self-propulsion and rotary diffusion.

6.3.2 Microorganisms in a stagnant, floating film

The major results to be reported in this section are: (i) swimmer distribution in the film, and, (ii) difference in swimmer accumulation at the two interfaces; quantified by: (i) $\mathcal{F}(\bar{z})$, and, (ii) $\Delta\mathcal{F} = \mathcal{F}^0 - \mathcal{F}^1$, respectively. In our simulations we take the films to

be relatively thick as compared to the swimmer size, i.e., we have $a/H = 1/50 \ll 1$. As a result, the viscosity ratio is expected to significantly alter the swimming behavior near the F-F, but not near the A-F. Thus for a fixed swimmer geometry, variation in $\mathcal{F}(\bar{z})$ and $\Delta\mathcal{F}$ with respect to the film viscosity (λ) can be explained on the basis of hydrodynamic interactions near the fluid-fluid interface itself. The variation $\mathcal{F}(\bar{z})$ and $\Delta\mathcal{F}$ as a function of the swimmer elongation (γ) however, will require careful consideration of hydrodynamic interactions near both interfaces.

Force dipolar interactions

The force dipole hydrodynamic interactions are the leading order effect/behavior of microbial swimming. The sign of the dipole strength, κ' , signifies two fundamentally distinct locomotion strategies. Microorganisms with $\kappa' > 0$ are called ‘pushers’ because they *push* fluid *outward* along their bodies as they swim. Exactly opposite to this, microorganisms with $\kappa' < 0$ are called ‘pullers’ as they *pull* fluid *inward* along their bodies as they swim. The pushing (resp. pulling) is achieved by locomotory appendages at the rear (resp. front) of the cell body [8].

It is common knowledge that a force dipole is always attracted to nearby interfaces. Hydrodynamic interactions cause pushers (resp. pullers) to orient parallel to (resp. perpendicular to, and ‘facing’ toward) a nearby interface and be attracted to it [147]. This explains Fig. 6.2 wherein we have almost symmetric distribution of swimmers across the film. There is slightly more accumulation near $\bar{z} \approx 0$ due to nominally stronger hydrodynamic interactions at the fluid-fluid interface. This behavior depends very weakly on both λ and γ , with $\mathcal{F}^0 = \mathcal{F}^1 + \epsilon$, $\epsilon \sim O(0.01)$ (see Fig. 6.11 in Appendix). However, one does see that pullers ($\kappa' < 0$) accumulate closer to both the interfaces than the pushers ($\kappa' > 0$). This is because hydrodynamics causes pullers to orient themselves toward the nearest interface, perpendicular to it; contrary to pushers who orient parallel to the interfaces. In this way the pullers’ motility acts in conjunction with their hydrodynamic attraction to enhance their interface

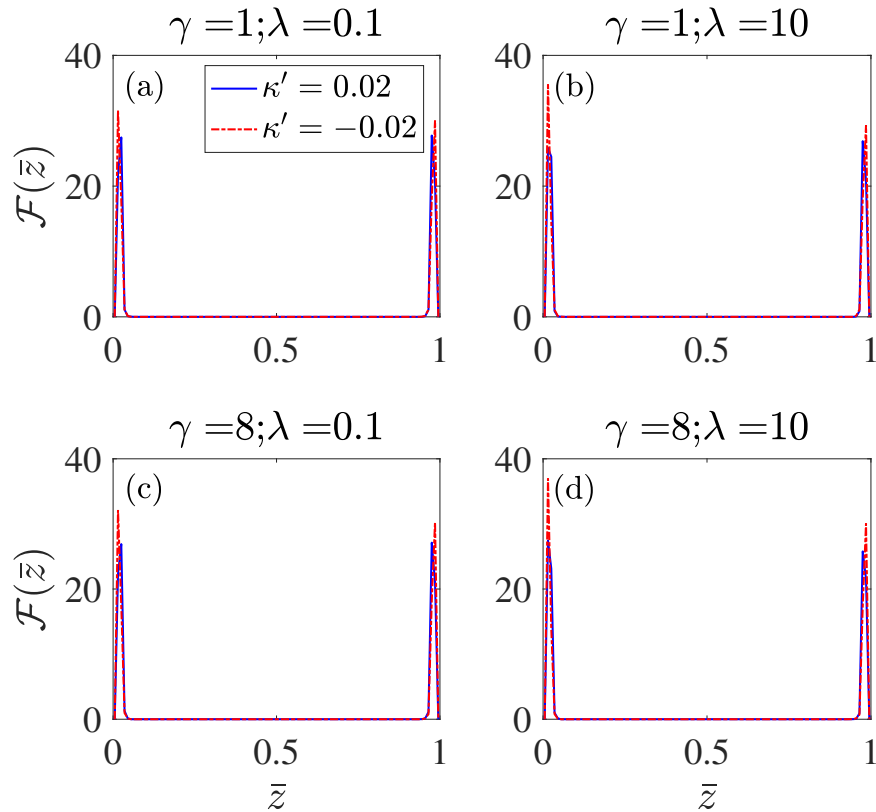


Figure 6.2. : Swimmer distribution in the film, $\mathcal{F}(\bar{z})$, as a function of λ and γ , for $\kappa' \neq 0, \sigma' = \nu' = 0$. Notice no appreciable difference between $\mathcal{F}(\bar{z} = 0)$ and $\mathcal{F}(\bar{z} = 1)$ for a wide range of swimmer elongation, γ , and the normalized film viscosity λ . The value of the dimensionless rotational diffusivity of the swimmers is $D_r / (V_s / H) = 0.2$.

accumulation as compared to pushers. We emphasize here that the stronger attraction of pullers toward a glass surface was recently observed in experiments of bi-modal *Vibrio alginolyticus*, albeit for swimming speeds larger than $20 \mu\text{m/s}$ [29]. Thus, dipolar hydrodynamic interactions, to some extent, do prove useful in explaining a salient feature of near surface swimming.

Unlike the distributions in Fig. 6.2, recent numerical simulations have suggested the existence of significant asymmetry in bacterial propulsion in both thick and thin fluid films resting on a rigid substrates [28]. This provides us a motivation to study

the hydrodynamic interactions resulting from higher order multipoles like the effects of the source dipole and the force quadrupole. We consider these one by one in the subsequent sections to identify key behaviors elicited by each, and comment on their combined effects at the end.

Source dipolar interactions

Source dipolar hydrodynamic interactions provide a finite size to the swimmer model by generating a separation of flow into regions inside and outside an impermeable boundary called the ‘hydrodynamic radius’ of the swimmer [234]. The flow due to a source dipole is representative of a ‘neutral’ swimmer, i.e., one that is neither a pusher or a puller (as its force dipolar contributions are negligible). The sign of the source dipole strength represents ciliated swimmers if $\sigma' > 0$, and non-ciliated/flagellated swimmers if $\sigma' < 0$ [14, 221].

The first important point to note about source dipolar interactions is the existence of ‘central oscillations’ for elongated ciliated swimmers ($\sigma' > 0$), as shown in Fig. 6.3(a-b). It is attributed to the finite-size-effects of the source dipole, which provides a ‘hydrodynamic repulsion’ by turning the swimmer away from any surfaces it is about to encounter. This has been extensively detailed in past studies by Mathijssen *et al.* [221, 234, 235]. They demonstrated how this ‘hydrodynamic regularization’ effect causes an elongated source-dipole swimmer to turn away from both a rigid wall and a free surface [221]. They also postulated the use of the source dipole to avoid non-singular flows due to model swimmers near walls [235]. This behavior is also consistent with numerical simulations of model squirmers by Ishimoto and Gaffney [160], wherein they demonstrated the tendency of source-dipole swimmers/neutral squirmers to rotate and swim away from rigid walls as well as free-slip surfaces after reaching a distance of closest approach. The ‘fluidity’ of the interface at $z' = 0$ does not significantly alter this oscillatory behavior. An increase in the viscosity ratio λ increases—ever so slightly—the mean height around which the swimmers oscillate [or,

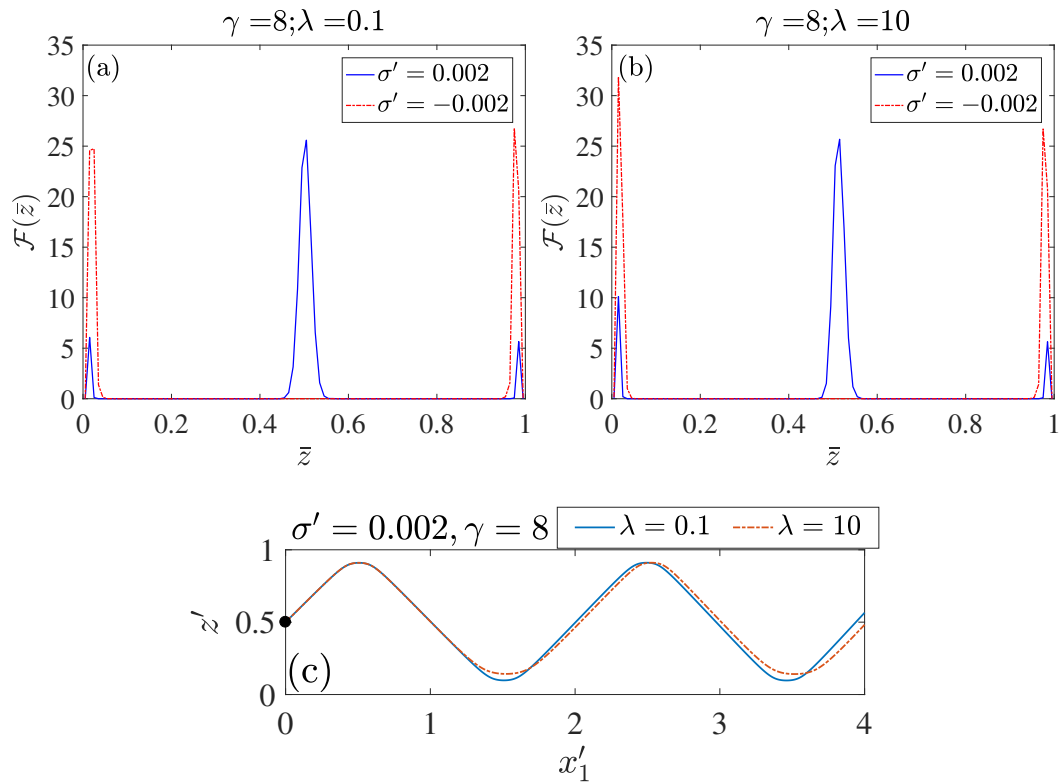


Figure 6.3. : (a-b) Swimmer distribution in the film, $\mathcal{F}(\bar{z})$, as a function of λ for $\gamma = 8$, for $\sigma' \neq 0, \kappa' = \nu' = 0$. (c) Trajectories for a source dipole swimmer with $\sigma' = 0.002$ and $\gamma = 8$. The value of the dimensionless rotational diffusivity of the swimmers is $D_r / (V_s / H) = 0.2$. The trajectories are shown for two different viscosity ratio values, $\lambda = 0.1, 10$. The initial position of the swimmer, $(x'(0), z'(0)) = (0, 0.5)$, is marked by the black circle and the initial orientation is horizontal, $\theta(0) = 0$.

alternatively, the \bar{z} position corresponding to the peak in $\mathcal{F}(\bar{z})$]. This can be seen qualitatively in the sample trajectories of the source dipole swimmers in Fig. 6.3(c).

A second important concept is the distinctly different spatial distribution for spherical swimmers, depending on the sign of σ' , as seen in Figs. 6.4(a-b). We can get useful insights into this behavior by referring to the deterministic $z'(t) - \theta(t)$ phase portraits of the swimmer dynamics, shown in Fig. 6.4(c-d). Let us consider the fate of swimmers located initially at the film center, i.e., $z'(0) = 0.5$. Swimmers with

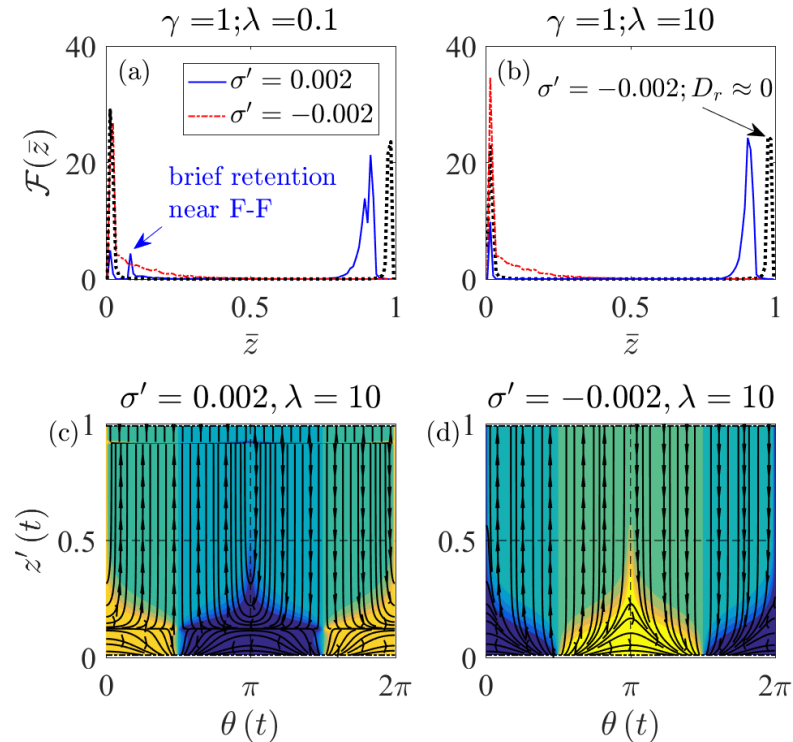


Figure 6.4. : (a-b) Swimmer distribution in the film, $\mathcal{F}(\bar{z})$, as a function of λ for $\gamma = 1$, for $\sigma' \neq 0, \kappa' = \nu' = 0$. Panel (a) marks a slight peak near $\bar{z} \approx 0.1$ by the text ‘brief retention near F-F’. This corresponds to the brief time spent by swimmers near the F-F as they reorient from $\theta > \pi$ to $\theta < \pi$ and then begin their swimming toward the A-F. This peak is even smaller (barely visible) for $\lambda = 10$. (c-d) $z' - \theta$ phase planes for spherical swimmers with non-zero source dipoles, demonstrating how/why hydrodynamics in conjunction with rotary diffusion causes, (c) ‘top accumulation’ for $\sigma' > 0$, and, (d) ‘bottom accumulation’ for $\sigma' < 0$. The contour represents the angular velocity, Ω_{HI} , of the swimmer; note that $\Omega_{HI} \approx 0$ near the A-F, i.e., near $z' = 1$. The thick dotted lines in panels (a-b) represent the distributions for swimmers with negative source dipolar coefficients when the rotary diffusion is neglected. In all other cases, the swimmers’ rotational diffusivity is taken to be $D_r = 0.2V_s/H$.

a positive source dipolar coefficient (i.e., ciliated swimmers) accumulate near the free surface and are oriented toward it. Any such swimmer heading toward the fluid-fluid surface at an angle $\theta(0) = \theta_i > \pi$, is turned away at a height of about $z' \approx 0.1$, after which it swims toward the free surface with a ‘reflected angle’ $\theta_f = 2\pi - \theta_i$. The mechanism of turning away approaching swimmers is quite rapid, to an extent that there aren’t significant (time-averaged) concentrations near the fluid-fluid interface at $z' \approx 0.1$ [see arrow and text in Fig. 6.4(a)]. This effect is prevalent for a range of viscosity ratios, with the ‘residence time’ near the fluid-fluid interface (value of local maxima at $z' \approx 0.1$) decreasing with an increase in the viscosity ratio: from a modest value in Fig. 6.4(a) to being barely visible in Fig. 6.4(b). This generalizes past predictions of “an extended residence of the swimmer in the vicinity of the free surface during scattering, compared to a no-slip boundary” [160]. It is also in qualitative agreement with the numerical simulations of Schaar *et al.*, wherein they report very low near-surface retention times for neutral swimmers [111]. In contrast to ciliated swimmers ($\sigma' > 0$), the behavior of non-ciliated swimmers ($\sigma' < 0$) is affected acutely by a combination of hydrodynamic interactions and rotational diffusion. Hydrodynamic interactions alone would cause significant accumulation at both interfaces [thick dotted line plot in Fig. 6.4(b)], depending on the initial swimmer orientations. Swimmers with $\theta(0) < \pi$ accumulate at the A-F ($z' \approx 1$) without changing their angle of approach, while those with $\theta(0) > \pi$ accumulate at the F-F ($z' \approx 0$) at an angle $3\pi/2$, i.e., pointing toward the F-F. However, as seen in eqn. 6.29 in the Appendix, the angular velocity ($\mathbf{\Omega}_{HI}^{SD} \cdot \mathbf{e}_2$) vanishes at the A-F for spherical swimmers. So the only source of reorientations at $z' \approx 1$ is rotational diffusion, i.e., the ‘ D_r term’ in eqn. 6.16. This can cause the non-ciliated swimmers at the free surface to eventually point downward, after which they get ‘pulled into’ the stable attractor in the $z' - \theta$ phase plane [see Fig. 6.4(d)], leading to accumulation at ($z' \approx 0, \theta = 3\pi/2$). We thus conclude that to accurately estimate the motility of spherical neutral swimmers near a free surface, it is crucial to consider the effects of rotary diffusion in conjunc-

tion with hydrodynamic interactions, as the latter alone predict drastically different spatial distributions.

In addition to the aforementioned trends of oscillations and asymmetric distributions, we note the small accumulation observed at $\bar{z} \approx 0$ in Figs. 6.4(a-b), for swimmers with $\sigma' > 0$. This accumulation occurs only for those swimmers whose initial positions lie within $z'(0) < 0.1 \approx 5a/H$, as is clear from the phase plane in Fig. 6.4(c). Thus, swimmers within a few body-lengths from the fluid-fluid interface cannot be ‘screened’ from it by the source dipolar interactions. The same effect also explains the minor peaks around $\bar{z} \approx 0, 1$ in Figs. 6.3(a-b).

Force quadrupolar interactions

The force quadrupolar singularity is associated with the flows produced by flagellated swimmers [209]. Swimmers with a longer flagellum and relatively smaller cell bodies correspond to a positive quadrupole strength, $\nu' > 0$, while those with a large cell body and relatively shorter flagellum correspond to a negative quadrupole strength, $\nu' < 0$ [14]. In this way, the sign of the force quadrupole indicates the region of the cell (body plus flagellum) where a greater part of the propulsive thrust or swimming drag is concentrated. Based on some of the observed geometries of bacterial cells, an example of a microorganism with $\nu' > 0$ could be *P. aeruginosa*, while one with $\nu' < 0$ could be *V. cholera* [31, 100].

The force quadrupolar interactions reveal two fascinating effects which highlight the utility of employing singularity models for microorganisms. The first effect is the preferential accumulation at the free surface for swimmers having larger cell bodies and shorter flagella (i.e., $\nu' < 0$). This is most noticeable for elongated, short-flagellated swimmers in less viscous films (see Fig. 6.5(d); recall that $\lambda = \mu_2/\mu_1$, and μ_1 is the viscosity of the fluid in which the microorganism swims; so less viscous floating films imply $\lambda > 1$). The asymmetry between accumulation at the free surface

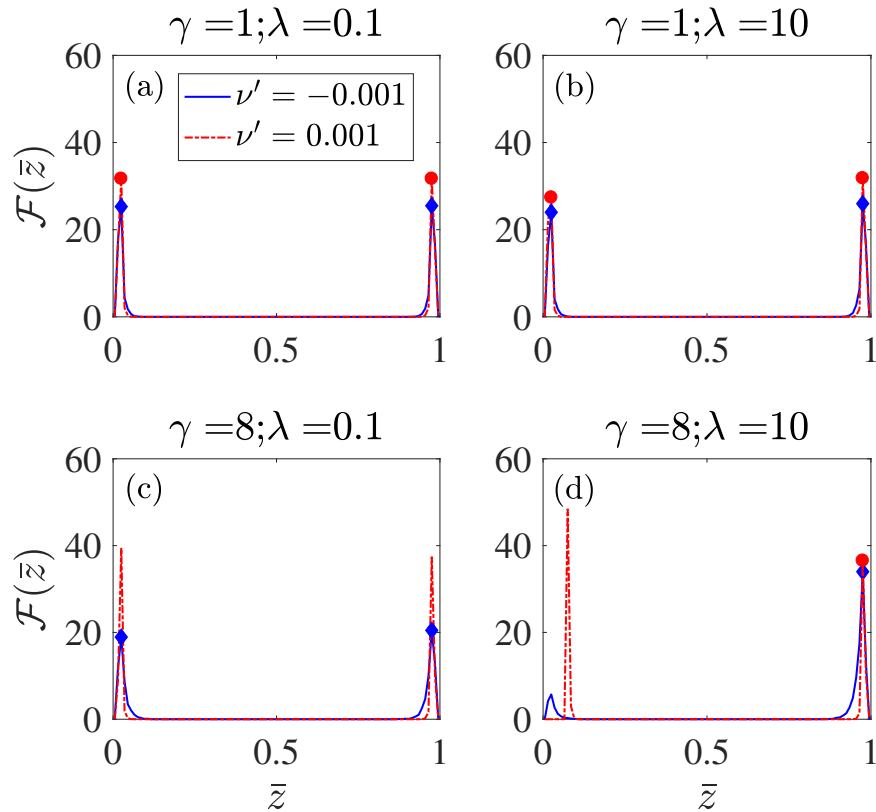


Figure 6.5. : Swimmer distribution in the film, $\mathcal{F}(\bar{z})$, as a function of λ and γ , for $\nu' \neq 0, \kappa' = \sigma' = 0$. Diamonds (resp. circles) denote maximum values of \mathcal{F} for $\nu' < 0$ (resp. $\nu' > 0$). The value of the dimensionless rotational diffusivity of the swimmers is $D_r / (V_s/H) = 0.2$.

versus accumulation at the fluid-fluid interface increases with an increase in both the swimmer elongation and the viscosity ratio.

The second important effect revealed by considering force quadrupolar hydrodynamic interactions is the existence of a stable swimming regime near the fluid-fluid interface, for swimmers having long flagella (i.e., for $\nu' > 0$). By stable swimming, we mean a regime wherein the microorganism swims parallel to the fluid-fluid interface at a fixed separation, solely due to hydrodynamic effects. It can be most easily seen in the phase-portraits in Fig. 6.6(b). The identification of a stable swimming regime

from the plots for $\mathcal{F}(\bar{z})$ requires some comment. The spatial distribution plots in Figs. 6.5(a-c) show a maximum in $\mathcal{F}(\bar{z})$ at either $\bar{z} \approx 0.02$ or at $\bar{z} \approx 0.98$. These maxima correspond to the microorganism being ≈ 1 body length away from either interface, owing to a balance between the hydrodynamics- and motility-based attraction and steric repulsion. It is only for the plot corresponding to $\nu' > 0$ Fig. 6.5(d) (red dashed line) that we see a clear maxima at $\bar{z} \approx 0.08$, a separation where the microorganism is not in contact with the fluid-fluid interface and so steric repulsion is absent. Thus, the peak in concentration at $\bar{z} \approx 0.08$ (for $\nu' > 0, \gamma = 8, \lambda = 10$) corresponds to a regime of parallel swimming by long-flagellated microorganisms. Interestingly, this peak corresponding to stable swimming occurs only for slender swimmers in films that are relatively less viscous ($\lambda > 1$).

It is worth noting that simulations of flagellated bacteria swimming in fluid films have also indicated that: (i) bacteria with shorter flagella ($\nu' < 0$ in our model) almost exclusively accumulate at the free surface in thick films, and, (ii) bacteria with longer flagella ($\nu' > 0$ in our model) either accumulate at the free surface, or swim stably at a few body lengths from the wall (see Figs. 4A and 2 in ref. [28]). These exact behaviors are seen in Fig. 6.5(d) as well, which is intriguing as we manage to replicate these trends while using a much simpler model for microorganism locomotion. Moreover, our calculations explain that an asymmetry in the propulsive forces exerted by bacteria is at the heart of these varied swimming behaviors. We note here that even though Fig. 6.5(d) shows the spatial distribution for viscosity ratio $\lambda = 10$, it is not very different from that for $\lambda \rightarrow \infty$. The differences in the accumulation characteristics saturate drastically for $\lambda > 10$ and $\lambda < 0.1$, as will be seen shortly in Fig. 6.7. In addition to the similarities of stable near surface swimming, we observe the absence of any stable swimming regime near the free surface, for any combination of γ, ν' (notice that all maxima in $\mathcal{F}(\bar{z})$ near the free surface occur at $\bar{z} \approx 1$). Once again this is in agreement with simulations by Pimponi *et al.* for flagellated swimmers [216], and by Ishimoto and Gaffney for spheroidal squirmers [160]. Additionally, our model is able to accurately predict the stable-swimming-height, say z^* , for the

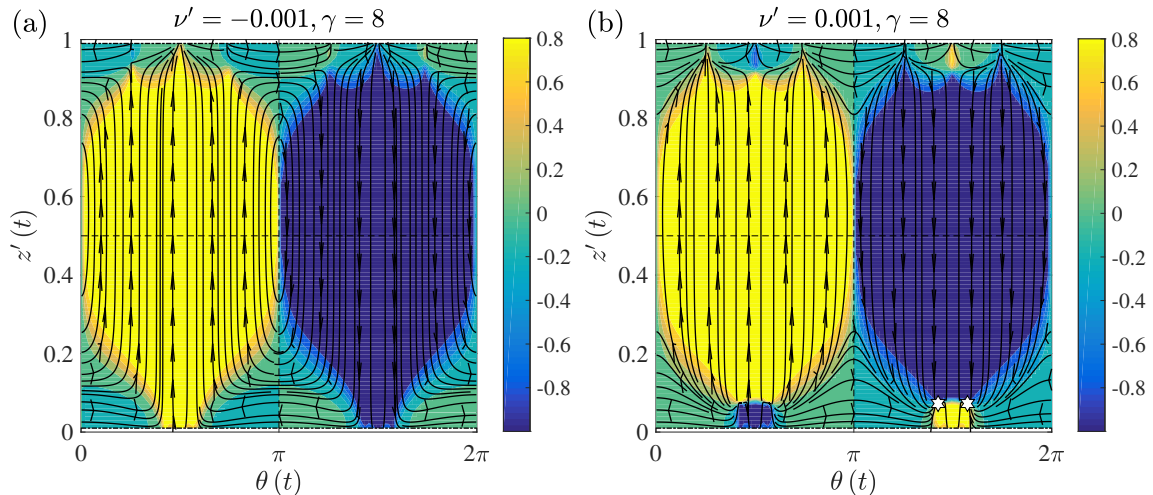


Figure 6.6. : $z'(t) - \theta(t)$ phase plane for force quadrupole swimmers with (a) $\nu' < 0$ corresponding to microorganisms with relatively shorter flagella, and, (b) $\nu' > 0$ corresponding to microorganisms with longer flagella. In panel (b), the hexagrams at $z' \approx 0.08, \theta \approx 3\pi/2$ show the fixed points near the fluid-fluid interface. These correspond to the stable swimming regime where the microorganism swims parallel to the interface. All other multipole coefficients are set to zero and the viscosity ratio is $\lambda = 10$. The phase plane diagrams for $\lambda \rightarrow \infty$ are quite similar, thus highlighting the similarities in swimming behavior between our reduced-order model and the numerical simulations involving bacteria with cell body and flagella.

elongated swimmer. In our simulations z^* is the location of the maximum value of $\mathcal{F}(\bar{z})$, found at $\bar{z} \approx 4a/H = 0.08$ in Fig. 6.5(d). This value of z^* corresponds to a few swimmer body lengths, and is quite close to that obtained from many other numerical studies for flagellated bacteria swimming near rigid surfaces [28, 31, 219].

While our multipole model very well predicts several phenomena describing dynamics of bacteria near surfaces, there also exist some differences between results of the multipole model and numerical simulations considering bacterial geometries; which does necessitate studies of bacterial propulsion by accounting for details of their morphology [31]. One major difference is the nature of bacterial orientation at the

stable swimming swimming height z^* : our approach predicts stable swimming of bacteria while they are oriented *toward* the fluid-fluid interface, but detailed simulations reveal that bacteria undergo stable near-surface motion while oriented *away* from the surface. A second important difference between the multipole model and detailed simulations is existence of certain initial position-orientation pairs $(z'(0), \theta(0))$, which lead to bacteria with longer flagella ‘colliding’ with nearby rigid walls instead of swimming parallel to them. We would also like to emphasize that simulations predict ‘loss’ of stable swimming when the confinement is increased, i.e., film height is reduced, but our analysis becomes invalid for this particular regime because higher order effects of ‘images of images’ become pronounced for thin films and the expression for \mathcal{H} used in eqn. 6.15 loses its applicability. Nevertheless, one can appreciate how multipole models—beyond the force dipole approximation—capture the many dynamical features displayed by microorganisms swimming near rigid and free surfaces.

Fig. 6.7 summarizes the distribution characteristics of force quadrupolar swimmers. In Fig. 6.7(a), we see that there is monotonic reduction in $\Delta\mathcal{F}$ with respect to both the viscosity ratio and the swimmer elongation. In the extreme case of elongated bacteria ($\gamma = 8$) residing in films resting on highly viscous substrates ($\lambda = 10$), the number density at the free surface can be $\approx 80\%$ larger than that at the fluid-fluid interface. Fig. 6.7(c) also shows that $\Delta\mathcal{F} < 0$ in much of the parameter space but the asymmetry in surface accumulation does not vary substantially; instead there are two regimes of spatial distributions: (i) nearly symmetric swimmer accumulation characterized by $|\Delta\mathcal{F}| \approx 0.05$, and, (ii) no accumulation *at* the fluid-fluid interface ($\bar{z} \approx 0$) due to stable swimming *near* it ($\bar{z} \approx 4a/H$), and a more or less constant accumulation at the free surface ($\bar{z} \approx 1$) with $\mathcal{F}^1 \approx 0.2$. The former regime is illustrated by the $\mathcal{F}(\bar{z})$ plots for $\nu' > 0$ in Figs. 6.5(a-c), while the latter in Fig. 6.5(d). Fig. 6.7(c) demonstrates a fine interplay between the aspect ratio of the swimmer and the film’s viscosity in ensuring stable swimming near the fluid-fluid interface, as shown by the evident demarcation between data points with $|\Delta\mathcal{F}| \approx 0.05$ and those with $|\Delta\mathcal{F}| \approx 0.20$.

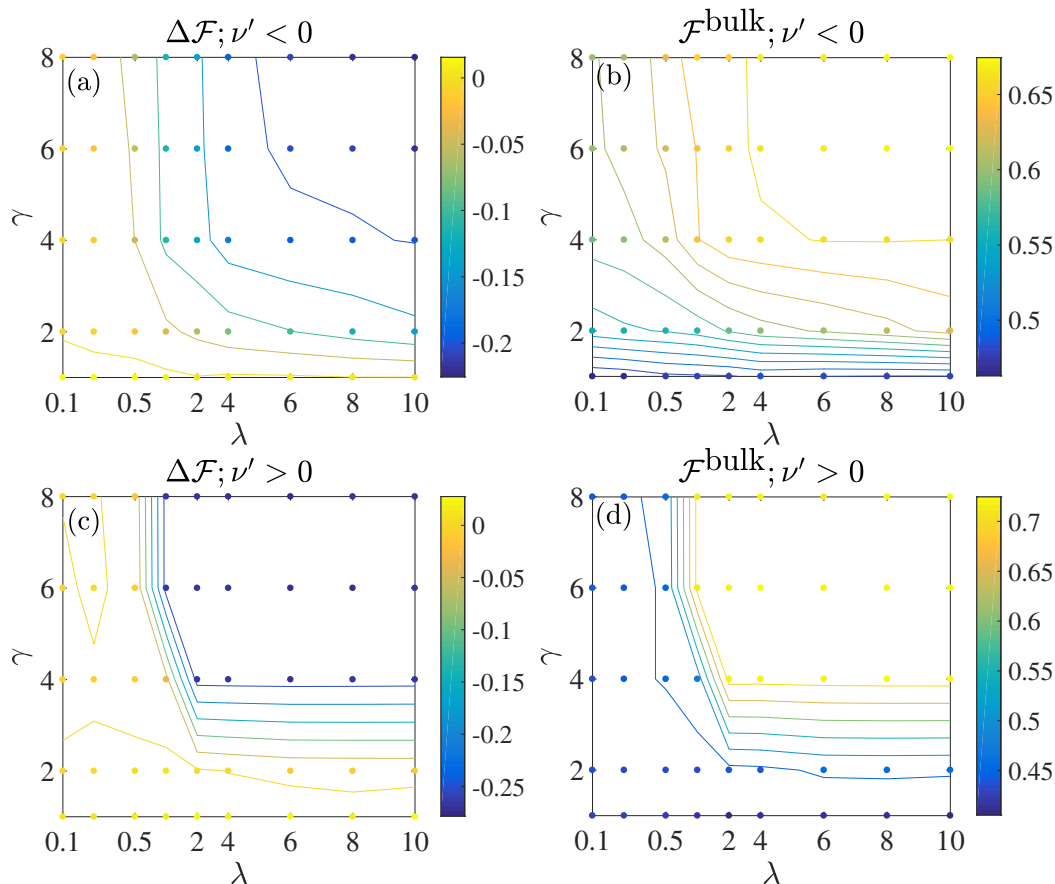


Figure 6.7. : Summary of boundary accumulation and bulk fraction, as a function of swimmer elongation (γ) and viscosity ratio (λ), for force quadrupole swimmers, i.e., for $\nu' \neq 0, \kappa' = \sigma' = 0$. The horizontal axis is logarithmically spaced (with base 2) until $\lambda = 1$, beyond which it is linear.

We end this section by postulating a rather insightful application of our mathematical model: its ability to predict the experimentally observed stable swimming regimes near surfactant-laden free surfaces [23, 25]. While numerical simulations successfully predict the experimentally observed stable swimming of bacteria and spermatozoa near solid walls [22, 31, 160], they fail to do so near free surfaces [28, 160, 216]. Experiments on the other hand *do* reveal that both bacteria (ref. [23]) and spermatozoa (ref. [25]) exhibit stable swimming even in the presence of a free surface. The

discrepancy between numerics and experiments is attributed to the presence of surfactant molecules—generated by the bacteria, or added artificially—on the air-water interface [160]. It is well known that hydrodynamic interactions of swimmers with surfactant-laden interfaces are markedly different than those for clean interfaces, e.g., bacteria follow circular trajectories of different handedness based on the type of surfactant added to an interface [23, 147]. In fact, any interface laden with an incompressible surfactant having high interfacial viscosity behaves in the same manner, hydrodynamics-wise, as a rigid/no-slip wall, as evidenced by studies on rotational motion of bacteria near interfaces (ref. [147]) and the hydrodynamics-mediated trapping of microswimmers around fluid drops and rigid spheres (ref. [64]). Therefore, we can predict that if the presence of an incompressible surfactant contributes a large enough surface viscosity to a free surface, then a ‘force quadrupolar swimmer’ will behave in the same way near the surfactant-laden free surface as it does near a wall. Consequently, one would see a fixed point near the surfactant-laden free surface in the $z'(t), \theta(t)$ phase plane of swimmers with long flagella ($\nu' > 0$), quite unlike the swimmer dynamics near a ‘clean’ free surface, the focus of this work. In this way, our multipole model can explain the observations of stable swimming near surfactant-laden free surfaces based on hydrodynamics alone.

6.3.3 Microorganisms in a flowing film

Thus far, we discussed how hydrodynamics dictates the spatial distribution of model microorganisms within the *stagnant* fluid film of Fig. 6.1, by separately considering the effects of the fundamental Stokes flow singularities. However, biofilms also exist under flowing conditions and exposure to fluid flow has been proposed as a means to either prevent biofilm formation, or erode biofilms whenever their effects are detrimental. We therefore move our attention to flowing films in this sub-section, to round-up a comprehensive analysis of microbial distribution in interfacial films. The key modifications in the mathematical model from Section 6.2 are the addition

of an external-flow-induced translational (\mathbf{u}_{ext}) and rotational ($\mathbf{\Omega}_{ext}$) velocity to the governing equations for swimmer dynamics, i.e., eqns. 6.16 change to:

$$\begin{aligned} \frac{d\mathbf{y}}{dt} &= V_s \mathbf{p} + \mathbf{u}_{HI}(\mathbf{y}, \mathbf{p}) + \mathbf{u}_{ext}(\mathbf{y}) + \mathbf{V}_{st}, \\ d\mathbf{p} &= \{\mathbf{\Omega}_{HI}(\mathbf{y}, \mathbf{p}) + \mathbf{\Omega}_{ext}(\mathbf{y}, \mathbf{p})\} \times \mathbf{p} dt \\ &\quad + \sqrt{4D_r dt} d\mathbf{W}, \end{aligned} \quad (6.21)$$

where $\mathbf{u}_{ext}(\mathbf{x})$ is a prescribed velocity profile depending on the problem geometry, and,

$$\mathbf{\Omega}_{ext} = \frac{1}{2} \nabla \times \mathbf{u}_{ext}(\mathbf{y}) + \frac{\gamma^2 - 1}{\gamma^2 + 1} \{\mathbf{p} \times (\mathbf{E}_{ext}(\mathbf{y}) \cdot \mathbf{p})\}. \quad (6.22)$$

Physically, the external flow tries to ‘carry’ the swimmers along with it; and the velocity gradients in the external flow cause the swimmers to reorient with a rate that balances their tendency to rotate with the local vorticity component (the ‘ $\nabla \times \mathbf{u}_{ext}$ ’ term), and to align with the principal axes of the local extensional flow (the ‘ \mathbf{E}_{ext} ’ term).

We first summarize the influence of external flow on microswimmer motion in a fluid film flowing over a no-slip wall. The external flow in this case is given by the coating-flow profile:

$$\mathbf{u}_{ext}(\mathbf{x}) = v_{max} \frac{x_3}{H} \left(2 - \frac{x_3}{H}\right) \mathbf{e}_1, \quad (6.23)$$

where v_{max} is the magnitude of fluid velocity at the free surface, and is used henceforth as a measure of the external flow strength. The dynamics can be viewed under two distinct categories: without and with the consideration of hydrodynamic interactions between swimmers and surfaces. The main result in the first category is that background flow alone can result in different accumulation behaviors of microswimmers in thin films [18]. A strong external flow results in swimmers being carried along the flow while ‘tumbling’ continuously in (near-wall) regions of high shear [red trajectory is Fig. 6.8(a)]. But for weak external flows, the swimmers spend much more time at the free surface while occasionally ‘dipping’ toward the rigid no-slip surface [18] [blue trajectory is Fig. 6.8(a)]. The major results in the second category hint at a competition between reorientation by external flow—abbreviated herein by Ω_{max} —and the attractive

nature of the force dipolar hydrodynamic interactions—abbreviated by Ω_{HI} —resulting in three kinds of behaviors: (i) $\Omega_{HI} \gg \Omega_{max}$: the external flow barely affects the swimmer distribution, which are akin to Fig. 6.2(d); (ii) $\Omega_{max} > \Omega_{max}^{cr.} > \Omega_{HI}$: above a critical flow strength $v_{max}^{cr.}$, dipolar swimmers can rotate to get “peeled off” the rigid substrate and then eventually swim to the free surface [red trajectory in Fig. 6.8(b)]; and, (iii) $\Omega_{max} \gg \Omega_{HI}$: even though the swimmers get detached from the wall, they do not swim up to the free surface, but just ‘tumble’ in the high-shear regions of the flow [orange trajectory is Fig. 6.8(b)]. The swimmer trajectories corresponding to these behaviors are shown in Fig. 6.8. An in-depth discussion of the interplay between motility, external flow and hydrodynamic interactions can be found in refs. [18, 225, 226, 236].

In our analysis, we discuss the significant differences, both qualitative and quantitative, between flow-induced “peeling” of spherical pushers and pullers as compared to elongated ones. We work with the dynamical equations 6.21 and have a new dimensionless parameter, v_{max}/V_s quantifying the strength of the background flow relative to the swimmer speed in an unbounded, quiescent fluid. In what follows, we only discuss the effects of external flow on the force dipole swimmers, i.e., on pullers ($\kappa' < 0$) and pushers ($\kappa' > 0$). This allows us to use simple physical ideas to explain some of the observed behaviors. Beyond a critical flow, say $v_{max}^{cr.}$, spherical dipolar swimmers pointing toward a wall are rotated away from it and get detached to join the bulk flow [18]. Here, we extend this analysis to the case of elongated/spheroidal dipolar swimmers. For the same absolute value of dipole strength, a spherical puller oriented toward the wall requires a larger external flow to be peeled off in comparison to a spherical pusher (see Fig. 6.9(a) and ref. [18]). The reason is simple: the orientation $\theta = 3\pi/2$ is a *stable* one for a puller but an *unstable* one for a pusher. Thus, the external flow must work against the hydrodynamic reorientation for a puller, and rotate it by a critical angle $\theta_c^{pull} = \pi/2$ before eventual escape. On the other hand, even a slightest perturbation to a pusher pointing toward the wall will cause it to

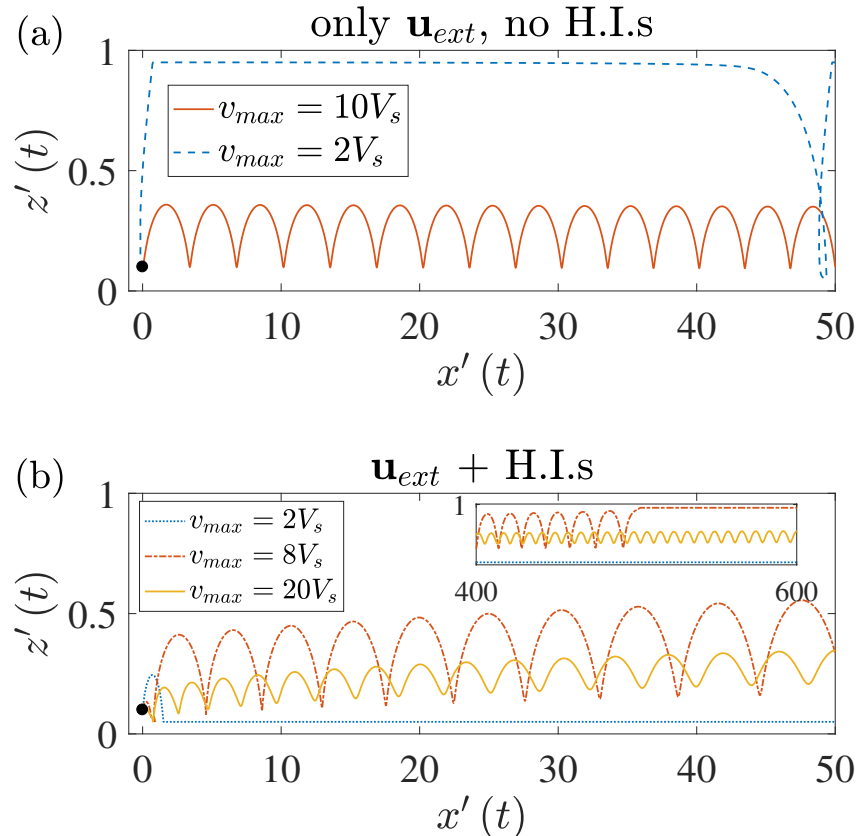


Figure 6.8. : Swimmer trajectories in a flowing film under external flow given by eqn. 6.23. (a) Trajectories without inclusion of hydrodynamic interactions (H.I.s), and, (b) trajectories with inclusion of H.I.s. The starting position (marked by the filled black circle) and orientation are $(x'(0), z'(0), \theta(0)) = (0, 0.1, \pi/4)$. It is important to note the enhanced time spent at the free surface (resp. near bottom wall) for weaker (resp. stronger) flows. The inset in panel (b) denotes how the swimmers under moderate external flow, $v_{max} = 8V_s$, can escape the rigid wall at $z' = 0$ and be trapped at the free surface at $z' = 1$; while under strong flows, $v_{max} = 20V_s$, the swimmers traverse the film centerline in ‘swinging’ trajectories.

rapidly reorient toward $\theta = \pi$ (owing to hydrodynamic interactions and the external flow), after which it must rotate by an amount θ_c^{push} ,

$$\sin \theta_c^{push} \geq \frac{3}{16} \frac{\kappa'}{(a/H)^2} \{3 \cos(2\theta_c^{push}) - 1\}, \quad (6.24)$$

to escape the hydrodynamic pull of the wall. Upon calculation, it is seen that $\theta_c^{push} < \theta_c^{pull}$, i.e., spherical pushers need to be rotated to a lesser extent to overcome any hydrodynamic attractive effects. Hence, spherical pushers can be peeled off the wall more easily, i.e., at a lesser value of $v_{max}^{cr.}$. We have plotted this critical external flow as a function of dipole strength in Fig. 6.9 along with the results of ref. [18] for the sake of completeness and also as a check for our calculations.

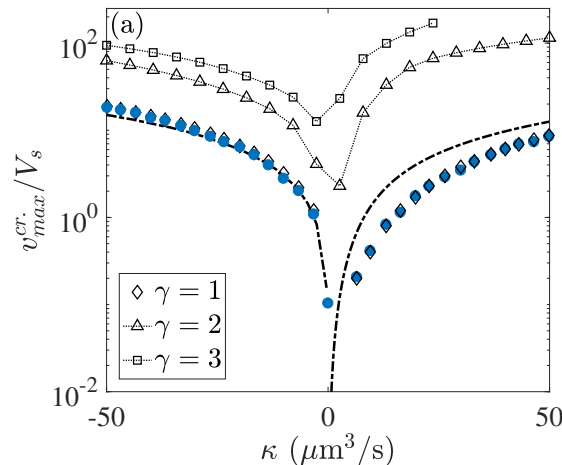


Figure 6.9. : The minimum/critical external flow required to detach swimmers off a wall, $v_{max}^{cr.}/V_s$, as a function of the swimmer dipole strength, κ , and swimmer elongation γ . Note that $v_{max}^{cr.}$ is higher for spherical pullers ($\gamma = 1, \kappa < 0$) than for spherical pushers ($\gamma = 1, \kappa > 0$). $v_{max}^{cr.}$ is lower for elongated pullers ($\gamma > 1, \kappa < 0$) than for elongated pushers ($\gamma > 1, \kappa > 0$). The thick lines represent the analytical estimates for the spherical swimmer case, borrowed from ref. [18] and the blue circles are the results of numerical calculations from ref. [18]. $\kappa > 0$ (resp. $\kappa < 0$) denotes pushers (resp. pullers). The swimmers are initially located near the wall at $z'(0) = a/H$ and oriented such that $\theta(0) = 3\pi/2$.

The dynamics becomes considerably more complex for elongated pushers and pullers, due to the interplay of the terms involving the rate-of-strain in the external fluid, i.e., the ‘G term’ in eqns. 6.21. The critical flow ($v_{max}^{cr.}$) required to detach

elongated pullers is now lower than that required for elongated pushers. While the actual value of $v_{max}^{cr.}$ stems from the numerical time-marching of the non-linear dynamical equations 6.21, the reasoning behind this can be physically intuited based on the nature of the stable orientations of elongated pushers and pullers, and the strength of flow-induced-rotation at these stable orientations: Ω_{ext} will be strongest for $\theta = 3\pi/2$ and weakest for $\theta = \pi$. Therefore, even though a spheroidal pusher with initial orientation $\theta(0) = 3\pi/2$ will quickly reorient to $\theta = \pi$, it will require a much stronger flow in the latter orientation to overcome the hydrodynamic pull, $\mathbf{u}_{HI} \cdot \mathbf{e}_3$, and a stronger hydrodynamic reorientation tendency owing to elongation. A spheroidal puller on the other hand faces stronger ‘overturning’ due to external flow (and steric effects) when it is at $\theta(0) = 3\pi/2$, thus making its reorientation to $\theta = \pi$ relatively easier and requiring lower $v_{max}^{cr.}$ than pushers (for same value of $|\kappa'|$, of course). These ideas are plotted in Fig. 6.9(a) and explained schematically in Fig. 6.10.

6.4 Discussion and conclusion

The objective of the current work was to investigate how motility and hydrodynamic interactions influence the spatial distribution of microorganisms in floating fluid films. We approached this problem by utilizing a general multipole-expansion-based singularity model for the swimming microorganisms and quantifying their hydrodynamic interactions with the two interfaces via the ‘method of images’. We then performed probabilistic simulations—with the stochasticity introduced by the swimmers’ rotational diffusion—to obtain statistically significant distributions of the mean swimmer position across the fluid film. The influence of each multipole singularity was explored in isolation and a number of interesting swimming behaviors were observed. An important aspect of our analysis was the generalization of past studies on near-surface swimming. Our simple model yielded many swimming behaviors that were similar to those seen in more complex numerical simulations, which highlighted

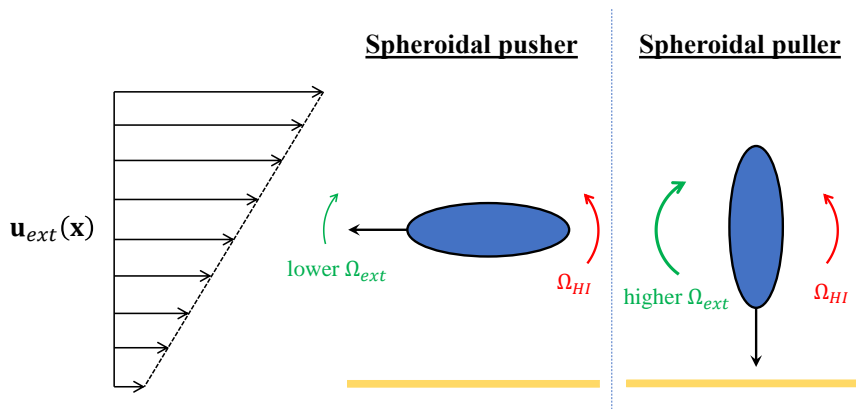


Figure 6.10. : Schematic depiction of why elongated pullers can escape from a wall at lower values of the critical external flow, v_{max}^{cr} . The angular velocity due to the external flow, Ω_{ext} , is largest when the swimmer is oriented toward the wall, and the angular velocity due to the hydrodynamic interactions, Ω_{HI} , is same for any perturbations to the stable swimmer orientation, i.e., $\theta = 3\pi/2 - \Delta\theta$ (resp. $\theta = \pi - \Delta\theta$) for a puller (resp. pusher). In this way, pullers face a greater ‘overtuning’ effect due to the external flow.

the value of performing a far-field, multipole-expansion analysis of swimming motion. Below, we highlight the main results:

1. The accurate predictions of the degree of interface retention of spherical neutral swimmers as a function of the viscosity ratio, λ , of the fluid-fluid interface. Our results were in accordance with previous numerical studies (ref. [111, 160]), and we extended the theory to scattering of neutral swimmers from interfaces with arbitrary viscosity ratios.
2. The surprisingly accurate predictions about behavior of flagellated microorganisms in fluid films resting on a solid substrate. Our results concurred with detailed numerical simulations of swimming bacteria in thick films [28]. We were able to reproduce key observations, e.g., in a thick film (i) bacteria with long flagella end up either accumulate at the free surface, or swim parallel to

the rigid surface at few body-lengths' separation, and, (ii) elongated bacteria with short flagella accumulate almost exclusively at the free surface.

3. The prediction of stable swimming of flagellated bacteria near *surfactant-laden* (as opposed to *clean*) free surfaces. This can be based solely on our calculations for $\lambda \gg 1$ in Section 6.3.2, and the well-known similarity between incompressible surfactant-laden interfaces and rigid surfaces [64, 146, 147].

The predictions mentioned in the second and third point above were obtained as a result of studying force quadrupolar hydrodynamic interactions, and noting that swimmers with $\nu' > 0$ (resp. $\nu' < 0$) have relatively longer (resp. shorter) flagella and smaller (resp. larger) cell bodies. It should be noted that even though we studied each singularity in isolation, the behaviors of near-surface stable swimming and preferential accumulation at the free surface (described in Section 6.3.2) are robust to the inclusion of all singularities considered, albeit for certain sets of relative strengths of the singularities. As long as the force quadrupole strength is assumed to be significant, our model gives good qualitative, and somewhat quantitative, agreement with many existing simulations of near-wall/near-free-surface swimming of helically flagellated swimmers [28, 31, 216, 219]. To the best of our knowledge, existing numerical studies of microswimmer dynamics near non-deforming, *clean* free surfaces have universally predicted the absence of a stable/parallel swimming regime [160, 216]. As a reconciliation with experimental observations, surfactant-induced hydrodynamic effects have been proposed (see ref. [160]) as one explanation of the observed parallel swimming regime of flagellated bacteria near free surfaces [23, 30]. If the surfactant effects are modelled as that due to an incompressible surfactant having large interfacial viscosity, then the force quadrupole model can indeed yield a stable swimming regime near *surfactant-laden* free surfaces.

While we performed studies near planar interfaces and compared them to numerical simulations under similar situations, we can also point toward the generality of near-surface motion of bacteria around spherical obstacles. The most important one

being that ‘long-tailed bacteria’ get trapped in hydrodynamic bound states around neutrally buoyant, spherical particles; and ‘short-tailed bacteria’ get scattered upon encountering the same spherical particles [237]. If the spherical particle is large enough in comparison to the swimmer, then, to a first approximation, the analysis of force quadrupolar interactions in Section 6.3 is able to predict these behaviors as well. We can even go a step further and hypothesize the behavior of flagellated swimmers near neutrally buoyant surfactant-laden drops. As an incompressible surfactant’s ability to cause fluid-fluid interfaces to behave like rigid walls is independent of the viscosity ratio of the interface, we can make a very general observation: as long as a drop is covered by an incompressible surfactant with large enough interfacial viscosity, it will act as a passive hydrodynamic trap for bacteria with long polar flagella, i.e., they swim along the drop’s surface for substantial times. This can prove to be a particularly useful observation as it will provide an interesting incentive for the use of dispersant in the aftermath of oil-spills, with implications in bacterial bioremediation of heavy oil drops.

The primary motivation of this manuscript was to study microorganism motion in biofilms floating over a base fluid. The spatial distributions discussed in Figs. 6.2, 6.3, 6.4 and 6.5 tell us how hydrodynamic interactions can affect bacterial concentration in different regions of a film and thus either aid in, or desist from colony formation. However, quite often biofilm formation is accompanied by the bacteria secreting surfactant and other polymeric substances which alter physico-chemistry of their surroundings, most importantly the bulk and interfacial rheology of the fluids involved. In this study, as a first step, we treated the fluids to be Newtonian and the interfaces to be clean but useful extensions can be pursued within the current framework. For example, the effect of interface rheology and more complicated boundary conditions can be probed via the Fourier-transform-based analysis detailed in refs. [147,238]. The effects of the bulk fluid’s rheology—at least in the weakly non-Newtonian limit—can be accounted for, rather straightforwardly as explained in refs. [235,239]. A second level of functional detail that can be added to our analysis is the inclusion of active

behavior by microorganisms. E.g., quite often biofilms form over nutrient-emanating substrates and thus chemotaxis–directed motion in search of nutrition [6, 171]—is expected to play an important role in biofilm incipience [65, 66]. Chemotaxis could lead bacteria toward the fluid-fluid interface if fluid-2 were to be a nutrient source, or toward the free surface in case of, say, aerotaxis by *B. subtilis* [240, 241]. Yet another form of directed motion, more relevant for algal biofilms, could be positive (resp. negative) phototaxis toward (resp. away from) light sources [242, 243]. The multipole representation would allow one to model a variety of microorganisms (by merely tweaking the multipole strengths in eqns. 6.13) and the incorporation of active effects would be relatively straightforward in our individual-based model [51]. It would then be an interesting endeavour to see how the more non-trivial hydrodynamic interactions listed in this work interact and compete with bacterial chemotaxis or algal phototaxis to dictate colonization hot-spots in the numerous scenarios involving films of microorganisms at interfaces [67, 231].

6.5 Appendix

6.5.1 Hydrodynamically induced linear and angular velocities

The swimmer’s translational velocities, for each of the singularities considered in this work, are:

$$\begin{aligned} \frac{\mathbf{u}_{HI}^D \cdot \mathbf{e}_3}{V_s} &= -\frac{\kappa' (3\lambda + 2)}{8(\lambda + 1)z'^2} (1 - 3p_3^2) \\ &+ \frac{\kappa'}{4(z' - 1)^2} (1 - 3p_3^2), \end{aligned} \quad (6.25)$$

$$\frac{\mathbf{u}_{HI}^{SD} \cdot \mathbf{e}_3}{V_s} = -\frac{\sigma' (4\lambda + 1)}{4(\lambda + 1)z'^3} p_3 + \frac{\sigma'}{4(z' - 1)^3} p_3, \quad (6.26)$$

and,

$$\begin{aligned} \frac{\mathbf{u}_{HI}^Q \cdot \mathbf{e}_3}{V_s} &= \frac{-\nu'}{4(\lambda + 1)z'^3} \{ (9\lambda + 6) p_3^2 + (-7\lambda - 4) \} p_3 \\ &+ \frac{\nu'}{2(z' - 1)^3} (3p_3^2 - 2) p_3; \end{aligned} \quad (6.27)$$

while, the swimmer's rotational velocities are:

$$\begin{aligned} \frac{\Omega_{HI}^D \cdot \mathbf{e}_2}{V_s/H} &= \frac{3\kappa'}{8z'^3} \left\{ 1 + G \frac{\lambda + (\lambda + 2)p_3^2}{2(\lambda + 1)} \right\} p_1 p_3 \\ &\quad - \frac{3\kappa'}{8(z' - 1)^3} (1 + G p_3^2), \end{aligned} \quad (6.28)$$

$$\begin{aligned} \frac{\Omega_{HI}^{SD} \cdot \mathbf{e}_2}{V_s/H} &= -\frac{3\sigma'}{8(\lambda + 1)z'^4} \left\{ \lambda + \frac{G}{2} (3\lambda + 1) (1 + p_3^2) \right\} p_1 \\ &\quad + G \frac{3\sigma'}{16(z' - 1)^4} (1 + p_3^2) p_1, \end{aligned} \quad (6.29)$$

and,

$$\begin{aligned} \frac{\Omega_{HI}^Q \cdot \mathbf{e}_2}{V_s/H} &= \frac{-3\nu'}{32(\lambda + 1)z'^4} \{ (12\lambda + 10)p_3^2 - 4\lambda - 2 \} \\ &\quad + \frac{-3\nu'}{32(\lambda + 1)z'^4} G \{ 3(\lambda + 2)p_3^4 - 2p_3^2 - (11\lambda + 4) \} p_1 \\ &\quad + \frac{3\nu'}{16(z' - 1)^4} [\{ 5p_3^2 - 1 \} + G \{ 3p_3^4 - p_3^2 - 2 \}] p_1 \end{aligned} \quad (6.30)$$

The super-scripts 'D', 'SD' and 'Q' in the above equations refer to the force dipole, source dipole and the force quadrupole, respectively. As a check for our derivations, we note that taking the limit $\lambda \rightarrow \infty$ in the expressions in eqns. 6.25 to 6.30 reduces them to those derived in ref. [18] for the case of a liquid film (wall at $z' = 0$, free surface at $z' = 1$). For the force quadrupolar expressions, \mathbf{u}_{HI}^Q and Ω_{HI}^Q , one must multiply our derivations by $-1/2$, because of the difference in the definition of \mathbf{u}^Q (see eqn. 6.13c) between refs. [14] (which is what we follow) and [18] (which is what we are comparing our calculations against).

6.5.2 Accumulation characteristics: additional information

In Section 6.3.2 we had mentioned that dipolar swimmers do not show any preference toward accumulation at either interface. This is quantified in Fig. 6.11 where we see that the difference in swimmer accumulation at the two interfaces, $\Delta\mathcal{F} = \mathcal{F}^0 - \mathcal{F}^1$

(see eqn. 6.20), is very small for both pushers and pullers, over a range of swimmer elongations, γ , and viscosity ratios, λ .

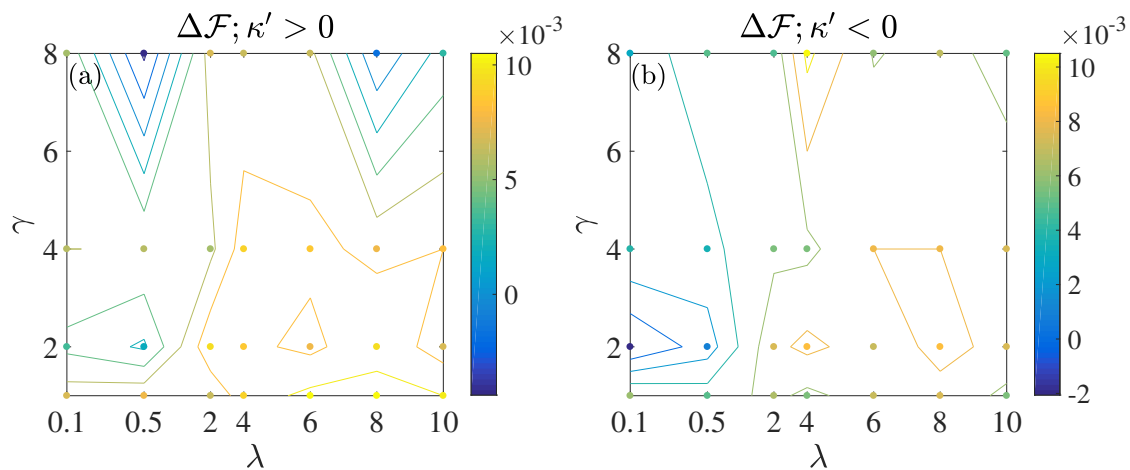


Figure 6.11. : The difference in interface accumulation $\Delta\mathcal{F}$ (see eqn. 6.20) for dipolar swimmers: (a) pushers, and, (b) pullers. As discussed in Section 6.3.2, and shown more qualitatively in Fig. 6.2, the accumulation when considering only the dipole effects is more or less symmetric with $\Delta\mathcal{F} > 0, \sim O(10^{-3})$.

7. CONCLUDING REMARKS

7.1 Conclusion

In this thesis, we described five studies that aimed to elucidate the effects of hydrodynamics and/or chemotaxis on interaction of microorganisms with fluid-fluid interfaces, with applications in bacterial bioremediation. A major motivation in each study was to isolate the influence of hydrodynamics on the physico-chemical interaction being studied. In the first study (Chapter 2) we looked at a somewhat indirect influence of hydrodynamics on the consumption of soluble nutrients by motile, chemotactic bacteria. We postulated that nutrient patches found in sub-marine environments get significantly distorted due to ambient fluid flow (generated by a swarm of rising drops; see Fig. 2.1), and that this in turn affects a marine bacterium's search for food. The distortion of nutrient patches—before subsequent mixing and homogenization—engendered local gradients in nutrient concentrations, which could be exploited by chemotactic bacteria. We found that chemotaxis enabled motile organisms to consume the nutrient/chemoeffector at rates that were $\approx 45\%$ faster than their non-motile counterparts (see Fig. 2.10). The chemotactic advantage depended most acutely on the bacterial swimming speed (see Fig. 2.6) and sensitivity toward chemoeffector/nutrient gradients [see Fig. 2.4(b)]. Furthermore, we showed that the chemotactic advantage reduced monotonically with an increase in the drop size, and it varied non-trivially with the volume fraction of the drops (see Fig. 2.7).

Next, we proposed that not only does hydrodynamics acutely affect the consumption of soluble nutrients, but that it also serves to enhance the colonization of insoluble nutrient sources—like a crude oil drop—that need to be broken down into simpler substances (Chapter 3). We described a purely hydrodynamic mechanism of microorganism capture onto the surface of oil drops. We showed that when a

microorganism/microswimmer impinges directly onto a drop that is larger than a ‘critical trapping radius’, then it is hydrodynamically bound to the drop’s surface (see Fig. 3.2). We reported the trapping characteristics of the microswimmer as a function of the drop’s viscosity and/or the properties of the surfactant covering the drop’s surface. We found that addition of surfactant reduces the critical trapping radius of a drop by $\sim 30\%$ (see Fig. 3.5). For hydrodynamics combined with diffusion based motion, we noted increments ranging from $\sim 5 - 25\%$ in the interface-retention times of surfactant-laden drops, as compared to clean drops (see Figs. 3.13, 3.14, 3.15). This was a particularly interesting result as it hinted at potential benefits of using dispersant in the aftermath of oil spills.

While Chapter 3 talked about the very interesting phenomenon of hydrodynamic trapping of microorganisms around oil drops, it also revealed that such a trapping is effective only within a ‘basin of attraction’ that extends 2-3 bacterial body lengths from the surface of the drop. This led us to ask: how then, do freely swimming bacteria colonize a distant food source effectively? In Chapter 4, we discussed an interesting possibility: that of chemotactic attraction of a bacterium to nutrient-effusing sources, followed by hydrodynamic capturing based on the mechanisms detailed in Chapter 3. The randomness of a bacterium’s ‘run-and-tumble’ motion and the rather limited extent of the basin of attraction meant that bacteria would, most likely, form a distribution around the source (see Fig. 4.4). We aimed to quantify the combined influence of hydrodynamics and chemotaxis on this distribution. In general, we unveiled four regimes (see Fig. 4.9) of bacterial distribution around the nutrient source: (i) strong surface colonization, (ii) rotary diffusion induced ‘off-surface’ accumulation, (iii) a depletion zone in the spatial distribution, and, (iv) no appreciable aggregation; with their occurrence dictated by the relative strengths of hydrodynamic and chemotactic effects. Thus by the end of Chapter 4, we had performed a detailed study of hydrodynamics- and chemotaxis-driven motion of microorganisms around stationary nutrient sources. The next question was: how are the aforementioned effects altered if the nutrient source is moving?

In Chapter 6, we moved on to the more general case of colonization of moving nutrient sources. We focused on settling marine snow particles as they are known sources of dissolved organic matter, even absorbed hydrocarbons. We performed a systematic analysis and studied how bacterial encounters with settling marine snow are affected by: (i) deterministic hydrodynamics (see Fig. 5.3), (ii) hydrodynamics and stochasticity in bacterial orientation (see Fig. 5.4), and, (iii) hydrodynamics combined with chemotaxis (see figures in Section 5.3.2). One of the first implications of colonization around a moving source was the existence of a threshold sinking speed of the marine snow beyond which bacteria are unable to colonize it even after a ‘head-on collision’ (see Fig. 5.3C,E). Even then, we were able to identify ‘trapping regimes’ for bacteria encountering the marine snow. These were dictated by a balance between the size and settling speed of the marine snow, and the dipole strength of the bacterium. Interestingly, we found that hydrodynamic capture around settling spheres was possible even when they move almost 10 times faster than the colliding bacteria (see Fig. 5.4D). When considering hydrodynamic attraction in conjunction with chemotaxis toward the nutrient plume emanating from the marine snow (see Fig. 5.1) we found a number of interesting behaviors: (i) strong hydrodynamic interactions amplified bacterial nutrient exposure by roughly 40% for nutrients with molecular diffusivity $\sim 10^{-7}$ cm²/s [see Fig. 5.6(b)], (ii) the nutrient exposure for chemotactic bacteria decayed monotonically with an increase in their mean run-length (see Fig. 5.7), and, (iii) hydrodynamic interactions were beneficial for even *non-chemotactic but motile* bacteria: strong hydrodynamic interactions almost doubled their nutrient exposure (when compared against non-motile bacteria; see Fig. 5.9B).

Chapters 3 to 5 modeled a single microorganism as a force dipole and studied its behavior near stationary and moving nutrient sources. In Chapter 6 we explored the effects of bacterial geometry and propulsion mechanism, as described by higher order multipoles in the multipole expansion of a point force placed in a fluid (see eqns. 1.4 to 1.7 in Chapter 1). Our aim was to study the hydrodynamics of a model microorganism confined by a free surface (air-fluid interface) on one side and

a fluid-fluid interface on the other (see Fig. 6.1). This system acts as a first approximation of an ‘interfacial biofilm’, a configuration of relevance in the context of bacterial bioremediation of oil films floating on the water surface. Through far-field hydrodynamics and stochastic simulations, we identified experimentally verifiable behaviors exhibited by microorganisms in a fluid film. First, we explained the recent findings [29] that ‘puller’ microorganisms accumulate more tightly near rigid/fluid surfaces than ‘pusher’ microorganisms (see Fig. 6.2), based on their respective hydrodynamic interactions with surfaces. Second, we revealed the benefits of far-field modeling of bacteria, beyond just the force dipole approximation, by showing that our predictions for bacterial distribution across films were consistent with detailed numerical simulations of flagellated bacteria [28,216] (see Section 6.3.2 and Fig. 6.5). Finally, using the implications of the previous result, we proposed an explanation of the hitherto unexplained phenomenon of bacteria swimming parallel to a surfactant-laden free surface and at a fixed distance from it. This was done by pointing out similarities between microbial motion near a plane wall and near an incompressible surfactant-laden interface [64,146,147]. Our reduced-order model is able to explain the parallel swimming of a bacterium near a plane wall, which is sufficient for proving that it will also predict parallel swimming near surfactant-laden interfaces. In this way, without solving a new problem we are able to extract useful information about it, thus highlighting the predictive capabilities of our work.

In summary, the most important conclusion from our studies is that hydrodynamics provides a ‘motility benefit’ to swimming bacteria beyond just enhanced access to nutrient landscapes. In other words, not only does motility enable the search for nutrition via chemotaxis, it also assists microorganisms in colonizing nutrient sources once they are located, via hydrodynamic attraction and—wherever applicable—resultant trapping.

7.2 Future Work

An important conclusion of our studies so far is that surfactant-laden drops can significantly influence biodegradation. It is well known that addition of a dispersant breaks down heavier oil plumes into smaller (10-60 μm) drops [3]. In Chapter 2 we saw that smaller drops—generated possibly due to dispersant addition—actually improved chemotactic performance; and in Chapter 3 we saw that surfactant-laden drops were more capable in hydrodynamically trapping nearby microswimmers. Therefore, investigation of the dynamics of microswimmer locomotion near surfactant-laden interfaces is a natural extension to the present research. In particular, there are relatively fewer numerical studies of microorganisms near surfactant-laden interfaces and this could be an interesting research direction. It is well known that certain microorganisms produce extracellular polymeric substances (e.g., see ref. [244]) that can change the properties of nearby interfaces as well as those of the surrounding fluid by imparting surface tension gradients and interfacial viscosity to the former, and viscoelasticity to the latter. Thus, it is natural to ask: how does fluid viscoelasticity (characteristic of surfactant-coated oil drops) and associated fluid flow alter microbial motility near free surfaces? The motion of microorganisms near interfaces consisting of at least one viscoelastic fluid is relatively less explored (e.g., see ref. [245]) and is a fertile avenue of research. However, because viscoelasticity introduces non-linearities, the use of a multipole representation becomes rather restrictive. Nonetheless, direct numerical simulations [246] and semi-analytical methods [235, 239] could be used to isolate the effects of viscoelasticity and fluid flow on the (possible) accumulation of microorganisms near a fluid-fluid interface. Another insightful extension to this thesis would be the inclusion of inter-swimmer hydrodynamic interactions. This means extending our analysis from the dilute to the semi-dilute regime. This can be done by using reduced-order mathematical models of active suspensions [247, 248]. The spatial distribution of swimmers around interfaces will then depend on their concentrations. It will be affected not only by the swimmer-surface hydrodynamic interactions but also

by the bulk fluid flow generated by the swimmers. The former will lead to greater colonization and the latter could hinder colonization via collective bulk-scale motion of microorganisms. One can expect a competition between these two effects, and results from this study could inform us about biofilm activity beyond the initial incipience, i.e., when the microorganisms have had time to proliferate. Finally, we invite detailed numerical and experimental studies to further probe some of our results and check our predictions. In particular, our results from Chapter 6 can be used as a springboard to perform numerical analyses of microorganisms swimming near surfactant-laden interfaces. The generalities afforded by numerical methods should reveal interesting behaviors in the truly non-linear regimes of microorganism dynamics. From an experimental perspective, it will be intriguing to see data about: (i) microorganism accumulation around oil drops (both clean and surfactant-laden), (ii) distribution of microorganisms with differing morphologies across fluid films resting on rigid and fluid substrates, and, (iii) rates of colonization of spherical nutrient sources—stationary and moving—by chemotactic bacteria of varying chemotactic strengths.

REFERENCES

REFERENCES

- [1] M.T. Madigan, J.M. Martinko, K.S. Bender, D.H. Buckley, and D.A. Stahl. *Brock Biology of Microorganisms*. Pearson, 14th edition, 2014.
- [2] Ian M. Head, D. Martin Jones, and Wilfred F. M. Röling. Marine microorganisms make a meal of oil. *Nature Reviews Microbiology*, 4(3):173–182, mar 2006.
- [3] Ronald M. Atlas and Terry C. Hazen. Oil Biodegradation and Bioremediation: A Tale of the Two Worst Spills in U.S. History. *Environmental Science & Technology*, 45(16):6709–6715, Aug 2011.
- [4] Eric A. Dubinsky, Mark E. Conrad, Romy Chakraborty, Markus Bill, Sharon E. Borglin, James T. Hollibaugh, Olivia U. Mason, Yvette M. Piceno, Francine C. Reid, William T. Stringfellow, Lauren M. Tom, Terry C. Hazen, and Gary L. Andersen. Succession of Hydrocarbon-Degrading Bacteria in the Aftermath of the Deepwater Horizon Oil Spill in the Gulf of Mexico. *Environmental Science & Technology*, 47(19):10860–10867, oct 2013.
- [5] H. C. Berg. *E. coli in Motion*. Springer-Verlag, New York, NY, 2004.
- [6] R. Stocker and J. R. Seymour. Ecology and Physics of Bacterial Chemotaxis in the Ocean. *Microbiology and Molecular Biology Reviews*, 76(4):792–812, dec 2012.
- [7] Jeffrey S. Guasto, Roberto Rusconi, and Roman Stocker. Fluid Mechanics of Planktonic Microorganisms. *Annual Review of Fluid Mechanics*, 44(1):373–400, jan 2012.
- [8] Eric Lauga and Thomas R Powers. The hydrodynamics of swimming microorganisms. *Reports on Progress in Physics*, 72(9):096601, sep 2009.
- [9] Eric Lauga. Bacterial Hydrodynamics. *Annual Review of Fluid Mechanics*, 48(1):105–130, jan 2016.
- [10] H. C. Berg. *Random Walks in Biology*. Princeton, Princeton, New Jersey, 2nd edition, 1993.
- [11] L. G. Leal. *Advanced Transport Phenomena*. Cambridge University Press, Cambridge, 2007.
- [12] E. M. Purcell. Life at low Reynolds number. *American Journal of Physics*, 45(1):3–11, jan 1977.
- [13] S. Kim and S. Karrila. *Microhydrodynamics: Principles and Selected Applications*. Butterworth-Heinemann, Boston, 1991.

- [14] Saverio E. Spagnolie and Eric Lauga. Hydrodynamics of self-propulsion near a boundary: predictions and accuracy of far-field approximations. *Journal of Fluid Mechanics*, 700:105–147, apr 2012.
- [15] J. M. Yeomans, D. O. Pushkin, and H. Shum. An introduction to the hydrodynamics of swimming microorganisms. *The European Physical Journal Special Topics*, 223(9):1771–1785, sep 2014.
- [16] Knut Drescher, Raymond E. Goldstein, Nicolas Michel, Marco Polin, and Idan Tuval. Direct Measurement of the Flow Field around Swimming Microorganisms. *Physical Review Letters*, 105(16):168101, oct 2010.
- [17] K. Drescher, J. Dunkel, L. H. Cisneros, S. Ganguly, and R. E. Goldstein. Fluid dynamics and noise in bacterial cell-cell and cell-surface scattering. *Proceedings of the National Academy of Sciences*, 108(27):10940–10945, jul 2011.
- [18] Arnold J. T. M. Mathijssen, Amin Doostmohammadi, Julia M. Yeomans, and Tyler N. Shendruk. Hotspots of boundary accumulation: dynamics and statistics of micro-swimmers in flowing films. *Journal of The Royal Society Interface*, 13(115):20150936, feb 2016.
- [19] M. A.-S. Vigeant, R. M. Ford, M. Wagner, and L. K. Tamm. Reversible and Irreversible Adhesion of Motile Escherichia coli Cells Analyzed by Total Internal Reflection Aqueous Fluorescence Microscopy. *Applied and Environmental Microbiology*, 68(6):2794–2801, jun 2002.
- [20] Eric Lauga, Willow R. DiLuzio, George M. Whitesides, and Howard A. Stone. Swimming in circles: Motion of bacteria near solid boundaries. *Biophysical Journal*, 90(2):400–412, jan 2006.
- [21] Allison P. Berke, Linda Turner, Howard C. Berg, and Eric Lauga. Hydrodynamic Attraction of Swimming Microorganisms by Surfaces. *Physical Review Letters*, 101(3):038102, jul 2008.
- [22] D. J. Smith, E. A. Gaffney, J. R. Blake, and J. C. Kirkman-Brown. Human sperm accumulation near surfaces: a simulation study. *Journal of Fluid Mechanics*, 621:289, feb 2009.
- [23] L. Lemelle, J.-F. Palierne, E. Chatre, and C. Place. Counterclockwise Circular Motion of Bacteria Swimming at the Air-Liquid Interface. *Journal of Bacteriology*, 192(23):6307–6308, dec 2010.
- [24] R. Di Leonardo, D. Dell’Arciprete, L. Angelani, and V. Iebba. Swimming with an image. *Physical Review Letters*, 106(3):038101, jan 2011.
- [25] S. Boryshpolets, J. Cosson, V. Bondarenko, E. Gillies, M. Rodina, B. Dzyuba, and O. Linhart. Different swimming behaviors of sterlet (*Acipenser ruthenus*) spermatozoa close to solid and free surfaces. *Theriogenology*, 79(1):81–86, jan 2013.
- [26] Hossein Jashnsaz, Mohammed Al Juboori, Corey Weistuch, Nicholas Miller, Tyler Nguyen, Viktoria Meyerhoff, Bryan McCoy, Stephanie Perkins, Ross Wallgren, Bruce D. Ray, Konstantinos Tsekouras, Gregory G. Anderson, and Steve Pressé. Hydrodynamic Hunters. *Biophysical Journal*, 112(6):1282–1289, mar 2017.

- [27] Silvio Bianchi, Filippo Saglimbeni, and Roberto Di Leonardo. Holographic Imaging Reveals the Mechanism of Wall Entrapment in Swimming Bacteria. *Physical Review X*, 7(1):011010, jan 2017.
- [28] Daniela Pimponi, Mauro Chinappi, and Paolo Gualtieri. Flagellated microswimmers: Hydrodynamics in thin liquid films. *The European Physical Journal E*, 41(2):28, feb 2018.
- [29] Kuan-Ting Wu, Yi-Teng Hsiao, and Wei-Yen Woon. Entrapment of pusher and puller bacteria near a solid surface. *Physical Review E*, 98(5):052407, nov 2018.
- [30] Silvio Bianchi, Filippo Saglimbeni, Giacomo Frangipane, Dario Dell’Arciprete, and Roberto Di Leonardo. 3D dynamics of bacteria wall entrapment at a water-air interface. *Soft Matter*, 15(16):3397–3406, 2019.
- [31] H. Shum, E. A. Gaffney, and D. J. Smith. Modelling bacterial behaviour close to a no-slip plane boundary: the influence of bacterial geometry. *Proceedings of the Royal Society A: Mathematical, Physical and Engineering Sciences*, 466(2118):1725–1748, jun 2010.
- [32] R M Macnab and D E Koshland. The gradient-sensing mechanism in bacterial chemotaxis. *Proceedings of the National Academy of Sciences of the United States of America*, 69(9):2509–12, sep 1972.
- [33] R. Thar and M. Kuhl. Bacteria are not too small for spatial sensing of chemical gradients: An experimental evidence. *Proceedings of the National Academy of Sciences*, 100(10):5748–5753, may 2003.
- [34] H. Szurmant and G. W. Ordal. Diversity in Chemotaxis Mechanisms among the Bacteria and Archaea. *Microbiology and Molecular Biology Reviews*, 68(2):301–319, jun 2004.
- [35] Renate Lux and Wenyuan Shi. Chemotaxis-guided Movements in Bacteria. *Critical Reviews in Oral Biology & Medicine*, 15(4):207–220, jul 2004.
- [36] George H. Wadhams and Judith P. Armitage. Making sense of it all: bacterial chemotaxis. *Nature Reviews Molecular Cell Biology*, 5(12):1024–1037, dec 2004.
- [37] M. Eisenbach, J. Lengeler, M. Varon, D. Gutnick, R. Meili, R. Firtel, J. Segall, G. Omann, A. Tamada, and F. Murakami. *Chemotaxis*. Imperial College Press, London, 2004.
- [38] Steven L. Porter, George H. Wadhams, and Judith P. Armitage. Signal processing in complex chemotaxis pathways. *Nature Reviews Microbiology*, 9(3):153–165, mar 2011.
- [39] Kwangmin Son, Filippo Menolascina, and Roman Stocker. Speed-dependent chemotactic precision in marine bacteria. *Proceedings of the National Academy of Sciences*, 113(31):8624–8629, aug 2016.
- [40] H. C. Berg and D. A. Brown. Chemotaxis in *Escherichia coli* analysed by Three-dimensional Tracking. *Nature*, 239:500–504, 1972.
- [41] D. A. Brown and H. C. Berg. Temporal stimulation of chemotaxis in *E. coli*. *Proceedings of the National Academy of Sciences*, 71:1388–1392, 1974.

- [42] Mercedes A. Rivero, Robert T. Tranquillo, Helen M. Buettner, and Douglas A. Lauffenburger. Transport models for chemotactic cell populations based on individual cell behavior. *Chemical Engineering Science*, 44(12):2881–2897, 1989.
- [43] Kevin C. Chen, Roseanne M. Ford, and Peter T. Cummings. Cell balance equation for chemotactic bacteria with a biphasic tumbling frequency. *Journal of Mathematical Biology*, 47(6):518–546, dec 2003.
- [44] Ganesh Subramanian and Donald L. Koch. Critical bacterial concentration for the onset of collective swimming. *Journal of Fluid Mechanics*, 632:359, aug 2009.
- [45] T. Ishikawa. Suspension biomechanics of swimming microbes. *Journal of The Royal Society Interface*, 6(39):815–834, oct 2009.
- [46] G. Subramanian and P. R. Nott. The fluid dynamics of swimming microorganisms and cells. *Journal of the Indian Institute of Science*, 91:283–313, 2011.
- [47] T. J. Pedley and J. O. Kessler. Hydrodynamic Phenomena in Suspensions of Swimming Microorganisms. *Annual Review of Fluid Mechanics*, 24(1):313–358, jan 1992.
- [48] N A Hill and T J Pedley. Bioconvection. *Fluid Dynamics Research*, 37(1-2):1–20, jul 2005.
- [49] David Saintillan. Kinetic Models for Biologically Active Suspensions. In *Natural Locomotion in Fluids and on Surfaces*, pages 53–71. 2012.
- [50] David Saintillan and Michael J. Shelley. Theory of Active Suspensions. pages 319–355. Springer, 2015.
- [51] Nikhil Desai and Arezoo M. Ardekani. Modeling of active swimmer suspensions and their interactions with the environment. *Soft Matter*, 13(36):6033–6050, 2017.
- [52] Evelyn F. Keller and Lee A. Segel. Model for chemotaxis. *Journal of Theoretical Biology*, 30(2):225–234, feb 1971.
- [53] A. Hillesdon, T. J. Pedley, and J. O. Kessler. The development of concentration gradients in a suspension of chemotactic bacteria. *Bulletin of Mathematical Biology*, 57(2):299–344, mar 1995.
- [54] A. J. Hillesdon and T. J. Pedley. Bioconvection in suspensions of oxytactic bacteria: linear theory. *Journal of Fluid Mechanics*, 324(-1):223, oct 1996.
- [55] A. M. Metcalfe and T. J. Pedley. Bacterial bioconvection: weakly nonlinear theory for pattern selection. *Journal of Fluid Mechanics*, 370:249–270, sep 1998.
- [56] A. M. Metcalfe and T. J. Pedley. Falling plumes in bacterial bioconvection. *Journal of Fluid Mechanics*, 445:121–149, oct 2001.
- [57] A. Chertock, K. Fellner, A. Kurganov, A. Lorz, and P. A. Markowich. Sinking, merging and stationary plumes in a coupled chemotaxis-fluid model: a high-resolution numerical approach. *Journal of Fluid Mechanics*, 694:155–190, mar 2012.

- [58] Christopher Dombrowski, Luis Cisneros, Sunita Chatkaew, Raymond E. Goldstein, and John O. Kessler. Self-Concentration and Large-Scale Coherence in Bacterial Dynamics. *Physical Review Letters*, 93(9):098103, aug 2004.
- [59] I. Tuval, L. Cisneros, C. Dombrowski, C. W. Wolgemuth, J. O. Kessler, and R. E. Goldstein. Bacterial swimming and oxygen transport near contact lines. *Proceedings of the National Academy of Sciences*, 102(7):2277–2282, feb 2005.
- [60] T. V. Kasyap and Donald L. Koch. Chemotaxis Driven Instability of a Confined Bacterial Suspension. *Physical Review Letters*, 108(3):038101, jan 2012.
- [61] J. R. Taylor and R. Stocker. Trade-Offs of Chemotactic Foraging in Turbulent Water. *Science*, 338(6107):675–679, nov 2012.
- [62] Romain Watteaux, Roman Stocker, and John R. Taylor. Sensitivity of the rate of nutrient uptake by chemotactic bacteria to physical and biological parameters in a turbulent environment. *Journal of Theoretical Biology*, 387:120–135, dec 2015.
- [63] Nikhil Desai, Sadegh Dabiri, and Arezoo M. Ardekani. Nutrient uptake by chemotactic bacteria in presence of rising oil drops. *International Journal of Multiphase Flow*, 108:156–168, nov 2018.
- [64] Nikhil Desai, Vaseem A. Shaik, and Arezoo M. Ardekani. Hydrodynamics-mediated trapping of micro-swimmers near drops. *Soft Matter*, 14(2):264–278, 2018.
- [65] Nikhil Desai and Arezoo M. Ardekani. Combined influence of hydrodynamics and chemotaxis in the distribution of microorganisms around spherical nutrient sources. *Physical Review E*, 98(1):012419, jul 2018.
- [66] Nikhil Desai, Vaseem A. Shaik, and Arezoo M. Ardekani. Hydrodynamic Interaction Enhances Colonization of Sinking Nutrient Sources by Motile Microorganisms. *Frontiers in Microbiology*, 10, mar 2019.
- [67] Liana Vaccari, Mehdi Molaei, Tagbo H.R. Niepa, Daeyeon Lee, Robert L. Leheny, and Kathleen J. Stebe. Films of bacteria at interfaces. *Advances in Colloid and Interface Science*, 247:561–572, sep 2017.
- [68] D. L. Valentine, J. D. Kessler, M. C. Redmond, S. D. Mendes, M. B. Heintz, C. Farwell, L. Hu, F. S. Kinnaman, S. Yvon-Lewis, M. Du, E. W. Chan, F. G. Tigreros, and C. J. Villanueva. Propane Respiration Jump-Starts Microbial Response to a Deep Oil Spill. *Science*, 330(6001):208–211, Oct 2010.
- [69] T. B. Ryerson, R. Camilli, J. D. Kessler, E. B. Kujawinski, C. M. Reddy, D. L. Valentine, E. Atlas, D. R. Blake, J. de Gouw, S. Meinardi, D. D. Parrish, J. Peischl, J. S. Seewald, and C. Warneke. Chemical data quantify Deepwater Horizon hydrocarbon flow rate and environmental distribution. *Proceedings of the National Academy of Sciences*, (50):20246–20253, Dec 2012.
- [70] B. Bunner and G. Tryggvason. Dynamics of homogeneous bubbly flows Part 1. Rise velocity and microstructure of the bubbles. *Journal of Fluid Mechanics*, 466, Sep 2002.

- [71] B. Bunner and G. Tryggvason. Dynamics of homogeneous bubbly flows Part 2. Velocity fluctuations. *Journal of Fluid Mechanics*, 466, Sep 2002.
- [72] S. Dabiri, A. Doostmohammadi, M. Bayareh, and A.M. Ardekani. Rising motion of a swarm of drops in a linearly stratified fluid. *International Journal of Multiphase Flow*, 69:8–17, mar 2015.
- [73] Frédéric Risso. Agitation, Mixing, and Transfers Induced by Bubbles. *Annual Review of Fluid Mechanics*, 50(1):annurev-fluid-122316-045003, jan 2018.
- [74] G. A. Jackson. Seascapes: the world of aquatic organisms as determined by their particulate natures. *Journal of Experimental Biology*, 215(6):1017–1030, mar 2012.
- [75] Salih Ozen Unverdi and Grétar Tryggvason. A front-tracking method for viscous, incompressible, multi-fluid flows. *Journal of Computational Physics*, 100(1):25–37, May 1992.
- [76] G. Tryggvason, B. Bunner, A. Esmaeeli, D. Juric, N. Al-Rawahi, W. Tauber, J. Han, S. Nas, and Y.-J. Jan. A Front-Tracking Method for the Computations of Multiphase Flow. *Journal of Computational Physics*, 169(2):708–759, May 2001.
- [77] T. J. Pedley, N. A. Hill, and J. O. Kessler. The growth of bioconvection patterns in a uniform suspension of gyrotactic micro-organisms. *Journal of Fluid Mechanics*, 195(-1):223, oct 1988.
- [78] A. Karimi and A. M. Ardekani. Gyrotactic bioconvection at pycnoclines. *Journal of Fluid Mechanics*, 733:245–267, oct 2013.
- [79] R. Beardon. Modelling Run-and-Tumble Chemotaxis in a Shear Flow. *Bulletin of Mathematical Biology*, 62(4):775–791, Jul 2000.
- [80] Pablo A Iglesias and Peter N Devreotes. Navigating through models of chemotaxis. *Current Opinion in Cell Biology*, 20(1):35–40, feb 2008.
- [81] Johannes Taktikos, Vasily Zaburdaev, and Holger Stark. Modeling a self-propelled autochemotactic walker. *Physical Review E*, 84(4), oct 2011.
- [82] Johannes Taktikos, Vasily Zaburdaev, and Holger Stark. Collective dynamics of model microorganisms with chemotactic signaling. *Physical Review E*, 85(5):051901, may 2012.
- [83] M. M. Hopkins and L. J. Fauci. A computational model of the collective fluid dynamics of motile micro-organisms. *Journal of Fluid Mechanics*, 455, Mar 2002.
- [84] Enkeleida Lushi, Raymond E. Goldstein, and Michael J. Shelley. Autochemotactic micro-swimmer suspensions: modeling, analysis and simulations. oct 2013.
- [85] A. J. Chorin. Numerical solution of the Navier-Stokes equations. *Mathematics of Computation*, 22:745–762, 1968.

- [86] M. Bayareh, A. Doostmohammadi, S. Dabiri, and A. M. Ardekani. On the rising motion of a drop in stratified fluids. *Physics of Fluids*, 25(10):103302, oct 2013.
- [87] B.P. Leonard. A stable and accurate convective modelling procedure based on quadratic upstream interpolation. *Computer Methods in Applied Mechanics and Engineering*, 19(1):59–98, jun 1979.
- [88] Charles S. Peskin. The immersed boundary method. *Acta Numerica*, 11, jan 2002.
- [89] B. Kubrak, H. Herlina, F. Greve, and J.G. Wissink. Low-diffusivity scalar transport using a WENO scheme and dual meshing. *Journal of Computational Physics*, 240:158–173, may 2013.
- [90] U.M. Ascher and L.R. Petzold. *Computer Methods for Ordinary Differential Equations and Differential-Algebraic Equations*. Society for Industrial and Applied Mathematics, 1998.
- [91] L. Karp-Boss, E. Boss, and P. A. Jumars. Nutrient fluxes to planktonic osmotrophs in the presence of fluid motion. *Oceanography and Marine Biology: an Annual Review*, 34:71–107, 1996.
- [92] William M. Durham, Eric Climent, Michael Barry, Filippo De Lillo, Guido Boffetta, Massimo Cencini, and Roman Stocker. Turbulence drives microscale patches of motile phytoplankton. *Nature Communications*, 4:1–7, jul 2013.
- [93] Claire B. Paris, Matthieu Le Hénaff, Zachary M. Aman, Ajit Subramaniam, Judith Helgers, Dong-Ping Wang, Vassiliki H. Kourafalou, and Ashwanth Srinivasan. Evolution of the Macondo Well Blowout: Simulating the Effects of the Circulation and Synthetic Dispersants on the Subsea Oil Transport. *Environmental Science & Technology*, 46(24):13293–13302, dec 2012.
- [94] Per Johan Brandvik, Øistein Johansen, Frode Leirvik, Umer Farooq, and Per S. Daling. Droplet breakup in subsurface oil releases Part 1: Experimental study of droplet breakup and effectiveness of dispersant injection. *Marine Pollution Bulletin*, 73(1):319–326, aug 2013.
- [95] Øistein Johansen, Per Johan Brandvik, and Umer Farooq. Droplet breakup in subsea oil releases Part 2: Predictions of droplet size distributions with and without injection of chemical dispersants. *Marine Pollution Bulletin*, 73(1):327–335, aug 2013.
- [96] Elizabeth W North, E Eric Adams, Anne E Thessen, Zachary Schlag, Ruoying He, Scott A Socolofsky, Stephen M Masutani, and Scott D Peckham. The influence of droplet size and biodegradation on the transport of subsurface oil droplets during the Deepwater Horizon spill: a model sensitivity study. *Environmental Research Letters*, 10(2):024016, feb 2015.
- [97] T. Kiørboe. *A mechanistic approach to plankton ecology*. Princeton University Press, 2008.
- [98] Kwangmin Son, Jeffrey S. Guasto, and Roman Stocker. Bacteria can exploit a flagellar buckling instability to change direction. *Nature Physics*, 9(8):494–498, jul 2013.

- [99] E. L. Cussler. *Diffusion: Mass Transfer in Fluid Systems*. Cambridge University Press, New York, NY, 2nd edition, 1997.
- [100] C. Brennen and H. Winet. Fluid mechanics of propulsion by cilia and flagella. *Annual Review of Fluid Mechanics*, 9:339–398, 1977.
- [101] Lisa J. Fauci and Robert Dillon. BIOFLUIDMECHANICS OF REPRODUCTION. *Annual Review of Fluid Mechanics*, 38(1):371–394, jan 2006.
- [102] E.A. Gaffney, H. Gadêlha, D.J. Smith, J.R. Blake, and J.C. Kirkman-Brown. Mammalian sperm motility: Observation and theory. *Annual Review of Fluid Mechanics*, 43(1):501–528, jan 2011.
- [103] Donald L. Koch and Ganesh Subramanian. Collective Hydrodynamics of Swimming Microorganisms: Living Fluids. *Annual Review of Fluid Mechanics*, 43(1):637–659, jan 2011.
- [104] M. C. Marchetti, J. F. Joanny, S. Ramaswamy, T. B. Liverpool, J. Prost, Madan Rao, and R. Aditi Simha. Hydrodynamics of soft active matter. *Reviews of Modern Physics*, 85(3):1143–1189, jul 2013.
- [105] J Elgeti, R G Winkler, and G Gompfer. Physics of microswimmers: single particle motion and collective behavior: a review. *Reports on Progress in Physics*, 78(5):056601, may 2015.
- [106] Raymond E. Goldstein. Green Algae as Model Organisms for Biological Fluid Dynamics. *Annual Review of Fluid Mechanics*, 47(1):343–375, jan 2015.
- [107] Willow R. DiLuzio, Linda Turner, Michael Mayer, Piotr Garstecki, Douglas B. Weibel, Howard C. Berg, and George M. Whitesides. Escherichia coli swim on the right-hand side. *Nature*, 435(7046):1271–1274, jun 2005.
- [108] Luis Cisneros, Christopher Dombrowski, Raymond E. Goldstein, and John O. Kessler. Reversal of bacterial locomotion at an obstacle. *Physical Review E*, 73(3):030901(R), mar 2006.
- [109] Guanglai Li and Jay X. Tang. Accumulation of microswimmers near a surface mediated by collision and rotational brownian motion. *Physical Review Letters*, 103(7):078101, aug 2009.
- [110] Mehdi Molaie, Michael Barry, Roman Stocker, and Jian Sheng. Failed Escape: Solid Surfaces Prevent Tumbling of Escherichia coli. *Physical Review Letters*, 113(6):068103, aug 2014.
- [111] Konstantin Schaar, Andreas Zöttl, and Holger Stark. Detention Times of Microswimmers Close to Surfaces: Influence of Hydrodynamic Interactions and Noise. *Physical Review Letters*, 115(3):038101, jul 2015.
- [112] George O’Toole, Heidi B. Kaplan, and Roberto Kolter. Biofilm Formation as Microbial Development. *Annual Review of Microbiology*, 54(1):49–79, oct 2000.
- [113] Thomas Danhorn and Clay Fuqua. Biofilm formation by plant-associated bacteria. *Annual Review of Microbiology*, 61(1):401–422, oct 2007.

- [114] A. Karimi, D. Karig, A. Kumar, and A. M. Ardekani. Interplay of physical mechanisms and biofilm processes: review of microfluidic methods. *Lab Chip*, 15(1):23–42, 2015.
- [115] Walter F. Paxton, Kevin C. Kistler, Christine C. Olmeda, Ayusman Sen, Sarah K. St. Angelo, Yanyan Cao, Thomas E. Mallouk, Paul E. Lammert, and Vincent H. Crespi. Catalytic Nanomotors: Autonomous Movement of Striped Nanorods. *Journal of the American Chemical Society*, 126(41):13424–13431, oct 2004.
- [116] S. Fournier-Bidoz, A. C. Arsenault, Ian Manners, and Geoffrey A. Ozin. Synthetic self-propelled nanorotors. *Chemical Communications*, (4):441, 2005.
- [117] Rémi Dreyfus, Jean Baudry, Marcus L. Roper, Marc Fermigier, Howard A. Stone, and Jérôme Bibette. Microscopic artificial swimmers. *Nature*, 437(7060):862–865, oct 2005.
- [118] Jonathan R. Howse, Richard A. L. Jones, Anthony J. Ryan, Tim Gough, Reza Vafabakhsh, and Ramin Golestanian. Self-Motile Colloidal Particles: From Directed Propulsion to Random Walk. *Physical Review Letters*, 99(4):048102, jul 2007.
- [119] Ambarish Ghosh and Peer Fischer. Controlled Propulsion of Artificial Magnetic Nanostructured Propellers. *Nano Letters*, 9(6):2243–2245, jun 2009.
- [120] Daisuke Takagi, Adam B. Braunschweig, Jun Zhang, and Michael J. Shelley. Dispersion of Self-Propelled Rods Undergoing Fluctuation-Driven Flips. *Physical Review Letters*, 110(3):038301, jan 2013.
- [121] Samuel Sánchez, Lluís Soler, and Jaideep Katuri. Chemically Powered Micro- and Nanomotors. *Angewandte Chemie International Edition*, 54(5):1414–1444, jan 2015.
- [122] Sambaeta Das, Astha Garg, Andrew I. Campbell, Jonathan Howse, Ayusman Sen, Darrell Velegol, Ramin Golestanian, and Stephen J. Ebbens. Boundaries can steer active Janus spheres. *Nature Communications*, 6:8999, dec 2015.
- [123] J. Katuri, K. D. Seo, D. S. Kim, and S. Sánchez. Artificial micro-swimmers in simulated natural environments. *Lab Chip*, 16(7):1101–1105, 2016.
- [124] Jeffrey L. Moran and Jonathan D. Posner. Phoretic Self-Propulsion. *Annual Review of Fluid Mechanics*, 49(1):511–540, jan 2017.
- [125] Daisuke Takagi, Jérémie Palacci, Adam B. Braunschweig, Michael J. Shelley, and Jun Zhang. Hydrodynamic capture of microswimmers into sphere-bound orbits. *Soft Matter*, 10(11):1784, 2014.
- [126] Juliane Simmchen, Jaideep Katuri, William E. Uspal, Mihail N. Popescu, Mykola Tasinkevych, and Samuel Sánchez. Topographical pathways guide chemical microswimmers. *Nature Communications*, 7:10598, feb 2016.
- [127] Saverio E. Spagnolie, Gregorio R. Moreno-Flores, Denis Bartolo, and Eric Lauga. Geometric capture and escape of a microswimmer colliding with an obstacle. *Soft Matter*, 11(17):3396–3411, 2015.

- [128] C. Pozrikidis. Interfacial Dynamics for Stokes Flow. *Journal of Computational Physics*, 169(2):250–301, may 2001.
- [129] David A. Edwards, Howard Brenner, and D. T. Wasan. *Interfacial Transport Processes and Rheology*. Butterworth-Heinemann, 1991.
- [130] L.E. Scriven. Dynamics of a fluid interface equation of motion for newtonian surface fluids. *Chemical Engineering Science*, 12(2):98–108, may 1960.
- [131] Jerzy Bławdziewicz, Vittorio Cristini, and Michael Loewenberg. Stokes flow in the presence of a planar interface covered with incompressible surfactant. *Physics of Fluids*, 11(2):251–258, feb 1999.
- [132] Jonathan T. Schwalbe, Frederick R. Phelan, Jr., Petia M. Vlahovska, and Steven D. Hudson. Interfacial effects on droplet dynamics in Poiseuille flow. *Soft Matter*, 7(17):7797–7804, 2011.
- [133] Shubhadeep Mandal and Suman Chakraborty. Influence of interfacial viscosity on the dielectrophoresis of drops. *Physics of Fluids*, 29(5):052002, may 2017.
- [134] Vaseem A. Shaik and Arezoo M. Ardekani. Point force singularities outside a drop covered with an incompressible surfactant: Image systems and their applications. *Physical Review Fluids*, 2(11):113606, nov 2017.
- [135] C. M. Reddy, J. S. Arey, J. S. Seewald, S. P. Sylva, K. L. Lemkau, R. K. Nelson, C. A. Carmichael, C. P. McIntyre, J. Fenwick, G. T. Ventura, B. A. S. Van Mooy, and R. Camilli. Composition and fate of gas and oil released to the water column during the Deepwater Horizon oil spill. *Proceedings of the National Academy of Sciences*, 109(50):20229–20234, dec 2012.
- [136] T. C. Hazen, E. A. Dubinsky, T. Z. DeSantis, G. L. Andersen, Y. M. Piceno, N. Singh, J. K. Jansson, A. Probst, S. E. Borglin, J. L. Fortney, W. T. Stringfellow, M. Bill, M. E. Conrad, L. M. Tom, K. L. Chavarria, T. R. Alusi, R. Lamendella, D. C. Joyner, C. Spier, J. Baelum, M. Auer, M. L. Zemla, R. Chakraborty, E. L. Sonnenthal, P. D’haeseleer, H.-Y. N. Holman, S. Osman, Z. Lu, J. D. Van Nostrand, Y. Deng, J. Zhou, and O. U. Mason. Deep-Sea Oil Plume Enriches Indigenous Oil-Degrading Bacteria. *Science*, 330(6001):204–208, oct 2010.
- [137] J. D. Kessler, D. L. Valentine, M. C. Redmond, M. Du, E. W. Chan, S. D. Mendes, E. W. Quiroz, C. J. Villanueva, S. S. Shusta, L. M. Werra, S. A. Yvon-Lewis, and T. C. Weber. A Persistent Oxygen Anomaly Reveals the Fate of Spilled Methane in the Deep Gulf of Mexico. *Science*, 331(6015):312–315, Jan 2011.
- [138] R. Camilli, C. M. Reddy, D. R. Yoerger, B. A. S. Van Mooy, M. V. Jakuba, J. C. Kinsey, C. P. McIntyre, S. P. Sylva, and J. V. Maloney. Tracking Hydrocarbon Plume Transport and Biodegradation at Deepwater Horizon. *Science*, 330(6001):201–204, Oct 2010.
- [139] William G. Pitt, Michael O. McBride, Alan J. Barton, and Richard D. Sagers. Air-water interface displaces adsorbed bacteria. *Biomaterials*, 14(8):605–608, jan 1993.

- [140] P. K. Sharma, M. J. Gibcus, H. C. van der Mei, and H. J. Busscher. Influence of Fluid Shear and Microbubbles on Bacterial Detachment from a Surface. *Applied and Environmental Microbiology*, 71(7):3668–3673, jul 2005.
- [141] Hongchul Jang, Roberto Rusconi, and Roman Stocker. Biofilm disruption by an air bubble reveals heterogeneous age-dependent detachment patterns dictated by initial extracellular matrix distribution. *npj Biofilms and Microbiomes*, 3(1):6, dec 2017.
- [142] T.S. Awad, H.A. Moharram, O.E. Shaltout, D. Asker, and M.M. Youssef. Applications of ultrasound in analysis, processing and quality control of food: A review. *Food Research International*, 48(2):410–427, oct 2012.
- [143] S. H. Lee, R. S. Chadwick, and L. Gary Leal. Motion of a sphere in the presence of a plane interface. Part 1. An approximate solution by generalization of the method of Lorentz. *Journal of Fluid Mechanics*, 93(04):705–726, aug 1979.
- [144] Sivabalan Sakthivel, Sugirtha Velusamy, Vishnu Chandrasekharan Nair, Tushar Sharma, and Jitendra S. Sangwai. Interfacial tension of crude oil-water system with imidazolium and lactam-based ionic liquids and their evaluation for enhanced oil recovery under high saline environment. *Fuel*, 191:239–250, mar 2017.
- [145] Clemens Bechinger, Roberto Di Leonardo, Hartmut Löwen, Charles Reichhardt, Giorgio Volpe, and Giovanni Volpe. Active Particles in Complex and Crowded Environments. *Reviews of Modern Physics*, 88(4):045006, nov 2016.
- [146] Vaseem A. Shaik and Arezoo M. Ardekani. Motion of a model swimmer near a weakly deforming interface. *Journal of Fluid Mechanics*, 824:42–73, aug 2017.
- [147] Diego Lopez and Eric Lauga. Dynamics of swimming bacteria at complex interfaces. *Physics of Fluids*, 26(7):071902, jul 2014.
- [148] M. Rosenberg, D. Gutnick, and E. Rosenberg. Adherence of bacteria to hydrocarbons: A simple method for measuring cell-surface hydrophobicity. *FEMS Microbiology Letters*, 9(1):29–33, sep 1980.
- [149] Michael Morse, Athena Huang, Guanglai Li, Martin R. Maxey, and Jay X. Tang. Molecular Adsorption Steers Bacterial Swimming at the Air/Water Interface. *Biophysical Journal*, 105(1):21–28, jul 2013.
- [150] Caroline Warne Zoueki, Subhasis Ghoshal, and Nathalie Tufenkji. Bacterial adhesion to hydrocarbons: Role of asphaltenes and resins. *Colloids and Surfaces B: Biointerfaces*, 79(1):219–226, aug 2010.
- [151] R. Van Houdt and C.W. Michiels. Biofilm formation and the food industry, a focus on the bacterial outer surface. *Journal of Applied Microbiology*, 109(4):1117–1131, oct 2010.
- [152] P.A. Rühs, L. Böcker, R.F. Inglis, and P. Fischer. Studying bacterial hydrophobicity and biofilm formation at liquidliquid interfaces through interfacial rheology and pendant drop tensiometry. *Colloids and Surfaces B: Biointerfaces*, 117:174–184, may 2014.

- [153] Ryan B. McLay, Hang N. Nguyen, Yuly Andrea Jaimes-Lizcano, Narendra K. Dewangan, Simone Alexandrova, Debora F. Rodrigues, Patrick C. Cirino, and Jacinta C. Conrad. Level of Fimbriation Alters the Adhesion of *Escherichia coli* Bacteria to Interfaces. *Langmuir*, page acs.langmuir.7b02447, oct 2017.
- [154] M. Rosenberg and E. Rosenberg. Bacterial adherence at the hydrocarbon-water interface. *Oil & Petrochemical Pollution*, 2:155–162, 1985.
- [155] Jasem M. Al-Besharah, Omar A. Salman, and Saed A. Akashah. Viscosity of crude oil blends. *Industrial & Engineering Chemistry Research*, 26(12):2445–2449, dec 1987.
- [156] Brent S. Murray and Eric Dickinson. Interfacial Rheology and the Dynamic Properties of Adsorbed Films of Food Proteins and Surfactants. *Food Science and Technology International, Tokyo*, 2(3):131–145, 1996.
- [157] Martin A. Bos and Ton van Vliet. Interfacial rheological properties of adsorbed protein layers and surfactants: a review. *Advances in Colloid and Interface Science*, 91(3):437–471, jul 2001.
- [158] H.C. Maru and D.T. Wasan. Dilational viscoelastic properties of fluid interfaces-II. *Chemical Engineering Science*, 34(11):1295–1307, 1979.
- [159] N.F. Djabbarah and D.T. Wasan. Dilational viscoelastic properties of fluid interfaces III Mixed surfactant systems. *Chemical Engineering Science*, 37(2):175–184, 1982.
- [160] Kenta Ishimoto and Eamonn A. Gaffney. Squirmer dynamics near a boundary. *Physical Review E*, 88(6):062702, dec 2013.
- [161] K.J. Duffy, P.T. Cummings, and R.M. Ford. Random walk calculations for bacterial migration in porous media. *Biophysical Journal*, 68(3):800–806, mar 1995.
- [162] K.J. Duffy, R.M. Ford, and P.T. Cummings. Residence time calculation for chemotactic bacteria within porous media. *Biophysical Journal*, 73(6):2930–2936, dec 1997.
- [163] R. Stocker. Reverse and flick: Hybrid locomotion in bacteria. *Proceedings of the National Academy of Sciences*, 108(7):2635–2636, feb 2011.
- [164] Guanglai Li, James Besson, Liana Nisimova, Daniel Munger, Panrapee Mahautmr, Jay X. Tang, Martin R. Maxey, and Yves V. Brun. Accumulation of swimming bacteria near a solid surface. *Physical Review E*, 84(4):041932, oct 2011.
- [165] G. A. Jackson. Simulating chemosensory response of marine microorganisms. *Limnology and Oceanography*, 32:1253–1266, 1987.
- [166] George A. Jackson. Simulation of bacterial attraction and adhesion to falling particles in an aquatic environment. *Limnology and Oceanography*, 34(3):514–530, may 1989.
- [167] Thomas Kiørboe and George A. Jackson. Marine snow, organic solute plumes, and optimal chemosensory behavior of bacteria. *Limnology and Oceanography*, 46(6):1309–1318, sep 2001.

- [168] T. Kiorboe, H.-P. Grossart, H. Ploug, and K. Tang. Mechanisms and Rates of Bacterial Colonization of Sinking Aggregates. *Applied and Environmental Microbiology*, 68(8):3996–4006, aug 2002.
- [169] R. N. Bearon. A Model for Bacterial Colonization of Sinking Aggregates. *Bulletin of Mathematical Biology*, 69(1):417–431, jan 2007.
- [170] J. T. Locsei and T. J. Pedley. Bacterial Tracking of Motile Algae Assisted by Algal Cell’s Vorticity Field. *Microbial Ecology*, 58(1):63–74, jul 2009.
- [171] R. Stocker. Marine Microbes See a Sea of Gradients. *Science*, 338(6107):628–633, nov 2012.
- [172] Enkeleida Lushi, Raymond E. Goldstein, and Michael J. Shelley. Collective chemotactic dynamics in the presence of self-generated fluid flows. *Physical Review E*, 86(4):040902, oct 2012.
- [173] Enkeleida Lushi. Stability and dynamics of anisotropically tumbling chemotactic swimmers. *Physical Review E*, 94(2):022414, aug 2016.
- [174] Greg M Barbara and James G Mitchell. Bacterial tracking of motile algae. *FEMS Microbiology Ecology*, 44(1):79–87, may 2003.
- [175] L. Turner, W. S. Ryu, and H. C. Berg. Real-Time Imaging of Fluorescent Flagellar Filaments. *Journal of Bacteriology*, 182(10):2793–2801, may 2000.
- [176] Min Jun Kim, Mun Ju Kim, James. C. Bird, Jinil Park, Thomas. R. Powers, and Kenneth S. Breuer. Particle image velocimetry experiments on a macro-scale model for bacterial flagellar bundling. *Experiments in Fluids*, 37(6):782–788, dec 2004.
- [177] Nicholas C. Darnton and Howard C. Berg. Force-Extension Measurements on Bacterial Flagella: Triggering Polymorphic Transformations. *Biophysical Journal*, 92(6):2230–2236, mar 2007.
- [178] Philip D. Cobb and Jason E. Butler. Simulations of concentrated suspensions of rigid fibers: Relationship between short-time diffusivities and the long-time rotational diffusion. *The Journal of Chemical Physics*, 123(5):054908, aug 2005.
- [179] M. De Corato, F. Greco, G. D’Avino, and P. L. Maffettone. Hydrodynamics and Brownian motions of a spheroid near a rigid wall. *The Journal of Chemical Physics*, 142(19):194901, may 2015.
- [180] Paul D. Frymier, Roseanne M. Ford, and Peter T. Cummings. Analysis of bacterial migration: I. Numerical solution of balance equation. *AIChE Journal*, 40(4):704–715, apr 1994.
- [181] K.J. Duffy, P.T. Cummings, and R.M. Ford. Random walk calculations for bacterial migration in porous media. *Biophysical Journal*, 68(3):800–806, mar 1995.
- [182] M. Abramowitz and I. A. Stegun. *Handbook of Mathematical Functions with Formulas, Graphs, and Mathematical Tables*. Dover, New York, NY, 9th printing edition, 1972.

- [183] David Saintillan. Rheology of Active Fluids. *Annual Review of Fluid Mechanics*, 50(1):annurev-fluid-010816-060049, jan 2018.
- [184] T. V. Kasyap and Donald L. Koch. Instability of an inhomogeneous bacterial suspension subjected to a chemo-attractant gradient. *Journal of Fluid Mechanics*, 741:619–657, feb 2014.
- [185] E. A Codling, M. J Plank, and S. Benhamou. Random walk models in biology. *Journal of The Royal Society Interface*, 5(25):813–834, aug 2008.
- [186] M. J. Tindall, S. L. Porter, P. K. Maini, G. Gaglia, and J. P. Armitage. Overview of Mathematical Approaches Used to Model Bacterial Chemotaxis I: The Single Cell. *Bulletin of Mathematical Biology*, 70(6):1525–1569, aug 2008.
- [187] Mehdi Molaei and Jian Sheng. Succeed escape: Flow shear promotes tumbling of Escherichia colinear a solid surface. *Scientific Reports*, 6(1):35290, dec 2016.
- [188] G. Subramanian, Donald L. Koch, and Sean R. Fitzgibbon. The stability of a homogeneous suspension of chemotactic bacteria. *Physics of Fluids*, 23(4):041901, apr 2011.
- [189] G.S. Perkins and R.B. Jones. Hydrodynamic interaction of a spherical particle with a planar boundary. *Physica A: Statistical Mechanics and its Applications*, 189(3-4):447–477, nov 1992.
- [190] B. Cichocki and R.B. Jones. Image representation of a spherical particle near a hard wall. *Physica A: Statistical Mechanics and its Applications*, 258(3-4):273–302, sep 1998.
- [191] R. B. Jones. Rotational diffusion of colloidal particles near confining walls. *The Journal of Chemical Physics*, 123(16):164705, oct 2005.
- [192] Jasem M. Al-Besharah, Omar A. Salman, and Saed A. Akashah. Viscosity of crude oil blends. *Industrial & Engineering Chemistry Research*, 26(12):2445–2449, dec 1987.
- [193] T. Kiørboe, H.-P. Grossart, H. Ploug, and K. Tang. Mechanisms and Rates of Bacterial Colonization of Sinking Aggregates. *Applied and Environmental Microbiology*, 68(8):3996–4006, aug 2002.
- [194] R. Stocker, J. R. Seymour, A. Samadani, D. E. Hunt, and M. F. Polz. Rapid chemotactic response enables marine bacteria to exploit ephemeral microscale nutrient patches. *Proceedings of the National Academy of Sciences*, 105(11):4209–4214, mar 2008.
- [195] M. Ramia, D.L. Tullock, and N. Phan-Thien. The role of hydrodynamic interaction in the locomotion of microorganisms. *Biophysical Journal*, 65(2):755–778, aug 1993.
- [196] Gaojin Li and Arezoo M. Ardekani. Hydrodynamic interaction of microswimmers near a wall. *Physical Review E*, 90(1):013010, jul 2014.
- [197] D. L. Kirchman. *Microbial Ecology of the Oceans*. Wiley, New York, 2008.
- [198] Alice L. Alldredge and Chris Gotschalk. In situ settling behavior of marine snow. *Limnology and Oceanography*, 33(3):339–351, may 1988.

- [199] Kwangmin Son, Jeffrey S. Guasto, and Roman Stocker. Bacteria can exploit a flagellar buckling instability to change direction. *Nature Physics*, 9(8):494–498, jul 2013.
- [200] S. Chattopadhyay, R. Moldovan, C. Yeung, and X. L. Wu. Swimming efficiency of bacterium *Escherichia coli*. *Proceedings of the National Academy of Sciences*, 103(37):13712–13717, sep 2006.
- [201] Kevin C. Chen, Peter T. Cummings, and Roseanne M. Ford. Perturbation Expansion of Alt’s Cell Balance Equations Reduces to Segel’s One-Dimensional Equations for Shallow Chemoattractant Gradients. *SIAM Journal on Applied Mathematics*, 59(1):35–57, jan 1998.
- [202] James D. Bowen, Keith D. Stolzenbach, and Sallie W. Chisholm. Simulating bacterial clustering around phytoplankton cells in a turbulent ocean. *Limnology and Oceanography*, 38(1):36–51, jan 1993.
- [203] Rainer M. W. Amon and Ronald Benner. Rapid cycling of high-molecular-weight dissolved organic matter in the ocean. *Nature*, 369(6481):549–552, jun 1994.
- [204] Marco G Mazza. The physics of biofilmsan introduction. *Journal of Physics D: Applied Physics*, 49(20):203001, may 2016.
- [205] Andreas Acrivos and J. D. Goddard. Asymptotic expansions for laminar forced-convection heat and mass transfer. *Journal of Fluid Mechanics*, 23(02):273, oct 1965.
- [206] R. Clift, J.R. Grace, and M.E. Weber. *Bubbles, drops and particles*. Academic Press, New York, 1978.
- [207] Jens Elgeti and Gerhard Gompper. Microswimmers near surfaces. *The European Physical Journal Special Topics*, 225(11-12):2333–2352, nov 2016.
- [208] Rasika M. Harshey. Bacterial Motility on a Surface: Many Ways to a Common Goal. *Annual Review of Microbiology*, 57(1):249–273, oct 2003.
- [209] D. J. Smith and J. R. Blake. Surface accumulation of spermatozoa: a fluid dynamic phenomenon. *Mathematical Scientist*, 34:74–87, 2009.
- [210] Darren G. Crowdy and Yizhar Or. Two-dimensional point singularity model of a low-Reynolds-number swimmer near a wall. *Physical Review E*, 81(3):036313, mar 2010.
- [211] Darren Crowdy. Treadmilling swimmers near a no-slip wall at low Reynolds number. *International Journal of Non-Linear Mechanics*, 46(4):577–585, may 2011.
- [212] P. D. Frymier, R. M. Ford, H. C. Berg, and P. T. Cummings. Three-dimensional tracking of motile bacteria near a solid planar surface. *Proceedings of the National Academy of Sciences*, 92(13):6195–6199, jun 1995.
- [213] Paul D. Frymier and Roseanne M. Ford. Analysis of bacterial swimming speed approaching a solidliquid interface. *AIChE Journal*, 43(5):1341–1347, may 1997.

- [214] MA Vigeant and Roseanne M Ford. Interactions between motile escherichia coli and glass in media with various ionic strengths, as observed with a three-dimensional-tracking microscope. *Appl. Environ. Microbiol.*, 63(9):3474–3479, 1997.
- [215] S. Wang and A. M. Ardekani. Swimming of a model ciliate near an air-liquid interface. *Physical Review E*, 87(6):063010, jun 2013.
- [216] D. Pimponi, M. Chinappi, P. Gualtieri, and C. M. Casciola. Hydrodynamics of flagellated microswimmers near free-slip interfaces. *Journal of Fluid Mechanics*, 789:514–533, feb 2016.
- [217] Renaud Trouilloud, Tony S. Yu, A. E. Hosoi, and Eric Lauga. Soft Swimming: Exploiting Deformable Interfaces for Low Reynolds Number Locomotion. *Physical Review Letters*, 101(4):048102, jul 2008.
- [218] D. Crowdy, S. Lee, O. Samson, E. Lauga, and A. E. Hosoi. A two-dimensional model of low-Reynolds number swimming beneath a free surface. *Journal of Fluid Mechanics*, 681:24–47, aug 2011.
- [219] Henry Shum and Eamonn A. Gaffney. Hydrodynamic analysis of flagellated bacteria swimming near one and between two no-slip plane boundaries. *Physical Review E*, 91(3):033012, mar 2015.
- [220] Paolo Sartori, Enrico Chiarello, Gaurav Jayaswal, Matteo Pierno, Giampaolo Mistura, Paola Brun, Adriano Tiribocchi, and Enzo Orlandini. Wall accumulation of bacteria with different motility patterns. *Physical Review E*, 97(2):022610, feb 2018.
- [221] A. J. T. M. Mathijssen, A. Doostmohammadi, J. M. Yeomans, and T. N. Shendruk. Hydrodynamics of micro-swimmers in films. *Journal of Fluid Mechanics*, 806:35–70, nov 2016.
- [222] Roberto Rusconi and Roman Stocker. Microbes in flow. *Current Opinion in Microbiology*, 25:1–8, jun 2015.
- [223] Roberto Rusconi, Jeffrey S. Guasto, and Roman Stocker. Bacterial transport suppressed by fluid shear. *Nature Physics*, 10(3):212–217, mar 2014.
- [224] Michael T. Barry, Roberto Rusconi, Jeffrey S. Guasto, and Roman Stocker. Shear-induced orientational dynamics and spatial heterogeneity in suspensions of motile phytoplankton. *Journal of The Royal Society Interface*, 12(112):20150791, nov 2015.
- [225] Andreas Zöttl and Holger Stark. Nonlinear Dynamics of a Microswimmer in Poiseuille Flow. *Physical Review Letters*, 108(21):218104, may 2012.
- [226] Andreas Zöttl and Holger Stark. Periodic and quasiperiodic motion of an elongated microswimmer in Poiseuille flow. *The European Physical Journal E*, 36(1):4, jan 2013.
- [227] L. S. Dorobantu, A. K. C. Yeung, J. M. Foght, and M. R. Gray. Stabilization of Oil-Water Emulsions by Hydrophobic Bacteria. *Applied and Environmental Microbiology*, 70(10):6333–6336, oct 2004.

- [228] Hassan Abbasnezhad, Murray Gray, and Julia M. Foght. Influence of adhesion on aerobic biodegradation and bioremediation of liquid hydrocarbons. *Applied Microbiology and Biotechnology*, 92(4):653–675, nov 2011.
- [229] Luanne Hall-Stoodley and Paul Stoodley. Biofilm formation and dispersal and the transmission of human pathogens. *Trends in Microbiology*, 13(1):7–10, jan 2005.
- [230] Roger S. Wotton and Terence M. Preston. Surface Films: Areas of Water Bodies That Are Often Overlooked. *BioScience*, 55(2):137–145, 2005.
- [231] Jacinta C. Conrad and Ryan Poling-Skutvik. Confined Flow: Consequences and Implications for Bacteria and Biofilms. *Annual Review of Chemical and Biomolecular Engineering*, 9(1):175–200, jun 2018.
- [232] K. Aderogba and J.R. Blake. Action of a force near the planar surface between two semi-infinite immiscible liquids at very low Reynolds numbers. *Bulletin of the Australian Mathematical Society*, 18(3):345–356, jun 1978.
- [233] N. Liron and S. Mochon. Stokes flow for a stokeslet between two parallel flat plates. *Journal of Engineering Mathematics*, 10(4):287–303, oct 1976.
- [234] A. J. T. M. Mathijssen, D. O. Pushkin, and J. M. Yeomans. Tracer trajectories and displacement due to a micro-swimmer near a surface. *Journal of Fluid Mechanics*, 773:498–519, jun 2015.
- [235] Arnold J. T. M. Mathijssen, Tyler N. Shendruk, Julia M. Yeomans, and Amin Doostmohammadi. Upstream Swimming in Microbiological Flows. *Physical Review Letters*, 116(2):028104, jan 2016.
- [236] Holger Stark. Swimming in external fields. *The European Physical Journal Special Topics*, 225(11-12):2369–2387, nov 2016.
- [237] Henry Shum and Julia M. Yeomans. Entrainment and scattering in microswimmer-colloid interactions. *Physical Review Fluids*, 2(11):113101, nov 2017.
- [238] Eric Lauga and Todd M. Squires. Brownian motion near a partial-slip boundary: A local probe of the no-slip condition. *Physics of Fluids*, 17(10):103102, 2005.
- [239] A. M. Ardekani and E. Gore. Emergence of a limit cycle for swimming microorganisms in a vortical flow of a viscoelastic fluid. *Physical Review E*, 85(5):056309, may 2012.
- [240] Barry L. Taylor, Igor B. Zhulin, and Mark S. Johnson. Aerotaxis and Other Energy-Sensing Behavior in Bacteria. *Annual Review of Microbiology*, 53(1):103–128, oct 1999.
- [241] Filippo Menolascina, Roberto Rusconi, Vicente I Fernandez, Steven Smriga, Zahra Aminzare, Eduardo D Sontag, and Roman Stocker. Logarithmic sensing in *Bacillus subtilis* aerotaxis. *npj Systems Biology and Applications*, 3(1):16036, jan 2017.
- [242] Donat-P. Häder and Kai Griebenow. Orientation of the green flagellate, *Euglena gracilis*, in a vertical column of water. *FEMS Microbiology Letters*, 53(3-4):159–167, may 1988.

- [243] Andrea Giometto, Florian Altermatt, Amos Maritan, Roman Stocker, and Andrea Rinaldo. Generalized receptor law governs phototaxis in the phytoplankton *Euglena gracilis*. *Proceedings of the National Academy of Sciences*, 112(22):7045–7050, jun 2015.
- [244] R. Zhang, L. Turner, and H. C. Berg. The upper surface of an *Escherichia coli* swarm is stationary. *Proceedings of the National Academy of Sciences*, 107(1):288–290, jan 2010.
- [245] Shahrzad Yazdi and Ali Borhan. Effect of a planar interface on time-averaged locomotion of a spherical squirmer in a viscoelastic fluid. *Physics of Fluids*, 29(9):093104, sep 2017.
- [246] G. J. Li, A. Karimi, and A. M. Ardekani. Effect of solid boundaries on swimming dynamics of microorganisms in a viscoelastic fluid. *Rheologica Acta*, 53(12):911–926, dec 2014.
- [247] Sandeep Chilukuri, Cynthia H Collins, and Patrick T Underhill. Impact of external flow on the dynamics of swimming microorganisms near surfaces. *Journal of Physics: Condensed Matter*, 26(11):115101, mar 2014.
- [248] Sandeep Chilukuri, Cynthia H. Collins, and Patrick T. Underhill. Dispersion of flagellated swimming microorganisms in planar Poiseuille flow. *Physics of Fluids*, 27(3):031902, mar 2015.

VITA

VITA

Research interests

My research interests include fluid mechanics of swimming microorganisms and of active suspensions. I identify and formulate application-oriented problems in these areas and use mathematical models, numerical simulations, semi-analytical methods to extract useful results.

Education

- Purdue University
PhD, Mechanical Engineering August 2015 - December 2019
- Indian Institute of Technology Kharagpur
BTech (Hons.), Mechanical Engineering July 2009 - May 2013
MTech, Thermal Science and Engineering July 2013 - May 2014

Publications**Accepted**

8. **N. Desai**, V. A. Shaik, A. M. Ardekani, “Hydrodynamics enables motile microorganisms to colonize sinking nutrient sources”, *Frontiers in Microbiology*, **10-289**, (2019)
7. **N. Desai**, S. Dabiri, A. M. Ardekani, “Nutrient uptake by chemotactic bacteria in presence of rising oil drops”, *Int. J. Multiphase Flow*, **108**, 156 (2018)

6. **N. Desai**, A. M. Ardekani, “Combined influence of hydrodynamics and chemotaxis in the distribution of microorganisms around spherical nutrient sources”, *Phys. Rev. E*, **98**, 012419 (2018)
5. **N. Desai**, V. A. Shaik, A. M. Ardekani, “Hydrodynamics-mediated trapping of micro-swimmers near drops”, *Soft Matter*, **14**, 264 (2018)
4. **N. Desai**, A. M. Ardekani, “Modeling of active swimmer suspensions and their interactions with the environment”, *Soft Matter*, **13**, 6033 (2017) (invited review article)
3. A. M. Ardekani, A. Doostmohammadi, **N. Desai**, “Transport of particles, drops, and small organisms in density stratified fluids”, *Phys. Rev. Fluids*, **2**, 100503 (2017) (invited article)
2. **N. Desai**, U. Ghosh, S. Chakraborty, “Capillary filling under electro-osmotic effects in the presence of electromagnetohydrodynamic effects”, *Phys. Rev. E*, **89**, 063017 (2014)
1. R. Agarwal, **N. Desai**, J. Chakraborty, R. Dey, S. Chakraborty, “Thermal Characteristics of Streaming Potential Mediated Flows of Non-Newtonian Fluids with Asymmetric Boundary Conditions and Steric Effect”, *Int. J. of Micro-Nano Scale Transport*, **4**, **3-4**, 147 (2014)

Under preparation/review

1. **N. Desai**, A. M. Ardekani, “Biofilms at interfaces: micro-swimmer dynamics in floating, flowing films”